REDUCED PM2.5 EMISSIONS FOR MILITARY GAS TURBINE ENGINES USING FUEL ADDITIVES

PP-1179

FINAL REPORT

AUGUST 2006

Dr. W. M. Roquemore
(Principal Investigator)
Air Force Research Laboratory

Prof. T. A. Litzinger
(Co-Principal Investigator)
Pennsylvania State University

REPORT DOCUMENTATION PAGE

Form Approved
OMB No. 0704-0188

1. REPORT DATE *(DD-MM-YYYY)*	**2. REPORT TYPE**	**3. DATES COVERED** *(From - To)*
12 August 2006	Final Report	October 2002 - June 2006

4. TITLE AND SUBTITLE
Reduced PM2.5 Emissions for Military Gas Turbine Engines Using Fuel Additives

5a. CONTRACT NUMBER

5b. GRANT NUMBER

5c. PROGRAM ELEMENT NUMBER

6. AUTHOR(S)
Dr. W. M. Roquemore

Prof. T. A. Litzinger

5d. PROJECT NUMBER

5e. TASK NUMBER

5f. WORK UNIT NUMBER

7. PERFORMING ORGANIZATION NAME(S) AND ADDRESS(ES)

Air Force Research Laboratory
Propulsion Directorate
AFRL/PRTC BLDG 490
1950 Fifth Street
WPAFB OH 45433-7251

8. PERFORMING ORGANIZATION REPORT NUMBER
PP-1179

9. SPONSORING / MONITORING AGENCY NAME(S) AND ADDRESS(ES)
Strategic Environmental Research and Development Program (SERDP)
901 North Stuart Street
Arlington, Virginia 22203

10. SPONSOR/MONITOR'S ACRONYM(S)
SERDP

11. SPONSOR/MONITOR'S REPORT NUMBER(S) PP-1179

12. DISTRIBUTION / AVAILABILITY STATEMENT
Approved for Public Release Distribution Unlimited

13. SUPPLEMENTARY NOTES

14. ABSTRACT The technical objective of this program was to develop fundamental understanding of the complex interactions of additives with the processes that lead to PM emissions from military gas turbine engines and to use that fundamental understanding to select and investigate the most promising additives for reducing PM emissions. Multiple laboratory devices were applied to study the effects of additives on soot formation processes including: a shock tube, a well-stirred reactor, premixed flames, diffusion flames, a spray flame, and a high-pressure turbulent reactor. Over the course of this program, three different classes of organic compounds (oxygenates, nitroalkanes, and nitrogen-heterocycles) were investigated along with phosphorus. Three primary mechanisms through which these compounds affected soot were uncovered through the course of the program: (1) changing the temperature in the fuel-rich, soot formation regions, (2) decreasing the production rates of aromatic species, and (3) increasing the number of C-atoms involved in strong chemical bonds such as C-O or C-N.

15. SUBJECT TERMS

16. SECURITY CLASSIFICATION OF: UNCLASSIFIED			**17. LIMITATION OF ABSTRACT**	**18. NUMBER OF PAGES**	**19a. NAME OF RESPONSIBLE PERSON**
a. REPORT	**b. ABSTRACT**	**c. THIS PAGE**			Dr. W. M. ROQUEMORE
U	U	U	UU	325	**19b. TELEPHONE NUMBER** *(include area code)* (937) 255-6813

Standard Form 298 (Rev. 8-98)
Prescribed by ANSI Std. Z39.18

PERFORMING ORGANIZATIONS AND RESEARCHERS

Air Force Research Laboratory (AFRL)
(CFM Burner, WSR, Mass Spec., T-63)

W. M. Roquemore (Principal Investigator)
V. Belovich
E. Corporan
C. W. Frayne
J. R. Gord
W. M. Harrison
A. Jacobson
H. Mayfield
R. F. Reich
R. Pawlik
D. K. Phelps
J. Zelina

United Technologies Research Center
(Kinetics, Modeling, Premixed Flame)

M. B. Colket (Lead)
R. J. Hall
D. Liscinsky

Yale University
(Kinetics and Modeling)

M. D. Smooke (Lead - Kinetics/Model)
M. B. Long
L. D. Pfefferle
B.C. Connelly
M. B. Fielding
C. S. McEnally

Innovative Scientific Solutions, Inc. (ISSI)
(Modeling and Laser Diagnostics)

V. R. Katta (Lead - Modeling)
T. R. Meyer (Lead - Diagnostics)
M. S. Brown

Pennsylvania State University(PSU)
(HP Reactor, Turbulent/Premixed Flame)

T. A. Litzinger (Co-Principal Investigator)
R. J. Santoro (Lead – HP Reactor)
D.C. Haworth
Darin J. Imschweiler
Suresh Iyer
Seong-Young Lee
Milton J. Linevsky
Matthew McKeand
Arvind V. Menon
P. Nag
K. H. Song
Juntau Wu

Army Research Laboratory (ARL)
(Opposed Jet Flame**)**

K. L. McNesby (Lead)
Valeri Babushok
Andrzej W. Miziolek
Thuvan Nguyen
R. Reynolds Skagg
W. Tsang

University of Dayton Research Institute
(Shock Tube and Well Stirred Reactor)

S. S. Sidhu (Lead - Shock Tube)
S. D. Stouffer (Lead - Well Stirred Reactor)
S. A. Corera
John Graham
M. S. Kahandawala
R.C. Streibich

LIST OF FIGURES

LIST OF FIGURES (CONT)

LIST OF FIGURES (CONT)

LIST OF FIGURES (CONT)

LIST OF FIGURES (CONT)

LIST OF FIGURES (CONT)

LIST OF TABLES

1. EXECUTIVE SUMMARY

The technical objective of this program was to develop fundamental understanding of the complex interactions of additives with the processes that lead to PM emissions from military gas turbine engines and to use that fundamental understanding to select and investigate the most promising additives for reducing PM emissions. Because of the inherent complexity of the combustion processes within gas turbine combustors and great difficulty in making measurements inside combustors, it was not possible to achieve the technical objective of this program by making measurements in gas turbine combustors. Furthermore, due to the complexity of the combustion process in a gas turbine combustor, no single laboratory flame or reactor will suffice as a model for a combustor. Therefore, multiple laboratory devices were applied to study the effects of additives on soot formation processes. These devices included a shock tube, a well-stirred reactor, premixed flames, diffusion flames, a spray flame, and a high pressure turbulent reactor. They were chosen to cover a range of complexity in terms of the chemical and physical processes involved from the shock tube, where chemical kinetics is the dominant process, to the high pressure turbulent reactor in which chemical kinetics, molecular diffusion, turbulent mixing, and spray processes are all involved. This set of devices was applied in a hierarchical manner to identify the key chemical and physical processes through which the additives affect soot.

Numerical simulation proved to be an invaluable tool for understanding the mechanisms by which additives reduce soot in the laboratory flames and reactors. Simulations were performed to the greatest extent possible for each additive. The major limitation was typically the availability of an appropriate kinetic mechanism for the additive; however, transport and thermodynamics properties were sometimes an issue as well. The research team created several new mechanisms in the course of the program, which can be obtained by contacting Dr. Vincent Belovich at the Air Force Research Laboratory, email: Vincent.Belovich@wpafb.af.mil.

Over the course of this program, three different classes of organic compounds, oxygenates, nitroalkanes, and nitrogen-heterocycles, were investigated along with phosphorus. These compounds added to the fuel are referred to as fuel additives even though their concentrations are usually in the percent range instead of the ppm that is typical for fuel additive concentrations.

Three primary mechanisms through which these compounds affected soot were uncovered through the course of the program:

1. changing the temperature in the fuel-rich, soot formation regions
2. decreasing the production rates of aromatic species
3. increasing the number of C-atoms involved in strong chemical bonds such as C-O or C-N

The temperature/thermal effect can be very significant but is also variable so this effect can be complex. As reaction temperature increases, soot production will increase initially, reach a maximum, and then decrease. At low temperatures, soot formation increases due to increasing rates of production of soot precursor species; but at elevated temperatures, soot formation decreases due to the thermal instability of the aromatic structure and key radical intermediary adducts. Hence, at low temperatures, increasing temperatures increase soot production, but at high temperatures, the converse is true. An additive can shift reaction temperatures by delaying or accelerating heat release rates, or by changing the peak flame (equilibrium) temperatures. Because of these complex dependencies, this temperature effect proved to be one of the most important to understand when comparing relative effects across the suite of devices that were used in the study.

Perhaps the most important characteristic of an additive in reducing the production rate of aromatics and, hence, soot is its ability to decrease the concentration of the propargyl radical (C_3H_3). Propargyl is known to be a key intermediate in the production of benzene (C_6H_6), the smallest aromatic species. Alternatively, increases in this radical will increase benzene and, hence, soot production. The very significant role of this single species can be recognized via the squared dependency of the rate of aromatic production on its concentration, i.e.,

$$C_3H_3 + C_3H_3 \Rightarrow C_6H_5 + H \text{ (or } C_6H_6)$$
$$d\{C_6H_5\}/dt = k\,[C_3H_3]^2$$

Through the course of the study evidence was also found that changes in "even-carbon" pathways to formation of the first aromatic ring, e.g., $C_4H_5 + C_2H_2$, can also be important under certain conditions.

Finally the presence of strong chemical bonds between carbon and oxygen or nitrogen were found to be important. Once bound in such strong bonds, these carbon atoms are not available to the carbon pool that can lead to soot production. Also, the program produced some evidence that nitrogen embedded in an aromatic ring can tie up all the carbon in that ring (e.g., pyridine) at least for a period of time leading to a reduction in the formation of aromatic species that are the building blocks of soot.

The following sections summarize findings for each additive. It is important to note that the relative roles of the above soot-reducing mechanisms can change for any single additive, depending on the experimental apparatus, fuel type or experimental conditions. In fact, such changes can be so dramatic that in one case, soot is decreased through the use of a selected additive but causes an increase or no change under other conditions. Such observed contrary effects have been commonly reported in the literature. This program has contributed significantly to the fundamental understanding of the chemistry behind such seemingly contradictory trends.

Oxygenated Compounds

The initial work on oxygenated additives focused on ethanol and its effect during the combustion of ethylene. To investigate effects of additive structure in soot reduction, experiments were also conducted in the premixed flame with dimethyl ether (DME). After completion of the ethylene studies, studies with liquid fuels were undertaken. In addition to ethanol and DME, cyclohexanone was studied because it was a component in a commercial additive that produced some soot reduction.

A very important observation can be made based upon the entirety of the results for the oxygenated compounds. Reduction in soot was achieved by the addition of oxygenated compounds in all of the devices studied, with the notable exception of the ethylene opposed-jet diffusion flame. Furthermore, reduction was achieved whether the fuel is introduced as a liquid or vapor. The ability to effect change in the suite of devices in which the key governing processes vary means that a process through which the soot reduction is effected must be common to all of the devices and that common process is chemical kinetics. Therefore, kinetic processes are driving the reduction in soot for the oxygenated additives.

Through detailed modeling studies, the mechanism by which soot is increased when ethanol is added to ethylene in the opposed-jet diffusion flame was determined to be kinetic in nature as

well. Soot was increased due to the enhancement of the "even-carbon species" pathway to benzene as a result of the production of methyl radicals from ethanol, not via the enhancement of the "odd-carbon species," as was originally expected. Detailed modeling of the results for DME and ethanol addition to the ethylene diffusion flames demonstrated that the reduction in these flames is via effects on the propargyl radical route to the first aromatic ring. These studies also demonstrated that the chemical structure of the additive does play a role in the effectiveness of oxygenated additives in reducing soot.

Due to its cyclic structure, cyclohexanone appeared to have the potential to remove six carbons from pathways to soot formation. It was studied in the various experimental test rigs to determine if it showed unusual effectiveness, which would lend credence to the hypothesis. However, its effectiveness was essentially the same as that of ethanol indicating that the mechanisms by which it reduced soot was likely the same as that of ethanol. A chemical kinetic mechanism was not readily available for this compound so detailed modeling was not pursued.

Nitroalkane Compounds

The commercial additive that was found to be effective in reducing soot was determined to be composed of nitroalkanes, cyclohexanone, toluene, and dichloroethane. The latter two compounds are known to increase soot so they were not investigated as possible additives. Cyclohexanone, as discussed above, is not unusually effective in reducing soot, so the nitroalkanes, the primary constituents in the commercial additive, were identified as the likely constituents leading to soot reduction. Consequently, these compounds were investigated in detail with experiments and modeling; the three compounds investigated were nitromethane, nitroethane, and nitropropane.

In the various test rigs, the nitroalkanes showed very complex effects on soot depending on experimental conditions and the structure of the additive. In the premixed flame, increasing the amount of nitropropane initially increased soot, but further increases in the amount of nitroproprane decreased soot. In the well-stirred reactor, all of the nitroalkanes showed similar effectiveness, but their effectiveness varied with equivalence ratio. In the atmospheric pressure spray flame and the high pressure turbulent combustor the effectiveness was dependent on the structure of the alkyl group.

Such a rich set of experimental results provide an excellent test for kinetic models of PAH and soot formation. In an effort to test a model for heptane/toluene combustion made available

by the NIST SERDP team, kinetics related to nitromethane were added to the model. Unfortunately, it failed to model accurately even the shock tube data where kinetic processes must be dominant. Therefore, we were unable to establish whether the model supported conjectures on the mechanisms underlying the trends in the premixed flame data and the opposed-jet diffusion flame results.

The NO_2 formed in the decomposition of the nitroalkanes was identified as a key intermediate species in soot reduction, so two studies were undertaken in an attempt to identify its role. The studies were performed in the shock tube and in the premixed flame. The premixed flame study yielded the very interesting and unexpected result that soot decreased even though polycyclic aromatic species increased. Detailed modeling was used to understand this trend.

Nitrogen-heterocycles

The effectiveness of the nitroalkanes led to consideration of other nitrogen-containing species as potential additives. Results available in the literature indicated that pyridine produces much less soot than benzene suggesting that the presence of the ring nitrogen is inhibiting soot formation. A possible mechanism for this effect is that the presence of the nitrogen in the ring is interrupting the addition of acetylene to the ring that is viewed as the major pathway to produce large aromatic species and soot. Pyridine was selected as the primary nitrogen-heterocycle for investigation.

Results from the addition of pyridine to the premixed flame and the turbulent spray flame showed substantial reductions in soot, so investigations in the other test rigs were undertaken. However, experiments in the shock tube show very interesting trends in soot and precursor species with addition of pyridine. Soot is unaffected at lower temperature and increases at higher temperature. Results from the well-stirred reactor showed reductions of soot at lower equivalence ratios and no effect over higher equivalence ratios, except for the highest tested at which soot increased.

A possible explanation for the complex trends that were observed across the suite of devices is that there are two competing effects: an inhibiting effect caused by the presence of the nitrogen in the ring that slows ring growth and an accelerating effect resulting from the reaction of the ring producing products that contribute to soot formation. The inhibiting effect requires the ring to remain intact and would be more important at lower temperatures.

To check this hypothesis, a chemical kinetic mechanism was created based on available pyridine chemistry which was added to the heptane/toluene mechanism. Modeling was undertaken for the shock tube and the premixed flame. The results showed that there were significant deficiencies in the model, so it was not possible to confirm or refute the hypothesis. Therefore, the data set stands as a challenge for future research after an improved mechanism can be formulated.

Phosphorus

The studies of the effects of phosphorus were done under supplemental funding for the program; therefore, the work performed was essentially screening studies to determine if the phosphorus showed sufficient reductions in soot to merit more detailed testing. Experiments were performed in the shock tube, the well-stirred reactor, the premixed flame and a combustor. In addition tests were performed in a coflow diffusion flame because this type of flame was used in the prior study at NBS that motivated the investigation. Overall the results from the various experiments are not encouraging in terms of the potential of phosphorus to reduce soot. Depending upon the device, and in some cases the experimental conditions, the phosphorus often had no effect, and in the test of a device that is closest to an actual combustor, it increased soot emissions.

An important and unexpected result, however, came out of the modeling work that was part of this study. The modeling results indicated that the addition of phosphorus would lower NOx emissions. As far as we can ascertain, this result has not been reported in the literature to date. This effect on NOx emissions was predicted prior to the studies in the CFM combustor, so those studies were modified to include measurements of NOx emissions. The measurements show that NOx decreases with the addition of phosphorus under certain test conditions, so the predictions were partially verified by the experimental data.

Implications of Results

This program represents the largest and most significant coordinated effort yet attempted to understand soot formation and fuel-based pathways to reducing it. The methodologies developed during the program led to a number of significant insights into the fundamental aspects of soot formation. The program demonstrated the value of tightly coupled experiments and modeling; unfortunately, it also showed that the lack of validated detailed kinetic models is a major stumbling block for such work. A major contribution to the soot modeling community is

the large database, documented in this report and other publications, that provide significant opportunities to validate soot models.

Unfortunately, the fundamental insights generated in the program have not led to the discovery of a compound that is truly an additive, i.e., one that functions at 1000 ppm or less in the fuel. Thus it appears that metal additives remain the only known pathway to a true additive for reduction of PM from military engines. They have been shown to be effective at reducing soot in gas turbines and diesel engines as well as in many fundamental studies. However, the potential adverse effects of metal additives on the engines and the potential health effects make the use of metals a high-risk path.

An alternative, longer-term path to reduction of PM emissions is the reformulation of military fuels. Following this path successfully will require the tight integration of chemical kinetic models capable of high-fidelity predictions of the effects of fuel composition on soot formation with the rapidly evolving simulation tools being used to design new engines. Combustor simulations will play an increasingly important role in the successful design of low emissions engines and have the potential to contribute significantly to the development of fuel-based methods to reduce PM from existing engines. Successful simulation of combustor and engine performance, including engine emissions, is critically dependent on the availability of comprehensive chemical models for realistic fuels as well as reduced models derived from the comprehensive models, that can only be created based on additional fundamental studies.

Experimental Data and Reaction Mechanisms

Experimental data and reaction mechanisms generated during this program are available on CD. If you wish a copy of the CD please contact Dr. Vincent Belovich at the following address:

Dr. Vincent Belovich
AFRL/PRTC BLDG 490
1950 FIFTH ST
WPAFB OH 45433-7251
E-mail: Vincent.Belovich@wpafb.af.mil

2. RESEARCH METHODOLOGIES

The technical objective of this program was to develop fundamental understanding of the complex interactions of additives with the processes that lead to PM emissions from military gas turbine engines and to use that fundamental understanding to select and investigate the most promising additives for reducing PM emissions. Because of the inherent complexity of the combustion processes within gas turbine combustors and great difficulty in making measurements inside combustors, it was not possible to achieve the technical objective of this program by making measurements in gas turbine combustors. Due to the complexity of the combustion process in a gas turbine combustor, no single laboratory flame or reactor will suffice. Therefore, multiple laboratory devices were applied to study the effects of additives on soot formation processes. These devices included a shock tube, a well-stirred reactor, premixed flames, diffusion flames, a spray flame, and a high pressure turbulent reactor.

These laboratory devices were chosen to cover a range of complexity in terms of the chemical and physical processes involved from the shock tube where kinetics is the dominant process to the high pressure turbulent reactor in which kinetics, molecular diffusion, turbulent mixing, and spray processes are all involved. Figure 2-1 illustrates the hierarchical nature of the set of devices. These devices were applied in a hierarchical manner to identify the key chemical and physical processes through which the additives affect soot production.

Numerical simulation of the devices proved to be an invaluable tool for understanding the mechanisms by which additives reduce soot in the laboratory flames and reactors. Simulations were performed to the greatest extent possible for each additive. The major limitation was the availability of an appropriate chemical mechanism that included the chemistry related to the additive. The research team created several new mechanisms in the course of the program, which can be obtained by contacting Dr. Vincent Belovich at the Air Force Research Laboratory, Propulsion Directorate, Turbine Engine Division, Wright-Patterson Air Force Base, Ohio.

The remainder of this chapter presents summaries of the research methodologies applied. It includes descriptions of the various devices used in the study along with the associated measurement methods. The basic computational methods are included with the CD mentioned above.

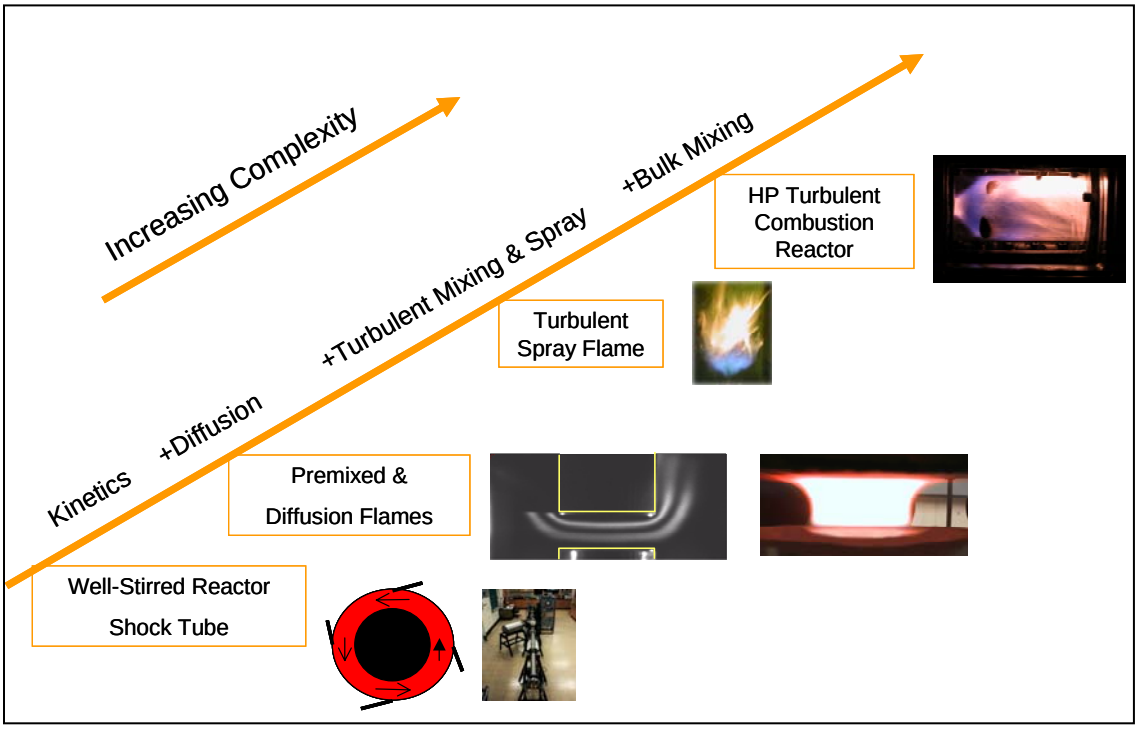

Figure 2-1. Hierarchy of Devices Used in This Study.

2.1 **EXPERIMENTAL**

2.1.1 SHOCK TUBE

A single pulse reflected shock tube, shown in Figure 2.1.1-1, will be used for all experiments. The shock tube is comprised of a 7.6 cm ID x 2.74 m long driver section, a 5.08 cm ID x 2.75 m long driven section, and a 5.08 cm ID x 0.9 m long test section. It also includes a 30.5 cm ID x 61 cm long dump tank and an evacuation subsystem. The driven and test sections are connected through a pneumatic ball valve (Jamesbury) controlled through the system's automatic digital firing system. A dump tank is connected to the system through a manually operated ball valve. The entire structure is made from 1.27 cm thick, 304 stainless steel.

As illustrated in Figure 2.1.1-1, the University of Dayton shock tube test section consists of six general purpose access ports, which can be fitted with a variety of devices such as injectors, samplers, sensors, and purging systems. It also consists of an interchangeable end plate that provides a further avenue for customizing the tube depending on the type of experiments to be conducted, either spray combustion or homogeneous combustion studies.

For the homogeneous combustion studies (see Figure 2.1.1-2) the test section is fitted with high-speed pressure transducers (PCB Piezotronics, Model 113A21), a fuel injection port connected to a sample preparation unit, optical sensor, helium purge, and an exhaust particle sampler. A 25 L sample bag (Tedlar™) is fitted after the particle sampler to trap the volatile and semi-volatile compounds.

The test fuel mixture will be prepared in a separate sample preparation unit (SPU) shown in Figure 2.1.1-3. It includes an injection port, a custom-made glass sample receiver, a 15 L silico-steel chemically inert gas handling canister (TO-Can, Restek), a pressure gauge and a stainless steel manifold for gas/sample inlet into the canister/test section connected to a vacuum pump. Stainless-steel fittings are used to prevent loss of sample. For the proposed study both the SPU and the shock tube will be heated to 120˚C to insure that all fuel fractions, especially the high molecular weight components, are in gas phase and are exposed to homogeneous combustion. Based on the desired composition of the test fuel to be investigated, liquid mixtures will made in 20 ml sample bottles and later stored in smaller 1.5 ml sample vials to ensure consistency of the mixture composition for all experiments and minimize losses due to evaporation.

Before injecting the fuel mixtures into the SPU, the unit will be flushed with ultra high purity zero grade argon before evacuating it to ensure minimum possible sample carryover from previous mixtures. After evacuating the SPU, liquid mixtures of the components of the test fuel will be injected into the glass sample receiver and allowed to evaporate into the canister and the final fuel mixture pressure will be determined. After allowing time for the fuel mixture to stabilize, the required amount of argon will be metered into the canister. From previous studies we have determined that the relative error during mixture preparation is << 0.5%. The fuel mixture composition will be verified by gas chromatography (GC) and mass spectrometry (MS) analysis by filling the test section with the fuel/argon mixture and after ~10 minutes (the approximate time it takes to complete the shock run after filling the test section during normal shock tube operation) purging it into a 25 L gas sample bag. This procedure will allow us to assess any possible losses due to surface condensation. The mass ratios from the gaseous samples will be compared against the mass ratios obtained by injecting samples of the liquid fuel mixtures. The gas used in the driver section will be predominantly helium with some argon added to help achieve the required longer dwell times that are needed to generate sufficient amount of soot to assess the impact of additives. The dwell time for this proposed study will be on the order of ~7.5 ms. For all experiments, the nominal test conditions are set by the initial state of the system and the actual test conditions are determined from the reflected shock velocity through the test gas. The high pressure, high temperature shock heated gas behind the reflected shock provides the fuels an exposure similar to that experienced in an engine combustion chamber. To determine the actual test conditions, the incident velocity is measured by dividing the distance by the arrival time of the shock past two piezoelectric pressure transducers mounted on the sidewall and end plate. The conditions in the test section will then be calculated using the shock solution model of CHEMKIN 4.0 [Howard 1996] for which the mechanism and thermodynamic data for the reacting species will be obtained for the National Institute of Standards (NIST) database.

All pressure events will be monitored using a single-sweep digital oscilloscope. Figure 2.1.1-4 shows sample oscilloscope traces. Two channels indicate events related to the pressure pulses generated from the pressure transducer mounted on the sidewall and endplate of the test section; a third indicates combustion monitored with a silicon optical pressure sensor (responsivity of 190-1100 nm) that detects the radiation emitted during combustion. The ignition

delay times will be determined with the optical sensor data and the data from the pressure transducer at the end plate (Figure 2.1.1-4). The fire control system closes the pneumatic test section isolation valve approximately 0.5 s after the diaphragm that separates driver and driven sections is ruptured, sealing the combustion products in the test section. For each test, the exhaust valve to the sampler is opened and the test section is purged with ~25 L (~10 change volumes) of dry helium immediately after the isolation valve closes. As the gas is swept from the system, the particulate fraction from the combustion products is captured on pretreated quartz filters using a high volume particulate sampler and the gas is captured in a 25 L Tedlar sample bag to identify and quantify the volatile and semi-volatile products. The filters are precleaned by baking them at 420°C to remove any organics from the surface of the filters that could contribute to soot yields. Previous studies have shown that > 98% of the combustion products are captured using this sampling method.

Measurement Methods

The mass of the collected particle samples were determined using the carbon burnoff method (LECO Model RC 412 Multiphase Carbon Determinator). The gases captured in the sample bag will be analyzed for volatile compounds by injecting gas samples directly on to the column (DB-5MS column) housed in HP5890GC-5970 MSD. Internal standards of benzyl chloride and carbon tetrachloride will be added to the sample bag to account for discrepancies in volume when purging the combustion products out of the test section. After determining the volatile compounds, the gas sample bag will be evacuated through a trap containing sodium sulfate to remove water vapor formed during combustion and an XAD-2 polymeric sorbent trap to collect the semivolatile compounds. After evacuating the sample bags, 10 µl of a mixture of semivolatile internal standards will be injected to each sorbent trap and then the traps will be extracted using 40 ml of methylene chloride (Pestisolv. Grade). The extracted sample will be concentrated and then analyzed using the Saturn GC/MS/MS 2000 (containing a DB-624MS column). A selected number of filter samples from each fuel sample covering the entire temperature range will be cut in half. One-half of the filter will be analyzed for nonvolatile compounds adsorbed on the surface of the particles by thermal desorption and Soxhlet extraction procedures and the other half will undergo LECO carbon burnoff analysis. Samples for thermal desorption will be placed in an injector probe, thermally desorbed to 350°C and analyzed using

the Saturn GC/MS/MS 2000 (DB-624MS column). For Soxhlet extraction, 10 µl of the mixture of semivolatile internal standards will be added to a portion of soot filter, then it will be Soxhlet-extracted using methylene chloride for 18 hours with an average of 4 cycles/hr (extraction efficiency >99% [Bjorseth 1985, Seizinger 1980]. The extracted samples will be concentrated to 0.5 ml and analyzed using the Saturn GC/MS/MS 2000 (DB-624MS column). Internal standards will be used to determine the mass yields using a point calibration of structurally similar classes of compounds. Where possible, standards will be used to identify products and others will be identified based on the match quality with respect to the mass spectral library. A PAH mixture of acenaphthene, acenaphthylene, anthracene, benz(a)anthracene, benzo(a)pyrene, benzo(b)fluoranthene, benzo(g,h,i)perylene, chrysene, dibenz(a,h)anthracene, benzo(k)fluoranthene, fluoranthene, fluorene, indeno(1,2,3-c,d)pyrene, naphthalene, phenanthrene, pyrene and coronene will be used as a standard. A detailed description of the experimental system and product analysis is given elsewhere [Kahandawala, 2004(a)].

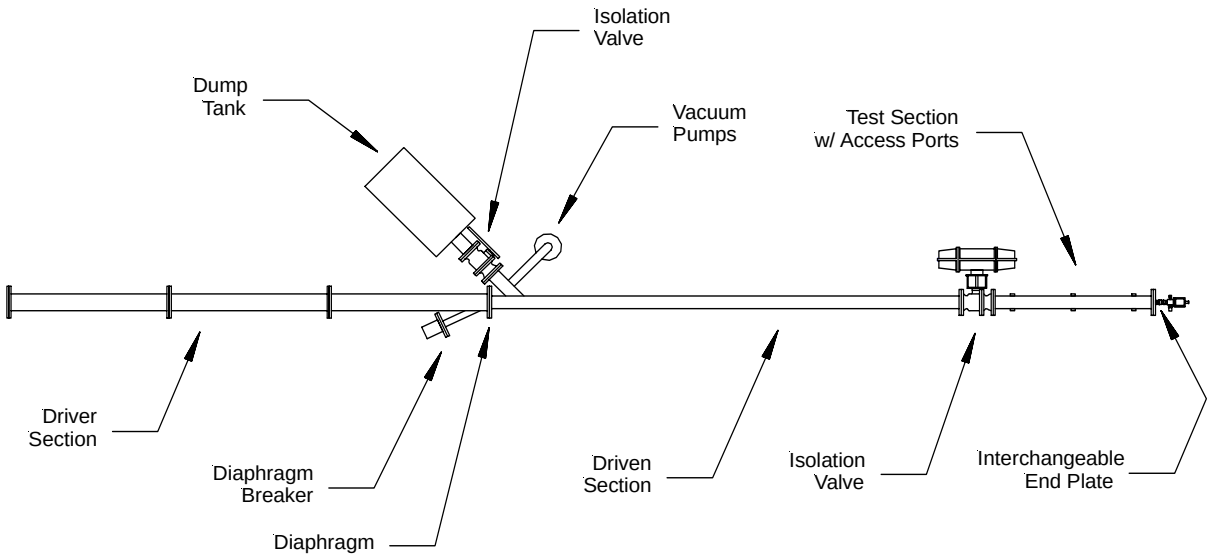

Figure 2.1.1-1. General Schematic of the Shock Tube.

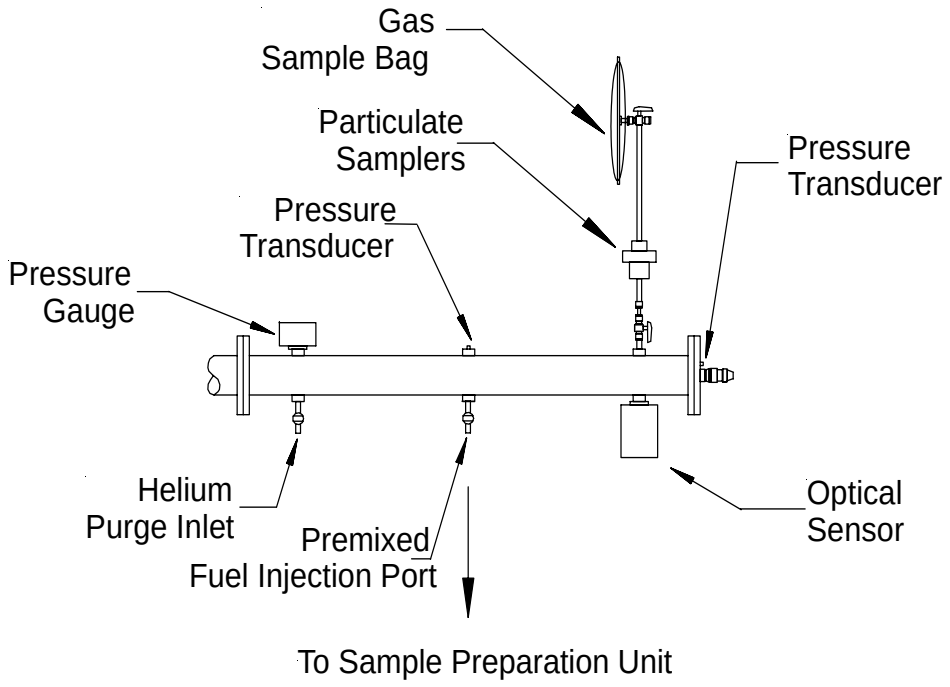

Figure 2.1.1-2. Shock Tube Test Section Configured for Homogeneous Combustion Particulate Sampling and Gas/Liquid Phase Fuel Injection.

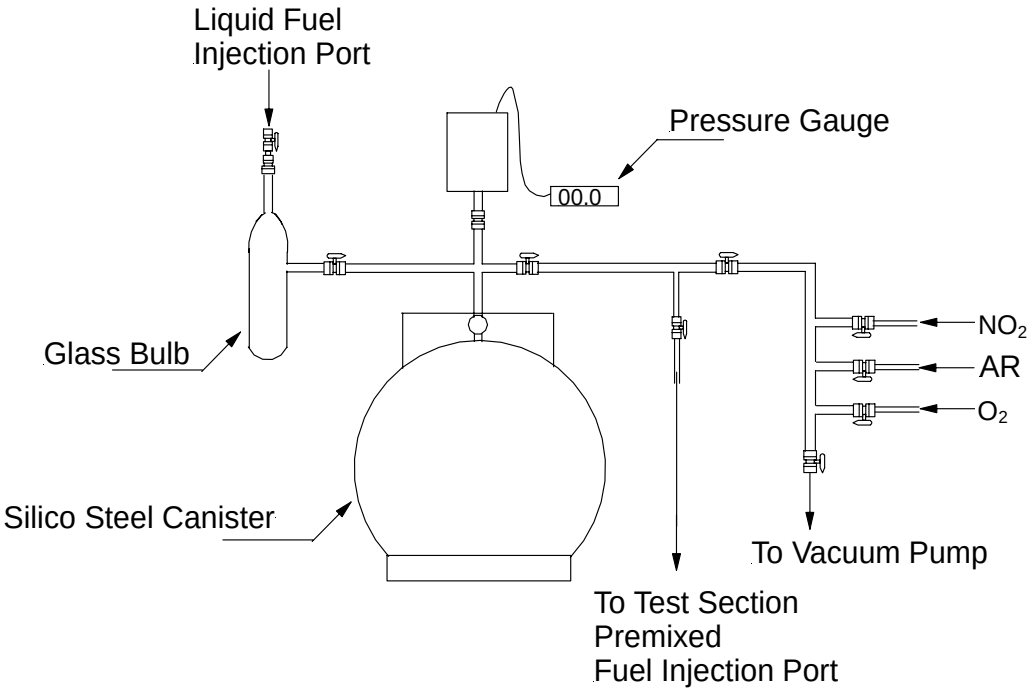

Figure 2.1.1-3. Sample Preparation Unit.

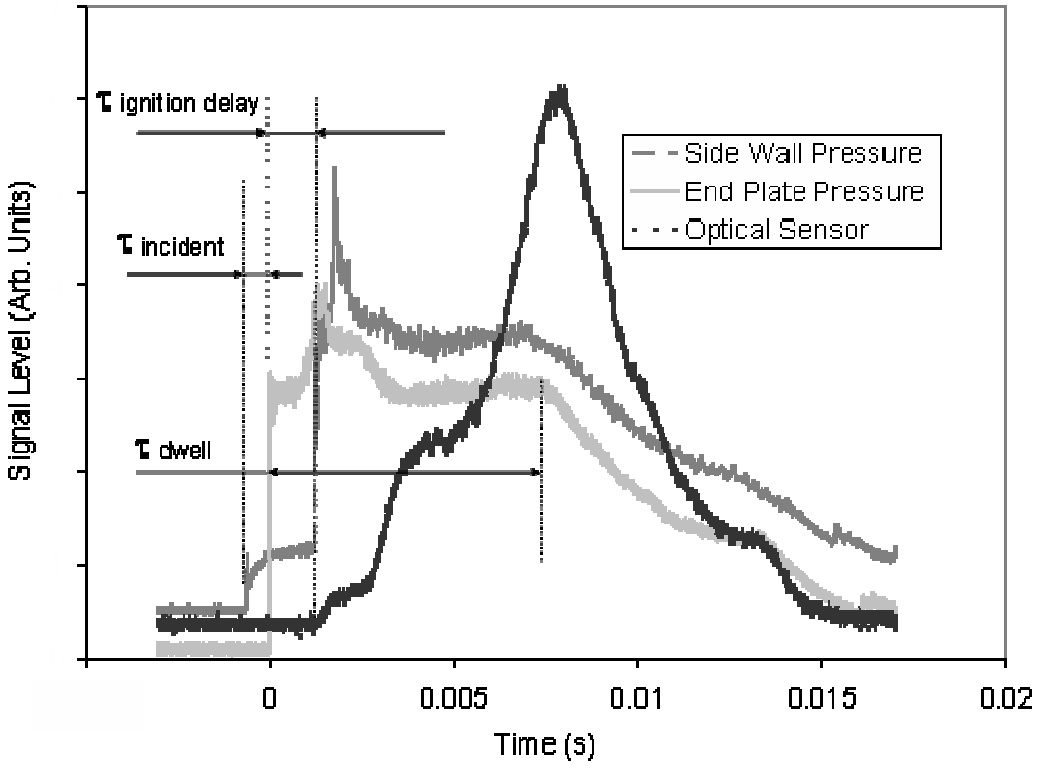

Figure 2.1.1-4. Example Oscilloscope Traces from Combustion of Heptane/Toluene Experiments Showing Pressure Transducers and Optical Sensor Data.

2.1.2 WELL-STIRRED REACTOR

The well-stirred reactor (WSR), located at Wright-Patterson Air Force Base, Ohio, is a versatile laboratory research combustor that simulates the highly turbulent combustion process in a practical gas turbine combustor. The WSR has been used to study high temperature chemical kinetics of gaseous and liquid fuel combustion, combustion stability, lean extinction and blowout limits, and gaseous pollutants (NO_x, CO, and unburned hydrocarbons) and particulate emissions in previous studies.

The purpose of the WSR is to create a combustion environment that allows chemical kinetic influences to be investigated without the physical complications associated with practical diffusion flame combustors. Specifically, the WSR uses premixed/prevaporized reactants to eliminate the complications of droplet combustion, a high velocity inlet flow to continuously stir

the reactants at high turbulence levels, and low-conductivity refractory wall materials to decrease reactor heat loss. With these simplifications, the products are only a function of the reactants, the inlet temperatures, residence time, and heat loss, and can be readily modeled with existing chemical kinetic codes, without the need to model the complications of turbulence, spray, evaporation, and mixing.

The most important characteristic that separates the WSR from other premixed combustion systems is the high rate of continuous mixing of the products and incoming reactants. Ideally, for a "Perfectly-Stirred Reactor" the intense mixing will result in a uniform profile of species and temperature throughout the reactor. However, because of practical limitations on mixing and reaction rates, it is impossible to achieve a perfectly stirred reactor over the entire combustor. For example, in the immediate vicinity of the fuel/air jets there will be a higher fraction of incoming reactants than products of combustion. However, over most of the reactor the products and incoming reactants are well mixed. The high degree of mixing with the current design is evident by the high equivalence ratio at the soot inception limit and by the measured temperature profiles across the WSR cross-section.

The toroidal WSR, as designed by Nenniger [1984] and modified by Zelina [1995] and later Stouffer [2002], has been used for the current experiments. A pair of ceramic toroid halves fitted around a jet ring injector forms the 250 ml toroidal combustor volume as shown in Figure 2.1.2-1. Prevaporized and premixed fuel and air continuously flows at high velocity around the outer diameter of the toroid, mixing and stirring the incoming reactants and the products. The mixture is then exhausted through eight radial ports at the toroid inner diameter, and turned and straightened before entering the plug flow reactor (PFR), which is a 5 cm diameter cylinder where additional measurements can be made along the axial length.

During early tests the jet ring injector was made of ceramic tubes and was cemented between the two ceramic toroid sections. This configuration was susceptible to thermal cracking and required at least a week to repair and rebuild after cracking. For this reason, an improved WSR design, using an inconel jet ring installed between the two spring-loaded ceramic sections, was developed. The inconel jet ring (shown in Figure 2.1.2-2) has 48 fuel/air jets of 0.034" diameter that are used to inject the prevaporized/premixed reactants at high subsonic or sonic velocity from the outer radius of the toroidal WSR combustor. The jet ring is cooled by nitrogen impingement cooling to avoid autoignition of the fuel/air mixture within the jet ring manifold.

The high velocity reactants continually stir and mix with the combusting gases producing high turbulence and mixing levels in the reacting flow field. The reactor is shown partially disassembled in Figure 2.1.2-3. This newer design allowed the fast detection of thermal-mechanical cracking problems and rapid replacement and reassembly of ceramic reactor parts. The WSR has several access ports for temperature, pressure, and emissions samples, located at the bottom of the WSR. All of the penetration paths to the reactor are sealed allowing the reactor to maintain a positive pressure of around 3-5 kPa above atmospheric pressure while running.

A variety of refractory materials have been used for the WSR walls. During the first set of tests, using ethylene fuel, zirconia oxide was used for the walls. Zirconia oxide was used because of its high melting point and low thermal conductivity. However, the zirconia oxide was shown to produce particles and was replaced with silicon carbide. Silicon carbide is resistant to cracking because of its higher thermal conductivity, however, the high thermal conductivity was also shown to lead to higher heat loss from the reactor, so that tests with silicon carbide reactor walls produced lower combustion temperatures than those using zirconia oxide. A third material, amorphous fused silica, was used for all of the experiments with heptane-toluene fuel mixtures. The fused silica had the lowest thermal conductivity of the three materials, which minimized the heat loss through the walls, and it had the desired property of low thermal expansion, which made it less susceptible to thermal cracking. Its melting point was below the highest flame temperatures for ethylene/air mixtures, but it was the preferred material for experiments with heptane/toluene fuel, which had lower reaction temperatures.

A facility schematic, shown in Figure 2.1.2-4, identifies components and instrumentation used for operation of the rig and acquisition of emissions samples. Heated air is premixed with fuel before entering the WSR through a jet ring injector on the outer radius of the reactor. Air and gaseous fuel flow rates are measured and controlled using thermal mass flow controllers. The air is supplied from a facility air compressor system and is dried and filtered before entering the lab. The fuel is supplied by compressed gas bottles and is regulated down to 650 kPa before passing into the laboratory. When using ethylene as a fuel, it was necessary to reduce the pressure over a series of regulators to avoid freezing the regulators.

The liquid fuel system uses a three-diaphragm pump to continuously pump the neat fuel mixture at a higher rate than required for the tests. Most of the fuel runs through a backpressure regulator that sets the pressure downstream of the pump, before passing through a heat

exchanger and back to the tank. A small fraction of the flow is then passed through a flow regulator that further reduces the pressure before it flows to the rest of the fuel control system. A combination of several pulse dampers and the two regulators creates a steady pressure source from the pulsing pump. Control valves are used to control the flow measured by a constant displacement piston flow meter using a proportional-integral-derivative (PID) loop for controlling the valve. For the early tests, a single control valve was used; later, a combination of two valves in parallel were used, a course manual valve and a fine automatic control valve. The use of the two valves in parallel significantly improved the control of the fuel flow rate from +/- 0.3% to less than +/- 0.12 % fluctuation. The additives were pumped and metered with a set of high pressure syringe pumps, and mixed with the neat fuel in a static mixer before passing through a heater and into the vaporizer nozzle. Because some of the additives in the study are sensitive to shock and rapid adiabatic compression, the syringe pumps were equipped with pressure relief valves set at 650 kPa above the normal operating pressure.

The liquid fuel is sprayed into the vaporizer using an air swirl atomizer nozzle, which uses approximately one-fourth of the total air to atomize fuel in the injector nozzle while the rest of the air is added as a coaxial stream in the vaporizer. The combination of the fuel temperature, air temperature, vaporizer air temperature and the flow rates are used to control the temperature of the air-fuel mixture entering the reactor. To avoid autoignition inside of the vaporizer both the fuel and air temperatures are limited to less than the autoignition temperature of the fuel. The vaporizer has been used to successfully and safely vaporize heptane, heptane/toluene mixtures and JP-8 fuel. The inlet temperature typically was controlled to levels between 370 and 460 K at the inlet of the jet ring injector.

An automated fail-safe retractable spark igniter is used to initiate combustion within the reactor. When the reactor is to be operated on a liquid fuel, it is first started on gaseous ethylene and then smoothly transitioned from the gaseous to a liquid fuel.

Measurement Methods

Temperatures were measured with thermocouples located in the air line, WSR jet ring, inlet, reactor, housing and stack. The reactor temperature was measured by a type B thermocouple (0.008" diameter), which was not corrected for radiation effects. Thermophoretic soot accumulation on the thermocouple caused a drop in the indicated temperature. To counter

the accumulation of soot, the capability was added to burn carbon off the thermocouple while a test was in progress. The thermocouple probes were constructed using four-hole round tubing. Two of the holes were used to guide the wires while the other two were used to direct air to the tip to burn off collected deposits. Usually a 1-second puff of air was used to clean the thermocouple. This in-situ thermocouple cleaning was performed between data collection periods. Late in the study, the capability to reliably scan the thermocouple across the cross-section of the toroidal reactor from the bottom to the top of the toroidal reactor was added to the experimental system [Stouffer 2005a]. Preliminary studies of the temperature scans have shown that the temperature can vary with position across the reactor. However, for a variety of reasons, including normal wear and tear on the reactor, emergency shutdowns, and reactor inspection, reactor reassembly resulted in small displacements of the thermocouple within the reactor. The position change of the thermocouple, in turn, affected the temperature recorded for a given set of conditions, due to the change in the spatial temperature distribution in the reactor. Unless otherwise noted, for each of the data sets obtained for a specific additive/fuel combination, the thermocouple was maintained at the same location in the WSR.

A circulating oil heater is used to cool gaseous emissions and particulate sampling probes to 420 K. Electrically heated sampling lines (420 K) were used to convey the particulate samples to the particulate instrumentation. After pulling through the heated line, samples of particulate mass were collected on filters of paper for semiquantitative and quartz for quantitative determinations of carbon particulate mass. For the samples on paper filters the smoke number was determined from reflectance measurements made before and after passing 7.08 liters of exhaust gas through the filters. Each sample required 30-60 seconds to collect. The samples acquired on the paper filters (Whatman #4) were analyzed to determine the smoke number based on relative change in reflected light from the samples.

The samples acquired on the quartz filters (Whatman type-QMA) were analyzed by measuring the amount of carbon burned off in a LECO RC-412 multiphase carbon analyzer, which measures the CO_2 produced as the filter is heated in the presence of an excess of oxygen. Early in the experimental program, comparisons of the carbon mass increase of the filter to the mass change of the filter were made and it was shown that the two were closely related. The carbon mass was used instead of the gravimetric method because it was not influenced by ambient humidity or inorganic deposits on the filter, caused by erosion of the reactor materials.

A typical plot of carbon given off by the filter versus the filter temperature is shown in Figure 2.12-5. For each of the samples there are two distinct major peaks. The low temperature peak (below 325°C) is thought to be mainly volatile carbon due to PAH, while carbon mass above 325°C is thought to be mainly due to carbonaceous soot. In addition to the carbon burn-off analysis, the quartz filter samples were also analyzed using gas chromatograph/mass spectrometry (GC/MS) Chromatoprobe analysis to determine the PAH content of the soot.

At the start of the study a 26-year-old Roseco smoke sampling unit, which was near the end of its useful life, was used to obtain samples. This unit was replaced in the third year of the study by a custom-built smoke sampling unit (see Figure 2.1.2-6) optimized to reliably obtain samples from a rich combustion environment. The new sampling unit is heated throughout and automated many of the operation tasks and has greatly improved the efficiency of collecting samples as well as the quality of the samples.

Gaseous emissions analyzers were used for on-line measurement of major species. The hot exhaust sample enters an Alpha Laval chiller, which provides the main sampling pump, condenses water vapor from the gas sample and sets the sample flow to the emissions analyzers. This dry sample is routed to a VIG Model FID 20 total hydrocarbon analyzer and a series of Horiba analyzers composed of a Model MPA-510 oxygen analyzer, and Model VIA-510 for CO and CO_2. NOx measurements were initially made with a Horiba CLA-510SS chemiluminescent NO_X analyzer; however, it was found that the analyzer was subject to interferences by the unburnt hydrocarbons present in the rich exhaust of the WSR. The analyzers are calibrated before each test using 2% certified standard gases and often spanned for verification of ~3% accuracy during the tests, using several calibration gas mixtures to check drift and maintain linearity. In addition, minor species were measured using FTIR and GC/MS analysis. The FTIR used was an MKS 2030 with a 5.1-m long gas cell path length. The FTIR software allows quick online detection of gaseous species along with subsequent detailed investigation of the spectra saved. The FTIR was also used to validate major species obtained from the on-line analyzers; it is capable of measuring species of CO, CO_2, H_2O, NO, NO_2, and other compounds that absorb infrared radiation. In practice, separation of many of the trace organic compounds from the strong background spectra of species at high concentration levels proved difficult.

In addition to the carbon burn-off analysis, the quartz filter samples were also analyzed using gas chromatograph/mass spectrometry (GC/MS) Chromatoprobe analysis to determine the

PAH content of the soot. The Chromatoprobe is a commercially available accessory for the Varian 1079 temperature programmable injection port, and it allowed sorbed organics to be thermally desorbed in the injection port for analysis by the gas chromatograph/mass spectrometer (GC/MS) [Reich 2003, Klosterman 2001]. Small strips were cut from the filters, weighed, and then placed in the sample cup of a Chromatoprobe. The Chromatoprobe was a commercially available accessory for the Varian 1079 temperature programmable injection port, and it allowed sorbed organics to be thermally desorbed in the injection port for analysis by the GC/MS.

The particulate matter characterization and measurement system (PMCMS) was brought into the WSR facility to provide analytical measurements of the WSR emissions during the experiments. Additional particulate and organic emission measurement equipment was also brought into the facility as needed to supplement the PMCMS system. The PMCMS was developed for the US Air Force and NASA under a jointly sponsored SBIR project, performed by Deposition Research Laboratory, Inc., St. Charles MO with much of the design and fabrication subcontracted to the University of Missouri, Rolla (UMR) [Chelli 1999, Chelli 2001]. The PMCMS was intended to provide a single package to characterize particulate matter aerosols with near real-time response. The instrument featured a particle sizing system that fractionated sampled aerosols according to the aerodynamic diameter of the particles, an inductively coupled plasma mass spectrometer (ICPMS) to provide elemental analyses from the fractionated aerosol streams, a GC/MS for organic analyses, and a thermal desorber-cryotrap combination intended to desorb organics from sampled aerosol particulates, concentrate the organics, and inject the organic compounds into the GC/MS for analysis. The particle sizing systems could be coupled to the ICP/MS, the GC/MS-Cryotrap system, or to a condensation nuclei counter (CNC) to provide the desired analyses from the selected aerosol size fraction. The GC/MS system also allowed normal GC injections for conventional GC/MS analyses. Figure 2.1.2-7 is a photograph of PMCMS with the major subsystems labeled.

Particle sizing by the PMCMS system was provided in two size ranges, 1-10 micron particles, and submicron particles. Particles with aerodynamic diameters in the 1-10 micron range could be size selected with a 3-stage virtual impactor system, that sorted them into the following ranges: <1μm, 1-2.5 μm, and 2.5-10 μm. It should be noted that the majority of the particulate matter observed during this study was in the size range below 1 μm. Figure 2.1.2-8 diagrams the major flowpaths of the PMCMS system.

Particle size profiles for submicron particles could be generated with a radial differential mobility analyzer (RDMA). Input aerosol to the RDMA passed through a bipolar charger, which utilized $_{84}Po^{210}$ to ionize the aerosol and thus generate a Boltzmann distribution of charges on the entrained particulates. The RDMA was fabricated after the design of Zhang [1995] to separate charged particles according to the flow rate of sample aerosol, flow rate of a particle-free sheath gas, and according to the voltage set on the plates of the RDMA. Charged particles of controlled electrical mobility could transit the RDMA at a given voltage and flow rate, and the mobility was strongly influenced by the particle diameter. By varying the voltage on the RDMA, varying sizes of aerosol particulates could be passed through the RDMA.

Particulates sampled by the PMCMS could be also characterized for elemental composition with the ICPMS system. Sampled aerosol, or aerosol from the particle sizing system, could be passed into the ICPMS by replacing the flow line from the normal ICPMS liquid sample nebulizer with the selected outlet line from the particle sizing system. Outlet lines from one of the virtual impactors or from the RDMA could be connected to the inlet of the ICPMS. The ICPMS component of the PMCMS was a Varian Ultramass™ ICPMS. The capability of the ICPMS was tested by doping selenium (Se) in small quantities into the ethanol additive to the WSR fuel and detecting Se in the particulates measured generated during combustion. Se was evenly distributed to all sizes of the fine particulates. This prompted questions whether the Se was present as fine combustion particulates or if it was present in the gas phase of the sample. However, because metals were not a major part of the program, the work with the ICPMS was not pursued further.

Particle number densities were measured with a CNC. Initially a MET One Airborn Special CNC was used but had too low of a maximum concentration level, and was replaced with a TSI Model 3022A that allowed concentrations 1000 times greater to be measured. The CNCs were also coupled with the output of the RDMA to measure particle size distributions.

The GC/MS component was a commercial ion trap GC/MS system (Varian Saturn 2200). The gas chromatograph was equipped with a temperature programmable split/splitless injector (Varian Model 1079) and an option for subambient oven operation with liquid nitrogen coolant. Subsequent to the delivery of the PMCMS a subambient cooling option, using liquid carbon dioxide, was added to the Model 1079 injector. Also, subsequent to the delivery, the Saturn ion

trap mass spectrometer was modified to permit selected ion storage (SIS) and MS/MS experiments.

The gas chromatograph of the GC/MS system was further modified as a component of the PMCMS system, with the addition of a desorber-cryotrap system mounted on top of the GC/MS system and controlled through the gas chromatograph's valve control circuits using solenoid valves. The desorber-cryotrap system was designed to admit a sample of aerosol from the particle sizing system, to a wide bore segment of deactivated fused silica tubing that ran through a heated block. At the end of the initial heating block, the flow changed directions to run through a second segment of fused silica tubing that ran through another section of heated block, but with an outer concentric jacket. The cryotrap operation was performed by flowing cold carbon dioxide, derived from a liquid CO_2 tank, through the outer jacket. Particulates flowing through the initial length of heated fused silica tubing were heated to desorb semivolatile organic compounds expected to be sorbed onto these particles. After heating, the sample was expected to consist of the carrier gas, particles, and desorbed gas-phase organics. When the sample passed into the second section of the system and the liquid CO_2 was allowed to flow from the coolant tank, the particles would be carried out of the system while the gas-phase organic compounds were expected to condense on the walls of the second segment of fused silica tubing. Following the end of a trapping period, the valving was switched to pass carrier gas instead of sample through the cryotrap, reverse the flow so that the injected organics flowed into the column, and the liquid CO_2 flow was discontinued so that the heated block would heat the trap and revolatilize these trapped organics. This system was fabricated from the designs of Gehrke [2001]. A 4-port low dead volume valve, positioned in the oven, allowed either desorbed materials from the cryotrap-desorber or material from the injection port to be directed onto the head of the GC column. Figure 2.1.2-9 illustrates the oven plumbing of the Saturn GC/MS and the cryotrap-desorber system.

In an effort to examine the operation of the system with known particulates, a NIST-traceable supply of monodisperse glass microspheres was obtained, and a weighed sample was coated with a known standard solution of PAH compounds. The coated microspheres were used to generate an aerosol which was sampled through the cryotrap-desorber/GC/MS and the cryotrap-desorber system appeared to exhibit discrimination in favor of PAH near naphthalene in volatility.

The PMCMS components were controlled by a personal computer running Windows 95 plus commercial instrument control and data acquisition software. The ICPMS was controlled and reported data through the Varian WinMass software. The GC/MS system was controlled by Varian STAR instrument control software, which provided instrument control, gas chromatographic and mass spectral data display, quantitative analysis, and library search capability. Automated solenoid valves, mass flow controllers, and the RDMA in the particle sizing system were controlled and monitored using Opto-22 software and components.

The instrumentation provided by PMCMS was supplemented with particle size profiling instrumentation constructed by combining commercial linear differential mobility analyzers (TSI 3080 SMPS) that included data acquisition and control computers to rapidly provide profiles of particle counts versus particle diameter. The PMCMS RDMA and CNC could provide similar profiles, but the control software was less convenient, requiring 30 to 40 minutes per size distribution from the RDMA versus 1 to 3 minutes for the TSI SMPS system. Therefore, the TSI instruments were used during times that they were available.

Following the initial checkout of the PMCMS, the heated sample line and probe were adapted to the WSR installation. Initial combined operations between the WSR and PMCMS were conducted using ethylene as WSR fuel. Figure 2.1.2-10 shows the variation in the particle size distribution as the WSR was operated with ethylene at varying fuel/air ratio (Phi). It is thought that the large particle sizes measured are due to coagulation of the high concentration aerosol during the long residence time in transit to the instrument.

One of the lessons learned over the course of the study was the large effect that coagulation had on the measured versus the actual particle number densities. In comparison to particle number and size distribution measurements, particle mass measurements are less susceptible to transport system effects, such as coagulation. For the tests in the WSR the particle number densities often exceeded 10^8 particles/CM3 even at dilution levels as high as 98%. At such concentrations the soot rapidly coagulates to shift to higher apparent sizes and lower apparent number densities. This tendency to coagulate was decreased by reducing the sample transit time, which was accomplished by decreasing line lengths and increasing diluted sample volume flow, and by increasing dilution. The size distribution obtained at the start of the study in Figure 2.1.2-10 was measured at low flow rates (1.25 lpm) over a long tube (10 m). As a result of cooperation with the group at NIST [Manzello 2005] a higher dilution sampling technique was

developed based on work by Zhao [2003]. Earlier measurements of particle size distributions have been obtained using a probe with dilution limited to approximately 50:1 by the ability to accurately subtract mass flow measurements in order to determine the dilution ratio. With the high dilution ratio probe the dilution ratio was determined by comparing measurements of the CO in the diluted and undiluted streams. The particle size distributions shown in Figure 2.1.2-11 were obtained using an SMPS system with higher flow rates (10 lpm), and a shorter sampling line length (3 m) than used for the particle size distributions shown in Figure 2.1.2-10. A further decrease in the peak particle size is shown with the increase in the dilution ratio.

There was the intent to repeat a subset of the experiments with this high dilution sampling system toward the end of the program, with the intent of obtaining higher quality data for particle number densities and size distributions. However, a major steam leak occurred in the laboratory filling it with saturated steam and disabled many of the instruments and we were not able to make further measurements of particle number and particle density before the end of the program.

In the second year of the project, emphasis shifted to measurement of organic precursors of soot, with benzene being selected as a representative precursor that was included in the combustion models supporting the WSR experiments. In order to measure benzene produced in the WSR, gases were sampled from a cooled probe in the bottom of the reactor and pulled through a glass sample bulb. Several options were then tried in order to measure benzene in the WSR exhaust gases using the GC/MS system of the PMCMS. These options included direct injections of gases trapped in the sampling bulb, Solid Phase MicroExtraction (SPME) sampling of the gases trapped in the sampling bulb, direct mass spectral measurement of benzene in the gases, and sampling organics in the effluent gases via a sorbent collection system.

Gas injection and SPME could be conducted together, with suitable design of the WSR experiment. When the sample line became available, a clean gas-sampling bulb was fitted and the stopcocks were opened for a minute to allow the bulb contents to become fully replaced with WSR effluent gases. A short GC/MS run was used to analyze for benzene, and two or three gas aliquots of 100 μL could be withdrawn from the bulb and injected into the GC/MS while the WSR remained on a condition, usually to measure smoke number or collect other data. An SPME fiber was inserted into the sample bulb with the exhaust gases, and typically exposed for 1 minute. A field sampling SPME fiber was used to allow the fiber to be withdrawn and stored

until the GC/MS was available for analysis with little concern for sample degradation. A longer GC/MS run was used to analyze the exposed SPME fiber.

The gas injections provided benzene data, but statistical evaluation of the data showed a need for improved precision. The SPME technique also yielded benzene responses, along with data from a number of other gas phase compounds, which included aromatic compounds, alkenes, polynuclear aromatic hydrocarbons (PAH) and other organics probably produced as products of incomplete combustion.

The interest in focusing on benzene in the WSR effluent gases, and the need for faster analyses, greater convenience, and additional data prompted modifications to the GC/MS to bypass the gas chromatographic column and directly introduce sample gases into the mass spectrometer. These direct sampling modifications involved addition of another rotary, low dead volume valve into the oven region, along with modifications to route the sample from the valve into the mass spectrometer inlet, while retaining access for the normal GC column. A further modification to achieve these ends was the addition of a restricted flow adapter (MS No-Vent™, SGI, Inc.) between the column and the mass spectrometer transfer line. This feature was expected to allow a gas sample from the sampling valve to be admitted to the mass spectrometer, to allow access from the GC column, and further allow rapid GC column changes without venting. The MS No-Vent™ was found to increase the carrier gas head pressure necessary to achieve the previously used column flows beyond the pressures available with the GC/MS. This limited the ability to use this configuration. Figure 2.1.2-12 shows the plumbing sketch for the GC/MS with the gas sampling valve and cryotrap-desorber.

By the time direct gas sampling was being considered, the ion trap mass spectrometer had been altered with the ability to perform selected ion storage (SIS) and mass spectrometry/mass spectrometry experiments. In the Varian Saturn ITMS, ionization takes place by electron impact processes by filaments within the ion trap. During SIS experiments, the electron impact ionization process is complemented by setting the trap to store only selected ions while rejecting all other ions. At the end of an ionization period, the stored ions can then be evaluated directly by the ITMS's detector or they can serve as precursor (mother) ions in MS/MS experiments to follow the fragmenting of the selected precursor ions.

A series of direct gas sampling methods were developed and evaluated, using normal mass spectral procedures to analyze for benzene, MS/MS procedures, and SIS procedures. The

GC/MS system was calibrated for benzene using samples from a sample bag filled with a known volume of dry air and spiked with a known volume of benzene to produce air samples ranging in concentration from 10 – 1600 μg/L. During the initial attempts to analyze these standards, it was noted that while using a large (500 μL) sample loop on the direct sampling valve, the benzene peak appeared to split. Further analyses of the mass spectra indicated that the benzene mass spectrum distorted at the high concentration regions of the analysis bands. These distortions were attributed to space charging, a phenomenon that was encountered with early attempts to use ITMS instruments for GC/MS. During space charging problems, the concentration of ions in the ion trap became so high that the sample ions distorted the electrical field impressed on the trap by the electrodes and control electronics. The effect is seen in distorted mass spectra, with peaks being assigned to erroneous mass-to-charge values. The ITMS response for benzene was monitored over several further runs while a series of sample loops, with volumes ranging from 10-500 μL, were tried. This resulted in standardization for the technique with 50 μL sample loops.

A final technique utilized to measure benzene in the WSR effluents was to sorb benzene and other organics onto Tenax resin packed in a tube that matched the normal Varian injection port liner, and thermally desorb the organics into the GC/MS system for analysis. This proved cumbersome because of the design of the injection port, which utilized septum supports and needle guides in an upper section of the injection port, which had to be reassembled to place each tube in for desorption. When using this technique it was found that several of the major components were overloaded, producing asymmetric and noisy peaks. Potential existed to improve the technique by optimizing the sample size collected and by storing exposed tubes for analysis after the WSR experiment was completed. Adsorbent tube desorbers are commercially available, but their costs precluded their selection for the WSR experiments.

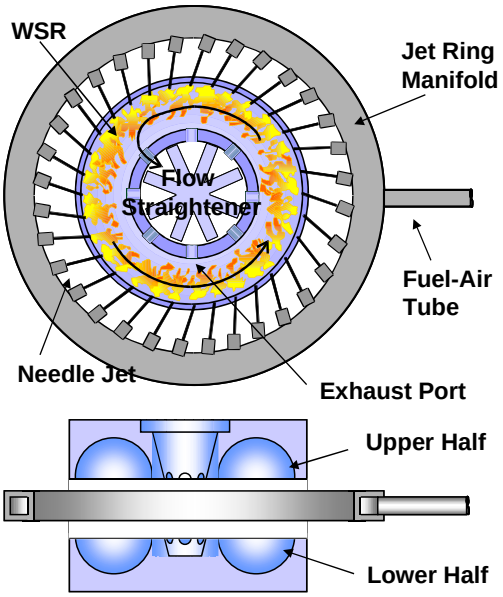

Figure 2.1.2-1. Schematic of Toroidal WSR.

Figure 2.1.2-2. Inconel Jet Ring Containing 48 Fuel/Air Jets.

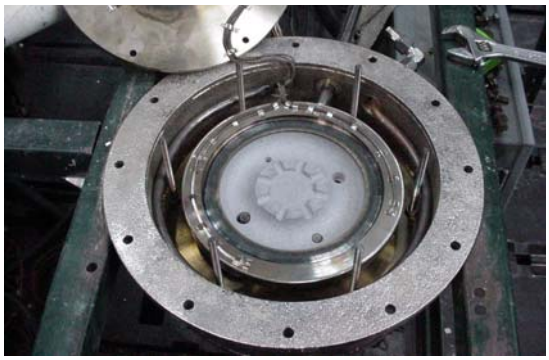

Figure 2.1.2-3. Jet Ring on Top of Bottom Half of Reactor Mounted in Housing.

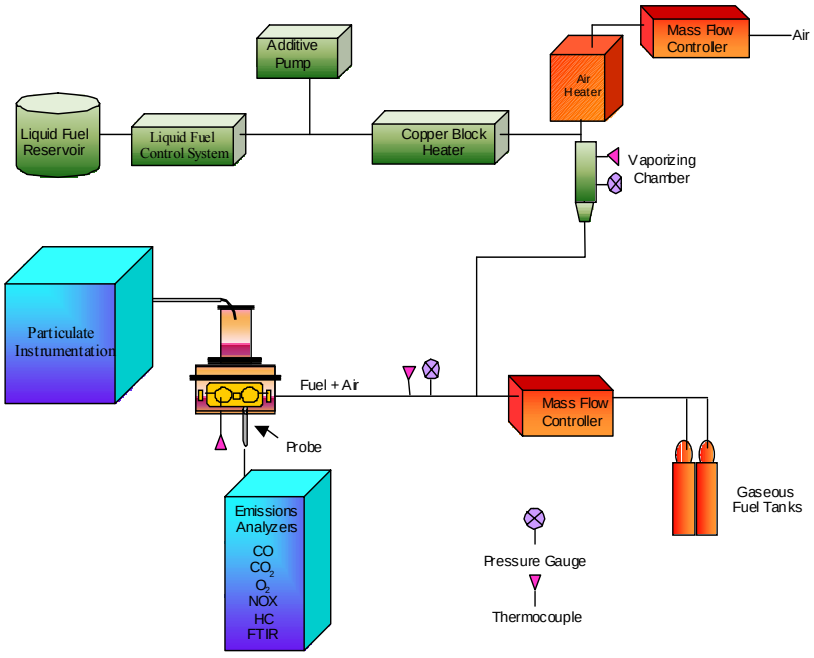

Figure 2.1.2-4. Well-Stirred Reactor Air, Fuel and Instrumentation Systems.

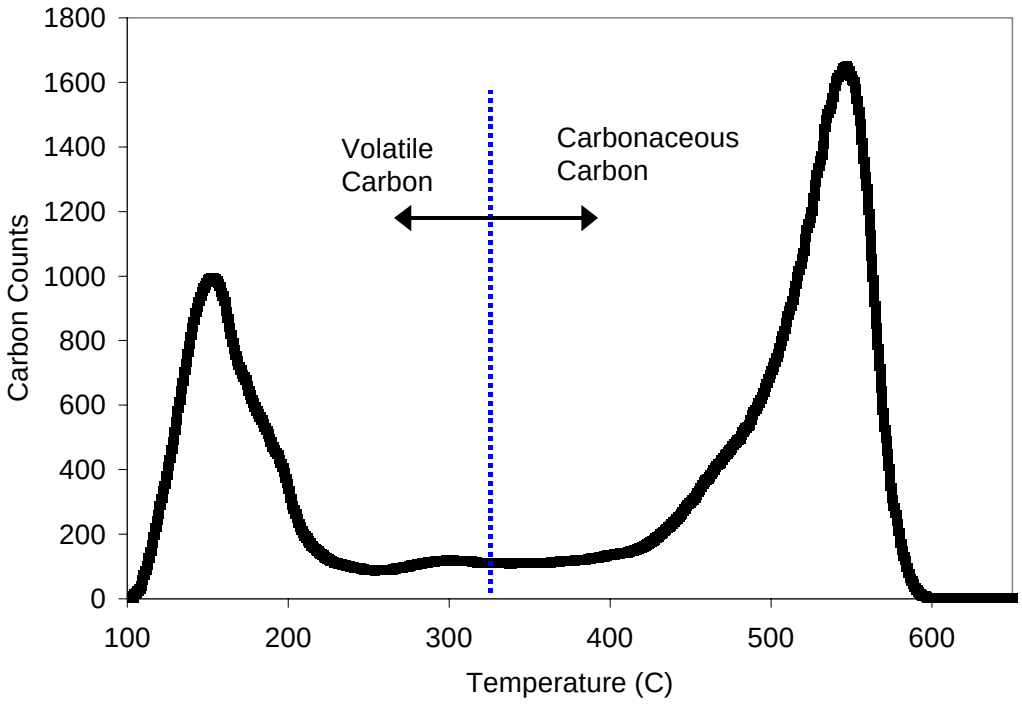

Figure 2.1.2-5. Carbon Signal vs Burn-off Temperature for a Typical Quartz Filter Sample.

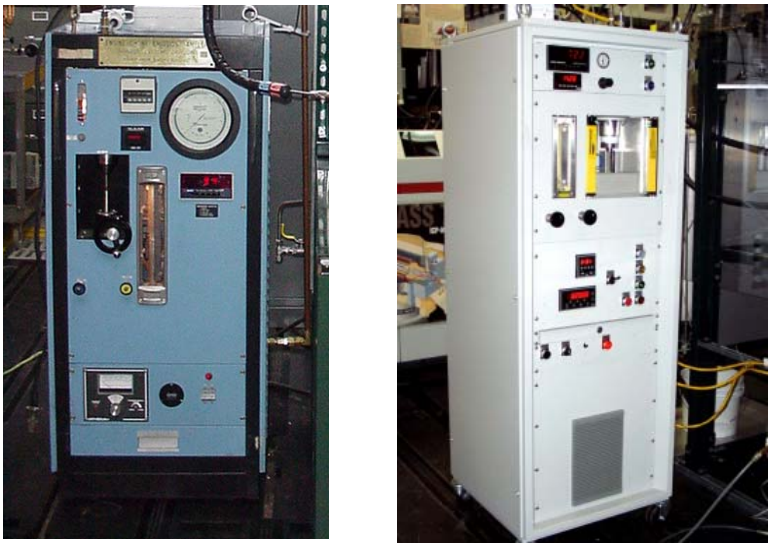

(A) (B)

Figure 2.1.2-6. (A) Old Smoke Sampling Unit. (B) Custom-Built Smoke Sampling Unit.

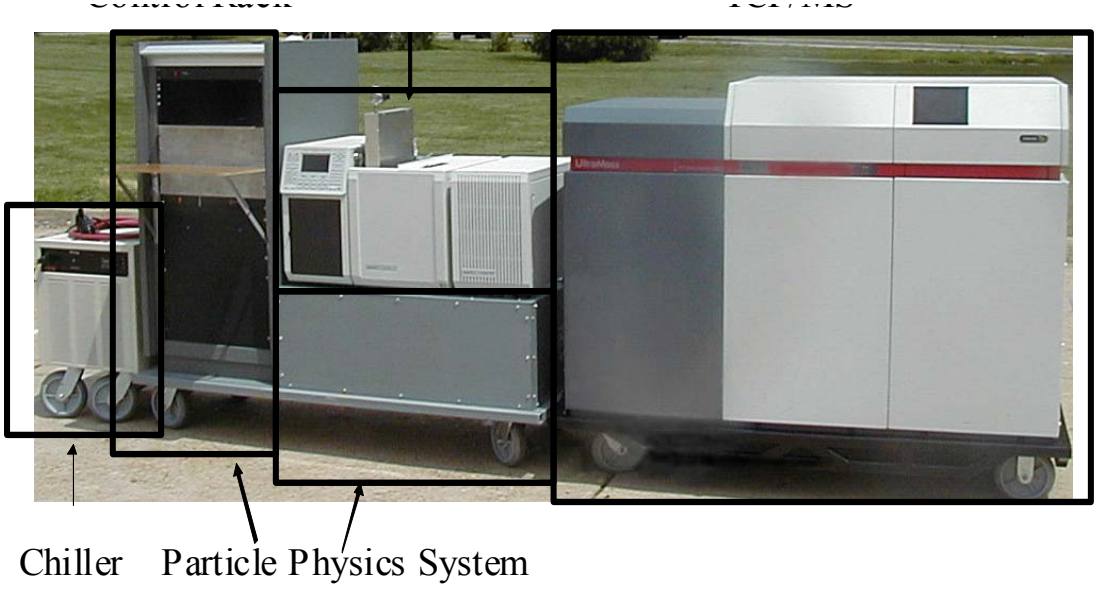

Figure 2.1.2-7. PMCMS System.

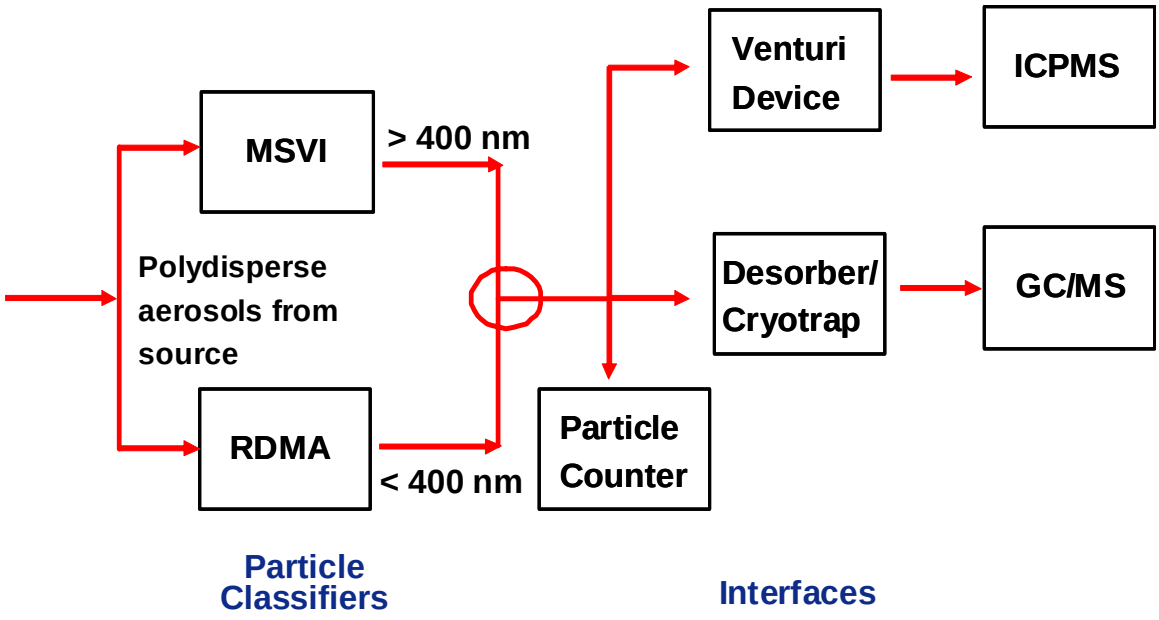

Figure 2.1.2-8. Diagram of Major PMCMS Subsystems.

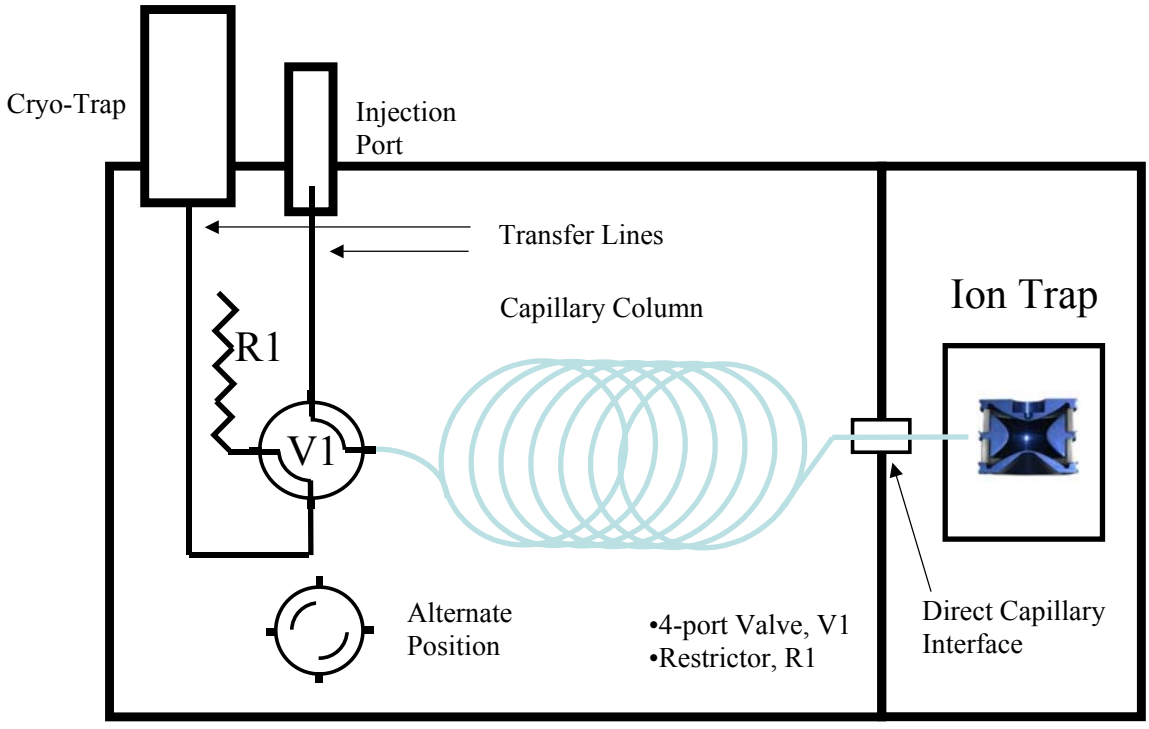

Figure 2.1.2-9. Plumbing Diagram of Saturn GC/MS Subsystem of PMCMS in the Original Oven Configuration.

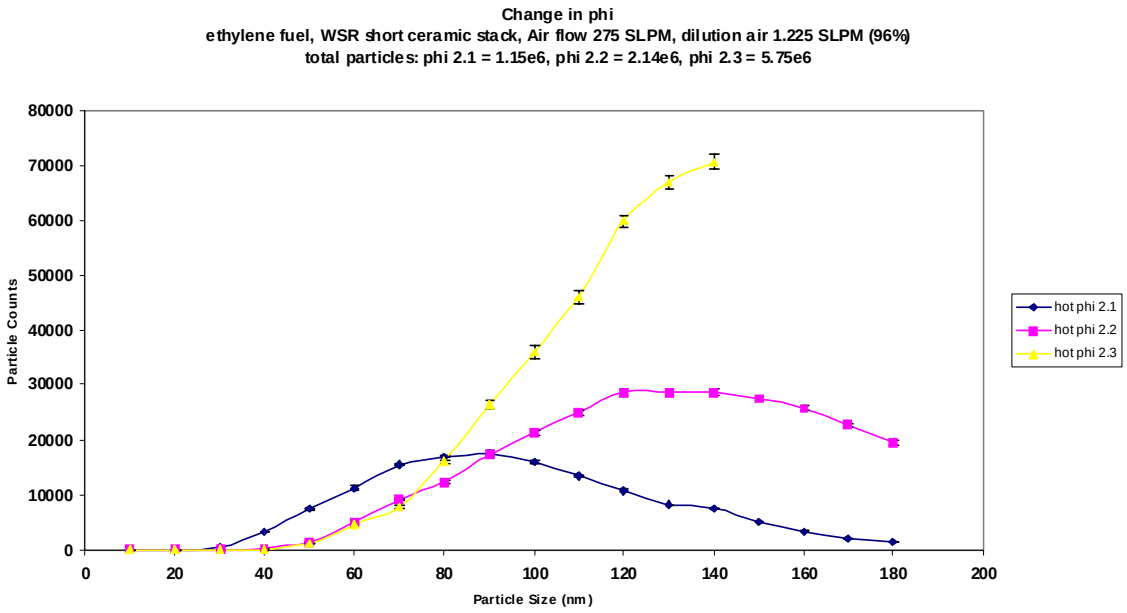

Figure 2.1.2-10. Particle Size Distribution for WSR on Ethylene Fuel vs Equivalence Ratio.

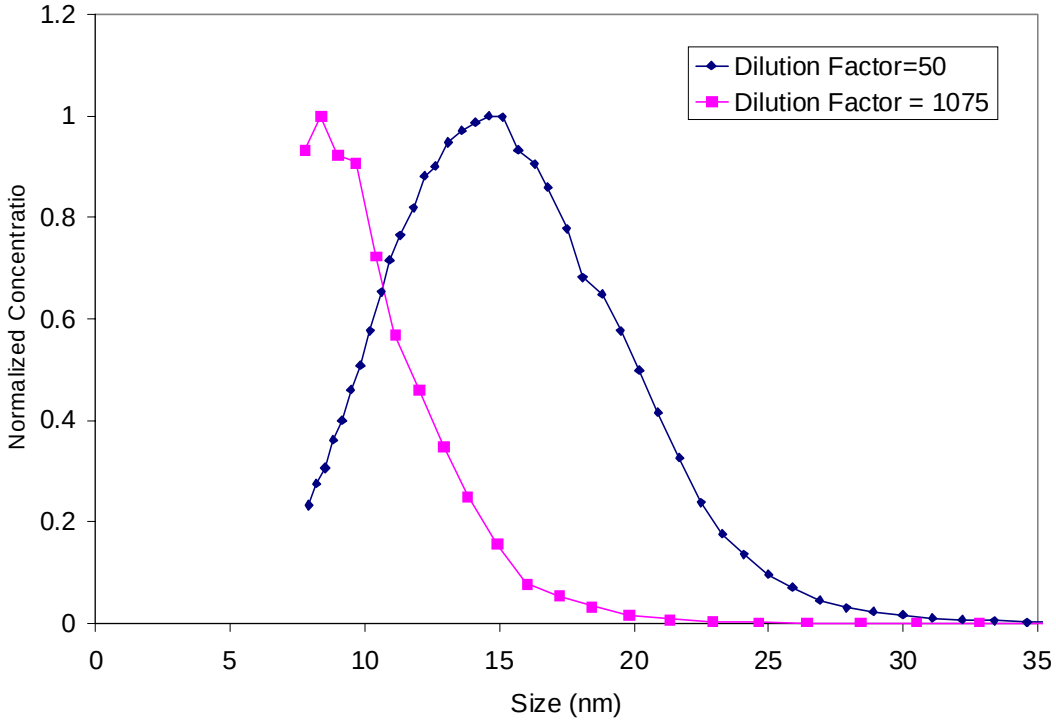

Figure 2.1.2-11. The Effect of Dilution Ratio on the Normalized Particle Size Distribution for the WSR (Fuel: 80%Heptane/20%Toluene).

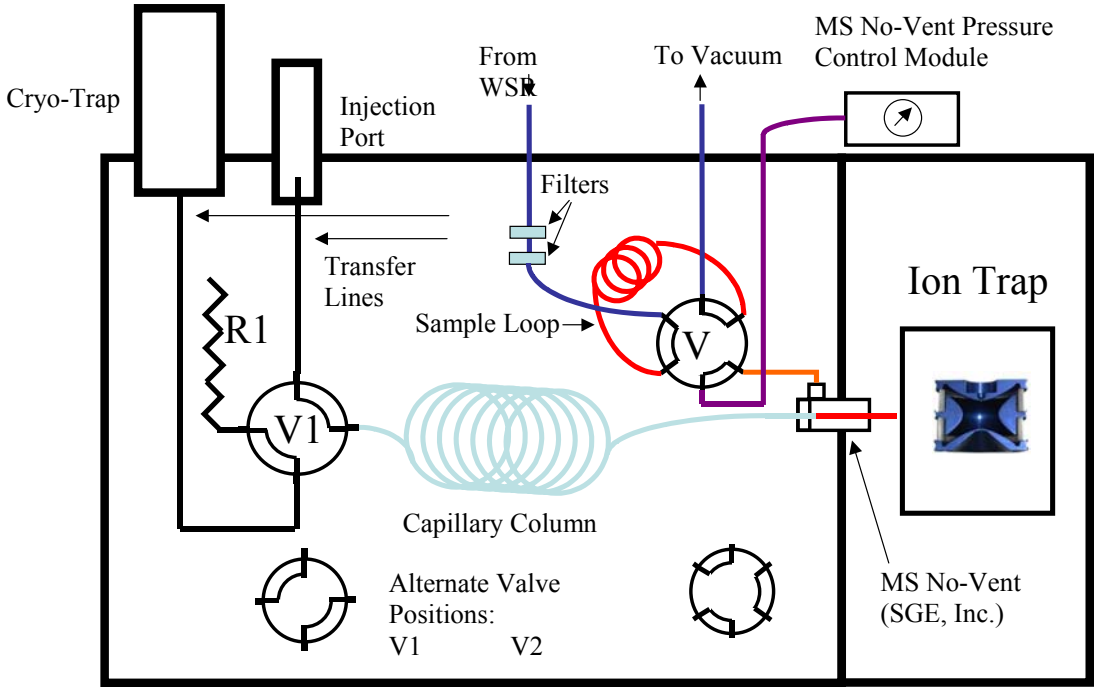

Figure 2.1.2-12. Plumbing Diagram of Saturn GC/MS Configured for Direct Sampling of Gases from WSR.

2.1.3 PREMIXED FLAME (PSU)

An unconfined flat laminar premixed flame was established using a commercial McKenna Burner with a 60.2 mm-diameter water-cooled porous plate. The flame was stabilized using a flat plate. To facilitate measurements of profiles using line-of-sight optical methods, the burner could be moved in a vertical direction with a precision of 100 μm, using an adjustable jack. The air, fuel and additive delivery systems are illustrated in Figure 2.1.3-1. The air to the burner was metered with a rotameter, and the flow rate of fuel was controlled by a mass flowmeter. The rotameter and mass flowmeter were calibrated with bubble meters. Additives, which were supplied by a precision syringe pump, were vaporized and mixed with the fuel in a vaporizer. The temperature of the vaporizer was maintained at 80ºC by electric heating tape, which is controlled by an Omega temperature controller.

Two mixing processes occurred in turn: first, fuel mixed with additive in the vaporizer; after that, the fuel/additive mixture mixed with preheated air in a 160 cm-long mixing chamber.

The mixing chamber consists of 5 equally spaced orifices mounted inside the chamber, and the mixing chamber length-to-diameter ratio was roughly 80 in order to attain fully mixed conditions. To prevent condensation of the ethanol, the mixing chamber and fuel tube were heated with 5 heating tapes. By varying the electric voltage applied to the heating tapes, the temperature of the flow at the inlet of the burner was maintained at 53ºC for all mixtures regardless of whether a liquid additive was introduced. This approach ensures that all the flames were established at the same ambient condition.

Measurement Methods

A variety of diagnostic methods were applied to these flames including laser induced incandescence (LII) and extinction for soot, laser induced fluorescence (LIF) for PAH, and thermocouples for temperature measurements. Figure 2.1.3-2 illustrates the configurations of the equipment used in these measurements. In studies using NO_2, thermocouples were of limited use due to the chance of catalytic reactions of the NO_2 on the thermocouple; therefore, alternative methods including potassium line reversal were applied (Figure 2.1.3-3).

LII was applied to obtain the spatial distribution of soot volume fractions in the flames; the setup for this system is illustrated in Figure 2.1.3-2. A doubled Nd:YAG laser (Surelite, Continuum) of 532 nm operating at 10 Hz was used to irradiate the soot particles. The induced incandescence at 90° to the incident beam was imaged with a 105 mm UV camera lens (Nikon, f/4.5) onto an intensified charge coupled device (ICCD) camera (Princeton Instruments, Model ICCD 576S/RB). The camera gate time was set as 80 ns to include the laser pulse duration. A narrow band interference filter with a wavelength range of 425-435 nm was placed in front of the camera to prevent laser light scattering from soot particles from reaching the detector and to reject most background luminosity and LIF. LII signals can be categorized into two distinct regimes depending on the laser energy fluence, i.e., a linear regime with respect to the laser energy fluence and a saturated regime in which the signal is independent of the laser energy fluence [Ni et al 1995]. In present study, the laser pulse energy fluence was measured approximately to be 0.6 J/cm^2, which is in the saturated LII regime. LII images were acquired by averaging over 300 laser pulses. The statistical uncertainties in the soot volume fractions derived from the LII measurements were less than 5%.

Laser extinction measurement was used to calibrate the LII signals to obtain absolute local soot volume fraction. The extinction measurements were made using an Argon ion laser

and a chopper (1 KHz) lock-in amplifier. Since the flame was quite uniform in the radial direction and edge effects were negligible, data collection was simplified by taking line-of-sight average absorption measurements through the center of the flame. The 514.5 nm laser beam was focused onto the flame using a 1 m focal length lens and was received by a Silicon photodiode detector. Because the location of the laser beam on the detector surface fluctuated due to the large temperature gradient across the flame, an additional shorter focal length lens was employed to focus the laser beam to maintain its location on an area of a photodiode detector, over which variations in sensitivity were small. The system was calibrated against a series of Standard Natural Density Filters and the linearity was better than 99%. Data were recorded using a National Instruments data acquisition system (NI-PCI-6110) with a sampling rate of 1000 samples/sec; the mean voltage value was obtained by averaging over a period of one minute.

Aromatic species were measured using LIF following the work of Sgro et al [2001]. The LIF signal of PAH was produced by employing the fourth harmonic wavelength of Nd:YAG at 266 nm. The UV beam of 266 nm excites both small aromatic species and large PAH species. During the development of the method, the broadband spectral characteristics of the fluorescence were observed using a 1/4-meter spectrometer (GCA-McPherson EU-700) over the spectral region from 250 to 600 nm, corrected by spectrometer efficiency. On an optical axis perpendicular to the laser beam, a 100 mm focal length UV lens collected light over an 8 mm length of the beam in the flame and focused the image onto the entrance slit of the spectrometer. Calibration using a 6035 Hg(Ar) lamp showed that the spectrometer had a resolution of 5 nm with a 0.4 mm-wide slit, which was positioned parallel to the propagation direction of the laser beam. The spectrometer was automatically driven by a LabView® program at 5 nm/min. The signal from the photomultiplier (RCA Model 4840), which operated at 800 V, was processed by a BOXCAR and recorded using the NI data acquisition system with a sampling rate of 1000 samples/sec.

Wavelength bands for the collection of fluorescence characteristic of small aromatic species and large PAH were selected based on the work of Beretta et al [1992], who assigned the UV fluorescence to small aromatic species of one or two rings and the visible fluorescence to larger PAH. For small aromatic species a combination of a 320 nm cutoff filter (WG320) and a UV pass filter (UG11) were used to collect the fluorescence in the wavelength range between 320 and 380 nm. For large PAH of three or more rings the wavelength range from 420 to 480 nm

was observed using a combination of high pass filter (GG420) and low pass filter (BG12). The camera was gated on for 35 ns during the laser pulse. Fluorescence from 500 laser pulses was accumulated to generate a PAH LIF intensity profile. Obtaining quantitative information from the LIF technique is difficult due to quenching, broadening of the absorption line, absorption of incident light and the selfabsorption of fluorescence. No feasible method of calibration was found, so only relative concentration results of PAH are presented.

Temperature profiles for each flame were measured using traditional thermocouple method. The probe configuration and methodology used were those of McEnally et al [1997], who built upon the work of Cundy et al [1986]. The thermocouple was uncoated, pre-welded type R (Pt/Pt-13%Rh) wire pairs. The junction was nearly spherical. Diameters of wire and junction bead are approximately 76μm (0.003 inch) and 239μm, respectively. The starting point for the temperature measurement was 2 mm above the burner surface, and temperatures were measured at 0.5mm spacing intervals near the main reaction zone, where the temperature gradient is steep. In the post-flame zone where the temperatures were changing more slowly, temperature was measured with 1 mm or 2 mm intervals up to a maximum height of 20 mm. The average insertion time to reach the final position was approximately 400 ms. Data points were recorded on IBM compatible PC using commercial LabView® software. The final junction temperature was obtained from a linear extrapolation of the temperature history to time zero, representing the moment when the junction reached its final position. Temperatures presented in this paper were corrected for heat loss, following the methodology of Shaddix [1999].

For the studies using NO_2, potassium line reversal was used to measure temperature in the non-sooting regions, enabling measurements far closer to the burner surface than possible with more traditional techniques such as thermocouples (Figure 2.1.3-3). The line reversal technique, or the sodium D-line reversal technique, as it is more widely known, is based on the following principle: The flame is seeded with sodium atoms using a suitable seeding method. The seeded sodium atoms have to be in local thermodynamic equilibrium with the hot gases in the flame. As a result of the increased temperature due to the combustion process, the outer electron in the sodium atom will be excited from the ground state to a higher resonance level. The excited sodium atoms will emit radiation at the characteristic emission wavelengths, particularly in the D-line or the doublet consisting of the 589 and 589.9 nm emission lines. The

intensity of the emitted signal is proportional to the population of the excited sodium atoms as well as the local temperature of the hot gases.

The true temperature of the hot gases can be measured by comparing the emission signal intensity against a calibrated background continuum source using a combination of a spectrometer and an optical detector array. The typical light source is usually in the form of a tungsten lamp, calibrated for apparent temperature of the tungsten filament against lamp current. When the temperature of the lamp filament is lower than that of the flame, the D-line will still be in emission. But the D-line will go into absorption when the lamp temperature is higher than that of the local flame temperature. The apparent temperature of the lamp filament will be equal to the true local temperature of the flame when the intensity of the emission line is equal to the intensity of the background continuum at the same wavelength. The same principle holds true for other alkali metals such as lithium and potassium.

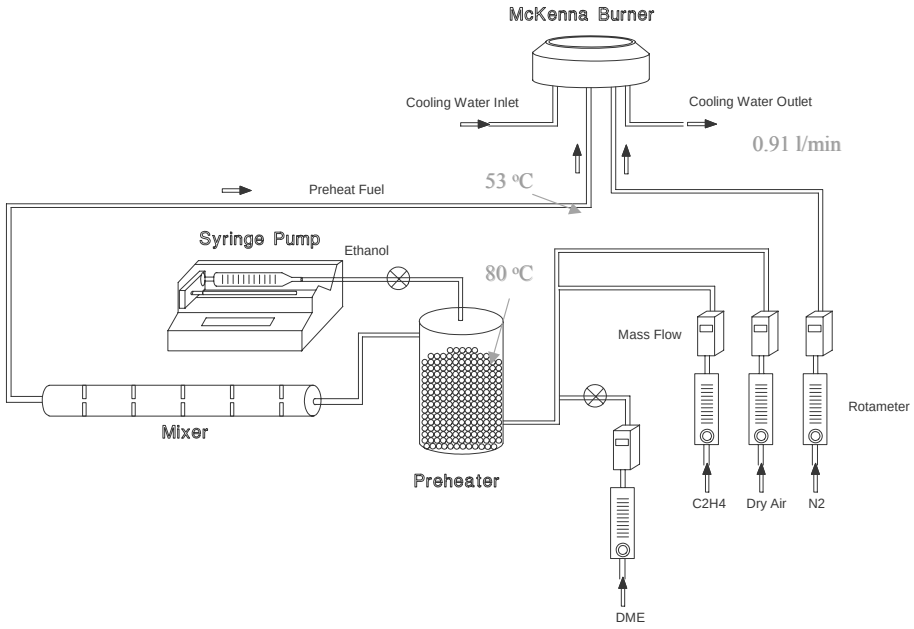

Figure 2.1.3-1. Schematic of Fuel, Additive, and Air Delivery Systems for Premixed Flame Experiments at Penn State.

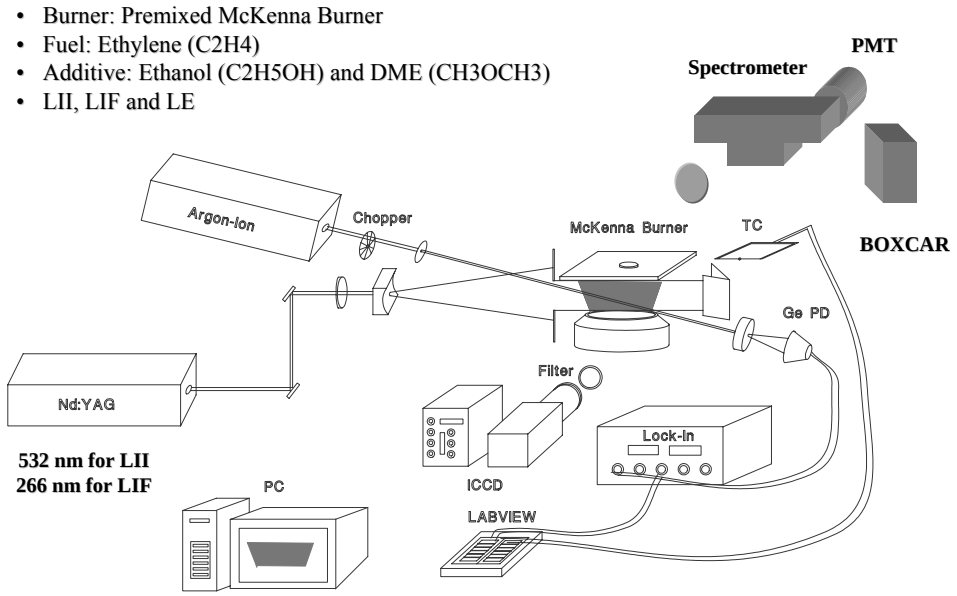

Figure 2.1.3-2. Experimental Setup for Measurements of Soot and PAH.

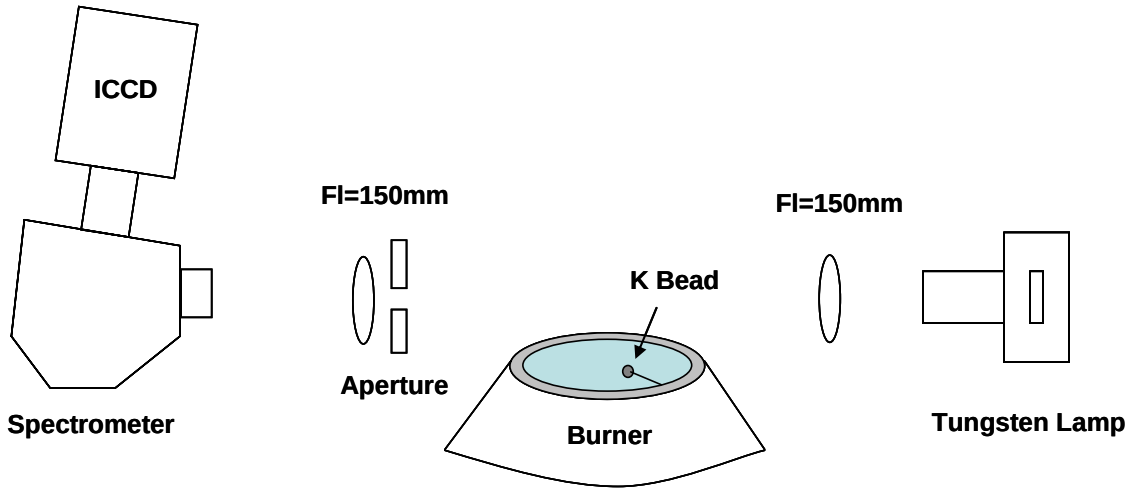

Figure 2.1.3-3. Schematic of Line Reversal Technique. The potassium (K) at 770 nm is seeded in the flame.

2.1.4 PREMIXED FLAME (UTRC)

Experiments were initiated in 2001 using a flat flame burner as shown in Figure 2.1.4-1. The perforated surface of the hastalloy burner consists of 513 holes which are 1 mm in diameter arranged as a regular octagonal. This design was utilized to avoid potential problems associated with coking and reaction within narrow passages in conventional porous plug burners. The laminar flame is stabilized using a 20 cm diameter ceramic plate located 30 mm above the burner surface and by using an argon coflow. The facility is partially shown by the photo in Figure 2.1.4-2 with a close-up of the flame shown in Figure 2.1.4-3. Open area of the 513 holes is 4.0 cm^2 and the effective burner area is estimated to be 19.6 cm^2. In 2002, the burner surface was changed to a porous plug due to concerns that jetting was creating localized non-uniformities in the flame. The burner surface is shown in Figure 2.1.4-4. In 2005, a McKenna burner was deployed at UTRC to more closely match test conditions being used at PSU. A photo of the burner and flame is shown in Figure 2.1.4-5.

Control of reactant gas and coflow to the premixed burner was performed using Brooks 5800 series mass flow controllers which were calibrated using wet-test meters prior to use. The additives were introduced (along with the reactants) into a 1 L vaporization/mixing chamber maintained at 200°C. The mixing chamber was connected to the base of the burner with 50 cm of 6.35mm OD heated stainless steel tubing. Initially the introduction of the liquid additives (ethanol) was performed using concentric, high flow, high efficiency, Meinhard Nebulizers (HEN model). Calibration of the borosilicate nebulizers showed that liquid delivery versus flow (and pressure) was highly reproducible and that a stream of fine droplets was produced. By introducing the stream of fine droplets into the heated chamber, vaporization and mixing with the reactants was achieved.

Although the nebulizers worked well, more flexibility is afforded by use of high pressure syringe pumps, especially for experiments with liquid fuel, i.e., heptane/toluene mixtures. Two ISCO 500D precision syringe pump systems were installed which allowed on-demand control of fuel and additive(s) at any given flow rate from 0.001 to 200 ml/min. Delivery flow rates were verified to be better than 1% of setpoint by experiment. The additives and fuel were mixed with air and introduced into the heated vaporization chamber.

In an effort to use fuels more similar to JP-8, the opposed flow burner was modified to use heptane, or a mixture of heptane and toluene, as fuel (Figure 2.1.4-7). Air continued to be the oxidizer. For the experiments described here, an effort was made to avoid the use of a carrier gas (such as N2) as a vehicle for delivery of heptane vapor. The modification to allow the use of fuels that are liquids at room temperature was achieved by using an injection pump to deliver known quantities of liquid fuel to a vaporization chamber maintained at a temperature above the boiling point of the fuel. By heating the entire fuel duct, flow of fuel vapor is maintained at a constant rate. We estimate the oxidizer strain rate for the heptane/air and heptane/toluene/air/ flames reported here to be approximately 38 sec^{-1}. The pressure generated by the vaporization of the liquid fuel in a confined environment was used to provide flow velocity into the burner ducts.

Measurement Methods

During this program four different methodologies were used to characterize soot evolution in the premixed flat flames with respect to: (1) particle size distribution, (2) particle number concentration, and (3) particle morphology. A brief discussion of each of these experimental methods follows:

Soot volume fraction was measured using temperature particle densitometry (TPD). The technique, described in detail by McEnally et al [1997], consists of rapid insertion of a thermocouple into the flame and recording the junction temperature (T_j) as a function of time. The T_j history responds to soot deposition that consists of a transient-response stage (0 – 0.2s), a variable-emissivity stage (0.2 – 5s) and a variable-diameter stage (>5s). T_{jo} is obtained from a linear extrapolation of the temperature history to time zero and then corrected for radiation to obtain gas temperature (T_g) by calculating a heat balance:

$$\varepsilon_j \sigma T_{jo}^4 = (k_{go} Nu_j / 2d_j)(T_g^2 - T_{jo}^2) \qquad (1)$$

The thermophoretic mass transfer model used by McEnally was used to calculate the local soot volume fraction. The slope of a linear fit to the temperature history in the variable diameter stage is proportional to the soot volume fraction:

$$m = \beta f_v \quad (2)$$

where,

$$\beta = 2D_T \varepsilon_j \sigma^2 T_s^4/(\phi k_{go}^2 Nu_j) \quad (3)$$

Note that a thermophoretic model can be used since particles <1um will not deposit on the bead by inertia but rather follow the gas streamlines. Furthermore, Rosner et al [1991] have shown that Brownian diffusion is small relative to thermophoresis.

The thermocouple assembly also follows that of McEnally in that the bead is stretched (to avoid sagging) between two supports that are 50mm apart (to avoid conduction losses). Uncoated type R thermocouples (Pt-Pt/13%Rh) of several spherical bead sizes (0.165 to 0.203 mm) as well as butt-welded 0.076 mm beads were used. The assembly was driven pneumatically and the data acquisition system was triggered optically to begin recording with thermocouple insertion times being less than 100 ms. Data points were recorded at 200Hz for 40 seconds using LabView® to sample an I/O interface card (National Instruments AMUX-64T) that has an integrated circuit temperature sensor and electronic cold junction compensation, i.e. thermocouple inputs.

One of the parameters used in the calculation of f_v is the soot deposit solid fraction (ϕ), or void fraction. Soot deposit density for the flame was obtained by collecting soot on a Pt wire. The weight and diameter of the wire was determined before the experiment and after collecting the soot. Knowing the volume and mass of the soot, the density of the deposited soot particles could be calculated. ϕ is the ratio of the soot deposit density to the material density of soot (1.8 g/cc). In the post flame front regions of both flames, ϕ was measured to be 0.013 ($\pm$ 0.001).

Laser extinction is widely used to measure soot volume fraction (f_v) in flames because of its simplicity and non-intrusive nature. Number density (N) is derived from the measured light incident on (I_o) and transmitted through the flame (I), the extinction cross section ($\sigma_{e)}$ and extinction path length (L) which are related by Beer's law:

$$I = I_o(\exp(-N\sigma_e L)) \quad (4)$$

A schematic of the laser extinction setup used for this work is shown in Figure 2.1.4-6. A cw Spectra-Physics 10mW HeNe laser (632.8 nm) was used as the light source for the extinction

measurements because of its good stability and low noise characteristics. Variable diameter apertures located 10cm from the burner centerline on either side of the burner were used to reject diverging beams and forward scattered light. Typically the laser side aperture diameters were less than 1 mm and the detector side aperture diameter was 5 mm. After passing through the flame the light was collected by an integrating sphere that ensured that the measured transmitted intensity was not affected by changes in beam direction due to beam steering. The light intensity was measured with a photodiode (Newport 818SL) after passing through a narrow band optical filter (12 nm) to reduce broadband flame radiation and an OD 3 neutral density filter to prevent saturation of the sensitive detector. Although suitable measurements can be made without signal processing, signal-to-noise ratio can be improved by removing practically all flame emission with the addition of a mechanical chopper (Ithaco model 220) and lock-in amplifier (Stanford Research Model SR510). A modulation frequency of 400 Hz was used.

To calculate f_v, the extinction coefficient must be known in addition to the light intensities. The extinction coefficient depends on the complex refractive index (n) and wavelength of the incident light (λ):

$$\sigma_e = 6\pi E(n)\, f_v / \lambda \qquad (5)$$

where,

$$E(n) = -\mathrm{Im}(n^2-1) / (n^2+2) \qquad (6)$$

Rayleigh theory for small particles ($d_p << \lambda$) was applied to relate absorption to volume fraction. Although it will be shown that high in the flame, chains of agglomerates are not in the Rayleigh range, theory shows that the absorption is simply the sum of the primary particles regardless of whether they are isolated or agglomerated [Berry and Percival 1986]. As long as the primaries are in the Rayleigh range, the effect of agglomeration is small (1.8% or less) as has been shown by Charalampopoulos and Chang [1991]. Since transmission is a relative measurement, the extinction coefficient requires no calibration, however, the path length must be known and homogeneous. For each flame σ_e was determined at several heights using tomographic reconstruction to deconvolve the local soot absorption coefficient from a set of parallel measurements of transmission. Each dataset consisted of 60 measurements spaced at 1mm intervals starting over the coflow and progressing toward the centerline of the burner. Finally, a soot refractive index (n) of $1.57 - 0.56i$ [Dalzell and Sarofim 1969] was used although there is

some range to the values reported in the literature (1.90 – 0.55*i* [Lee and Tein 1982]). Therefore:

$$f_v = -\ln(I/Io)\,\lambda / 6\pi E(n)L \qquad (7)$$

When particles that are small with respect to the gas mean free path are exposed to a significant temperature gradient, the particles move in the direction of decreasing temperature with a velocity that is independent of particle diameter [Waldman and Schmitt 1966] and morphology [Rosner et al 1991]. Therefore, insertion of a cold surface into the flame results in soot deposition by thermophoresis. Methodology developed by Dobbins and Megaridis [1987] was used to perform thermophoretic sampling. Specifically, a computer controlled two-stage sampling system was built using bidirectional pneumatic cylinders (Bimba Manufacturing) and fast acting solenoids. The first cylinder positioned the probe assembly in the flame, while the second cylinder deployed a thin probe holder to collect the sample. The sample is collected onto a standard 3 mm diameter carbon coated microscope grid (Ted Pella, Inc., pn 01810 – 200 mesh copper grid and 20 nm thick carbon substrate) which was protected in a sheath during the first stage of insertion. The grid was exposed to the flame for 10 to 40 ms before retracting into the sheath and withdrawing from the flame. The entire sampling sequence generally required less than 400 ms with the timing chosen so that soot coverage of the grid was about 10%. A two-stage system was built to allow short exposure (sampling) times while minimizing flame disturbances. Although intrusive, this extractive technique preserves particle morphology since the cold surface stops heterogeneous reactions of the particles as they are captured.

The grids obtained by thermophoretic sampling were analyzed by bright field transmission electron microscopy (TEM). Photomicrographs were made at magnifications up to 100,000X on a Philips EM 400. Computer assisted image analysis (NIH Image) provided measurement of soot primary particle diameter (d_p) and morphology. This analysis is made tedious by the minimal contrast between the background (the carbon substrate) and the soot. In addition the edges of the particles tend to be amorphous and therefore not sharply defined. Several characteristic dimensions can be obtained from these photomicrographs. The first is the primary particle diameter (d_p). This measurement is straightforward. The second is $L_{max,}$ or Feret's diameter. This is the maximum distance between any two points on the perimeter of an agglomerate. These two parameters can be used to calculate the number of primary particles per

agglomerate (N_p). These parameters were estimated using an empirical relation reported by Megaridis [1990]:

$$N_p = k_f (L_{max}/d_p)^{D_f} \qquad (8)$$

where k_f is a prefactor and D_f a fractal dimension that accounts for the three-dimensional shape of the agglomerate, i.e,. "compactness" (values of from 1.62 to 1.85 have been reported).

Electrostatic forces are commonly used to separate particles. Since the electrical mobility of a particle can be accurately calculated, particle size and particle distribution can be measured using electrophoresis. This approach is particularly effective for spherical particles with submicrometer diameters. An electrostatic classifier (TSI 3071) and a condensation nucleus counter (CNC, TSI 3022) were used with a dilution probe to obtain soot size distributions in the 10 to 500 nm size range (Figure 2.1.4-9). The classifier separates particles by their drift in an electric field. The velocity a particle acquires is a function of size and charge. After an impactor removes particles greater than 1 um and a radioactive source "neutralizes" all particles (ensured that they have equilibrium distribution of charges), a known size range of particles can be selected by choice of electric field and instrument flow parameters. The particles are detected using the CNC which uses a supersaturated vapor that can condense on the particles to form droplets that can be counted optically. The instrument is operated in a scanning mode so that a complete size distribution can be acquired in as little as 60 seconds. The combination of the classifier and CNC operated in a scanning mode is referred to as a scanning mobility particle sizer (SMPS).

Based on the drift time through an electric field, the classifier separates particles based on their "aerodynamic" diameter, d_{aero}, which is the equivalent diameter of a spherical particle drifting through the field. For an irregularly shaped particle such as soot agglomerates, this parameter in general is not identical to any fundamental parameter of the agglomerate. As a preliminary means of interpreting size information provided by the SMPS, we recognize [Willeke and Baron 1993] that $d_{aero} = \chi d_{ev}$, where d_{ev} is the equivalent volume diameter and χ is the dynamic shape factor. Furthermore, we have derived an approximate expression:

$$L_{max} = A(d_p)^a (d_{aero}/\chi)^b \qquad (9)$$

based on the relationships developed by Koylu et al [1997]. L_{max} is Feret's diameter as discussed previously. We utilize a value of 1.7 for χ and have determined constants A, a, and b in order to enhance the comparison between our SMPS and TEM results. Values of d_p are extracted from the TEM results to reduce the data. No information is provided from the SMPS to assess whether or not a particle is a single (nearly spherical) particle or a complex aggregate. Hence, we have also adopted simple algorithms to transition the values of the constants to appropriate numbers to ensure that the above equation reduces to $L_{max} = d_p$ for a single particle. Using this procedure and expressions provided by Koylu et al. [1997], we are then able to compute distributions of L_{max}, and N_p, as well as N and f_v using d_p from the TEM and the distributions from the SMPS:

$$f_v = \pi/6 d_p^3 \Sigma N_p(300/T_g) \qquad (10)$$

To use the SMPS, samples were extracted from the flame using a stainless steel dilution probe (Figures 2.1.4-8 and 2.1.4-9). The inner wall of the probe was a 0.125" ID porous tube. The probe was operated at a water temperature of ~90°F. Nitrogen dilution was metered to the probe and sample was drawn into the probe using an eductor instead of a pump. The motive flow added a second stage of dilution. Dilution rate was determined by online monitoring of CO and conditions were set to be isokinetic at the probe entrance before initiating data collection.

Extraction of particle samples from the premixed flame requires rapid dilution to avoid particle coagulation and water condensation. These two sample transport factors can drastically alter measured particle size distributions. In addition, particle concentrations are generally too high for direct measurement with standard instrumentation, such as a differential mobility analyzer, as particle-particle collisions rapidly alter the size distribution at high number densities. Three different dilution probes were used during the premixed flame experiments. The first was briefly described in the previous section when the differential mobility methodology was discussed. A second probe, as shown in Figure 2.1.4-9, was deployed in a prior effort at UTRC [Colket et al 2001]. This probe has a porous wall and can provide high dilution ratios but suffers in that the water cooling near the tip thermophoretically collects particles on the wall of the sample tube which tends to choke the flow as particles deposit. A variety of operational issues, however, make this probe awkward to use, with no guarantee of rapidly freezing the particle size distribution.

A more reliable probe design for high dilution and small particle sampling is one described in detail by Zhao et al [2003, 2005]. We deployed the probe in a similar fashion to that described in the literature as shown in Figure 2.1.4-9. In this sampling system a ¼-inch diameter stainless steel tube with a 0.007" machined (EDM) hole was placed horizontally to the burner with the hole facing the flow. Nitrogen is metered into the tube and exhausted with a pump. By monitoring the pressure differential, the sample could be drawn into the nitrogen flow and dilution ratios of 1000 or higher could be achieved. This probe/sampling system was found to work well at flame stoichiometries near the onset of sooting, however, it was difficult to operate the system for extended periods at equivalence ratios of interest, i.e., 2.5. Still samples could be obtained on the order of 10 min before the orifice clogged.

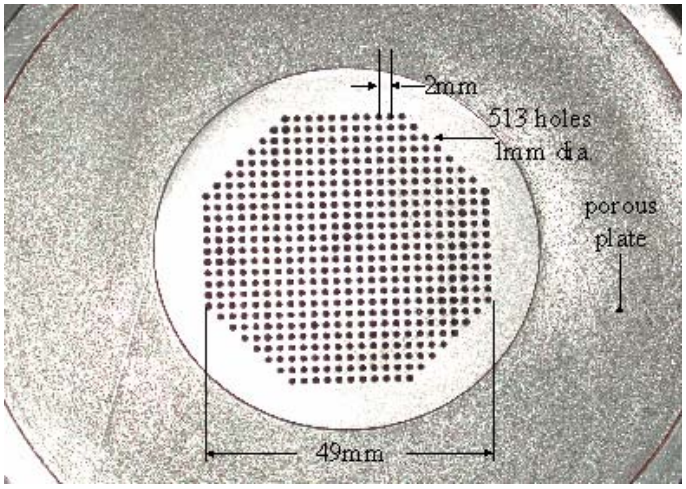

Figure 2.1.4-1. Photograph of the Burner Surface.

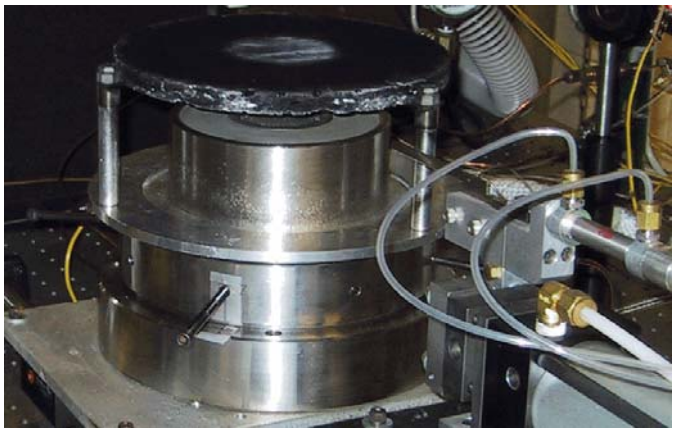

Figure 2.1.4-2. Flat Flame Facility.

Figure 2.1.4-3. Premixed Ethylene/Air Flame at Equivalence Ratio 2.34.

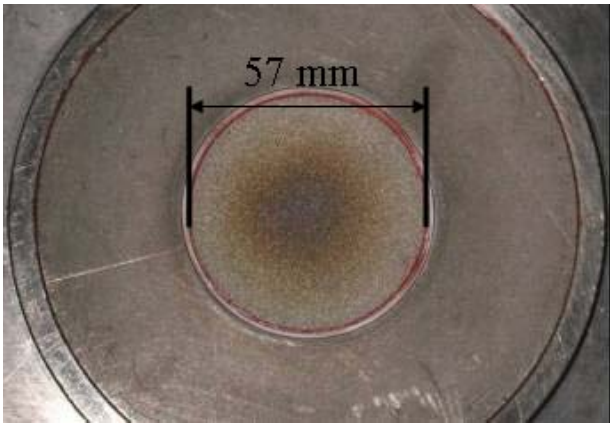

Figure 2.1.4-4. Photograph of the Porous Plug Burner Used from 2002 to September 2005.

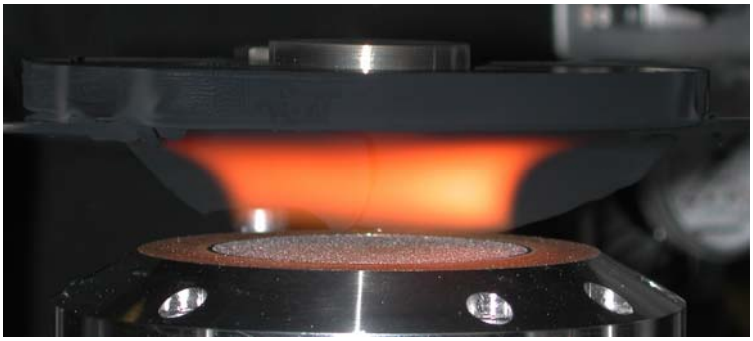

Figure 2.1.4-5. UTRC McKenna Burner.

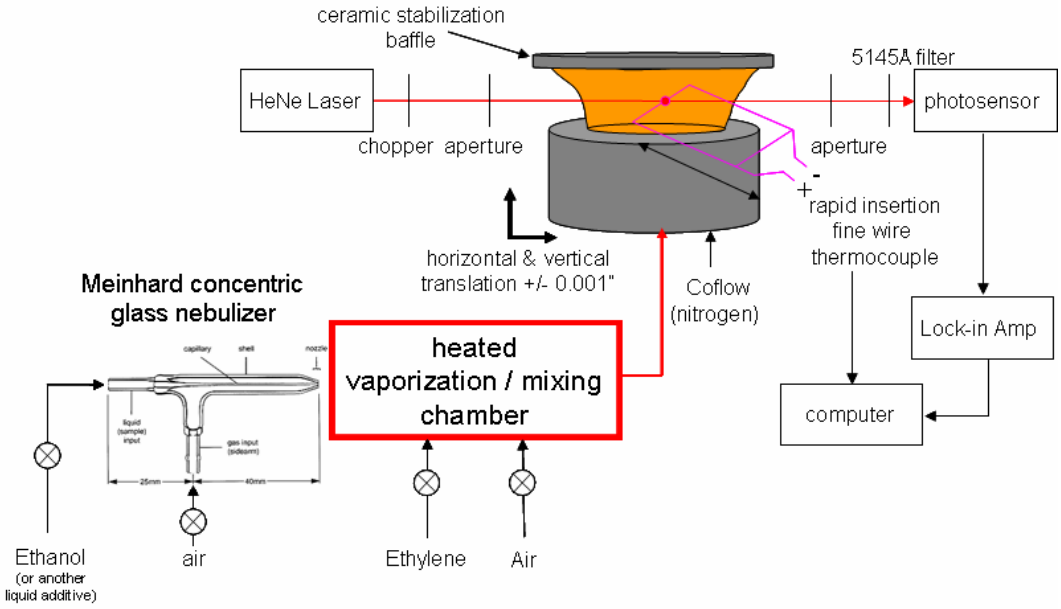

Figure 2.1.4-6. Experimental Setup for the Ethanol/Ethylene Flame Experiments.

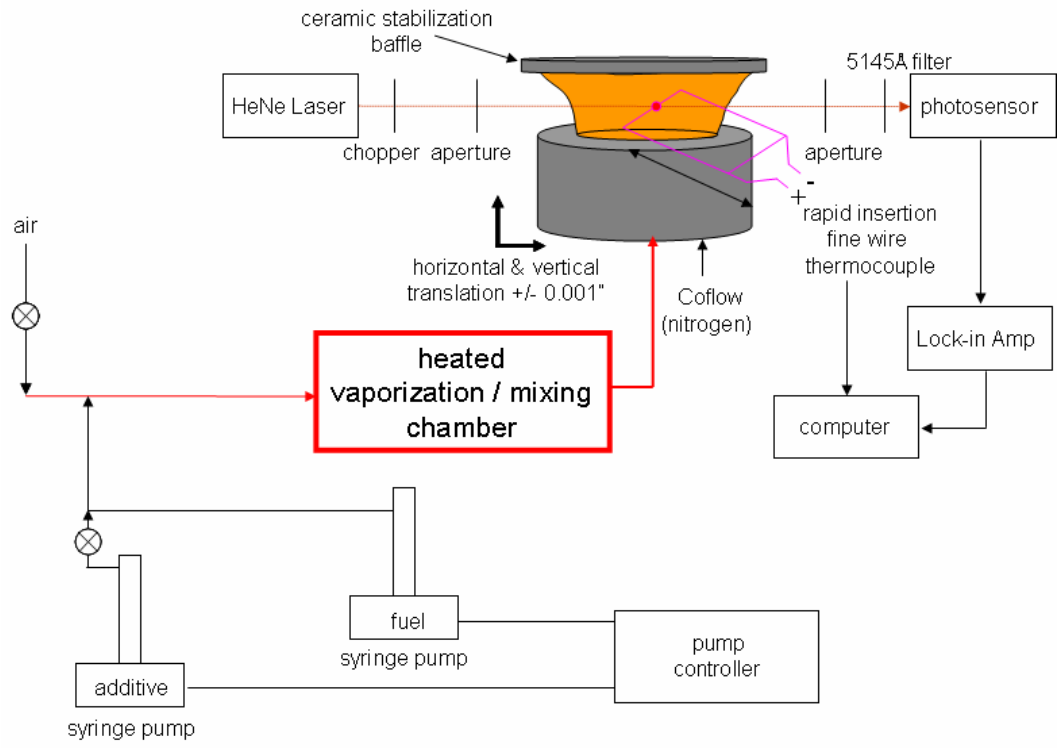

Figure 2.1.4-7. Experimental Setup for the Heptane Flame Experiments.

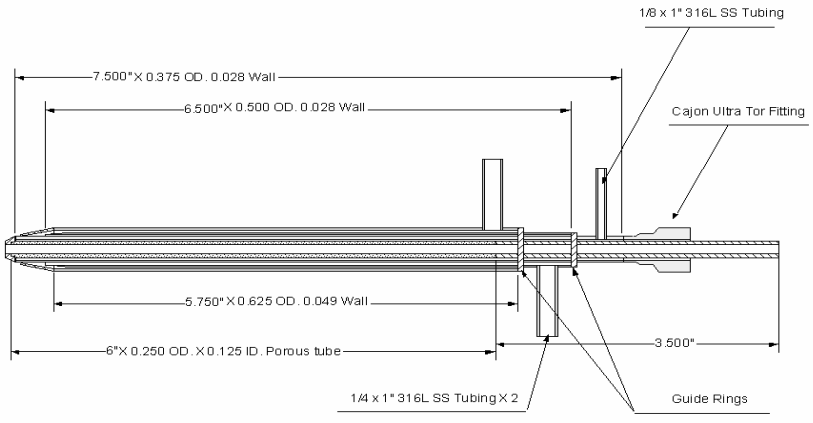

Figure 2.1.4-8. UTRC Porous-Wall Particle Sampling Probe.

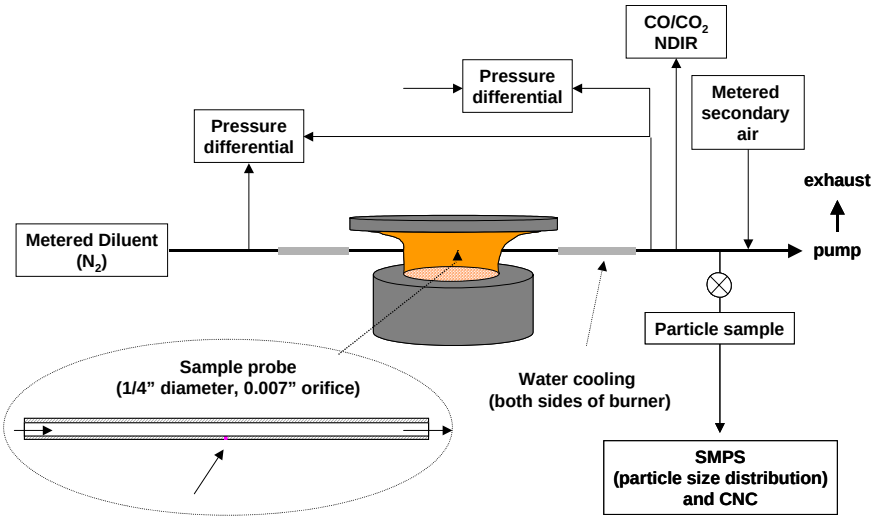

Figure 2.1.4-9. Rapid, High-Dilution Particle Sampling System (Original Concept by H. Wang).

2.1.5 OPPOSED-JET DIFFUSION FLAME

An opposed flow burner, designed to be operated at atmospheric pressure, was constructed at the ARL, for investigation of particulate reduction in flames by using additives to the fuel and oxidizer gases. For many sooting flames, the opposed flow burner allows separation of the regions of particulate formation (sooting region) from the main combustion region. In general, soot formation occurs in fuel-rich areas at temperatures slightly lower than peak combustion temperatures. In opposed flow flames, combustion occurs at a spatial location where the fuel and oxidizer are in stoichiometric proportions which satisfy combustion chemistry. As an example, for the ethylene/air flame the overall chemical reaction (undoped, and disregarding N_2) is:

$$C_2H_4 + 3O_2 + \rightarrow 2CO_2 + 2H_2O \qquad (1)$$

For equal fuel and oxidizer flow rates, the stagnation plane in an opposed flow burner (where the axial velocity of the two opposed gas streams goes to zero) will be fuel-rich, and will be the location of peak soot formation. The combustion region will be on the oxidizer side of the

stagnation plane, at the point where enough fuel has diffused into the oxidizer stream to satisfy the stoichiometry of the combustion reaction. For flames employing approximately equal flow rates for fuel and oxidizer gases, the oxidizer is *convected* into the flame zone, but the fuel must *diffuse* into the flame zone (Figure 2.1.5-1).

The burner is constructed of 304 stainless steel, and is based upon the design of Chelliah [Lentati 1998]. Fuel (ethylene or heptane) and oxidizer (air) ducts are 15 mm in diameter, and are separated by 10 mm. Flow rates for the ethylene/air experiments reported here were 4.6 liters per minute ethylene, and 6.2 liters per minute air. These values were chosen because they gave the most stable flame. Liquid additive was added to fuel or oxidizer gases using an injection pump (Isco). The additive was injected as a liquid into a heatable vaporization chamber prior to entering the fuel or oxidizer gas lines approximately 2 m upstream from the gas entrance into the burner assembly and was assumed to vaporize completely. As an example of additive loading amounts, ethanol addition was up to 0.08 mole fraction (8%) in the fuel or oxidizer gas stream. A shroud gas (nitrogen) surrounded both fuel and oxidizer ducts within the burner assembly to minimize entrainment of room air into the flame. The burner was enclosed in a chamber that was capable of being evacuated. However, for these experiments the access ports of the chamber were left open, so all experiments were run at atmospheric pressure. A schematic of the experimental apparatus (including optical diagnostics) is shown in Figure 2.1.5-2. Photographs of the optical setup and of the flame are shown in Figures 2.1.5-3, 2.1.5-4, and 2.1.5-5.

Measurement Methods

The experimental procedure was as follows: A flame source was placed between the burner ducts and gas flow was then commenced, with the opposed flow flame igniting immediately. The nitrogen shroud gas flow (5 L/min total) was initiated and the flame was allowed to stabilize for 5 minutes. For experiments using fuel or oxidizer additive, a valve on the injection pump was opened and flow of additive into the air or fuel streams was begun. After approximately 1 minute of flow of additive, a sheet of pulsed laser radiation (typically 0.5 mJ/pulse, approx. 20 nsec duration, formed using a double apertured, half cylindrical lens) near a wavelength of 308 nm (Lambda Physik) was passed through the flame region. A gated, intensified CCD camera (Roper Scientific, 256 X 1024 pixels), equipped with a Nikor 1:4.5 UV lens, was used to measure laser scatter during and immediately following the laser pulse (gate

width = 80 ns). The images produced by 100 laser pulses were averaged in the camera memory. From this average image, the maximum value at a given pixel location along the centerline between the fuel and oxygen ducts was selected in the sooting and combustion regions of the flame (see Figure 2.1.5-6). A background value at that pixel location, measured prior to the flame initiation (also 100 averaged images), was subtracted from this value.

This background corrected pixel value became the data point representing peak particle or OH concentration. Following data collection, the injection pump valve was closed, the pump flow parameters were reset, and the process repeated. Planar laser induced fluorescence and light scatter measurements at the beginning and end of each run series were performed to check that the flame returned to normal after the ethanol flow was stopped. Laser power was measured before and after each experimental run and typically varied by less than 2 percent.

Other than subtraction of background, no corrections were made for changes in laser power or variations in spatial intensity, and no other specific dark field pixel corrections were made, although previous measurements of the CCD dark field (camera blocked) showed pixel to pixel output to vary by less than 2%.

The region of the flame referred to here as the sooting region may contain particles and polyaromatic hydrocarbons (PAH). These PAH are known to fluoresce when exposed to ultraviolet radiation. For the experiments reported here, we are assuming that the bulk of the signal observed in the sooting region is from scattered laser radiation. To evaluate the part of the observed image in the sooting region due to light scatter, we divided the theoretical treatment of the scattering process into an extinction part and a Mie theory part.

The intensity of scattered laser light (assuming unit incident intensity and zero absorption) by particles in the flame may be approximated by Bouguer's Law:

$$I = \exp\left(-3Q_e m_p L / 2\rho d\right) \qquad (2)$$

Here, I is the intensity of the scattered light, Q_e is the soot extinction coefficient, m_p is the weight of soot particles per unit volume, L is the path length, and ρ and d are the density and diameter of the average soot particle. This equation predicts that as soot particle size (d) decreases for a fixed soot mass per unit volume, scattering intensity increases.

According to Mie's solution of Maxwell's equations in spherical coordinates for an electromagnetic wave incident on a sphere, the angular distribution of intensity and degree of polarization of the light scattered by a collection of particles is related to both the size and index of refraction of the particles. The general solution describing scattering of monochromatic light by a single particle of any size may be described by:

$$I_\theta = \lambda^2/(8R^2\,\pi^2)\,[i_1(\theta) + i_2(\theta)] \quad . \qquad (3)$$

Here, I_θ is the light intensity scattered at angle θ , λ is the wavelength of the incident radiation, R is the distance from the particle to the point of observation, and $i_1(\theta)$ and $i_2(\theta)$ are angular distribution intensity functions that are dependent upon the intensities of the two plane polarized components of the scattered monochromatic incident light.

Application of Mie's solutions for light scattering by particles is usually simplified by considering the limiting cases where the particle diameter is much smaller than the wavelength of light (Rayleigh scattering, λ^{-4} intensity dependence), near the wavelength of light (Mie scattering), or much greater than the wavelength of light (diffractive optics). For light scattering by nascent soot particles in opposed flow flames (soot particle sizes of tens to hundreds of nanometers), the scattering is typically categorized as having characteristics of Rayleigh and Mie scattering. For observation at 90° to the incident beam, scattering in both Rayleigh and Mie regions is predicted to be perpendicularly polarized and nonzero. So, for measurement of scattering intensity perpendicular to the incident laser beam, by a cloud of spherical particles with fixed size distribution, in the limit of $(3Q_e\, m_p\, L / 2\rho d) << 1$, the scattering intensity should be approximately proportional to m_p and, hence, to soot volume fraction.

For experiments using heptane/air and heptane/toluene/air opposed flow flames, a more direct measure of particulate formation is achieved by observing planar laser induced incandescence (PLII). The PLII is excited using a pulsed, Nd:YAG laser source (Continuum), operating at a wavelength of 1064 nm and a repetition rate of 5 Hz. Pulse duration is approximately 10 ns. Base power is adjusted by varying the Q-switch delay (relative to the flash lamp pulse). The output laser beam is then passed through two polarizing beam splitter cubes (the second cube in a rotation stage) to condition the beam and to provide a finer power adjustment. This output beam is then passed through a beam condenser, and then apertured, to

yield a beam diameter near 0.5 mm. This apertured beam is then passed through a half cylindrical lens to form a sheet. This laser sheet is then directed into the flame region of the opposed flow burner, parallel to the burner axis. Laser energy per unit area per pulse through the burner region was approximately 0.28 J/cm^2. PLII was observed at a right angle to the direction of laser propagation using a gated, intensified CCD camera (Roper Scientific). No filter was used in front of the camera lens, so PLII images were not corrected for emission from non-soot species excited by the laser (e.g., C_2). The camera intensifier gate width was 50 ns, and the gate was initiated by the onset of the laser pulse. A simplified schematic of the experimental apparatus is shown in Figure 2.1.5-7.

Figure 2.1.5-6 shows images of simultaneous light scattering and OH LIF taken perpendicular to the plane of the laser sheet. In this figure, the regions of maximum particle concentration and OH formation are seen to be well separated. Also shown in the figure is an image taken of the same flame with the laser tuned off of resonance with the OH absorption transition ((1,0) $A^2S \leftarrow X^2P$). Figure 2.1.5-8 shows an image of the heptane/air diffusion flame and PLIF/light scattering images on and off resonance with the OH absorption near 308 nm.

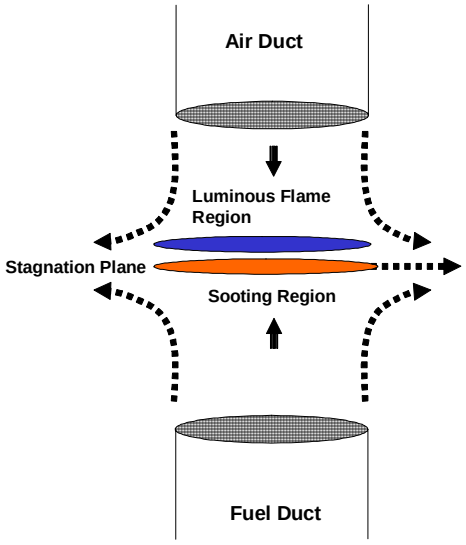

Figure 2.1.5-1. A Schematic of an Opposed Flow Burner with Flame.

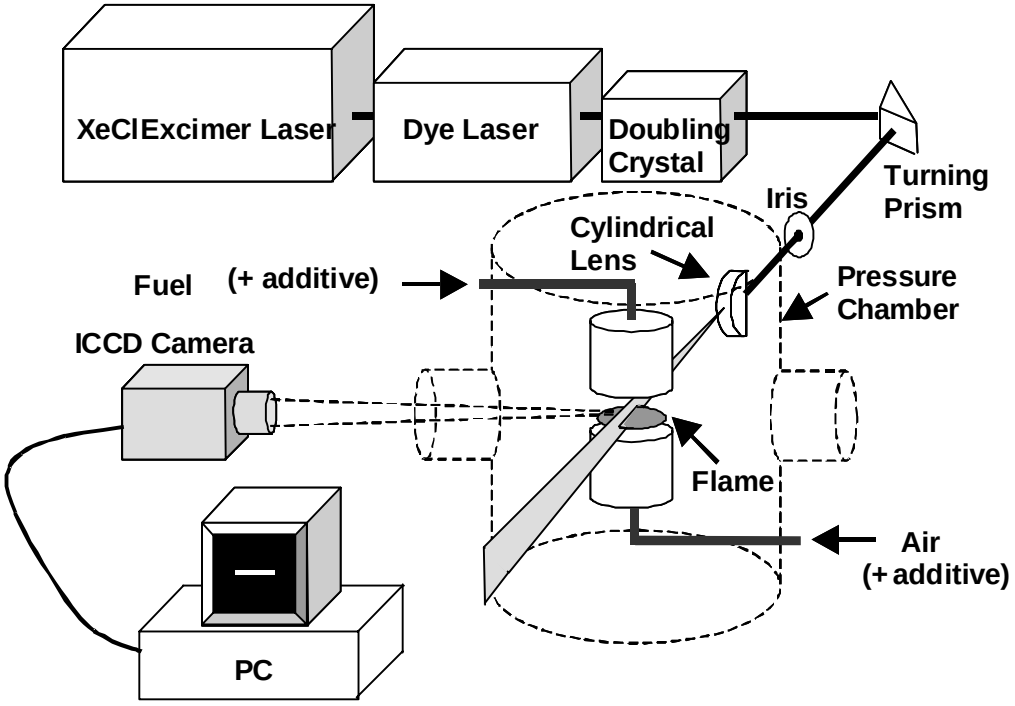

Figure 2.1.5-2. A Schematic of the Experimental Apparatus, Including Optics.

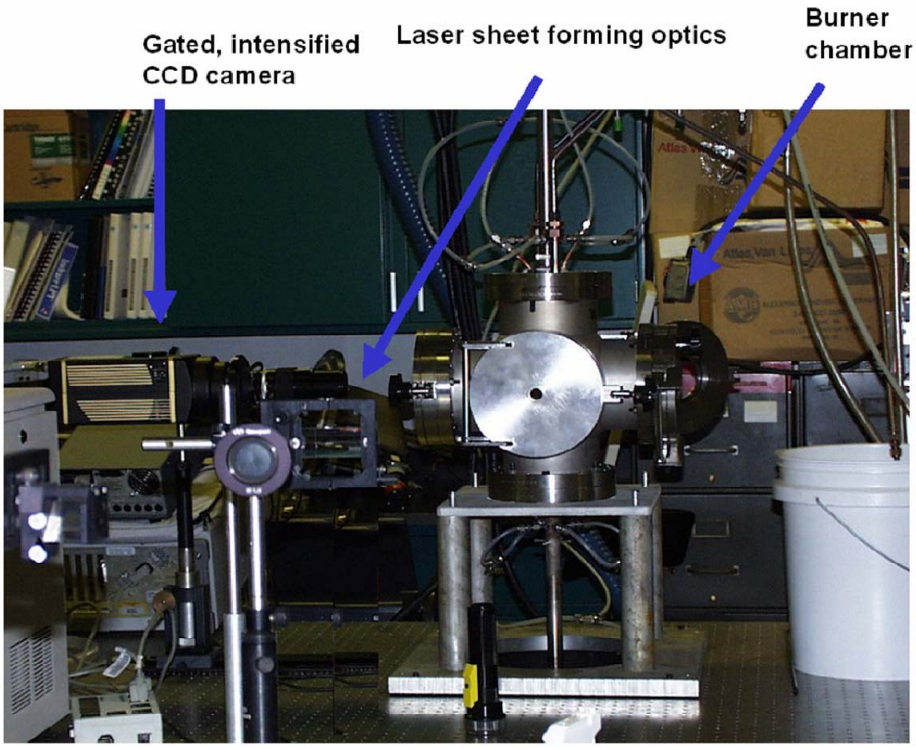

Figure 2.1.5-3. A Photograph of the Burner Chamber with Some Associated Optics.

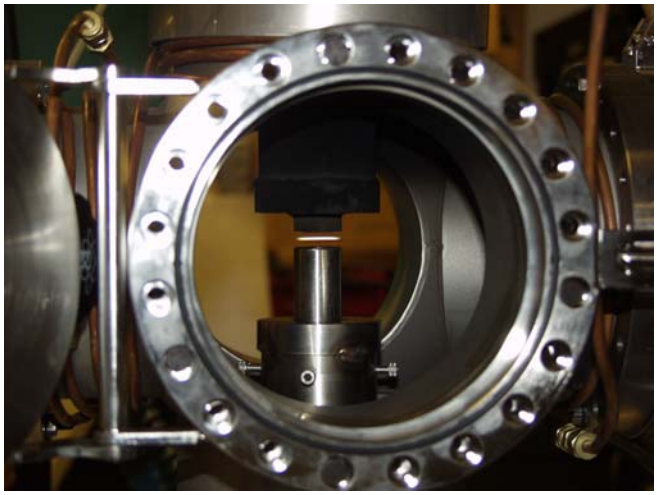

Figure 2.1.5-4**.** An Ethylene/Air Opposed Flow Flame.

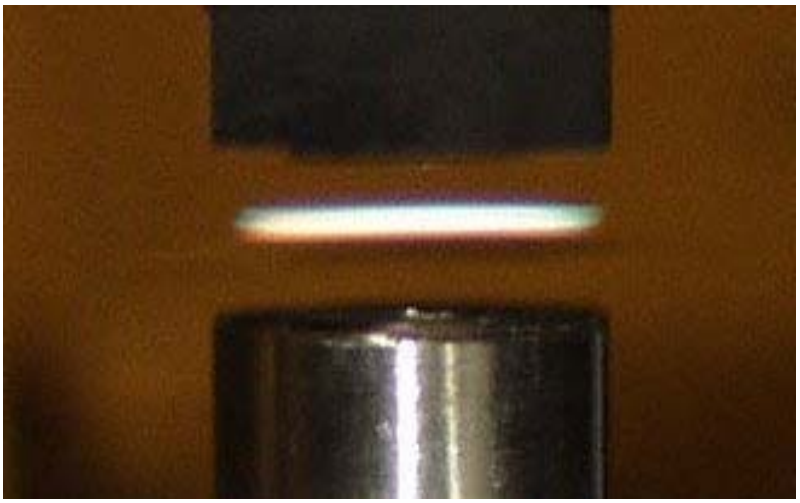

Figure 2.1.5-5. Detail of an Ethylene/Air Opposed Flow Flame.

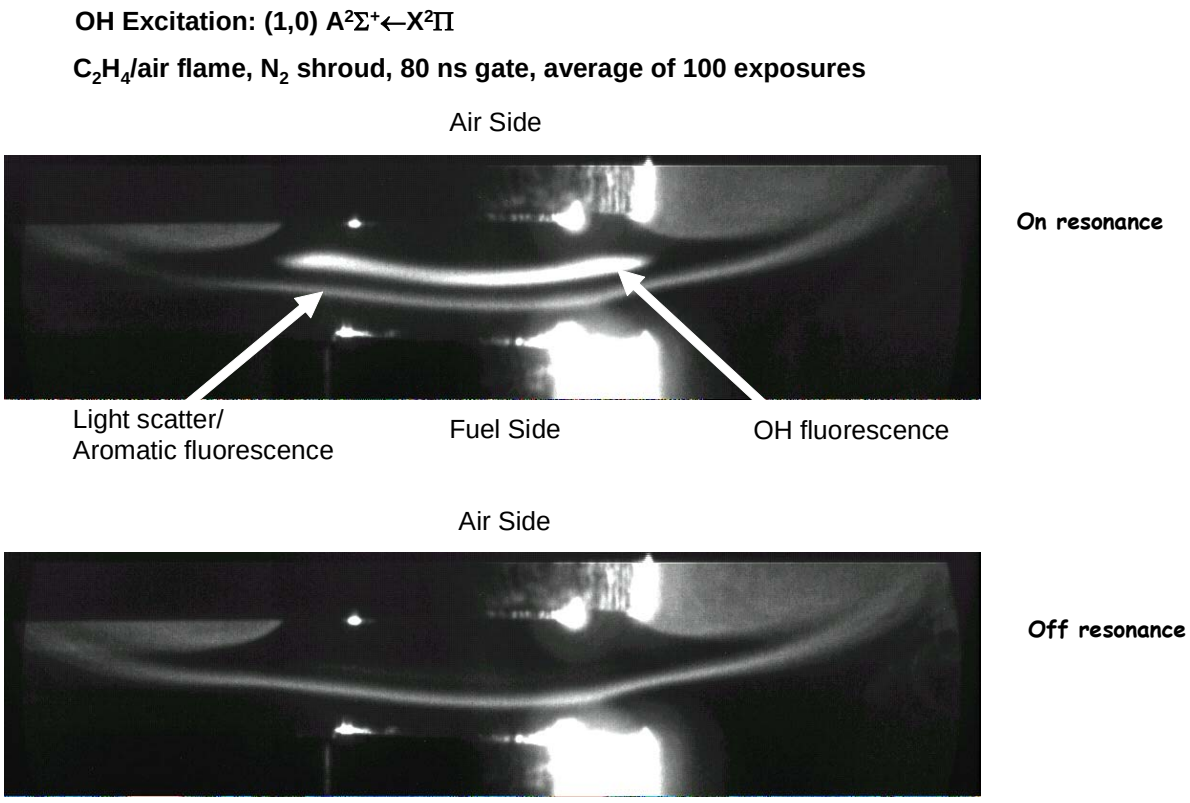

Figure 2.1.5-6. On and Off Resonance Images Showing the Sooting and OH Regions in an Opposed Flow Ethylene/Air Flame.

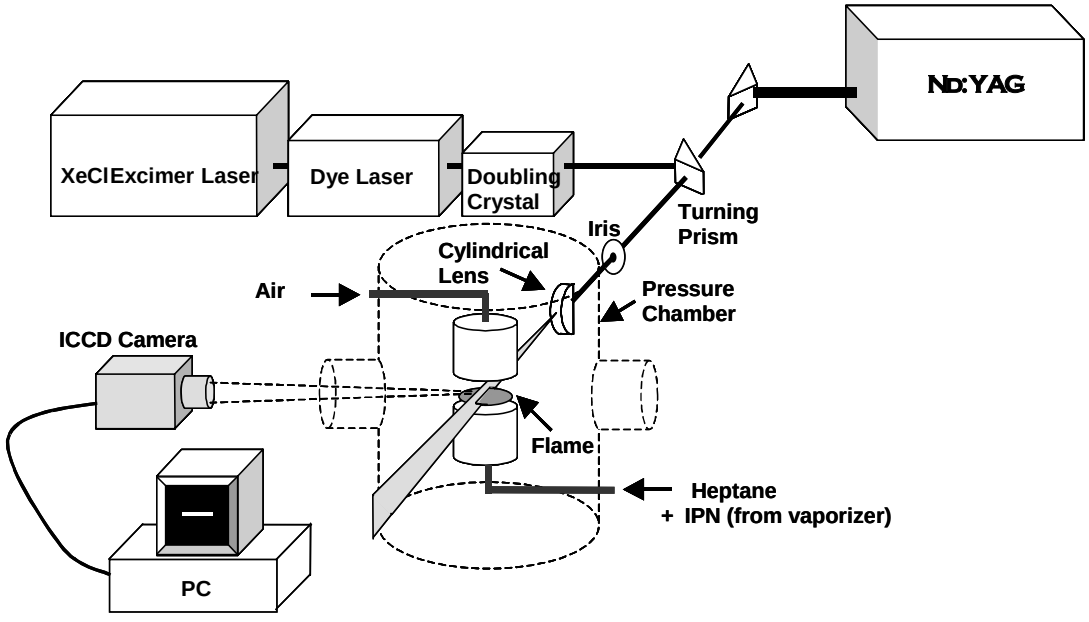

Figure 2.1.5-7. A Schematic of the Experimental Apparatus Used for Measuring PLII and PLIF.

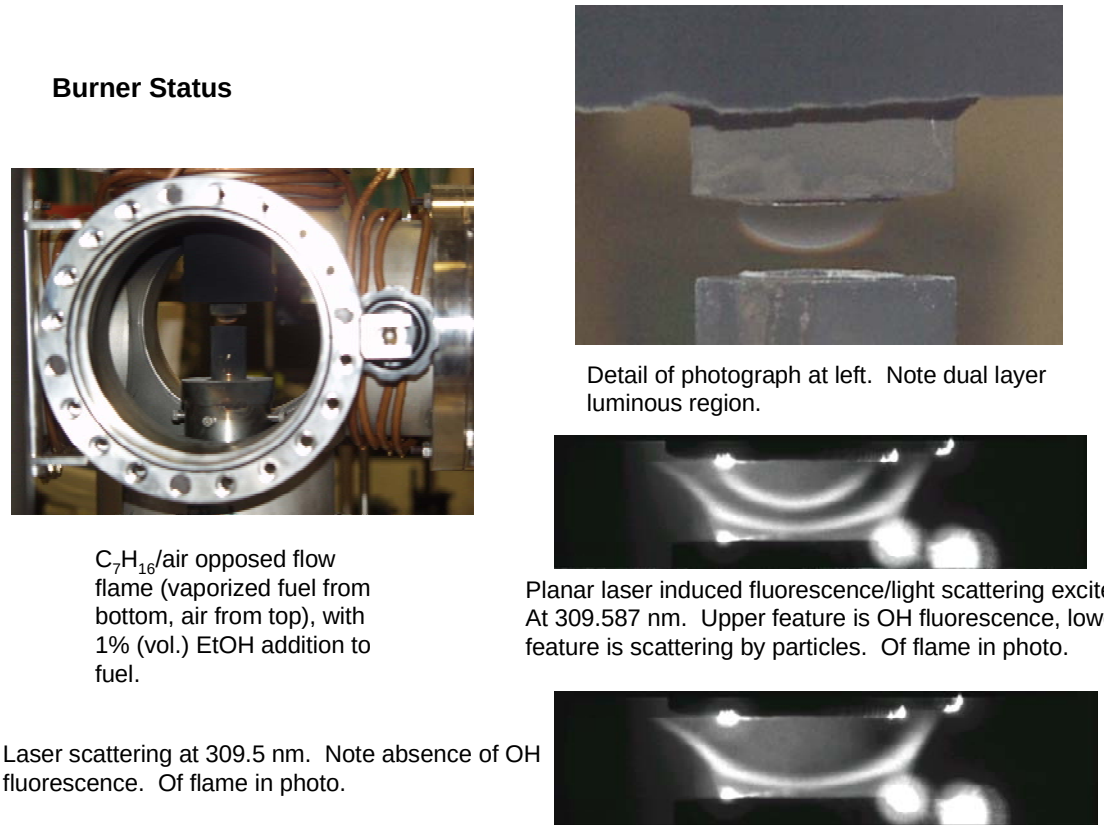

Figure 2.1.5-8**.** Normal and PLIF Images of the Heptane/Air Diffusion Flame.

2.1.6 COFLOW DIFFUSION FLAME

The coflow diffusion flame was not part of the suite of burners used in the original study. It was included in the program only for the study of phosphorus which was an add-on to the original program. The coflow diffusion flame was included because the work of Hastie and Bonnell [1980], which motivated the phosphorus work, included experiments in a small scale, coflow diffusion flame.

The coannular laminar diffusion flame burner that was used is described in detail by Santoro et al [1983], who designed and fabricated the original burner on which the one used in this study is modeled. The burner consists of an inner brass fuel tube of 10.8 mm inner diameter surrounded by an outer brass tube of 100 mm outer diameter. The coannular diffusion flame

burner which has been used extensively in flames research consisted of an inner brass fuel tube of 10.8 mm inner diameter surrounded by an outer brass tube of 100 mm outer diameter. A schematic of the burner is shown in Figure 2.1.6-1. The annular space between the two tubes provided a region for an air coflow. In order to maintain uniform and steady flow conditions at the burner exit, a series of flow restricting devices were placed within the burner. The annular air passage was packed with 3 mm glass beads and a series of fine mesh wire screens. A 25.4 mm thick ceramic honeycomb section (Corning 1.5 mm cell size) was used as the final flow conditioning device in the annular region. The fuel tube extended 4.8 mm above the ceramic honeycomb and it was also filled with 3 mm Pyrex beads to within 50 mm of the top of the burner to condition the fuel flow. A 405 mm long brass cylinder was used to shield the brass cylinder from laboratory air currents. Slots machined in the chimney provided appropriate optical access. Each slot was 6 mm wide and 25 mm high. In order to minimize scattered light, the chimney was painted with flat black paint. The chimney was mounted on a thin ball bearing in such a manner that the chimney can rotate on the burner axis, and translate on the horizontal plane perpendicular to the incident beam, while being centered on the axis of the burner.

In order to facilitate quick and accurate translation, the burner was mounted on a two-dimensional stepper motor (Daedal Series 44040 and 44060) controlled translating stage. These stepper motor driven stages provided both horizontal and vertical movements perpendicular to the incident laser beam. Stage positioning could be made with increments of 0.0127 mm in the vertical direction and 0.0254 mm in the horizontal direction, with accuracies of 0.0025 mm and 0.005 mm, respectively. The stepper motor stages were controlled using a stepper motor controller (Daedal PC-410). The procedure for locating the absolute position of measurement in the flame was important since extinction and multiangle scattering measurements are made simultaneously from the same point in the flame. To establish zero position along the vertical direction, a laser attenuation technique was used. In this procedure, the laser extinction setup was employed and the burner was translated until the fuel tube exit interrupted 50 % of the laser beam intensity as determined by a photodiode. Care was taken to ensure that the fuel tube was level so that the laser beam propagated normal to the fuel tube exit. Since the diameter of the laser beam was 0.25 mm, a positioning accuracy of ± 0.125 mm could be achieved. This accuracy was by far the limiting error in determining the vertical position in the flame since the stepper motor system had significantly more positioning accuracy. The absolute horizontal

position with respect to the flame centerline was subsequently determined, based on symmetry of the radial profiles, after data had been acquired. This system did not have a translation along the direction of the incident beam. Therefore, to ensure that the laser beam waist was centered along the fuel tube, the position of the focusing lens was adjusted during setup.

Fuel flow rate was determined using a calibrated mass flowmeter. The mass flowmeter for the fuel used, in this case ethylene, was calibrated using a bubble meter technique where the volumetric displacement of a soap bubble in a glass cylinder was equated to the volumetric gas flow through the mass flowmeter. With the calibrated mass flowmeter, flow rates could be set to accuracies of better than 2%. Air was measured using a Matheson Instruments Model FM-1050 rotameter capable of measuring up to 0.86 L/sec. This rotameter was also calibrated using the bubble meter technique. This system was found to establish flames that remain stable for hours at a time. Fuel used was ethylene of ultrahigh purity of 99.999 %. Air from an in-house compressor was used with suitable filters placed in line to remove both particulates and moisture.

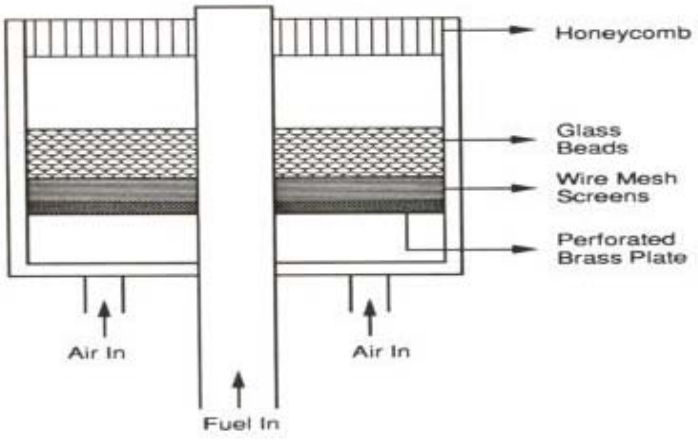

Figure 2.1.6-1. Schematic of Coflow Diffusion Flame Burner.

2.1.7 TURBULENT SPRAY FLAME

The turbulent spray burner was designed and fabricated as part of the SERDP project. The goal of the design was to create a small spray flame with substantial access to allow optical measurements to be made. The burner was successful in early use, but nozzle fouling problems

ultimately made it difficult to get consistent results from the test-to-test. The poor test-to-test repeatability limited the utility of the burner in the overall study so the amount of quantitative data generated in this facility was less than originally anticipated. It did, however, provide important confirmation of the effects of a number of the additives in a spray environment.

The turbulent spray burner consists of two concentric cylindrical stainless steel tubes (see Figure 2.1.7-1). Fuel flows through the inner tube while the oxidizer flows through the annulus between the two tubes. The inner tube, through which the liquid fuel flows, has an inner diameter of 6.2 mm and an outer diameter of 9.5 mm. The outer tube has an outer diameter of 25.4 mm, a wall thickness of 0.9 mm, and length of 178 mm. A peanut nozzle made by Delavan, Inc., shown in Figure 2.1.7-2 , was used for the atomization of the liquid fuel in this study; it has an outside diameter of ¼-inch and provides a nominal 80° hollow cone spray. The flow number of the nozzle is 0.3. Such a low flow number was required to achieve the small scale flame required for these experiments; however, it ultimately led to the fouling problems. The oxidizer, in this case air, enters into the plenum from the four sides of the chamber simultaneously. From the mixing plenum the air flows through a wire mesh and a honeycomb that produce a nearly uniform velocity profile at the exit plane.

The burner is operated at atmospheric pressure. The tip of the peanut nozzle is centered in a 55º swirl vane assembly (see Figure 2.1.7-2), which creates a recirculating flow field, stabilizing the combustion process. The swirler has an O.D. of 20.3 mm and an ID of 9.5 mm with 8 vanes and provides a swirl number of 1.1. Liquid fuel is sprayed into this swirling airflow that operates at a sufficiently high velocity that the flow field becomes turbulent. Within this burner, spray processes and turbulent mixing are important in addition to chemical kinetics and molecular diffusion. Some of the fuel droplets evaporate, and the vapor mixes with air to form premixed combustion regions. However, some of the fuel does not completely evaporate or mix with enough air for premixed combustion, so diffusion flames are also present.

In order to produce a steady flame and for the safety consideration, it is necessary to shield the flame with a chimney from laboratory air currents and put it under an exhausted vent. A 12 inch high X 9 inch wide high temperature window was mounted in three of four walls of the square chimney. Two windows are for optical access of the excitation laser source; the other, which is 90° to the laser beam path, is for the LII signal measurement. The hole, which is

covered with a shutter on the wall without the window, is used for ignition. The flames were ignited by means of a torch. Once the flame was lit, the torch was withdrawn.

The fuels and air supply systems are shown in Figure 2.1.7-3. The fuels with and without the additive are stored in two different tanks. The fuel flow can be easily switched by a three-way valve connecting the fuel tanks. The fuels are pumped into the nozzle by pressurizing them with argon. The fuel and the airflow rates are controlled by pressure regulator and rotameters, which were calibrated with Ventura and standard gas meters. The pressure dispensing fuel tank has a capacity of three gallons. Its maximum working pressure is 150 psig. At the experimental conditions in this work, the pressure, which is directly related to the fuel flow rate, is around 100 psig. The fuel is conditioned by a 15 micron filter. In addition, the whole fuel line can be purged by pure argon. A switch value was installed in the argon supply line to permit easy switching between pressurizing the fuel and purging the fuel line.

LII was the major diagnostic used in the turbulent spray flame to image the soot in the flames. Due to the turbulent nature of the flame, it was important to be able to get high time resolution so LII was well suited to the experiment. The LII signal was produced by excitation with a Continuum Nd:YAG Q Switched pulse laser, Surelite NY-61. It is equipped with a second harmonic generator to produce the 532 nm laser output. The output beam has a diameter of approximately 8 mm with measured divergence of 0.5 mrad. It can produce approximately Gaussian spatial energy profiles, with pulse duration of 5 to 7 ns FWHM. The Q Switch delay and the flash lamp voltage were held constant during the experiments. As discussed above, LII signals were observed through a narrow band pass filter, 430 ± 10 nm, so the interference from any fluorescence present could be minimized. A schematic of the optical layout is shown in Figure 2.1.7-4. A dichroic mirror directed the incident laser through a cylindrical lens and into the combustor. A cylindrical lens was used to form the 270 mJ per pulse laser beam into a 7.5 inch wide sheet. Since LII is generated for a short time after a cloud of soot is irradiated with an intense laser light, synchronization between the laser pulse and the collection of the LII signal is required. An oscilloscope was used to detect the laser output and set the gate for the camera.

Two-dimensional images were collected at 90º to the propagation direction of the laser beam using a Princeton Instruments intensified charge-coupled device (ICCD) camera with a UV Nikkor f/4.5 105 mm. lens. This orientation reduced the Rayleigh scattering present in the signal. Camera timing was provided by a Princeton Instruments Controller (Model ST 138), and gating

was controlled by a Princeton Instruments pulse generator (Model FG 100). The detection system was triggered from a synchronous trigger output of the laser. A standard timing configuration was used to obtain imaging rates as high as 10 Hz. The ICCD camera has a 14-bit resolution. The LII signal dependence on particle size and the soot volume fraction is valid only if the soot approaches its maximum temperature when LII signal is at its peak value. Therefore, a narrow gate width of 50 ns, and a short delay of 10 ns were used in this experiment. The prism, focus lens, and sheet forming lenses were set on an adjustable scaled stage, so the laser sheet could be adjusted along the height direction of the flame. The ICCD camera also sat on an adjustable scaled stage. In order to obtain satisfactory spatial resolution, multiple fields of view were required to capture the full flame height, which was facilitated by movement of the optics and camera.

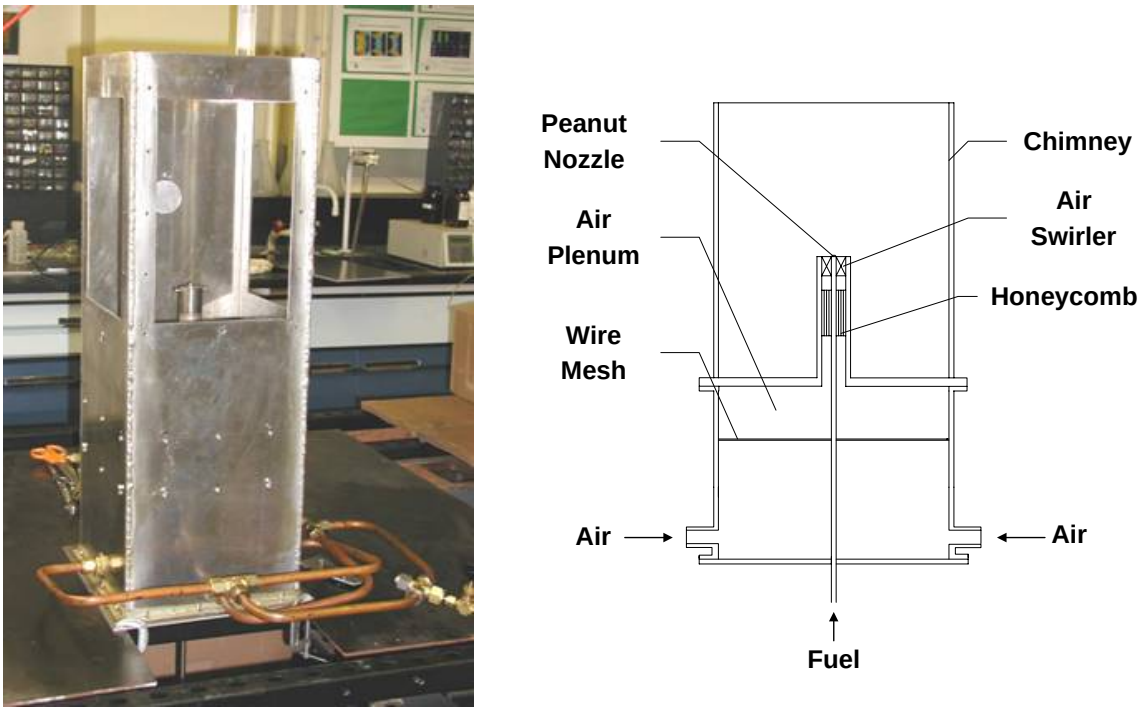

Figure 2.1.7-1. Image and Schematic of Turbulent Spray Burner.

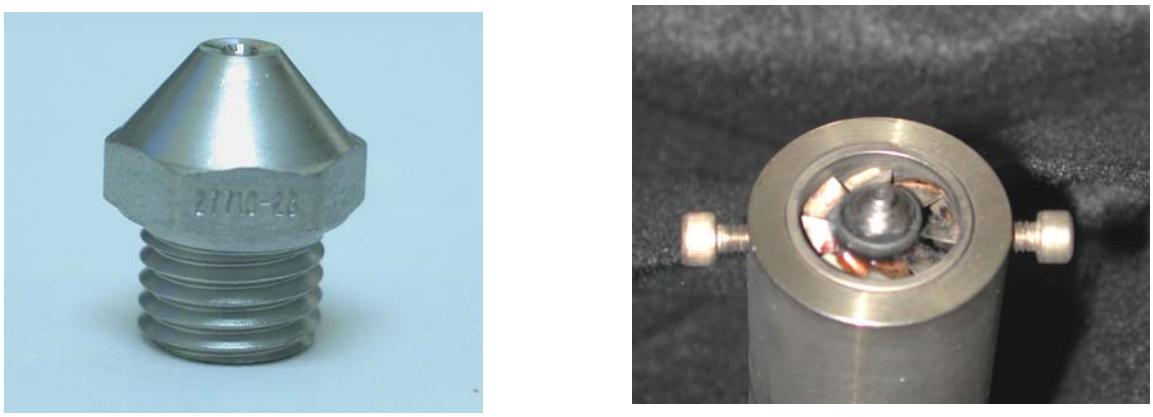

Figure 2.1.7-2. Nozzle and Air Swirler for Turbulent Spray Burner.

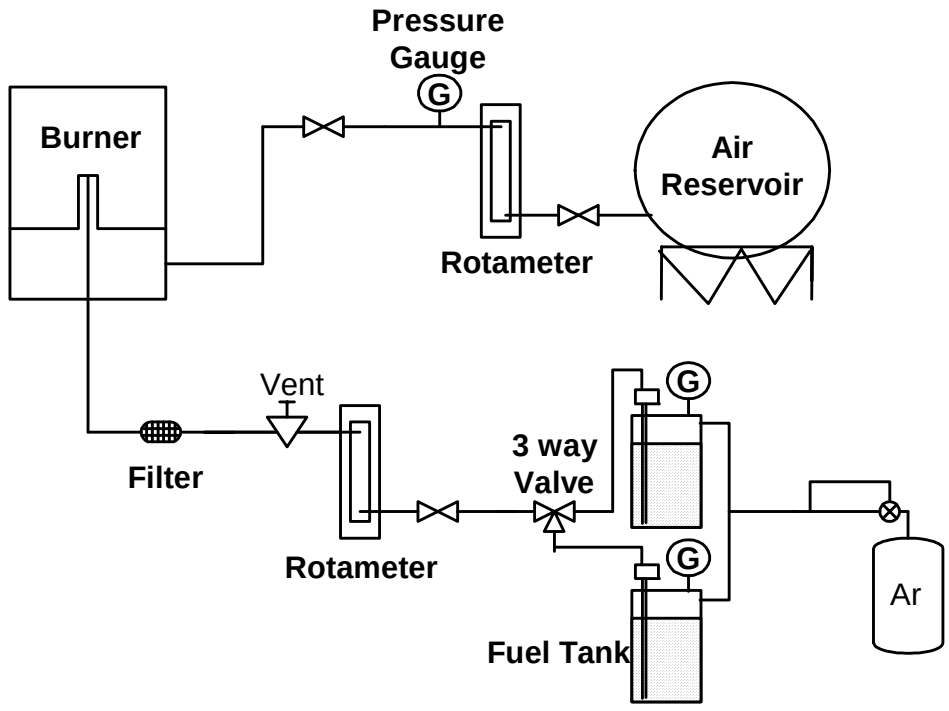

Figure 2.1.7-3. Flow Control System for Turbulent Spray Burner.

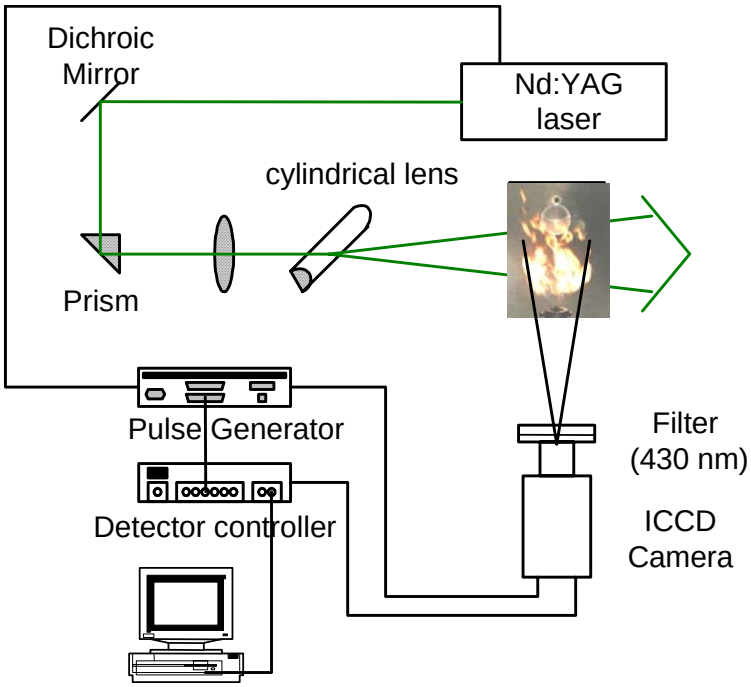

Figure 2.1.7-4. Optical Setup for LII Measurements for Turbulent Spray Flame.

2.1.8 HIGH PRESSURE TURBULENT REACTOR

A schematic diagram of the high pressure turbulent reactor is shown in Figure 2.1.8-1. The combustion chamber itself consists of several modular stainless steel sections that allow changes in the overall length of the combustion chamber as well as the location of any of the measurement devices or diagnostics being used. The first chamber section from the dump plane is optically accessible through a 2 mm thick, 104 mm long cylindrical quartz window. The outer portion of this section consists of a stainless steel housing containing three separate quartz windows providing optical access to the internal quartz combustion chamber. The following two stainless steel sections are 114 mm and 51 mm long. The 51 mm long section contains two flat horizontally opposed quartz windows which are 13 mm in diameter, through which extinction measurements can be made. These windows are cooled and kept clean by flowing nitrogen gas over them at a flow rate of approximately one gram/sec.

The last section is a 30° converging exit nozzle which is 39 mm long with an exit diameter of 10 mm. Note that all stainless steel sections have an internal coating of cubic

zirconium oxide to provide a heat resistive barrier which protects the stainless steel from the intense heat produced by the combustion. After the exit nozzle, the combustion products enter the inner portion of a heat exchanger, consisting of two concentric stainless steel pipes, before exhausting into the chimney. The liquid fuel supply tube consists of two concentric stainless steel tubes in which the inner tube is used for liquid fuel and the outer tube is used for cooling air. An annular flow of cooling air, about 8% of the total combustion air flow, is maintained along the outside of the inner tube in order to prevent fuel from vaporizing prior to reaching the injector tip. The cooling air is injected radially outward into the mainstream combustion air immediately downstream from the swirler.

In the present study, a Delavan pressure atomizer, commonly referred to as a peanut injector, was used as the fuel injector. The peanut injector has a flow number of 2.0 and a full spray angle of 90° with a hollow cone spray pattern. The flow number of a liquid injector indicates the effective flow area of a pressure atomizer. The flow number is expressed as the ratio of the nozzle throughput to the square root of the fuel injection pressure differential and liquid density. The fuel additives were introduced into the liquid fuel line using a high accuracy syringe pump (0.5% of set point) located approximately 4.7 m upstream of the liquid fuel injector. Uniform mixing of the additive and the fuel was obtained using an inline static mixer.

Temperatures and pressures at various locations along the rig were monitored by using K-type thermocouples and Setra pressure transducers. In addition, the upstream pressure of the fuel injector was closely monitored to ensure that the fuel injector did not become clogged. High-frequency piezoelectric pressure transducers were also used to monitor pressure fluctuations of the chamber pressure to ascertain that the combustor was operating under stable conditions throughout the experiment.

Due to the complexity of flow conditions in this apparatus, repeatable experimental data was very hard to achieve on a regular basis and great emphasis had to be taken to assure proper operating conditions were repeatably achieved. For example, self-sustained pressure oscillations can lead to a significant decrease in the amount of soot formed due to an enhanced burning rate, leading to more intense mixing processes and shorter residence times. Thus, a number of preliminary test experiments were conducted to determine a range of optimum flow conditions needed to produce a steady flame over a wide range of fuel consumption rates.

Soot volume fractions were determined by laser extinction measurements using an argon-ion laser operating at 514.5 nm. The collimated laser beam was mechanically chopped at approximately 1000 Hz and then directed through the two nitrogen purged quartz windows located 248 mm downstream from the dump plane. A portion of the incident laser beam, I, passed through the combustion chamber and its intensity was monitored using a silicon photodiode. The output signal was amplified by a Stanford Research System Model SR530 lock-in amplifier. Concurrently, the incident laser beam intensity, I_o, was also monitored by a separate silicon photodiode and lock-in amplifier. The signal output from the lock-in amplifiers was collected at a sampling rate of 3 Hz using an A to D system, and processed with LabView® software. The soot volume fraction was estimated using Rayleigh's approximation with the refractive index of soot particles taken as 1.57-0.56i at 514.5 nm[9], and a known path length of 45 mm. All measurements were made over a 30-second time duration. In the case of the atmospheric turbulent spray burner, measurements were made at a location of 178 mm above the injector tip. The soot volume fractions were estimated using flame width measurements obtained from digital camera images of the flame.

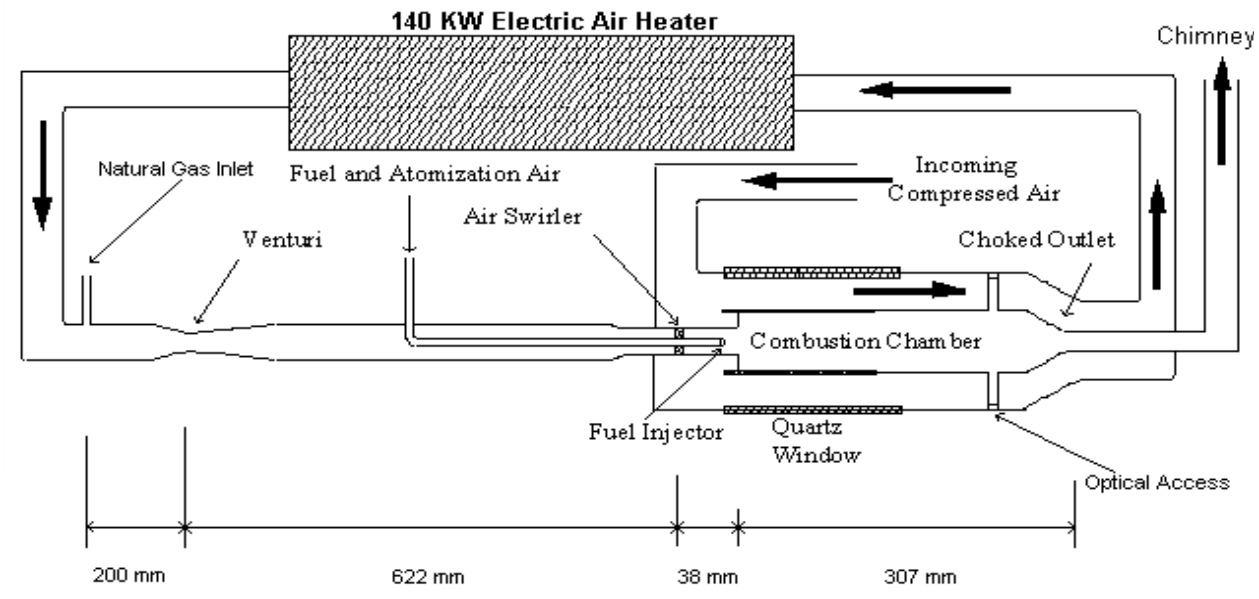

Figure 2.1.8-1. Schematic Diagram of High Pressure Turbulent Reactor.

2.1.9 CFM COMBUSTOR

An atmospheric pressure, swirl-stabilized combustor is located in the Atmospheric Pressure Combustor Research Complex of the Air Force Research Laboratory's Propulsion Directorate. The combustor consists primarily of a fuel injector, a square cross-sectional flame tube (combustion section), and an exhaust nozzle (Figure 2.1.9-1). It is primarily used to study the performance characteristics of model gas turbine engine fuels and fuel additives. The injector configuration, shown in Figure 2.1.9-2(a), is a generic swirl-cup, liquid-fuel injector, consisting of a commercial pressure-swirl atomizer (Delavan Model 27710-8) with a nominal flow number of 1.6. Surrounding the nozzle are dual, radial, counter-swirling air coflows to entrain the fuel, promote droplet breakup, and enhance mixing.

The 4 cm exit diameter fuel injector/swirler assembly is centrally located in the 15.25 cm x 15.25 cm square cross-sectional dome. Most of the air to the combustor enters through the swirl-cup injector, while a small percentage enters through small holes along the dome wall. The near-field structure of the swirl-stabilized flame is determined by the characteristics of the fuel injector, the swirl geometry, and the surrounding flame tube. As shown in Figure 2.1.9-2(b), the three-dimensional conical flame is composed of an outer droplet vaporization and preheat region (A) and an inner turbulent flame-brush region (B) [Lee 1995]. The flame is stabilized by a recirculation zone (C) that brings hot combustion products upstream along the centerline. After exiting the primary flame zone, the combustion products are allowed to mix thoroughly along the 48 cm long flame tube before entering a 43 cm long, 5.7 cm exit diameter exhaust nozzle. The nozzle is designed to create fairly uniform exhaust gas temperature and concentration profiles.

The combustor is optically accessible for in-situ laser-based diagnostics and video images via quartz windows along the top and sides. The combustor is capable of operating at equivalence ratios (Φ) of 0.5 to 1.2, which corresponds to a fuel flow rate of approximately 80 ml/min to 165 ml/min, respectively for JP-8 fuel. This is achieved by holding the airflow constant at 28 gm/sec and changing the fuel flow rate. The fuel flow rate was measured using a Max Machinery positive-displacement flowmeter and the airflow with a sonic nozzle. The inlet air was heated to 204°C with an electric heater. The air pressure drop across the combustor dome was approximately 4.5% of the main supply.

Measurement Methods

Particulate matter (PM) emissions from the research combustor were captured and transported to the analytical instruments via an oil-cooled probe. The probe was installed facing the flow in the center and at the exit of the combustor. In order to minimize particle loss by diffusion, impaction and static charge buildup, the probe and sample lines were built out of stainless steel tubing, and sharp bends were avoided. The exhaust sample was immediately diluted at the probe tip and the sample line was maintained at 75°C to minimize water condensation and particulate loss due to thermophoresis and agglomeration. Sample dilution also prevented saturation of the analytical equipment at the high equivalence ratios. Dilution ratios of approximately 17:1 were used in these studies. The diluted sample was drawn into the instruments via a vacuum pump, and the dilution air and sample flows were controlled and measured with high precision flow controllers. All particulate measurements were corrected for dilution flow to obtain actual values. On-line analysis of the mostly non-volatile particulate emissions was performed using a TSI Model 3022A Condensation Nuclei Counter (CNC) to provide a count of the total particles per unit volume (particle number density) and a TSI Model 3936 Scanning Mobility Particle Sizer (SMPS) to obtain a particle size distribution. For the SMPS, a nano Differential Mobility Analyzer (DMA) TSI Model 3085 with a Model 3025 CNC were used to classify and quantify the particles 4-160 nm in diameter. Gaseous emissions were extracted using an undiluted, oil-cooled probe and quantified using an MKS MultiGas 2030 Fourier-Transform Infrared (FTIR) based gas analyzer.

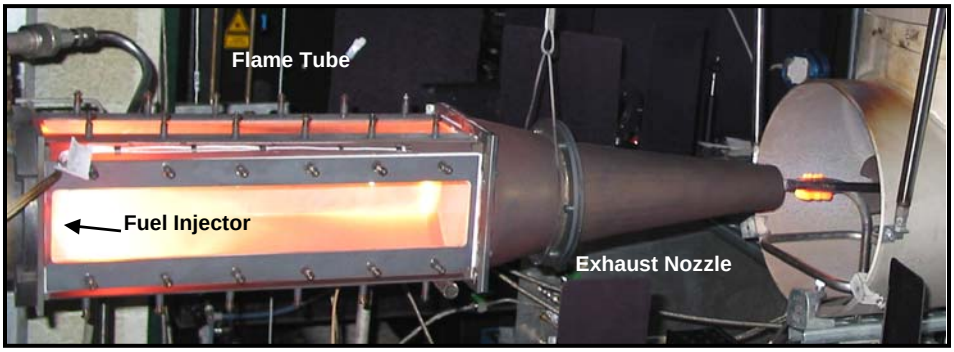

Figure 2.1.9-1. Swirl-Stabilized Atmospheric Pressure Research Combustor.

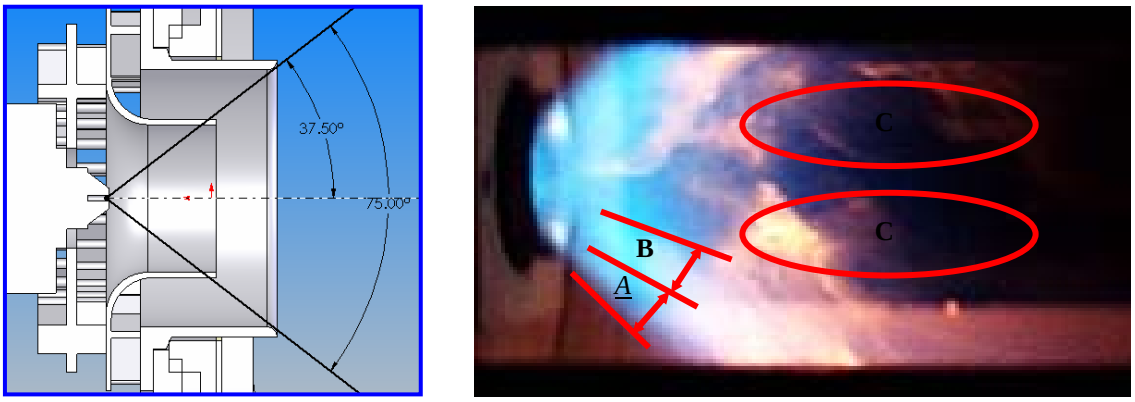

(a) (b)

Figure 2.1.9-2. Fuel Injector Geometry and Near-Field Flame Structure. Flow is from left to right.

2.2. COMPUTATIONAL

2.2.1 *CHEMKIN*

The CHEMKIN package from Reaction Design was used to simulate the shock tube, the premixed flames and the opposed-jet diffusion flame.

For the shock tube, CHEMKIN was used to estimate the precombustion conditions to which the fuels are exposed and the postcombustion conditions in the shock tube test section. The input parameters to obtain the fuel exposure conditions in the test section were the initial test gas composition in mole fractions, initial test section pressure and temperature, the incident shock velocity, test section diameter, viscosity and an arbitrary reaction time. For model validation simulations, the input parameters are reflected shock velocity precombustion temperature and pressure, initial test gas composition, shock tube diameter, viscosity of the bath gas and reaction time. The test section diameter and viscosity are required to correct for boundary layer effects, and the mixture viscosity was assumed to be that of the bath gas used, which was argon in this study. The flow inside a shock tube is assumed to be adiabatic, and transport phenomena associated with mass diffusion and thermal conduction are assumed to be negligible. Since the test times behind shock waves are very small, neglect of these transport processes is of little consequence. Also, viscous effects are assumed to be negligible and a vibrationally relaxed state of the test gas behind the reflected shock in the test section is assumed, i.e., a constant postreflected shock pressure model is assumed during simulations. The postcombustion temperature calculated is the final temperature at the end of the specified reaction time (see Figure 2.2.1-1).

To identify the most important reactions from the mechanism for a particular species, the top reactions based on the species rates of production were obtained by specifying the required number of top most reactions. This was required since conventional sensitivity analysis by simulating the shock tube experiments requires long computational times as well as very high computational power. The species rate of production is a measure of the rate at which a particular species is produced or consumed. Since CHEMKIN allows the user to identify the most important reactions that are involved in producing or consuming a species through rate of production analysis, the reactions with the highest rates of production were obtained by

simulating the shock tube. Since the species rates of production are temporal profiles, to obtain their net contribution so that the reactions could be compared as in conventional sensitivity analysis, their net production was calculated by integrating the area under the temporal profile.

For the premixed flames, simulations were conducted with the PREMIX subroutine of the CHEMKIN package. Although the program is capable of computing the temperature profile, experimentally measured temperature profiles were used for all simulations. Use of a measured temperature profile in the computations eliminates the need to model heat loss in the energy equation, which significantly reduces computing time. Mass flow rate through the burner, gas composition, pressure, temperature and estimated initial solution profile were used as input.

Additional analysis of the results was conducted using a postprocessor, XSenkplot, which determines the production and destruction fluxes of a given species for all reactions involving that species, and an in-house post-post processor that uses the output from XSenkplot. The reaction flux analysis was used to identify primary reaction sequences leading to PAH formation and growth pathways. XSenkplot, developed at NIST, is an interactive graphics postprocessor for numerical simulations of chemical kinetics to postprocess the CHEMKIN family software package. It displays mole fractions, production and destruction rates of species, and reaction pathways as a function of time or distance. The inputs for this software are binary files of the chemical mechanism and a solution file describing time or space dependent species concentrations in reacting systems. An important feature of XSenkplot is calculation of the net rate profiles of production of species of interest, which facilitates the development of a fundamental understanding of coupled chemically reacting systems by providing the ability to probe the impact of process parameters and reaction mechanisms. Utilizing XSenkplot, reaction pathways from initial hydrocarbon fuel to soot precursors, production and destruction rate of each species, and net production profile of PAH species were obtained as a function of height above the burner surface.

For the opposed-jet diffusion flames, calculations used the OPPDIF flow code, based upon the CHEMKIN database, marketed by Reaction Design, Inc. Input conditions for the calculations assumed initial gas temperatures at 300K, 1 atmosphere total pressure, and initial fuel and oxidizer gas stream velocities of 40 cm/sec. For the burner system used in the experiments, the fuel velocity was approximately 41 cm/sec, and the oxidizer velocity was approximately 55 cm/sec. An attempt was made to run the OPPDIF code using these settings but

difficulty was encountered with convergence, so settings of 40 cm/sec were used for fuel and oxidizer velocities in the calculations. Each calculation required approximately two hours to reach convergence on a Pentium-based desktop computer.

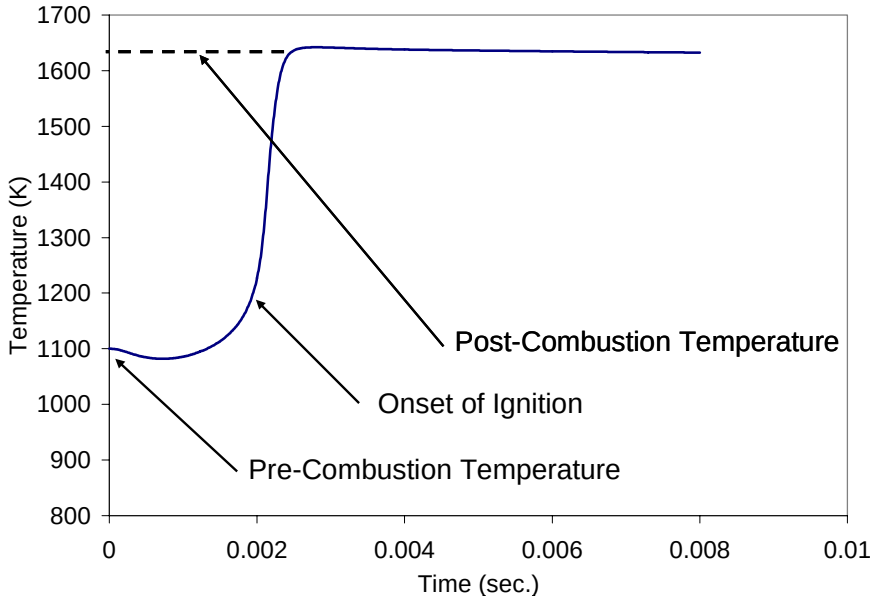

Figure 2.2.1-1. Model Temperature Profile for Heptane/Toluene at 1100 K, 21 atm.

2.2.2 WSR MODELING USING CHEMKIN

For the WSR, the chemical kinetic modeling was performed utilizing a modified version of the CHEMKIN II-based code for stirred reactors [Glarborg et al 1986, Kee et al 1991]. A conceptual schematic of a stirred reactor is provided in Figure 2.2.2-1.

For a perfectly stirred reactor (PSR), sufficiently intense mixing is assumed such that the concentrations of all species and temperature are uniform throughout the reactor and that these values are identical to the exit conditions. Additional equations have been added to include computations of soot formation. The original equations treated by the PSR code include the species and energy conservation equations:

$$\dot{m}(Y_k - Y_k^*) - \dot{\omega}_k^g W_k V = 0, \qquad k = 1,2,....K$$
$$\dot{m}\sum_{k=1}^{K}(Y_k h_k - Y_k^* h_k^*) + Q = 0$$

where Y_k is the mass fraction of the kth species (a total of K species); $\dot{m}$ is the mass flow rate through the reactor volume, V; W_k, the molecular weight of the kth species; $\dot{\omega}_k^g$, the molar rate of production by chemical reaction of the kth (gaseous) species per unit volume; h_k, the specific enthalpy per unit mass of the kth species; and Q, the reactor loss. The superscript (*) indicates the inlet conditions.

The growth of soot spheroids in the reactor has been modeled as a classical aerosol dynamics problem, involving the division of the size range of interest into discrete intervals or size classes with a logarithmic transformation of the size range, and then deriving a source for the size class mass densities with terms representing inception, surface growth (or oxidation) and coalescence. The sectional analysis follows the analysis developed by Gelbard and Seinfeld [1980]. The method used in this work incorporates selected algorithms of the well-known MAEROS program. Surface growth and coalescence are assumed to take the free molecular form and the spheroids consist of the single component carbon. Furthermore, it is assumed for this sectional analysis that the boundaries of the sections vary on a log scale. The total number of particle sections is M. Additional details of the application of the sectional analysis to modeling soot formation have been developed and described in detail by Hall et al [1997]. The extension to stirred reactors is made through the use of the modified governing equations:

$$\begin{aligned}
&\dot{m}(Y_k - Y_k^*) - \left(\dot{\omega}_k^g + \dot{\omega}_k^s\right) W_k V = 0, \quad k = 1,2,....K \\
&\dot{m}(Y_k - Y_k^*) - \dot{Q}_k V = 0, \quad k = K+1, K+2,...K+M \qquad (3) \\
&\dot{m}\sum_{k=1}^{K}(Y_k h_k - Y_k^* h_k^*) + Q = 0
\end{aligned}$$

where the extra equation (series) represents the conservation equations for the sectional (particulate) species. Y_k (k = K+1 to M) represents the mass fractions of the M sectional "species" or particulates; $\dot{\omega}_k^s$ is the molar rate of production of the kth gaseous species per unit volume due to reactions involving soot particulates (i.e., scrubbing/replenishment of gaseous species from surface reactions during soot growth/oxidation processes); and $\dot{Q}_k$ is the net mass

rate of change of particulates in section *k* per unit volume due to aerosol processes (including soot inception, surface growth and oxidation, as well as collisional dynamics). The enthalpy of all the sectional species were assumed equivalent to a large PAH, that is, slightly larger but nearly identical to that for condensed carbon (0.0 kcal/gm). A total of 20 soot sections were assumed for this study, ranging from an equivalent midpoint particle diameter of 0.78 nm to 10.8 μm (assuming a soot density of 1.8 gm/cc).

The soot dynamics model generally follows the schematic depicted in Figure 2.2.2-2. The model treats gas-phase kinetics, soot inception/nucleation, surface growth and oxidation, as well as collisional coalescence; ageing/carbonization and coagulation effects are not included. For simplicity, nucleation is computed based on the formation of naphthenyl radicals as described by Hall et al [1997], although there is ample justification for using a higher molecular weight polycyclic aromatic hydrocarbon for description of inception rates. Surface growth is based upon the work by Harris and Weiner [1983] and, hence, acetylene is assumed to be the only surface growth species. Note, that since small PAH are treated as soot in this model, the mass growth due to PAH addition to soot is not excluded. Oxidation by OH [Neoh et al 1981] and O_2 [Nagle and Strickland-Constable 1962] were included utilizing the formulism presented by Hall et al [1997]. For this PSR modeling, the collisional efficiency of OH reaction with soot was reduced by a factor of three in an attempt to model the earlier data of Zelina [1995]. Temperature data was not available for those simulations; hence, simulations were performed assuming adiabatic conditions.

For the atmospheric pressure conditions of this investigation, the coalescence rates were assumed to be in the free molecular regime; an average collisional enhancement factor or 1.5 has been utilized to simulate attractions from van der Waals forces.

The PSR model was run with the detailed reaction set for ethylene that has been utilized in previous soot modeling efforts [Colket and Hall 1994, Hall et al 1997] in laminar premixed and diffusion flames. To this mechanism, species, reactions and related thermodynamics for ethanol chemistry originally developed by Marinov [1998], and as assembled by Song et al [2003] has been included. The total mechanism has 67 species and 388 reactions.

Normally, exit species concentrations and temperatures are determined by the PSR code; this modified code also computes the particle size distribution, from which total particle mass and number densities can be calculated. A correlation developed by Colket et al [2003] for the

relationship between smoke number and total particle mass, m, in mg/m^3, where the volume is based upon conversion of the flame gases to atmospheric pressure at 289K. Ambient conditions are utilized for the reactor studies as they are close to characteristic conditions for the smoke number (SN) measurement device. The correlations developed by Colket and coworkers are:

$$\text{if m } (mg/m^3) < 2.5 \text{ then: } \quad SN = -1.8743*m^2 + 12.117*m \qquad (4)$$

$$\text{if m } (mg/m^3) > 2.5 \text{ then: } \quad SN = 12.513*m^{0.4313}$$

or

$$\text{if SN} < 18.7, \text{ then: } \quad m = 3.232*(1-(1-SN/19.58)^{1/2}) \qquad (5)$$

$$\text{if SN} > 18.7, \text{ then: } \quad m = 0.002751*SN^{2.319}$$

These empirical curves were shown to be in good agreement with other literature data.

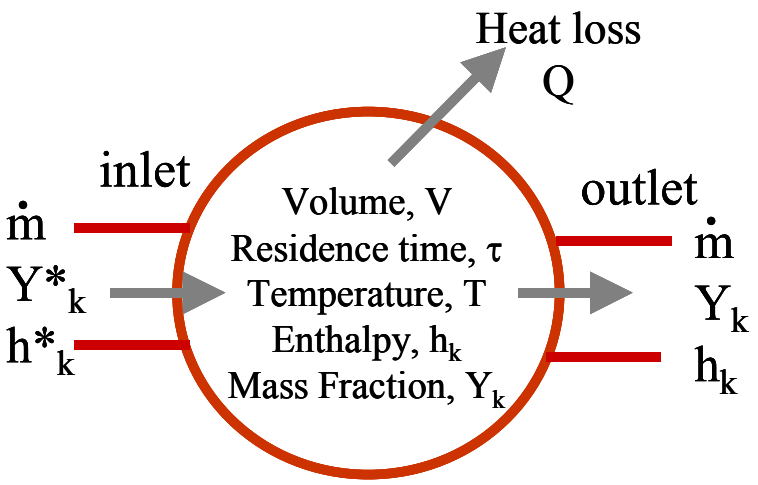

Figure 2.2.2-1. Schematic of Perfectly Stirred Reactor.

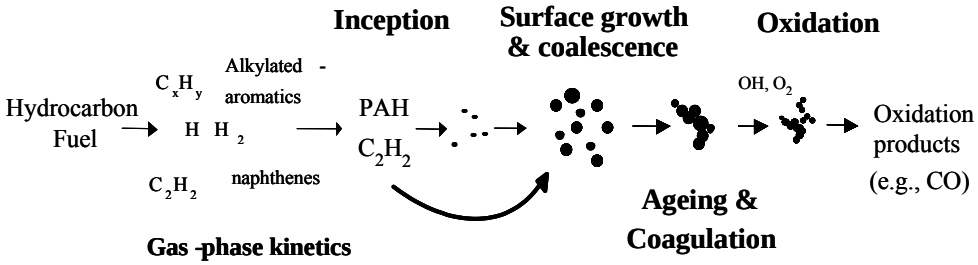

Figure 2.2.2-2. Sequence for Soot Formation and Oxidation.

2.2.3 UNICORN CODE

UNICORN (UNsteady Ignition and COmbustion using ReactioNs) code is a time-dependent, axisymmetric mathematical model, which is used for the simulation of unsteady reacting flows. The UNICORN code was used to make predictions for coflow flames, which is currently not possible with CHEMKIN. UNICORN offers additional advantages over CHEMKIN including an ability to handle large kinetic mechanisms relatively easily.

UNICORN is capable of handling large eddy simulations and has been developed over a 10-year period. Its evolution has been in conjunction with experiments conducted to test its ability to predict ignition, extinction, stability limits, and the dynamic characteristics of diffusion and premixed flames of various fuels. It solves for u- and v-momentum equations, continuity, and enthalpy- and species-conservation equations on a staggered-grid system. The body-force term due to the gravitational field is included in the axial-momentum equation for simulating vertically mounted flames. A clustered mesh system is employed to trace the large gradients in flow variables near the flame surface. Detailed chemical-kinetics models for various fuels are incorporated. Thermophysical properties such as enthalpy, viscosity, thermal conductivity, and binary molecular diffusion of all the species are calculated from the polynomial curve fits developed for the temperature range 300 to 5000 K. Mixture viscosity and thermal conductivity are then estimated using the Wilke and Kee expressions, respectively. Molecular diffusion is assumed to be of the binary-diffusion type, and the diffusion velocity of a species is calculated using Fick's law and the effective-diffusion coefficient of that species in the mixture. A simple radiation model based on the optically thin-media assumption is incorporated into the energy equation.

The finite-difference forms of the momentum equations are obtained using an implicit QUICKEST scheme, and those of the species and energy equations are obtained using a hybrid scheme of upwind and central differencing. At every time step, the pressure field is accurately calculated by solving all the pressure Poisson equations simultaneously and using the LU (Lower and Upper diagonal) matrix-decomposition technique. Chemical source terms are treated implicitly while solving the species and energy conservation equations. Such treatment allowed UNICORN to simulate reacting flows with chemical mechanisms that are significantly stiff.

Different types of boundary conditions such as adiabatic wall, isothermal wall, symmetric surface, outflow, and inflow can be applied to the boundaries of the computational domain.

The simulations can be performed on a personal computer with 2.0 GB of memory. Execution times strongly depend on the number of species considered in the model and the grid size. Typically with 197 species and 2926 reactions (heptane model) on a 400X180 grid system, simulations take ~110 s/timestep on an AMD-Opteran-250 computer with 2 GB memory. Steady state flames are usually obtained in about 2000 time steps and unsteady simulations can be performed for several thousands of time steps.

Validation Studies

UNICORN code has been extensively validated [Katta and Roquemore 1993, Roquemore and Katta 2000] by simulating various steady and unsteady counterflow [Katta et al 1998] and coflow [Katta et al 1994, Katta and Roquemore 1998] jet diffusion flames and by comparing the results with experimental data. More recently UNICORN has been used for the investigation of nonadiabatic-equilibrium flame temperatures developed during millimeter size vortex/flame interactions [Katta et al 2003] and unsteady extinction behavior of H_2/air diffusion flame [Katta et al 2004]. Figure 2.2.3-1 demonstrates the ability of the UNICORN code in predicting dynamic flames through the comparison of measured and computed methane jet diffusion flame shown in left and right halves, respectively. This simulation used 31-species, 346-reactions GRI mechanism. A laminar jet diffusion flame established with a low speed fuel and a negligibly small annular air flow generates large scale, low frequency (1-40 Hz), organized buoyancy-induced vortices on the air side of the flame--very similar to pool fires. Because of the similarities between buoyant jet diffusion flames and practical uncontrolled fires, the former are often investigated to understand the effect of gravity on vortical structures, flame-vortex interactions, and entrainment characteristics of the latter. The central fuel jet of the flame in Figure 2.2.3-1 is issued from a 10 mm-diameter nozzle at an exit velocity of 0.5 m/s. The annular air jet has a diameter of 245 mm and a velocity of 15 cm/s. Because of the buoyancy force and the absolute instability associated with the hot gases, this flame became a dynamically oscillating one. Unsteady axisymmetric calculations for this flame were made on a physical domain of 250 x 150 mm utilizing a 171 x 71 nonuniform grid system. The frequency corresponding to the passage of these outer vortices (also known as the flame-flickering frequency) is ~ 12 Hz. The predicted flame structure compares well with that of experiment.

Calculations have even predicted the recirculation region that is developed inside the flame and traveling ahead of the outer vortex.

The complex interactions between isolated vortices and the flame surface are studied using UNICORN code. A counterflow flame formed between hydrogen and air jets is used. Vortices are shot toward the flame surface from the air-side by injecting a specified amount of air through the syringe tube and then through a 0.2 mm-diameter micro injection tube. Evolution of the injected microvortex (initial diameter < 1 mm) and its interaction with the flame surface is dependent on the injection duration. In general, with the shorter injection times, the generated vortices travel faster toward the flame surface and influence the flame structure as the local flow time scales approach the chemical time scales. A typical experimental image of the millimeter-size vortex/flame interaction is shown in Figure 2.2.3-2. This represents the OH concentration field captured using the PLIF measurement technique and clearly shows the significant increase in OH concentration in the head region of the vortex. Results obtained from the calculations are shown in Figure 2.2.3-2 on the right-hand side. Calculations also predicted the significant increase in the concentration of OH in the head region. The computed OH distribution matches well with the experimental OH-PLIF data.

Working with Large Mechanisms

Detailed chemical kinetics for aviation fuels could involve hundreds of species and thousands of reactions. Such large mechanisms can be used for performing multidimensional reacting flow simulations by either calculating reaction rates at each grid point by the calling mechanism subroutine or integrating the mechanism with the Computational Fluid Dynamics (CFD) code. The former approach eliminates any possible errors in incorporating the chemical-kinetics mechanism; however, it puts significant burden on computational resources and it may become an impractical approach for a reasonably large mechanism. Also, calling subroutine approach requires the chemical source terms to be treated explicitly, which is known for its limitations in handling stiff reactions. On the other hand, incorporating large chemical-kinetics mechanisms in a CFD code is a formidable task and is highly susceptible to typographical and programming errors--mainly because of the implicit treatment of the reaction-rate terms for a stable solution procedure. Because of these difficulties it is very rare to see scientists/engineers using large mechanisms for performing multidimensional reacting flow simulations. As

described earlier, UNICORN code is developed based on implicit algorithm for chemical reactions and the reaction mechanism must be integrated with the code. During the early stages of the UNICORN development small chemical mechanisms for fuels such as hydrogen and methane were incorporated manually, which was found to be very cumbersome and led to several errors. As an example, the total time taken for incorporating a 21-species, 81-reactions mechanism was about a month, which includes debugging for the typographical and programming errors. Such developmental time was expected to reach several months for medium mechanisms with less than 100 species and found to be an impractical approach for large mechanisms with greater than 200 species. For circumventing this laborious and error-prone development, a new approach was conceived. A logical program (software) was developed through incorporating all the logics that are needed for placing chemical mechanisms implicitly into UNICORN. As software generates FORTRAN code, typographical and programming errors in modifying UNICORN code for large chemical kinetics was eliminated. With this approach UNICORN, for a given chemical kinetics model, independent of its size, can be developed in a few hours. The developed software directly reads the kinetics data prepared in standard CHEMKIN format and writes the modified UNICORN code for that chemistry. This software has been rigorously tested on smaller mechanisms to ensure that it generates an error-free code for the given chemistry. In this way, human involvement in preparing the CFD code is minimized; hence, errors associated with it are eliminated. Using this strategy (i.e., accurately developing modified UNICORN code), a number of reacting flow simulations have been performed such as ethylene flames using 99 species and 1066 reactions, propane flames using 105 species and 1200 reactions, heptane flames using 366 species and 3698 reactions, methane+halon flames using 92 species and 1644 reactions, and JP-8 flames using 216 species and 3000 reactions.

Soot Model

Computational soot models based on the fundamental physics of soot formation and oxidation are not yet available. The research groups around Moss and Lindstedt have made some progress in modeling soot formation using semiempirical models based on the mechanisms of particle inception, agglomeration, surface growth, and oxidation. The soot model included in UNICORN utilizes a two-equation model with transport equations for particle number density,

N_s, and soot mass fraction, Y_s. The source terms in these transport equations are obtained using Lindstedt's model, which is based on the simplifying assumption that nucleation and growth are first-order functions of acetylene and benzene concentrations. Soot oxidation is treated as chemical reactions between soot and O2 and OH. Physical process of soot agglomeration is also included as a source term.

Figure 2.2.3-1. Buoyant Jet diffusion Flame Measured (left) and Computed (right).

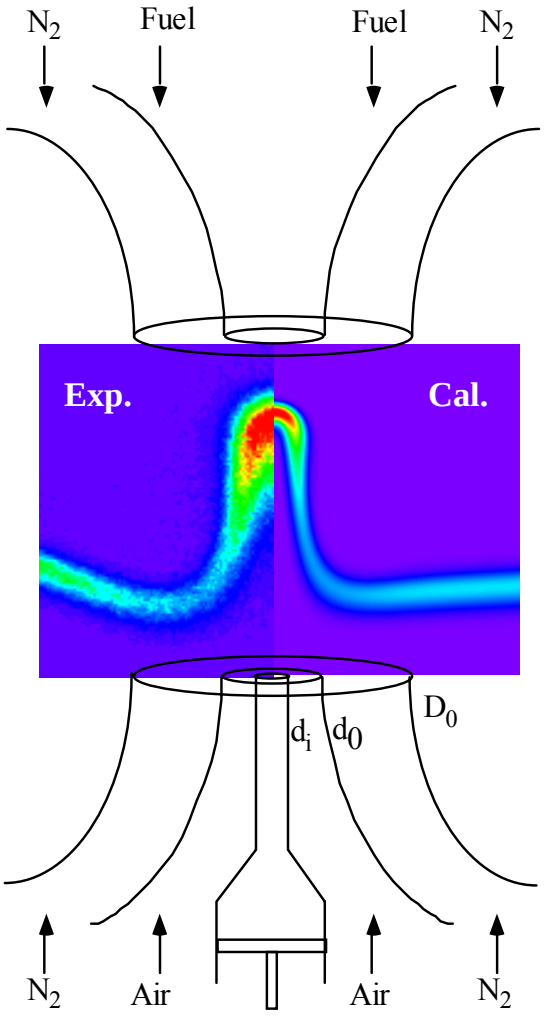

Figure 2.2.3-2. Schematic Diagram of Opposing-Jet Burner Used in the Studies of Vortex-Flame Interactions. Inserted images (measured and computed on the left and right halves, respectively) are that of a typical protruded flame obtained with a micro airside vortex showing an increase in the concentration of OH at the tip.

2.2.4 REACTION MECHANISMS

In collaboration with the NIST SERDP team a number of mechanisms were created during this program that were required for simulation of the effects of the additives. The mechanisms are available on CD from AFRL.

Two kinetic mechanisms for ethylene were used in this study. The first was the detailed reaction set provided by M. Frenklach [Frenklach and Wang 1990(a)] and modified at PSU to include oxygenated compounds. It includes species as large as pyrene (a four-ring polycyclic aromatic hydrocarbon, $C_{16}H_{10}$, with a mass of 202 atomic mass units, or amu). For the WSR modeling, a second set of reactions was used that has been utilized in previous soot modeling efforts [Colket and Hall 1994, Hall et al 1997] in laminar premixed and diffusion flames. To this mechanism, species, reactions and related thermodynamics for the ethanol [Curran et al 2001] and DME [Curran et al 1998] chemistry originally developed at Lawrence Livermore Laboratories were extracted and added to the mechanism.

This mechanism has also been extended and utilized by team members to evaluate the impact of the addition of nitroalkanes. NIST created a mechanism for nitromethane in heptane/toluene based on the nitromethane reactions of Zhang and Bauer, (1997). A mechanism for isopropyl nitrate was also developed during the course of the work at ARL.

In addition, a chemical kinetics submodel for the pyrolysis and oxidation of pyridine has been developed and added to the reaction set for heptane. Pyridine (C_5H_5N), which has a nitrogen atom embedded into the aromatic ring, had been identified in previous work at UTRC to reduce soot from fuel-rich premixed flames. Levels as high as 100,000 ppm pyridine (in a heptane/toluene fuel blend) were used to achieve as much as 40% reduction in the soot produced from a premixed flame. Results obtained at other team-member laboratories have been mixed, although soot reductions had been observed at one other organization (PSU) in a turbulent flame. Based on these results, an effort was initiated to develop a modeling capability for examining effects from pyridine. A submechanism was assembled based upon the pyrolytic studies of Mackie et al [1990] and subsequent work on the oxidation of pyridine [Ikeda et al 2000]. This submechanism was added to the heptane reaction set and several additional steps were added to include trapping of C2 hydrocarbons by fragments of the pyridine molecule. The revised, total reaction set consisted of 314 species and 1713 reactions.

The NIST heptane model proved to be computationally challenging for CHEMKIN so a reduced version was created. Reduction of the original NIST heptane mechanism was a relatively straightforward effort, consisting of elimination of reactions and species larger than pyrene ($C_{16}H_{10}$). The reduction was motivated by the added computational expense associated with the original mechanism that included species ($C_{30}H_{14}$) and reaction mechanisms that were nearly twice as large as pyrene. The reduction process was justified by increasing uncertainties in the thermodynamics, the reaction processes, and reaction rates with increasing molecular size with little added benefit to assessing the relative effectiveness of a soot-reducing additive. The net result was a reduction in the number of species by 20% (367 to 283) and the elimination in the number of elementary reactions (1850 to 1647). Furthermore, in most soot formation models, soot inception is based upon species (or their formation rates) that are equivalent to or smaller than the molecular weight of pyrene.

Finally, for the kinetics of phosphorous-containing compounds, a portion of the phosphorous kinetics set developed by Glaude et al [2000] has been extracted and added to the base kinetics mechanism.

3. RESULTS

3.1 OXYGENATED ADDITIVES

3.1.1 SUMMARY OF MAJOR RESULTS

The initial work on oxygenated additives focused on ethanol and its effect during the combustion of ethylene. To investigate effects of additive structure in soot reduction, experiments were also conducted in the premixed flame with dimethyl ether (DME). After completion of the ethylene studies, studies with liquid fuels were undertaken. In addition to ethanol and DME, cyclohexanone was studied because it was a component in a commercial additive that produced some soot reduction.

Table 3.1.1-1 presents a summary of the effects of ethanol and cyclohexanone on soot in the hierarchy of devices used in this study. A very important observation can be made based upon this summary:

> Reduction in soot can be achieved by the addition of oxygenated compounds in all of the devices studied, with the notable exception of the ethylene opposed-jet diffusion flame. Further, reduction can be achieved whether the fuel is introduced as a liquid or vapor. Therefore, the process governing the reduction of soot must be common to all of the devices, and that process is chemical kinetics.

The other major findings from the study of oxygenated compounds are:

1. The effects on chemical kinetics can be "direct" through introduction of new species or increases in concentrations of key intermediates or it can be "indirect" through temperature changes that lead to shifts in the relative importance of competing reactions.
2. Through detailed modeling studies, the mechanism by which soot is increased when ethanol is added to ethylene in the opposed-jet diffusion flame was determined to be the enhancement of the "even-carbon species" pathway to benzene due the production of methyl radicals from ethanol, not via the enhancement of the "odd-carbon species," as was originally conjectured.
3. Detailed modeling of the results for DME and ethanol addition to the ethylene diffusion flames verified that the chemical structure of the additive does play a role in the effectiveness of oxygenated additives in reducing soot.

Table 3.1.1-1. Summary of the Effect of Additives on Soot.

	Additive	**Fuel**	**Effect on Soot**	**Comments**
Shock tube	Ethanol	Ethylene	Decrease	
	Cylcohexanone	Heptane/ Toluene	Decrease	
Well-stirred reactor	Ethanol	Ethylene	Varies: decrease to slight increase	Effect is dependent on reactor temperature
	Cyclohexanone	Heptane/ Toluene	Decrease	
Premixed flame	Ethanol	Ethylene	Decrease	
	DME	Ethylene	Decrease	DME shows slightly greater effectiveness
Opposed-jet flame	Ethanol	Ethylene	**Increase**	
	Ethanol	Heptane	Decrease	
Turbulent spray flame	Ethanol	Heptane	Decrease	
HP turbulent reactor	Ethanol	JP-8	Decrease	
	Cyclohexanone	JP-8	Decrease	

3.1.2 SHOCK TUBE

The complete experimental conditions for premixed gas-phase ethylene and ethylene+ethanol experiments are listed in Table 3.1.2-1. The test section for all premixed experiments contained 5% fuel (v/v), 6.4% oxygen (v/v), and the balance argon. For ethylene+ethanol experiments, ethanol was added such that 5% (m/m) of ethylene-ethanol mix was oxygen. The temperature, $T_{5,}$ and pressure, $P_{5,}$ are postshock, preignition conditions. Since the diluent gas (Ar) is approximately 90%, the heat release from combustion will only cause a minor change in temperature. Several experiments were also conducted with cyclohexanone, the oxygenated component in the commercial additive that was found to reduce soot. Those experiments were performed with heptane/toluene as the fuel.

A limited number of JP-8 experiments was also conducted and is summarized in this section as well. In these experiments, liquid fuel (JP-8 and JP-8+additives) was introduced using a Bosch diesel fuel injector fitted with a single stroke positive displacement fuel pump. The fuel is introduced 500 μs behind the reflected shock, which allows for the vibrational relaxation of the bath gas prior to injecting the fuel. For each liquid fuel test, approximately 46.5 ml of fuel was injected into shock-heated gas consisting of 4.6% oxygen and 95.4% argon. Given the volume of the system and assuming all of the oxygen is available for combustion, the density of the fuel is 0.8 gm/ml and the oxygen demand to be 0.107 moles of oxygen per gram of fuel, this gives a mean equivalence ratio of 0.601, or 66% excess air. The overall mean condition of the shock-heated gas (preignition) was 1272°C at 13.5 atm. The complete experimental conditions for liquid injection experiments are listed in Table 3.1.2-2. The fuels tested included JP-8, JP-8+100, JP-8 with 13.4 % (v/v) diethyl maleate, and JP-8 saturated with diethyl maleate. The exact concentration of the saturated system is unknown, but we estimate it to be slightly greater than 13.4% (approximately 15%). Specifically, the saturated sample was prepared from the 13.4% stock sample and an immiscible layer was seen to form almost immediately on adding additional diethyl maleate. Each fuel was tested over a 2-day period over which 8 individual tests were performed.

Soot Yields from Premixed Experiments

The results from ethylene and ethylene+ethanol experiments are shown in Tables 3.1.2-3 and 3.1.2-4, respectively. The comparison of the sample means from ethylene and ethylene+ethanol experiments shows that addition of ethanol decreased the mean soot yield by 18.2 ug, a 19.5% decrease in mean soot production. The confidence level for the hypothesis that the population mean soot level from ethylene is greater than that of ethylene+ethanol as compared to the hypothesis that the soot levels are the same using the 2-sample t-test is 91.4%.

Figure 3.1.2-1 compares averaged carbon signal obtained by desorbing soot samples collected from ethylene and ethylene+ethanol experiments listed in Table 3.1.2-1. Figure 3.1.2-1 shows that the soot produced in both sets of experiments has a high soluble organic fraction (carbon desorbed below 300°C) compared to diesel soot whose soluble organic fraction is usually in 5 to 25% range [Morawsaka 1998]. This high soluble organic fraction is perhaps due to low post-shock temperature in these premixed experiments. Figure 3.1.2-1 also shows that addition of ethanol did not change the molecular weight distribution of soot; the soot yield was just lowered in all molecular weight divisions.

Soot Yields from Liquid Fuel Experiments

Figure 3.1.2-2 shows that addition of cyclohexanone lowers particulate yield at all temperatures studied. As shown in Figure 3.1.2-2, particle yield data for the base fuel forms a bell-shaped curve. The lower soot yields at the lower temperatures (~1150 K) are due to the slower rate of formation of soot precursors and the reduced combustion time due to the increased ignition delays. However, the lower soot yield at higher temperatures (~1500 K) is due to the rates of oxidation dominating the rate of particle formation. The maximum in soot yield curves thus occurs when temperatures are high enough for particle formation processes (e.g., precursor formation, nucleation and surface growth) but are still too low for particle oxidation to be significant. Regardless of conditions, however, the cyclohexanone was effective in reducing soot.

In the JP-8 soot formation study, we tested JP-8, JP-8+100, JP-8 + 13.4 % (v/v) diethyl maleate, and JP-8 saturated with diethyl maleate. Each liquid fuel was tested over a two-day period over which 8 individual tests were performed. The means and 90% confidence intervals of the exposure conditions and soot yields were calculated from each sample of 8 tests using the

t-distribution. Furthermore, the sample means were compared using a two-sample t-test with pooled variances. For this analysis (see Table 3.1.2-5) the sample mean of JP-8 was compared with the three fuel blends. The confidence levels were calculated for rejecting the null hypothesis (the sample means were the same) compared to the hypothesis that the soot yield of the JP-8 was greater than the soot yield of the fuel blends. These results show that the null hypothesis cannot be rejected for JP-8+100 (the confidence level for this rejection is only 58%). However, the confidence levels for the rejection of the null hypothesis for the JP-8 blended with diethyl maleate is greater than 99%, indicating in both cases these blends produced less soot than the JP-8.

Figure 3.1.2-3 compares averaged carbon signal obtained by desorbing soot samples collected from JP-8, JP-8+100, and JP-8 + 13.4% diethyl maleate experiments listed in Table 3.1.2-2. Unlike premixed experiments, soot collected from JP-8 experiments has elemental carbon (carbon desorbed after 300°C) as its dominant carbon fraction. This is perhaps due to the fact that reflected shock temperatures (T_5) in JP-8 experiments were at least 400 to 500°C higher than the premixed experiments. Figure 3.1.2-2 also shows that addition of diethyl maleate decreases the overall soot yield but increases the yield of carbon fraction that is desorbed between 50 to 150°C. Addition of +100 additive, on the other hand, did not change molecular weight distribution of JP-8 soot; it just caused a slight decrease in elemental carbon fraction.

Interpretation of Results

Both premixed and liquid injection experiments show that the addition of oxygenates can decrease the overall soot yields. In premixed experiments, addition of ethanol decreased the soot by approximately 20% and increased the mean ignition delay time from 1640 μs for ethylene experiments to 1747 μs for ethylene/ethanol experiments. The increase in ignition delay is because addition of low cetane number additive (ethanol - 10 CN) decreased the overall cetane number of the fuel mix. Soot suppression by ethanol is the result of increase in oxidation by an oxygenated radical such as hydroxyl and due to reduced hydrogen atom concentration. It is known that the concentration of the hydrogen atom is very important in soot formation since the hydrogen abstraction reactions reactivate and propagate the molecular growth process and the overshoot of hydrogen atoms beyond their equilibrium concentration accelerates the reactivation step [Frenklach 1987, Frenklach 1998, Frenklach 1990]. One of the ethanol dissociation

channels (rxn1) produces water, which can then react with hydrogen atom to form molecular hydrogen and hydroxyl radical (rxn 2). This results in net decrease in hydrogen radical concentration and increase in hydroxyl radical concentration. Both these actions lead to soot suppression.

$$C_2H_5OH \rightarrow C_2H_4 + H_2O \qquad \text{(rxn 1)} \qquad (1)$$

$$H_2O + H \rightarrow H_2 + OH \qquad \text{(rxn 2)} \qquad (2)$$

In liquid fuel experiments, the addition of +100 additive failed to cause any appreciable decrease in soot yields but did decrease mean ignition delay time from 1428 μs to 1400μs. This result is not consistent with the anecdotal evidence that addition of +100 additive can decrease soot yields. This inconsistency can perhaps be explained by the fact that observed decrease in soot in field studies has been attributed to the detergent properties of +100 additive. Since our injector was clean, that perhaps is the reason that addition of +100 additive caused no changes in soot yields in our experiments. Addition of diethyl maleate to JP-8, however, did decrease soot yield and increased mean ignition delay time from 1428 μs to1469 μs in our experiments. At present, the exact mechanism by which diethyl maleate suppresses soot formation is not known, but several plausible explanations do exist. Diethyl maleate contains four oxygen atoms, so the presence of diethyl maleate in JP-8 fuel drop results in lower local equivalence ratio. The addition of diethyl maleate also increases the oxidation radical pool as each diethyl maleate can dissociate to give two hydroxyl radicals and two carbonyl radicals. Another clue for diethyl maleate soot suppression can be obtained from Figure 3.1.2-2. Figure 3.1.2-2 shows that addition of diethyl maleate increases yield of lower molecular weight PAHs and decreases yield of elemental carbon. This means that addition of diethyl maleate inhibits the molecular growth process. One way diethyl maleate could inhibit molecular growth is by decreasing hydrogen radical concentration. Any of these three arguments could explain decrease in soot yields by addition of diethyl maleate, however, more experiments are needed to verify these and other plausible explanations.

Another observation based on both premixed and liquid fuel experiments is that the additive, which caused decrease in soot yields, also caused increase in ignition delay time. Are

these two related? Again, it is difficult to answer this question based on these limited sets of experiments.

Table 3.1.2-1. Experimental Conditions for Premixed Experiments.
5% fuel (v/v), 6.4% oxygen (v/v), and 88.6% argon; □ = 2.34.

Fuel Injected	P_1 (atm.)	T_1 (K)	V_s (m/s)	P_5 (atm)	T_5 (°C)
Ethylene	0.76	294.35	700	16.2	777
			707	16.6	793
			707	16.6	793
			705	16.54	790
Ethylene + Ethanol (5% O_2 m/m)	0.76	294.15	704	16.5	787
			703	16.4	785
			701	16.3	780
	0.76	294.55	704	16.5	788
			704	16.5	788

Table 3.1.2-2. Experimental Conditions for Liquid Fuel Experiments.
46.5 ml fuel, 4.6% oxygen and 95.4% argon.

Fuel Injected	P_1(atm)	T_1(K)	V_s(m/s)	P_5(atm)	T_5(°C)
JP-8	0.43	294.25	829	13.99	1300
			826	13.85	1290
			826	13.85	1290
			827	13.92	1295
	0.43	294.15	827	13.93	1295
			826	13.86	1290
			827	13.93	1295
			814	13.3	1249
JP-8 + 100	0.43	294.75	821	13.61	1275
			821	13.61	1275
			813	13.2	1245
			817	13.39	1259
	0.43	294.65	823	13.69	1280
			820	13.54	1269
			832	14.11	1311
			824	13.75	1285
JP-8 + 13.4 %Diethyl Maleate	0.43	294.35	811	13.16	1240
			811	13.16	1240
			804	12.84	1216
			817	13.42	1259
	0.43	294.55	826	13.83	1290
			815	13.34	1254
			808	13.01	1230
			813	13.22	1245
JP-8 + Saturated Diethyl Maleate	0.43	294.15	814	13.3	1249
			818	13.5	1264
			821	13.64	1274
			802	12.78	1211
	0.43	294.35	823	13.69	1279
			823	13.69	1279
			832	14.12	1310
			817	13.42	1259

Table 3.1.2-3. Summary of Soot Yields from Premixed Ethylene Experiments.

	Temperature, T_5, (°C)	Pressure, P_5, (atm)	Soot Yield (□g)
	777	16.2	75.8
	793	16.6	112
	793	16.6	107
	790	16.5	77.4
Sample Mean	788	16.5	93.1

Table 3.1.2-4. Summary of Soot Yields from Premixed Ethylene+Ethanol Experiments.

	Temperature, T_5, (°C)	Pressure, P_5, (atm)	Soot Yield (□g)
	787	16.5	73.8
	785	16.4	72.5
	780	16.3	78.3
Sample Mean	784	16.4	74.9

Table 3.1.2-5. Comparison of Mean Soot Yields from Liquid Fuel Experiments
Mean T_5 = 1272 °C , Mean P_5 = 13.5 atm.

Fuel	Soot Yield[1]	Confidence Level[2]
JP-8	2.65% (+/-0.22%)	n/a
JP-8+100	2.62% (+/-0.14%)	58%
JP-8 +13.4% Diethyl Maleate	2.17% (+/-0.20%)	99.57%
JP-8 Saturated w/ Diethyl Maleate	2.15% (+/-0.18%)	99.70%

[1]Values in parentheses are the 90% confidence intervals.
[2]Confidence level for the reject of the null hypothesis; the soot yield is the same as for JP-8 vs the yield is less.

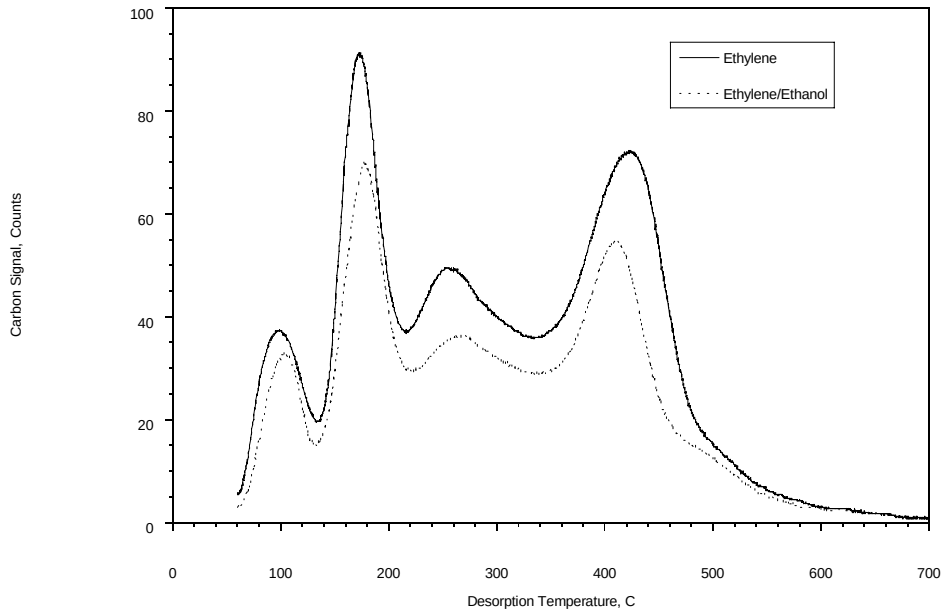

Figure 3.1.2-1. Averaged Carbon Signal Obtained by Desorbing Soot Samples Collected from Ethylene and Ethylene+Ethanol Experiments Listed in Table.

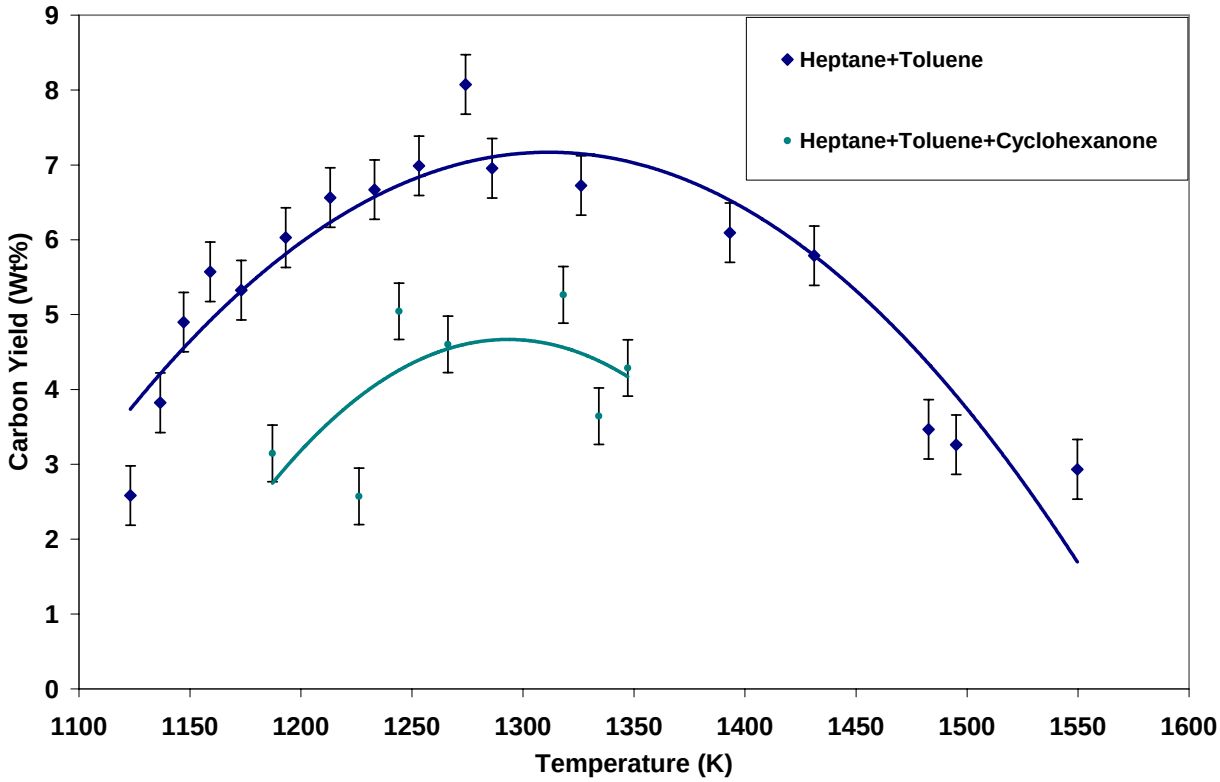

Figure 3.1.2-2. The Effect of Cyclohexanone on Soot Yield.

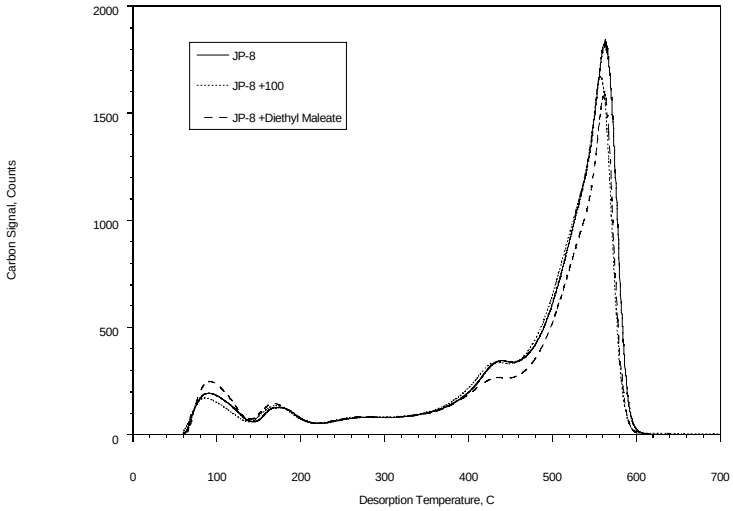

Figure 3.1.2-3. Averaged Carbon Signal Obtained by Desorbing Soot Samples Collected from JP-8 and Additized JP-8 Experiments Listed in Table 2.

3.1.3 WELL-STIRRED REACTOR

Experiments were conducted in the WSR to determine the effect of ethanol as an additive to reduce soot. Two groups of experiments were conducted: initial experiments using a reactor constructed from zirconia-oxide and ceramic fuel air jets, and experiments with an inconel jet ring injector and high thermal conductivity silicon carbide ceramic materials. It was found that the increased wall thermal conductivity for the silicon-carbide reactor led to lower combustion temperatures which, in turn, led to differences in the results between the two reactors constructions. In addition to these experiments, cyclohexanone, an oxygenated component in the commercial additive, was also investigated. Those results are presented after the discussion of the experimental and modeling results for ethanol.

Zirconia Oxide Reactor Results

Initial studies were conducted with ethylene fuel and prevaporized premixed ethanol additive in the WSR with zirconia oxide walls. The air was preheated and the ethylene and ethanol were added downstream of the air heater. The inlet air temperatures for the experiments ranged from 90 to 125°C. The air flow for the experiment was 240 g/min which corresponded to average residence times in the reactor of approximately 9.6 ms for the ethylene tests. Ethanol was added such that the mass fraction of oxygen in the fuel was 5.3 % or 10.5 %. It should be noted that the original targets were 5% and 10 % oxygen in the fuel. The reason for the difference between the target and actual values is that at the time the experiments were conducted, the reference temperature for the gaseous fuel flow and airflow measurements was thought to be lower than it was, resulting in mass measurements for the air and ethylene that were both 7% low, resulting in slightly higher equivalence ratios for the ethanol additive cases than had been intended. Further details of the experiment are presented in the references by Stouffer [2002] and Colket et al [2004].

Smoke number results for neat ethylene are compared to the results for tests using ethanol additives in Figure 3.1.3-1. The results show that there was a slight change increase in soot formation with the addition of ethanol as an additive. Note that there was also large scatter in the data. It is thought that part of the scatter is due to temperature differences between samples with similar reactants, equivalence ratios and inlet conditions. Smoke number at the exit of the stirred

reactor was plotted versus the recorded temperature in Colket et al [2004]. The data (both ethanol-free and with ethanol) is shown in shown in Figure 3.1.3-2. The trends are similar, for any given mixture with or without additive. (Some of the data sets have been averaged for purposes of clarity.) Recall that for these early experiments, the walls of the reactor were constructed out of zirconia. Zirconia has a low thermal conductivity and hence it took a long time for the reactor to stabilize. Data was collected during this period and for a given equivalence ratio, several data points were collected, but at varying temperatures. Whether the data from a fixed equivalence ratio or data for a range of equivalence ratios are considered, the data clearly show smoke/soot decreases with increasing temperature and, hence, the experiments were performed on the high temperature side of the soot bell.

Silicon Carbide Reactor Results

Shortly after completing the experiments with the zirconia-oxide reactor, the materials for the reactor were changed in an effort to minimize cracking of the ceramic pieces. The results for the experiments are discussed below. Further details are presented in Stouffer [2002] and Reich [2003]. After constructing the new reactor, experiments were conducted for the smoke number versus ϕ at a fixed airflow rate (330 g/min) over the large range of equivalence ratios. Figure 3.1.3-3 shows two sets of data corresponding to two different ring cooling nitrogen flow rates. Recall that the ring cooling was necessary in the new design to reduce the temperature of the gas in the ring to a level low enough to avoid autoignition in the jet ring and the subsequent destruction of the ring. The cooling of the ring has the secondary effect that the outside of the reactor is also cooled, further lowering the temperature in the WSR. Rather than continuously increasing as ϕ increased, the smoke number initially increases between ϕ = 1.9 and 2.3 and starts to decrease as ϕ is increased further showing both the high and low temperature sides of the soot bell. Note that the soot produced is higher for the case that has the lowest cooling of the injector ring. This is consistent with the result that the soot level is highest for the cases with the least cooling for equivalence ratios above 2.3.

The same smoke number data from Figure 3.1.3-3 was replotted versus the reactor temperature and is plotted in Figure 3.1.3-4. The peak sooting was observed to occur between 1560 K and 1620 K for both cooling levels. The results show that on the high temperature side

of the soot bell, decreases in the reactor temperature (caused by lower inlet temperatures or lower energy additives) tend to increase the soot levels, while the opposite is true on the lower temperature side of the soot bell.

The effect of ethanol as an additive in the same silicon carbide reactor was considered by Reich et al [2003]. The air flow for the experiments was set at a constant 240 g/min with an inlet temperature set at 392 +/- 5K. The fuel/air equivalence ratio, ϕ, ranged from 1.9 to 2.6 for both neat and ethanol added to raise the oxygen mass fraction of the fuel to 5%. Soot samples for mass measurements were made in the plug flow region, downstream of the reactor and within the toroidal WSR.

Figure 3.1.3-5 shows the smoke number measured from filter samples extracted from both the reactor and the plug flow section. The addition of ethanol results in a reduced smoke number for all ϕ measured, with the greatest reduction shown at $\phi = 2.2$ and 2.3. This trend is different from the one observed with the reactor with zirconia walls where the addition of ethanol was seen to slightly increase the soot production. However, it should be noted that the temperature inside the reactor in the previous study was higher (by approximately 110°C) than the reactor temperature in the current study because lower thermal conductivity ceramics were used for the wall materials in the previous study. It is thought that the combustion temperatures significantly affect the soot production mechanism. Note that the smoke number measured in both the reactor section and the plug flow regions are approximately equal for the same fuel at the same reactor conditions for $\phi < 2.4$. As the fuel flow is further increased, the smoke number is seen to be lower in the reactor section than it is in the PFR implying that the additional time in the PFR allows further reaction toward formation of soot.

Figure 3.1.3-6 shows total carbon analysis of the quartz filter samples extracted from both the reactor section and the plug flow sections of the WSR. The results show that the addition of ethanol decreases the carbon mass for all of the cases. The overall shape of the integrated carbon mass plot shown in Figure 3.1.3-6 shows trends similar to those shown for the smoke number plots in Figure 3.1.3-5. A significant difference is that an increase was shown in the total carbon mass between the reactor and the plug flow section.

The relative carbon count plotted with increasing temperature for three equivalence ratios ($\phi = 2.1$, $\phi = 2.3$, and $\phi = 2.6$) are shown in Figures 3.1.3-7A, 3.1.3-7B, and 3.1.3-7C,

respectively, along with corresponding photographs of the filters before the carbon analysis was conducted. These figures show two distinct peaks, a low temperature peak located between 120 and 160°C, and a high temperature peak located between 450 and 560°C. The sample for the highest equivalence ratio (ϕ = 2.6 in Figure 3.3-7C) has the highest carbon content in the low temperature region and the filter stain is beige-colored, while the high temperature carbon peak is highest for the ϕ = 2.3 case, shown in Figure 3.1.3-7B, which shows a much darker filter stain. It is thought that the low temperature peak is due to the presence of PAHs while the high temperature peak is due to the presence of carbonaceous soot.

Particle size distributions and particle number densities were all measured with the PMCMS system and the results reported in Reich et al [2003] are summarized below. It is now recognized that because of the long sample residence time used in the system that the apparent particle size distributions are shifted to large diameters and the particle number densities were decreased because of coagulation in the sample lines. While the results presented below will be quantitatively in error, they still represent a valid comparison because the sample train and sampling conditions were the same between the neat and additive cases.

The particle size distributions sampled from the plug flow region of the reactor are shown in Figure 3.1.3-8 for both the neat ethylene and the ethylene-ethanol mixtures over a range of ϕ from 2.0 to 2.6. The ethylene-ethanol mixture was shown to reduce particle concentration at all ϕ compared to the neat ethylene fuel. The highest particle concentrations for ethylene and the ethylene-ethanol were measured at ϕ = 2.4 and ϕ = 2.3, respectively. The peak particle size increases as ϕ is increased from 1.9 to 2.3 for both fuels. As ϕ is further increased, the peak particle size decreases. The ethylene-ethanol fuel resulted in smaller peak particle sizes compared to the ethylene fuel over the entire range of test conditions. The total particle number densities obtained by integrating the areas under the curves also showed a reduction for the ethanol additive cases as compared to the neat ethylene case.

Summary

Two sets of experiments were performed with the ethanol as an additive to ethylene in the WSR. The first experiment conducted at high temperatures on the high temperature side of the soot bell showed that the soot mass was slightly increased by ethanol additive at

concentrations such that the oxygen content of the fuel was 5% by mass. A second set of experiments conducted at lower temperatures, because of increased heat transfer from the walls, showed that the use of ethanol as an additive at the same levels caused a pronounced decrease in soot mass, number density and diameter at maximum concentration. Further explanation for the differences between the high and low temperature cases will be discussed in the modeling section, which points to the important role of the effect of temperature on soot formation for these experiments. As a result of this finding, experiments with other additives were run in such a way as to keep the reactor temperature as constant as possible between tests, without and with the additive.

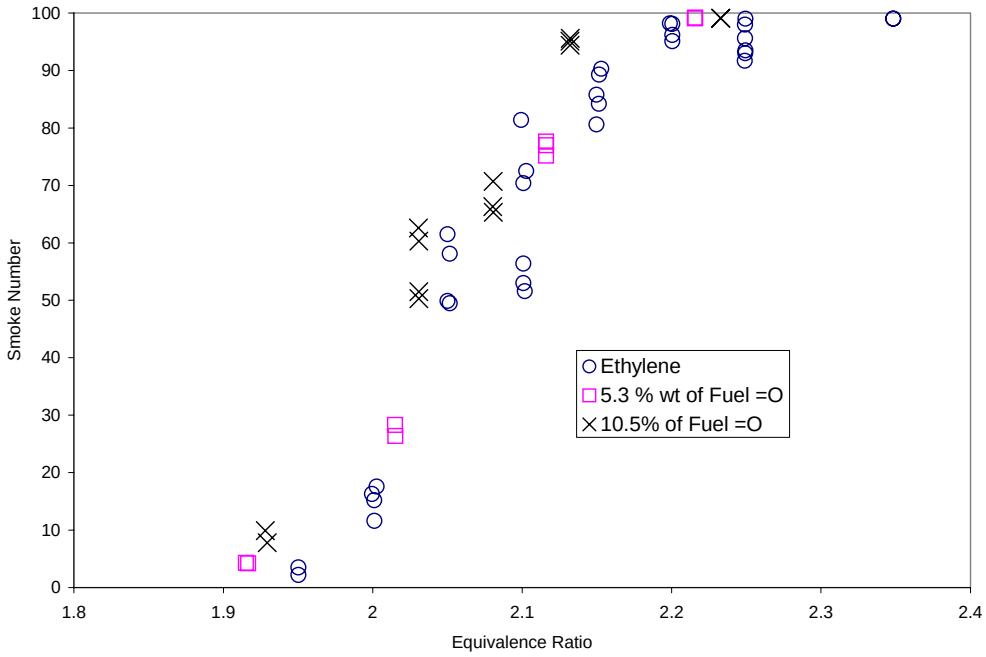

Figure 3.1.3-1. Smoke Number vs Equivalence Ratio for Ethanol Additive Experiments.

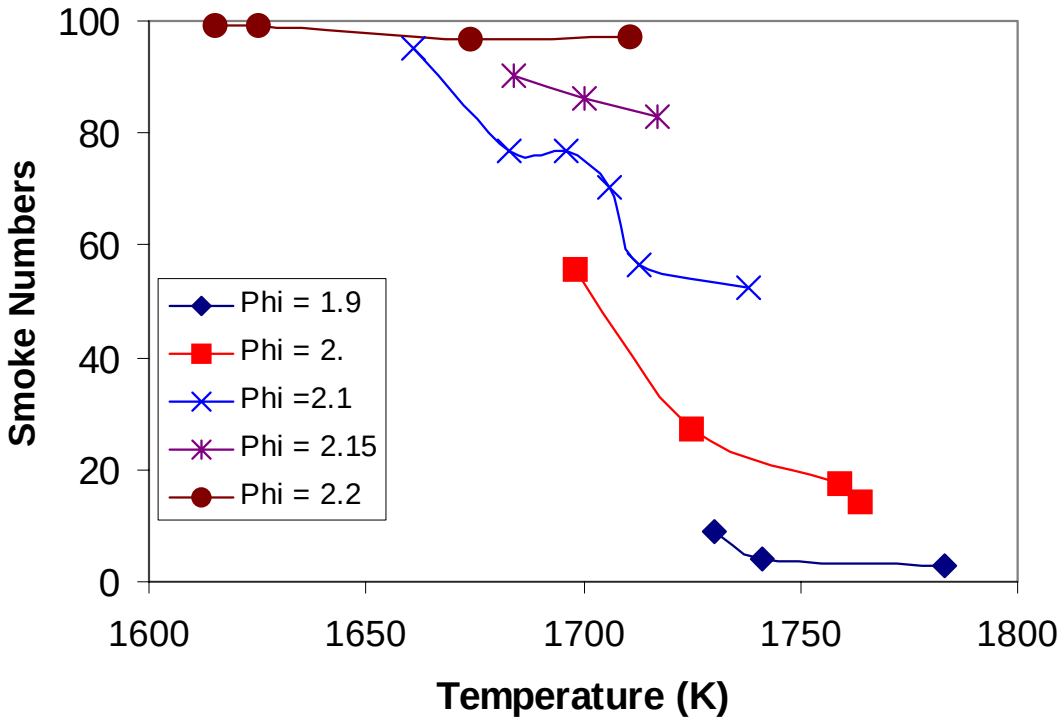

Figure 3.1.3-2. Smoke Number vs Temperature for Neat and Additive Cases.

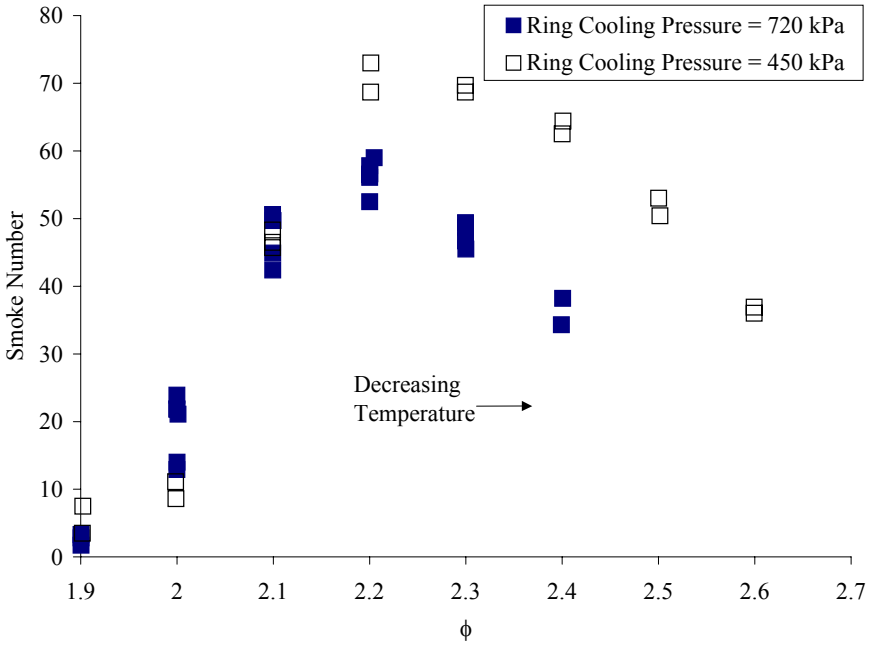

Figure 3.1.3-3. Smoke Number vs Equivalence Ratio for Ethylene-Air Mixtures Effect of Cooling.

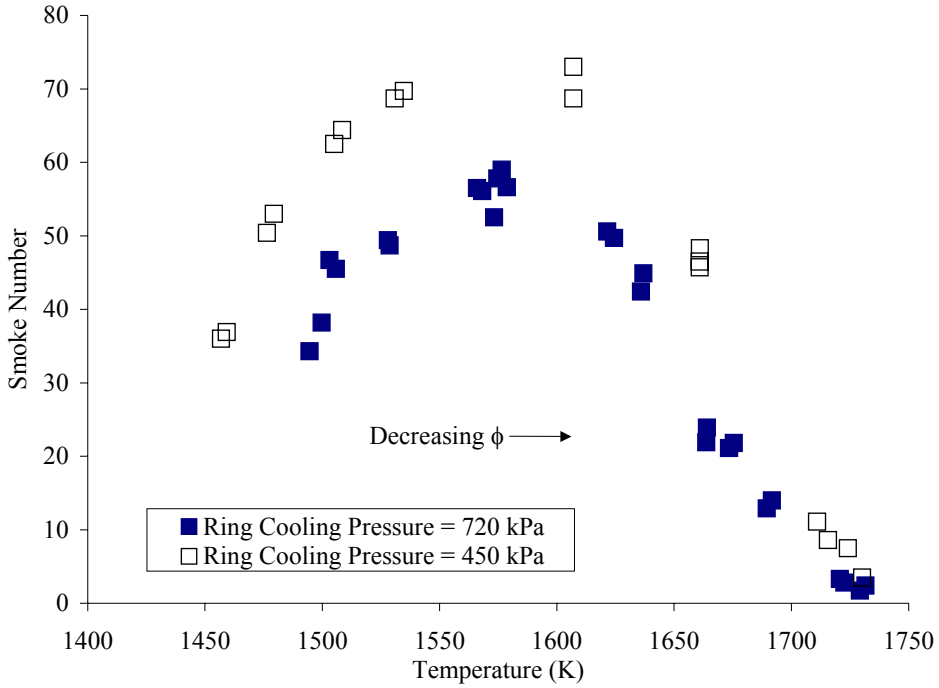

Figure 3.1.3-4. Smoke Number vs Temperature for Ethylene Air Cases Effect of Ring Cooling.

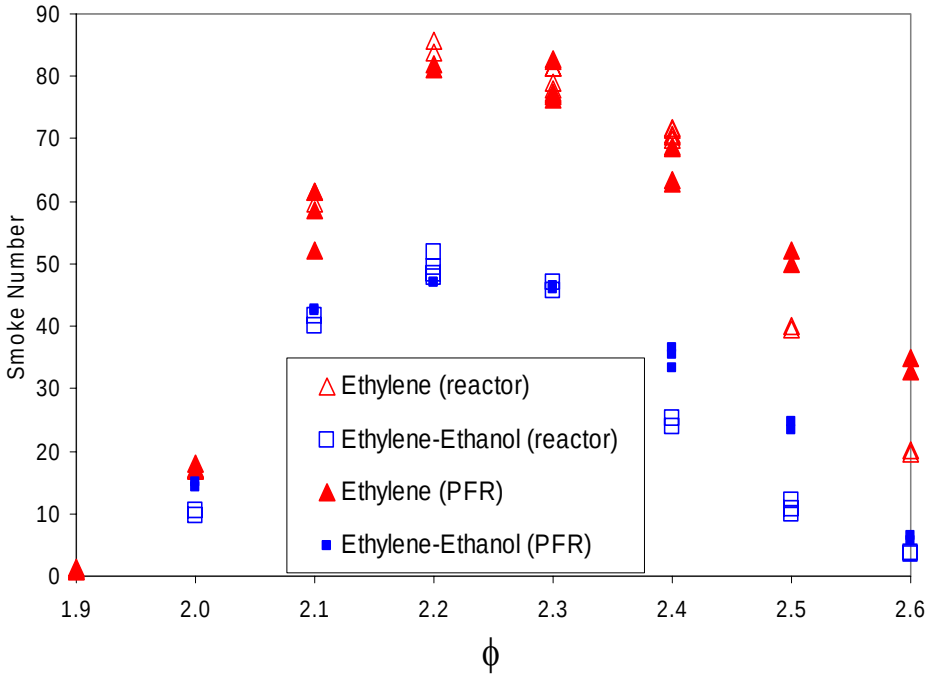

Figure 3.1.3-5. Smoke Number Results for Neat Ethylene and Ethanol Additive.

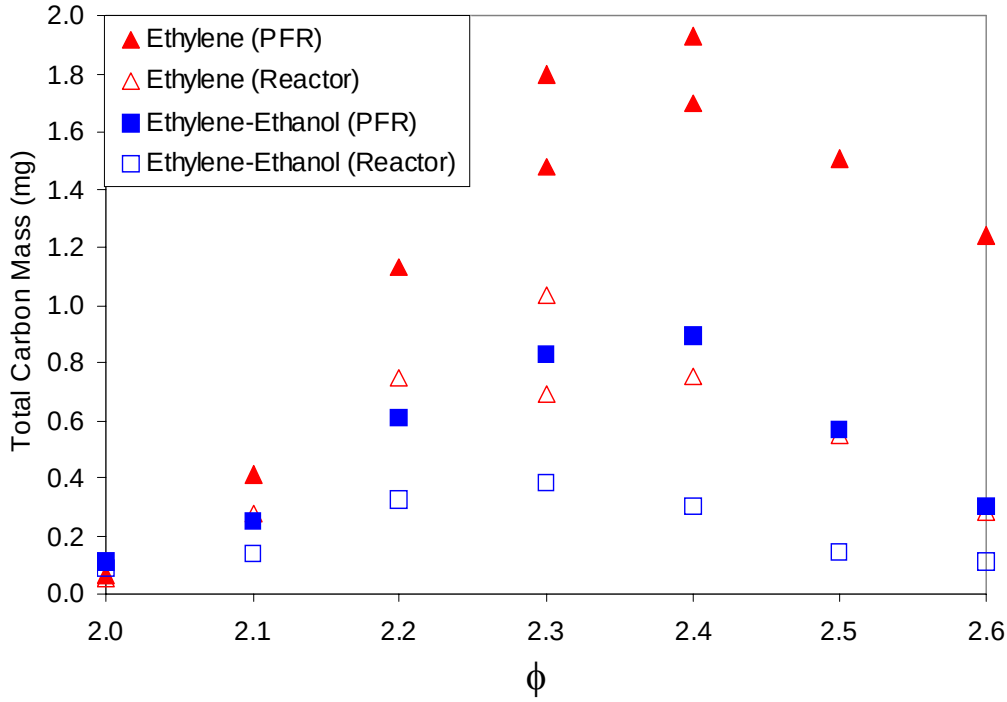

Figure 3.1.3-6. Total Carbon Measurements Results for Neat Ethylene and Ethanol Additives (Silicon Carbide Reactor).

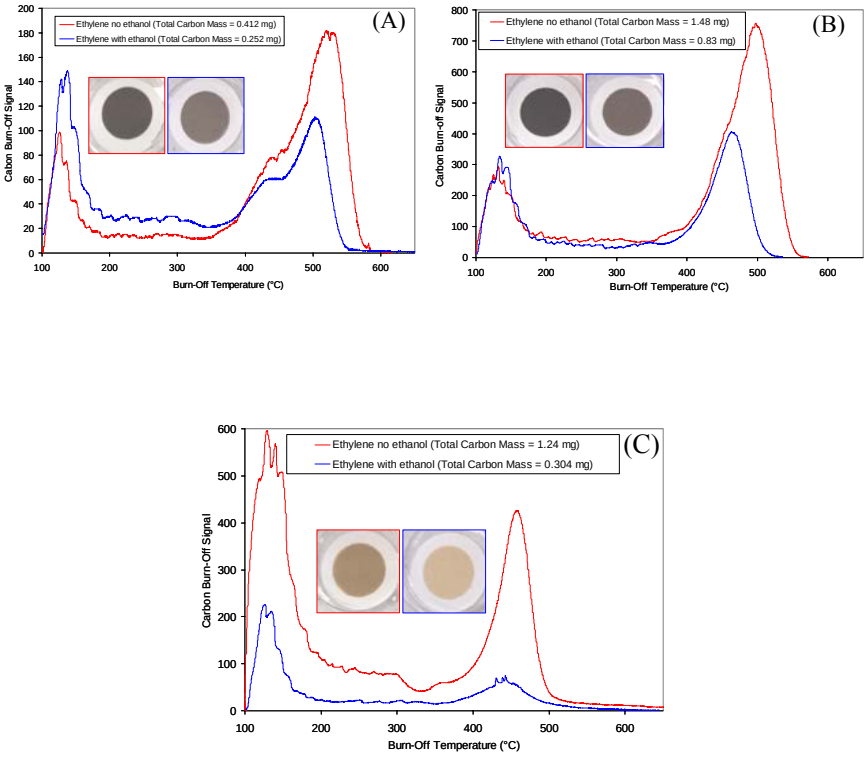

Figure 3.1.3-7. Carbon Mass Measurement vs Filter Temperature During Carbon Oxidation, A (ϕ = 2.1), B (ϕ = 2.3), and C (ϕ = 2.6).

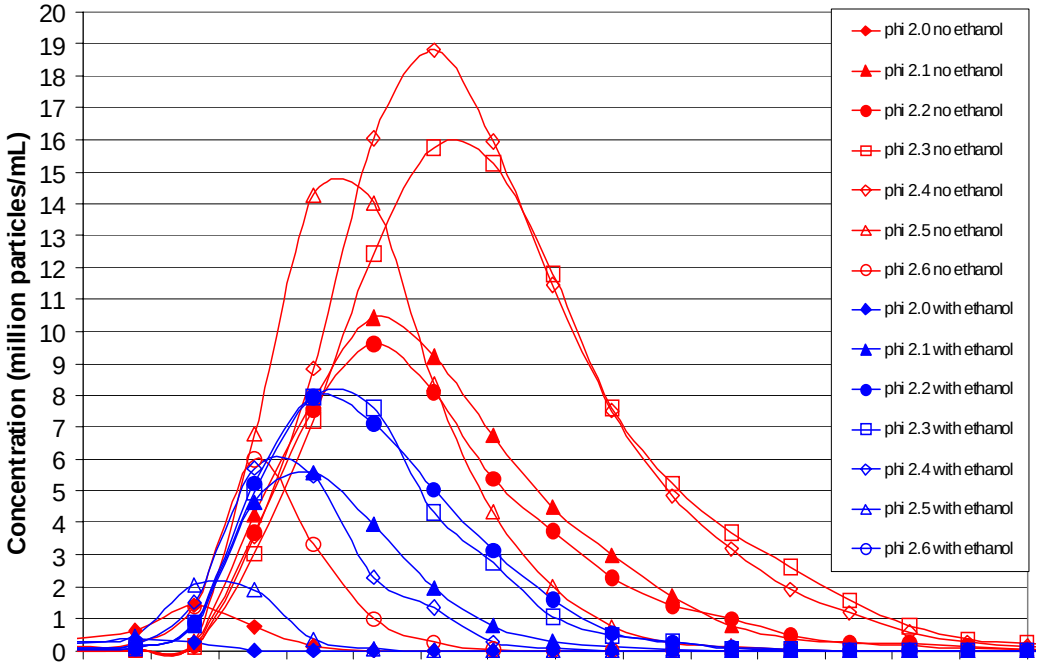

Figure 3.1.3-8. Particle Size Distributions for Ethylene and Ethanol Additive Cases.

Modeling of Ethylene-Ethanol Results

Simulations of the toroidal WSR experiments at WPAFB [Stouffer et al 2002] have been performed using a modified version of the Perfectly Stirred Reactor (PSR) code [Glarborg et al 1986]. The modified code has the soot equations fully coupled into the solution algorithms. In addition, a version of this "sooting" PSR code is available that also can be run with an arbitrary network of individual PSRs. Both the PSR and network PSR code have the soot sectional equations [Hall et al 1997] fully imbedded, treating inception, growth, particle dynamics, and oxidation. Scrubbing of the gas phase species due to their conversion to soot particles and gaseous species formed or altered during soot oxidation is included in this model. The reactors can be assembled for a streamline analysis or can be used in a network with any arbitrary sequence of reactors in series or parallel.

Normally, only exit gas-phase species concentrations and temperatures are determined by the PSR code. The modified code also computes the particle size distribution, from which total particle mass and number densities can be calculated. Details are provided in Colket et al [2004]. In addition, a correlation for the relationship between smoke number and total particle mass (mg/m^3) was used where the volume is based upon conversion of the flame gases to atmospheric pressure and at 289 K. Ambient conditions are utilized for the reactor studies as they are close to characteristic conditions for the smoke number measurement device.

Simulations of the jet-stirred reactor studies were performed with this "sooting" PSR code. Reactor volume and mass flow rates were matched to the experimental conditions for cases with pure ethylene as the fuel as well as for the ethylene/ethanol blend. Adiabatic conditions were assumed. For the UTRC reaction set, predicted smoke numbers are shown in Figure 3.1.3-9. Comparisons to experimental data sets indicate that the UTRC model underpredicts slightly the level of smoke produced in the experiment, although the trend is well matched [Colket et al 2004]. The UTRC model predicts a slight increase in smoke number when ethanol is added, consistent with a slight increase in soot mass. The experimental results exhibit a similar trend for the two fuels. The Frenklach model indicated soot reduces with added ethanol.

As shown in Figure 3.1.3-10, the computed temperatures are about 40 K lower for the cases with the additized fuel. Soot formation is known to be a strong function of temperature [Glassman 1989]; the difference in temperature likely contributes to the different soot levels. The dependence of soot formation on temperature depends on which side of the bell-shaped curve the

experiments have been performed. The negative trend (decreasing soot with increasing temperature) suggested the tests have been performed on the high temperature side of the soot bell.

A detailed analysis of the experiment indicates that this prediction was correct. A plot of the measured soot levels as a function of the reaction temperature is shown in Figure 3.1.3-11, where the data was obtained from S. Stouffer. The data clearly show how the temperature and soot are inversely related (either for different equivalence ratios, or for constant equivalence ratios); hence, the data were indeed obtained on the high temperature side of the bell curve and the results in Figure 3.1.3-11 are therefore explained. (The data for constant equivalence ratio and different temperatures were obtained during very slow transients after the reactor flows were readjusted to a new set of conditions, and before the reactor temperature had stabilized.)

Additional information on the computed solutions is provided in Figure 3.1.3-12 in which the size distribution of soot particles is provided for a range of equivalence ratios with and without the presence of the ethanol additive. The number densities keep increasing with decreasing particle size. These results are unusual with respect to typical profiles for combustors in which a clear maximum in the particle size distribution usually occurs [Liscinsky et al 2001]. The predicted results for this stirred reactor study need experimental confirmation.

Simulations were also performed using the Frenklach mechanism. Use of this detailed reaction set resulted in larger predictions of aromatics (typically more than a factor of 10) than those levels predicted from the UTRC mechanism and, hence, heavier soot loadings are also predicted. Trends with the Frenklach mechanism are similar to those described for the UTRC mechanism.

An issue of concern has been the understanding of the apparent increase in the soot production with the fuel-additive ethanol. Ethanol when added to ethylene fuel in the WSR experiments had the opposite effect on smoke number as did the premixed flame experiments. The stirred reactor environment is noticeably different from the premixed flame as the products are intermixed with the unburned reactants. Using correlations of smoke number, increases in particulate mass emissions with added ethanol were on the order of 20-40% for a given equivalence ratio. This contrasting effect has been traced principally to a temperature effect. In the case of the premixed flames, the computed flame temperatures increased by only about 5 K and the experimental temperatures increased by about 15 K, differences that are less than the

uncertainty of the measurement. In contrast, for the WSR and for constant equivalence ratio conditions, temperatures decreased by about 40-50 K for both the experiments and for the modeling results. Temperature is well known to be a key parameter in the formation of soot. Both experiments and modeling of soot formation in the WSR at a constant equivalence ratio (ethylene only) demonstrated that the conditions in the WSR are on the high temperature side of the bell. (The existence of a soot bell in which soot formation rates first increase with increasing temperature, but then decrease with further increases in temperature is well established.) Hence, decreases in temperature increase soot production. These effects are explained further in the following paragraphs.

At low temperatures when temperature and soot production follow parallel trends, the soot production is kinetically limited. But on the high temperature side of the soot bell, characteristic of our WSR, the thermal stability of aromatic species falls off with increasing temperature. Benzene and other aromatics are recognized to provide the foundation for soot formation (inception) and growth. Loss of these species directly inhibits the production of soot. Specifically, the thermal decomposition of a key intermediate species (e.g., phenyl radical or

$$C_6H_5) \text{ through } C_6H_5 \Rightarrow \text{l-}C_6H_5 \Rightarrow C_4H_3 + C_2H_2 \qquad \text{(R1)}$$

increases rapidly with increasing temperature and becomes first competitive with and then dominates over growth reactions (e.g., as initiated by $C_6H_5 + C_2H_2 \Rightarrow C_8H_7$).

This effort has demonstrated that in the case of the WSR, in which the reactants (e.g., molecular oxygen) are also present in the soot formation zone, low activation energy oxidation step(s), such as

$$C_6H_5 + O_2 = C_6H_5O + O \Rightarrow \text{oxidation products} \qquad \text{(R2)}$$

shift the soot bell to much lower temperatures than are normally observed in flames. Stirred reactors are often utilized to simulate combustor environments, and the (changing) shape of the soot bell may be an important concern as we apply our work to gas turbine engines.

Contrasting experimental trends observed in the well-stirred reactor experiments at WPAFB [Stouffer et al 2002, Reich et al 2003] have been examined and explained by utilizing a

modified version of the CHEMKIN II-based code for stirred reactors [Kee et al 1991, Glarborg et al 1986]. The code has been modified to include conservation equations for soot aerosols with treatment of particle inception, particle growth, aerosol dynamics, and particle oxidation. These equations are fully coupled to the gas-phase species by including terms to account for scrubbing of the species and by modifying the energy equation. Details of this work are documented by Colket et al [2004] and demonstrate the importance of temperature and its control to experimental programs on soot.

The model has been used also to predict particle size distributions produced by the reactor and these predictions have been compared to experimental data obtained this year. Comparisons are shown in Figures 3.1.3-12 and 3.1.3-13. There is a dramatic contrast between the model and the experiment, with the model predicting much greater fractions of small diameter particles. A preliminary analysis of both the experiment and the model has been performed to understand the differences. It was concluded that both the model and the experiment contributed to the differences shown in Figures 3.1.3-12 and 3.1.3-13.

The model predictions of particles with sizes less than 10 nanometers were shown to be sensitive strongly to the assumed inception species. The model in Yook and Pui [2005] assumed that naphthalene was the inception species. Preliminary calculations showed that the average particle size shifted to larger values as the inception model was changed to pyrene and then to coronene. Model revisions are underway to fully incorporate these effects. In addition, the model indicated that particle size distributions as well as soot mass were found to change as the exhaust flowed up the chimney towards the sampling probe. These effects need to be quantified in future modeling efforts.

Modeling Soot Dynamics and Sampling of Particles

The sampling process was also found to impact the experimental results. Computations using the TSI aerosol tool showed that line loss of the small particles (< 10 nm) can be very significant. Table 3.1.3-1 shows results of calculations for a sample stream at nearly ambient conditions. These results are independent of number density, so dilution (which is important to minimize perturbations to particle-particle collisions) will have no effect, except to reduce the transit time to the instrumentation. The results presented in Table 3.1.3-1 are indicative of the significant challenges when sampling particles with small size.

The stirred reactor code [Colket et al 2004] as modified to treat oxidation rates properly (rather than empirically) and to consider nonadiabacity has been used to predict particle size distributions and number densities from the WSR experiments. The revised analysis includes treatment of continued particle dynamics in the exhaust stream just down stream of the stirred reactor. Predicted particle sizes still were significantly smaller than that measured and reported in Reich et al [2003]. Preliminary analysis of sample line effects were found to be significant, particularly the rapid loss to walls for particles less than 10 nm in diameter, and agglomeration effects for sample streams with number densities higher than 10^8 #/cc. Very recent measurements by NIST [Manzello et al 2006] using a highly diluting sampling probe (~1000:1) for comparable conditions confirm the existence of small primary particles in the exhaust stream and the sample line effects as inferred from our modeling results.

To enable better quantification of particle losses in sampling lines, we have reproduced an analysis developed by Yook and Pui [2005] and computed the size-dependent loss of particles due to diffusional, inertial, electrostatic, and thermophoretic effects. Our procedure utilizes an Excel-based tool that can readily be converted to examine the performance of (i.e., losses in) a sample line. It does not account for particle coagulation, but rather is assumed that the system is diluted sufficiently to minimize such effects. Otherwise, coagulation must be treated separately. An example for sampling line conditions of 400 K (gas and wall temperature), one atmosphere, 20 slpm flow, 0.533 cm tube inner diamter, and 5 meters of sample line length is given in Figure 3.1.3-14.

For the flow parameters selected for this analysis, the electrostatic and thermophoretic penetration efficiencies are essentially unity, over most sizes of interest. The same is true for inertial losses, at least for the sizes < 100 nm, but above particle sizes of several hundred nanometers, the inertial losses become very significant and dominating, with penetration efficiencies approaching zero for particles above one micron in diameter (1000 nm). Hence, diffusional effects dominate, as shown in Figure 3.1.3-14.

Note that since these particle loss mechanisms are all first order in particle size, the computations are all independent of the particle number density. By far the dominant loss term is diffusional. Inertial effects become dominant at much larger diameters (100s of nm). These curves confirm the importance of wall losses and the likelihood that experimental particle size

distributions can well be skewed, especially for particles less than 20 nm. Careful attention to sample line design and its use must be considered paramount.

Another effect examined in this study and found to be important in simulations of particle size distributions and total particulate mass was the treatment of the plug flow reactor, downstream of the exit of the WSR. To demonstrate the importance of this exhaust stream effects, we utilized the network reactor version of the sooting PSR code. Reactors were assembled in a sequential manner to simulate processes occurring downstream of the reactor, as shown in Figure 3.1.3-15.

Several configurations were examined to assess appropriate treatment to ensure a solution that was independent of the network configuration. A plot of solutions of the empirical smoke number based upon using just one exhaust reactor or three, six and ten are shown in Figure 3.1.3-16, where the approximate residence times of the individual reactors are shown. Total exhaust residence time for these simulations was about 11 milliseconds.

Based on these results, a selection of about 10 reactors to simulate the downstream exhaust tube is recommended. A comparison of the (predicted) particle size distribution at the exit of the reactor and at the sampling point, 11 milliseconds downstream from the reactor exit, is shown in Figure 3.1.3-17. These simulations were performed with 10 reactors used to describe the exhaust conditions.

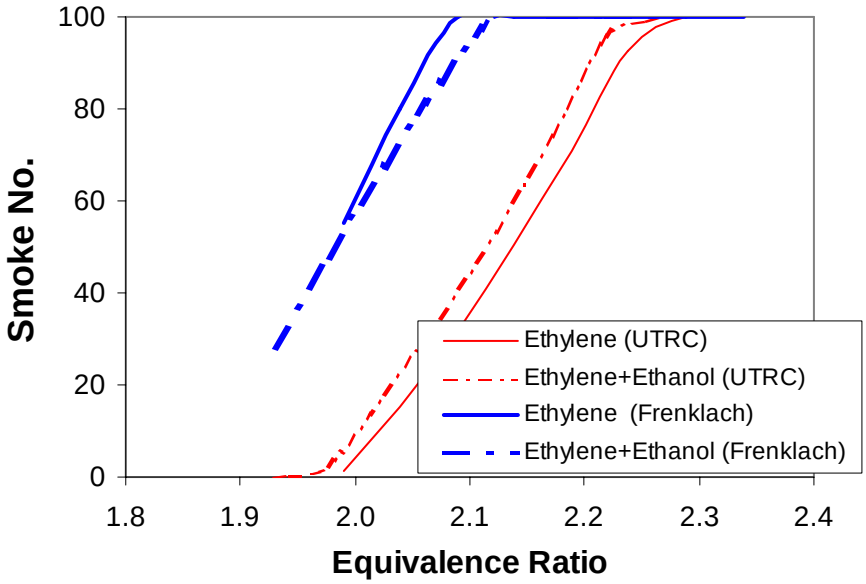

Figure 3.1.3-9. Predicted Smoke Numbers in PSR Using Two Kinetic Mechanisms for Ethylene and Ethylene with Ethanol Additive.

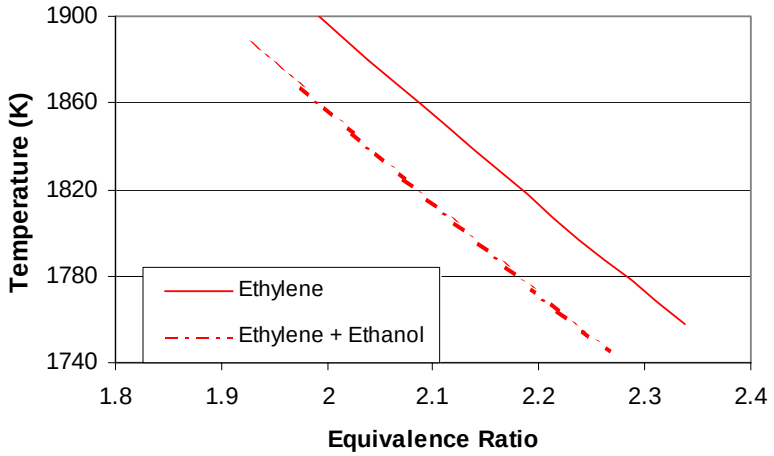

Figure 3.1.3-10. Predicted Temperatures in PSR for Ethylene and Ethylene with Ethanol Additive Using the UTRC Kinetic Mechanism.

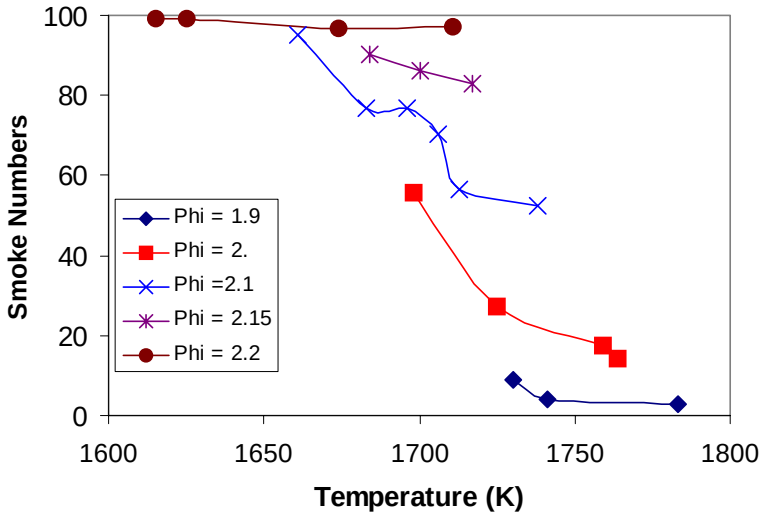

Figure 3.1.3-11. Measured Smoke Number as a Function of the Experimental Temperature.

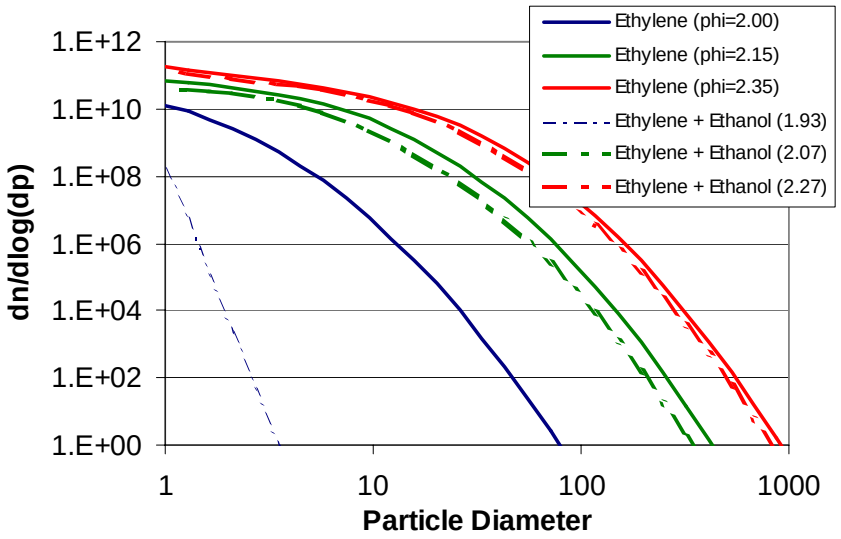

Figure 3.1.3-12. Predicted Particle Size Distributions for PSR Using UTRC Mechanism.

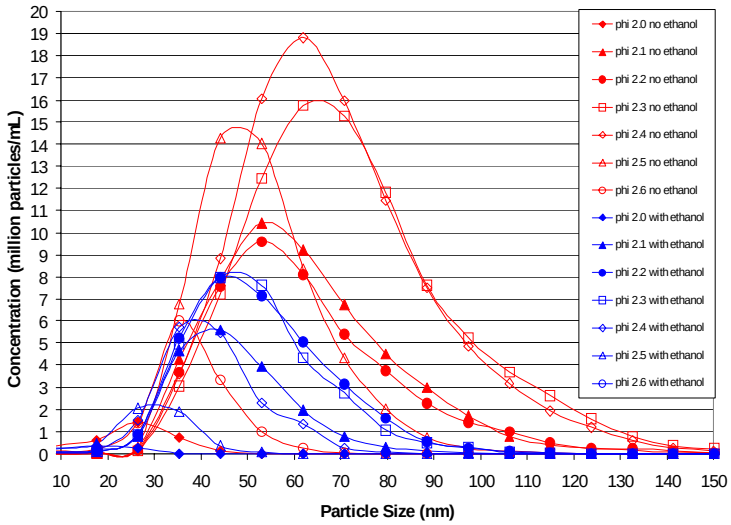

Figure 3.1.3-13. Experimental Particle Size Distribution for Stirred Reactor.

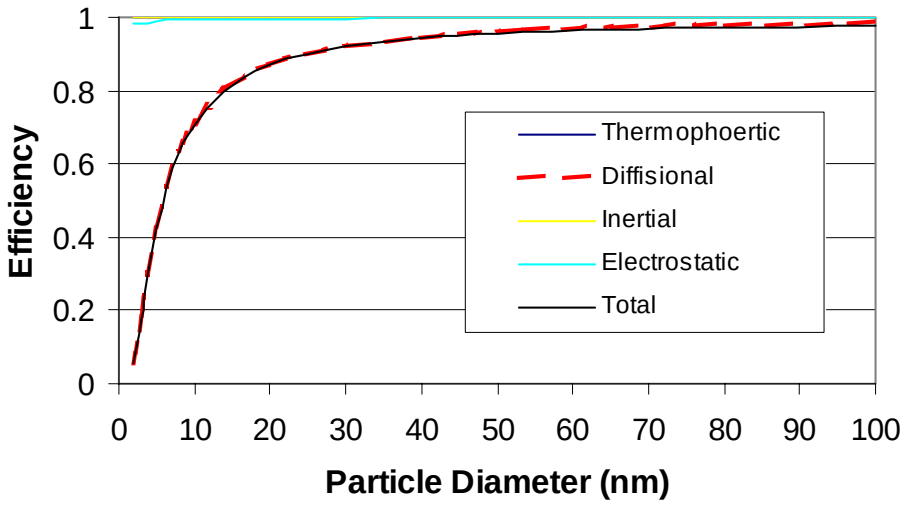

Figure 3.1.3-14. Computed Penetration Efficiencies of Particles through Sampling Lines.

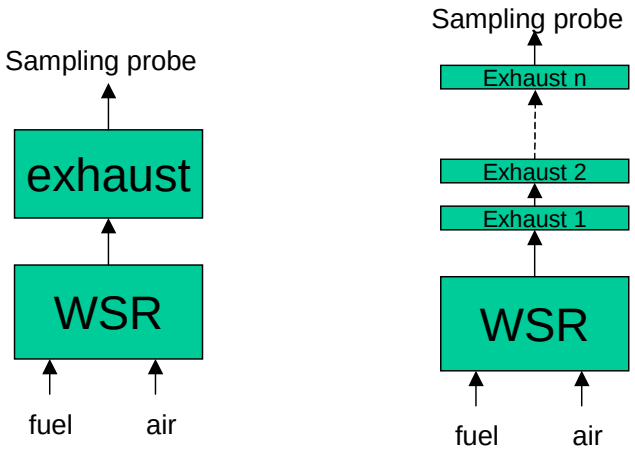

Figure 3.1.3-15. Construction of Reactors to Simulate the Coupled Stirred Reactor and Exhaust.

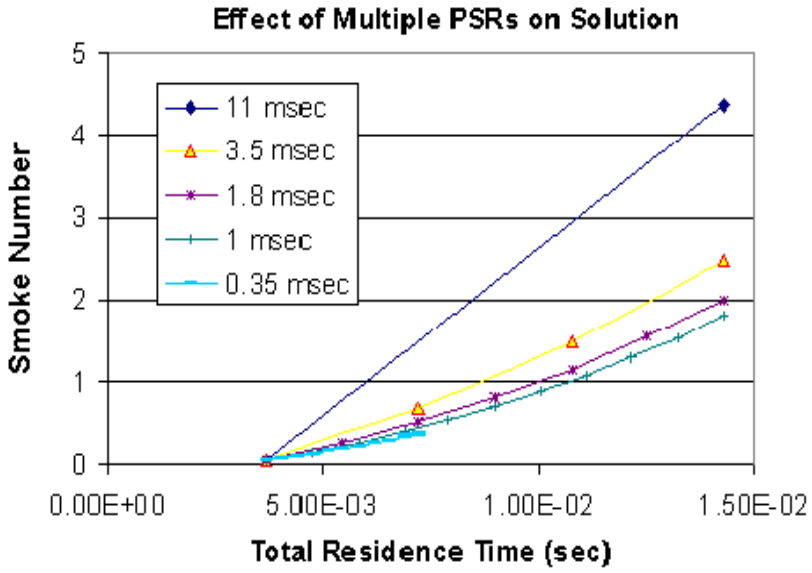

Figure 3.1.3-16. Effect of Multiple Reactors in Simulating the Exhaust from the Stirred Reactor.

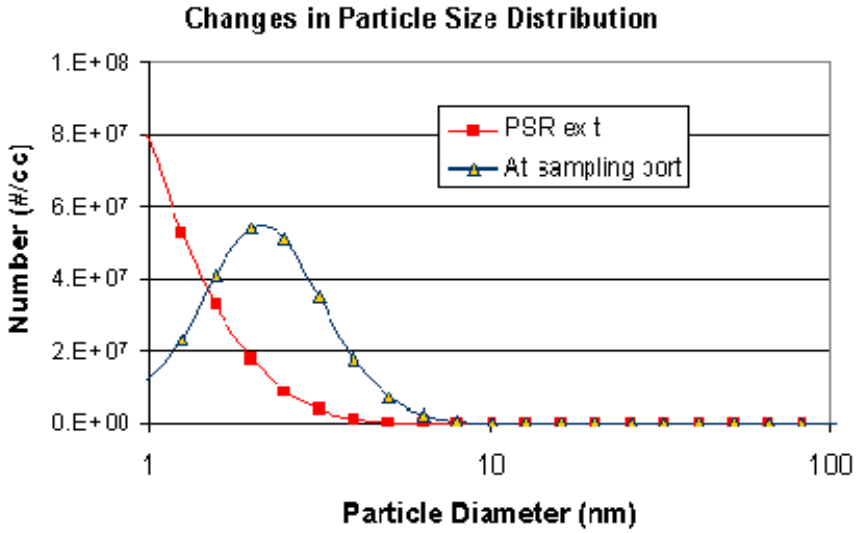

Figure 3.1.3-17. Comparison of Predicted Particle Size Distribution at Reactor Exit with that at the Sampling Port.

Table 3.1.3-1. Efficiency for Transport of Particles through Sample Line without Diffusional Loss to Walls (5 lpm, 0.18" ID Tube, 293K, 1 atm).

Transport				
Length	Time	Particulate Diameter		
m	sec	25 nm	10nm	5nm
1	0.2	0.98	0.94	0.86
5	1	0.93	0.8	0.6
10	2	0.75	0.68	0.45

Cyclohexanone Studies

The effectiveness of cyclohexanone was studied in the WSR with a neat fuel of 80% heptane/20% toluene by volume. The results are summarized below and presented in more detail in Stouffer [2005]. The reactor material for the experiments was amorphous fused silica which minimized both cracking and heat loss and could be used because the temperature in the reactor was less than the 1500°C melting point of the silica.

Equivalence ratios between 1.90 and 2.10 were studied. The WSR was limited to this equivalence ratio range on the low side by the melting point of the fused silica and on the high

side by the rich blowout limit. However, as will be shown later for the neat fuel under the conditions, this range of equivalence ratios captures the peak along with the low temperature and high temperature sides of the so-called "soot bell". The airflow was held at a constant 240 g/s and the average residence time in the reactor was 10 +/- 0.4 ms. The reactor pressure was slightly (0.6-1.4 kPa) over the ambient atmospheric pressure for all of the tests.

The cyclohexanone was added to the fuel at levels of such that either 2% or 4% of the fuel weight was from oxygen in the cyclohexanone. This corresponds to 96,140 ppm cyclohexanone for the 2% O level and 198,280 ppm for the 4% O level. The experimental results shown will be predominantly from the carbon mass determined from carbon burnoff from quartz filters. Particulate mass samples were drawn through an oil cooled probe at a location 16 cm downstream of the WSR in the plug flow reactor region. Due to instrument availability, particulate number densities and particle size distributions were not determined.

Figure 3.1.3-18 shows the total particulate carbon mass data for experiments with the cyclohexanone additive plotted versus temperature measured in the WSR. The curve shows a peak at ϕ= 2 and a familiar soot bell shape. Above this equivalence ratio the carbon mass increased as the temperature increased (as phi was lowered or inlet temperature was increased) and is commonly referred to as the low temperature side of the soot bell. On the opposite (high temperature) side of the soot bell, the carbon mass production decreases as the temperature increases. The presence of cyclohexanone was shown to reduce soot at all equivalence ratios. At ϕ = 1.95, the 4 % O additive case produced 36% less carbon mass than the neat case. The effect of cyclohexanone on the temperature changed depending on the equivalence ratio. For the high temperature side of the soot bell, the combustion temperature for the neat and the additive cases were nearly the same, implying that the effect of the additive in this region is chemical rather than thermal. On the low temperature side of the soot bell, the combustor temperature decreased for the additive case relative to the neat case as the equivalence ratio was further increased. For the highest equivalence ratio case studied (Φ=2.1), the combustion temperature using the 4% O additive was increased for one data point by increasing the inlet conditions, and the soot mass increased to match that for the neat case, implying that for the low temperature side of the soot bell the effect of the additive is mainly due to a decrease in the combustor temperature. The carbonaceous portion of the total carbon mass, determined by the carbon

burned off at temperatures above 325°C, is shown in Figure 3.1.3-19 and the results for the total carbon closely parallel the total carbon.

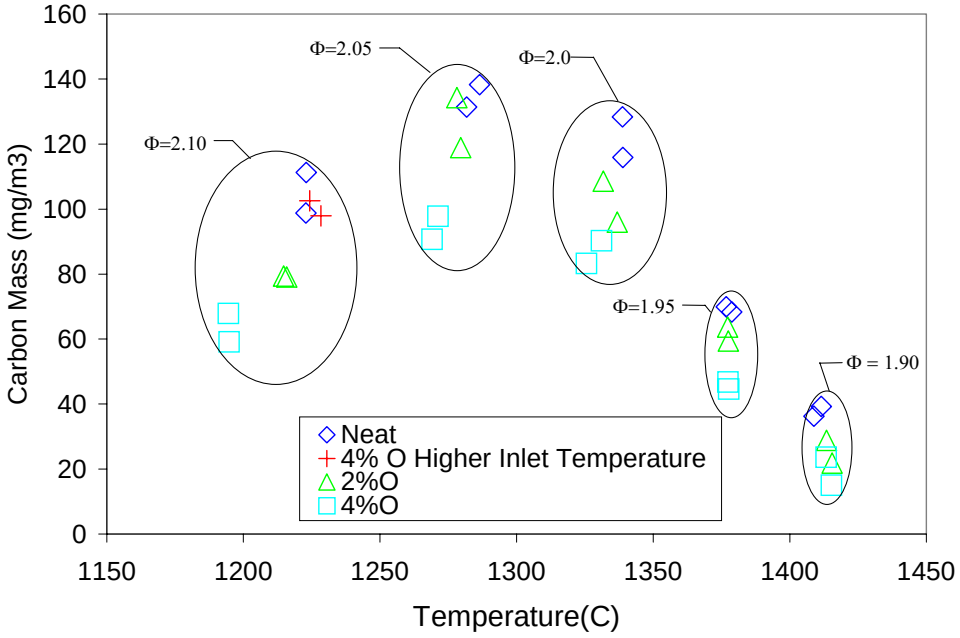

Figure 3.1.3-18. Total Carbon Mass for Cyclohexanone Additive.

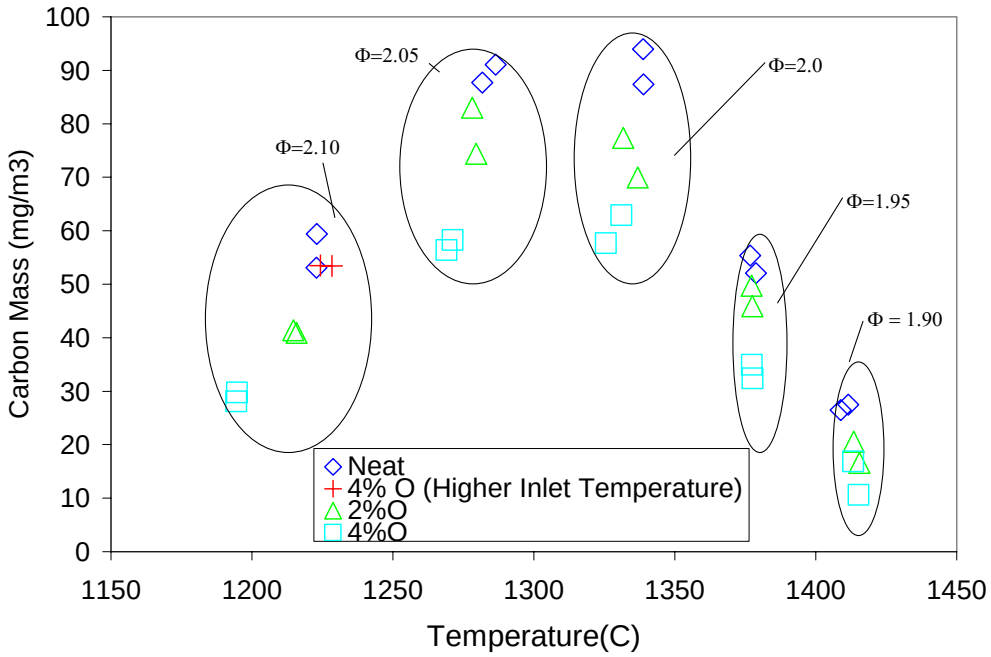

Figure 3.1.3-19. Carbonaceous Carbon Mass for Cyclohexanone Additive.

3.1.4 PREMIXED FLAME (UTRC)

The studies of oxygenated compounds in premixed flames at UTRC included investigation of ethanol addition to ethylene flames and ethanol addition to heptane and heptane/toluene flames. All of these experimental results are summarized in this section.

Ethylene/Ethanol

Results are reported here for an ethylene/air flame with an equivalence ratio of 2.34. These results were obtained using the perforated plate, flame holder. The flame was also probed after the addition of ethanol which introduced 5% oxygen (by weight) into the fuel (with fuel defined as ethylene+ethanol) while keeping the total carbon flow constant. The experimental conditions are shown in Table 3.1.4-1.

The equivalence ratio of the base ethylene flame (Flame 1) is 2.34, selected for comparison to literature results. The flow rates for Flame 2 were set to provide the same carbon flow rate and an oxygen/carbon mass ratio in the fuel of 0.05. Temperature of the flame, measured as a function of height above the burner surface using an uncoated, type R, 0.003" butt-welded thermocouple, is shown in Figure 3.1.4-1. At each height, the temperature is determined using the Thermocouple Particle Densitometry (TPD) technique described in Liscinsky et al [2000] whereby the thermocouple is rapidly inserted into the flame, using a pneumatically actuated sliding stage, while recording the temperature history of the bead. The bead response is corrected for radiation by balancing the heat transfer from the gas stream to the total radiation and then solving for gas temperature. Measured temperatures for both the ethylene and ethylene/ethanol flames are provided in Figure 3.1.4-1. Also reported in the figure are the predicted temperatures using the SANDIA Premix code and the UTRC chemical reaction mechanism. The rapid falloff in temperature in the post flame zone is underpredicted by the code, despite inclusion of energy loss due to radiation from gaseous species.

Soot volume fraction has been measured using Laser Extinction (LE) and TPD. A full discussion of these diagnostics are reviewed in Section 2.1 and can also be found in Liscinsky et al [2000]. Soot volume fraction as a function of height above the burner surface is shown in Figure 3.1.4-2. Results are shown for Flame 1 using both LE and TPD as well as those from Xu et al [1997] for a comparable flame with a carbon/oxygen ratio of 0.78. Despite the slight

variation in experimental conditions for the Xu et al work, the agreement between the three sets of measurements is very good. Soot volume fractions measured by TPD for Flame 2 are not in good agreement with the LE measurements, as there is nearly a factor of two between the two techniques. The TPD measurement depends not only on a curve fit to the temperature decay as the bead thermophoretically collects soot but also soot void fraction. Whereas measurements of soot void fraction for Flame 1 have been made previously, measurements for Flame 2 have not been collected and are recommended.

Heptane

The laminar, premixed flame burner facility was modified to vaporize liquid fuels, premix with air and inject fuel additives on-line. Heptane, initially selected as the surrogate fuel for analysis, was tested. Baseline studies indicated the existence of just a narrow operating region between the conditions at which sufficient soot was formed for reliable measurements and the flame lost its stability. Hence, data sets in premixed flames with only heptane as the fuel were not performed.

Heptane/Toluene

Addition of 10% (by volume) of toluene to heptane slightly increased the soot production and increased the flame stability. A flame at equivalence ratio of 2.4 was selected as a reference condition. Soot volume fractions were measured for this base flame with peak soot volume fractions of approximately 0.2 ppm. The effects of a variety of additives were examined, including a commercial additive, ethanol, BHT, Brij-92, and +100. For the latter three, there were uncertainties as it is unclear whether the fuel additives were fully vaporized in the premixing/prevaporization zone. However, both ethanol and commercial additive had measurable effects on reducing soot production at elevated additive levels (approximately 5%). Ethanol reduced soot levels by more than 70% and the commercial additive reduced soot production by about 20%.

Soot volume fractions as measured in the premixed 10% toluene/90% heptane flames with and without a variety of additives are shown in Figure 3.1.4-3. Additional results are summarized in Table 3.1.4-2 for each additive where the maximum fraction of soot reduced is indicated for a range of additive levels. This figure compares data from the reference, base flame

without additives to results for several flames with additive concentration levels near 8000 ppm. In the case of ethanol, the additive concentration is set to create 5% oxygen in the fuel. These results clearly indicate that oxygenates, particularly ethanol and nitromethane, have the largest impact on reducing soot production. Additional discussion on the nitromethane results are discussed in Section 3.2. Also shown in Figure 3.1.4-3 are some data with pyridine as the additive. Discussion of the pyridine results is in Section 3.4. A summary of results for a range of additives is shown in Table 3.1.4-2.

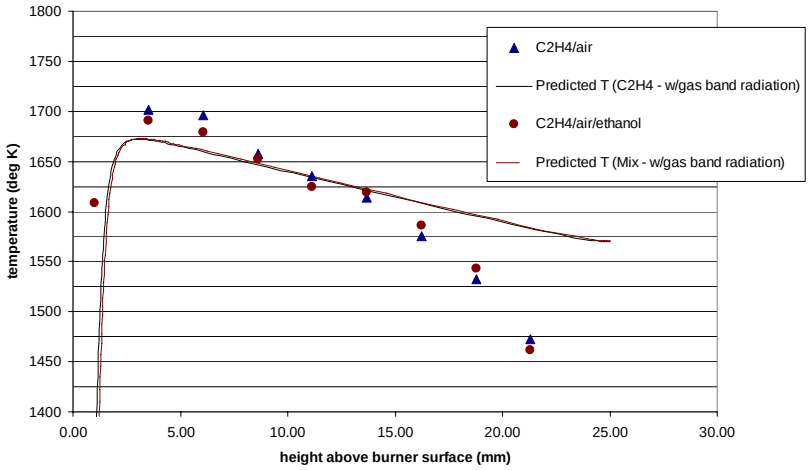

Figure 3.1.4-1. Temperature Along the Centerline of Flame 1 and 2.

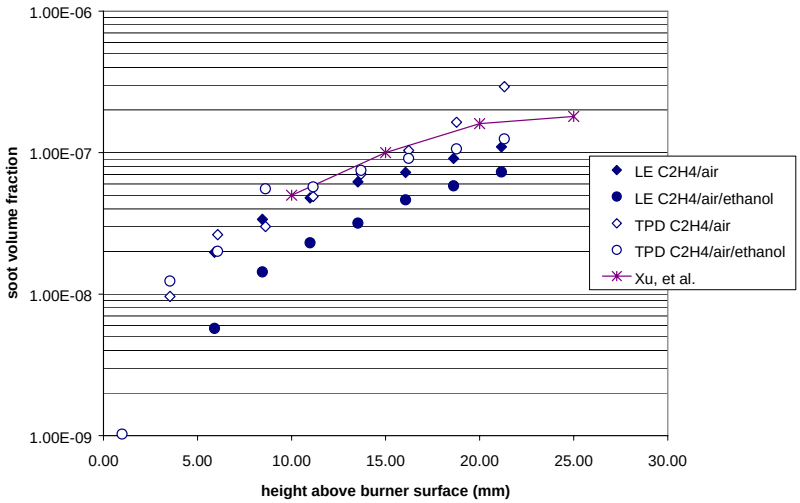

Figure 3.1.4-2. Soot Volume Fraction via Laser Extinction (LE) and Thermocouple Particle Densitometry (TPD) for Flame 1 and 2.

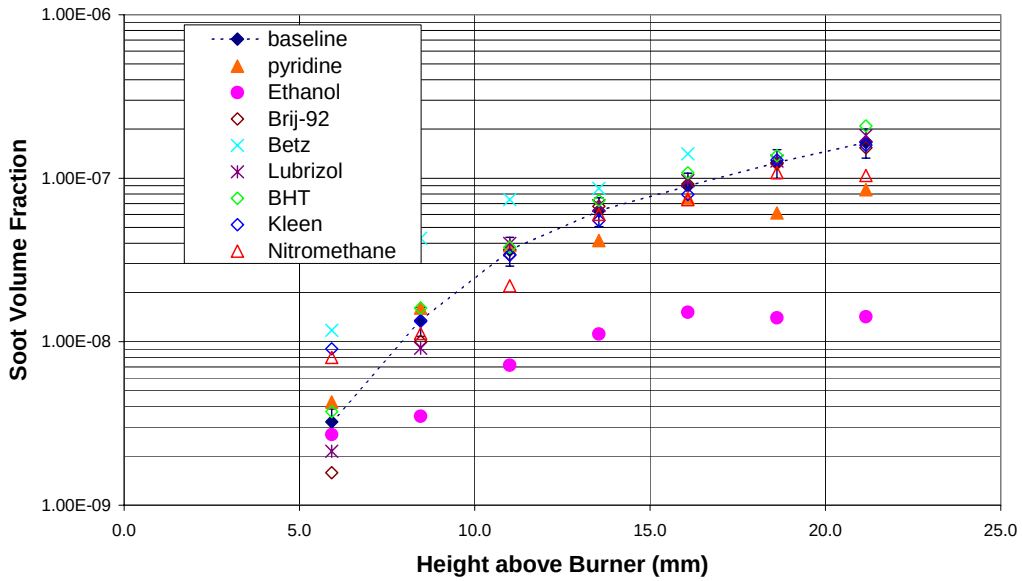

Figure 3.1.4-3. Soot Volume Fractions from Premixed, Laminar Flames. Base flame is 10% toluene and 90% heptane.

Table 3.1.4-1. Experimental Test Conditions for the Premixed, Fuel-Rich Flames.

	Ethylene	**Air**	**Ethanol**
Flame	(slpm)	(slpm)	(ml/min)
1	1.38	8.41	0.00
2	1.25	8.41	0.335

Table 3.1.4-2. Percentage Reductions in Soot Volume Fractions in Fuel-Rich Premixed Heptane/Toluene Flames due to Presence of Various Fuel Additives.

Flame	Additive	Additive Concentration	Soot reduction
1	-	-	baseline
2	ethanol	5% O in C	~70 %
3	Kleen*	400, 800, 8000 ppm	<10%
4		24000, 48000 ppm	~20 %
5	Brij-92	400, 800, 8000 ppm	<10%
6	+100	400, 800, 8000 ppm	<10%
7	PA	400, 800, 8000 ppm	<10%
8	BHT	400, 800, 8000 ppm	<10%
9	Pyridine	5000, 10000, 50000, 100000 ppm	~30%
10	Nitromethane	5000, 10000, 50000, 100000 ppm	~15%

3.1.5 PREMIXED FLAME (PENN STATE)

During the initial phase of the program, premixed flame studies were conducted at both Penn State and UTRC. The goal of the parallel experiments was to cross-check the results to ensure accuracy and consistency of the results. When the work shifted to liquid fuels, this parallel effort was deemed to be too costly in time and resources to be continued. No work with liquid fuels in the premixed flame was conducted at Penn State. The premixed flame studies of oxygenated additives at Penn State included ethanol and dimethyl ether (DME). The DME study was done to investigate the effect of structure on the effectiveness of an additive. Both sets of results are reported here. In each case modeling was used to understand the trends observed, so modeling results are also presented.

In the ethylene studies, flames with equivalence ratios of 2.34 and 2.64 were studied to facilitate comparison to past work on ethylene flames. Two oxygen concentrations, 5 and 10 wt% in the ethylene additive mixture, were studied. 5 wt% oxygen requires a 14.4% mass fraction of ethanol in the fuel stream, and 10 wt% requires approximately twice this amount.

When the ethanol was introduced into the fuel line, the ethylene flow rate was reduced in appropriate proportion in order to keep the total carbon flow rate constant. Because of the fuel and oxygenate selected, the equivalence ratio was not affected by the introduction of the ethanol so adjustment of the air flow rate was not required to keep the equivalence ratio constant. The mass fluxes used in the experiments are summarized in Table 3.1.5-1; the designation "UHP" denotes ultrahigh purity and implies that the ethylene was 99.9% pure.

The fluorescence spectra for flames with equivalence ratios of 2.34 and 2.64 as a function of height above the burner are presented in Figure 3.1.5-1. The fluorescence spectra show a broadband in the UV range centered around 340 nm where the intensities are almost constant along the flame height up to 10 mm; this band was used as an indicator of small aromatic species with one or two rings based on the work of Beretta et al [1992]. Another broadband peak in the visible range around 540 nm is observed for flame height above 6 mm, for which the intensity increases strongly as a function of flame height. This band was used as a qualitative measure of PAH species with three or more rings. The spectral features observed are in good agreement with those of Sgro et al [2001] in a similar ethylene/air flame at equivalence ratio of 2.31.

Figure 3.1.5-2 shows small aromatic species, large PAH, and soot volume fraction at equivalence ratios of 2.34 and 2.64 for the ethylene/air flames. Along the height above the burner surface, small PAH is first observed. The onset of small PAH appears to be located around 1 mm above the burner. After a sharp increase, the signal from the small aromatic species reaches a local maximum at the flame height of about 3 mm. At about 10 mm, the signal again rises, perhaps due to the growth of two-ring species. Large PAH begin to rise after the small aromatic species and continue to increase over the distance of measurement. Soot volume fraction follows the trends of the large PAH. However, the onset of soot is about 5 mm above the burner, which is much later than the onset of small aromatic species and large PAH. The clear time sequence among the development of small aromatic species, large PAH and soot is consistent with the expectations based on current theories of soot formation.

A comparison of the soot measurements to the work of Xu et al [1997] is presented in Figure 3.1.5-3. Below the flame height of 10 mm, the data show a good consistency with those of Xu et al, measured using both optical and gravimetric methods. The configuration of the stagnation plate used in this study is different than that used by Xu et al, which may account for a large portion of the differences observed. In the present study, a 100 mm-diameter, 10 mm-thick

aluminum plate was placed 36 mm above the burner surface to stabilize the flame. Xu et al also used a stagnation plate in their experiments, but their plate was made of stainless steel and had a 30 mm-diameter hole in the center and was placed 32 mm above the burner surface. In the present study, a stagnation plate identical to that of Xu et al was used. However, after one hour of testing, soot accumulated around the hole and filled it in so that the size of the hole was less than 10 mm. The filling of the hole caused measurable changes in the soot profile within the flame. In order to avoid these changes, a solid aluminum plate was used. Another contributing factor is that the total flow rate at Φ=2.64 was reduced to 80%, used by Xu et al in order to obtain a stable flame condition with the solid stagnation plate, so the 2.64 case had a lower mass flux than the corresponding flame of Xu et al. At Φ=2.34, the flow rates are exactly the same; much smaller differences are observed.

The effects of ethanol addition on aromatic species and soot are presented in Figure 3.1.5-4 and changes in maximum values relative to the baseline are presented in Table 3.1.5-2. For both equivalence ratios the addition of ethanol has a greater effect on large PAH and soot than on the smaller aromatic species. Also the data indicate that the effect of ethanol addition is greater at Φ=2.34 than at Φ=2.64.

The temperature profiles, which were obtained for use in the modeling studies, are presented in Figure 3.1.5-5. Each set of measurements was made at least twice in separate experiments; the repeatability of the temperature measurement was typically within ±20K. Temperatures are higher at ϕ=2.34 as expected; however, the trend of increasing maximum temperature with the addition of the ethanol was counter to expectations. Such a trend is also reported by Inal and Senkan [2002]; they do not, however, offer an explanation for it. A possible explanation for the unexpected trend in the flame temperature observed in the present study is that the addition of ethanol lowers the flame speed of the mixture. The lower flame speed causes the flame to stabilize further from the burner, lowering heat loss and counterbalancing the effect of ethanol on the adiabatic flame temperature.

Modeling Results

Figure 3.1.5-6 presents comparisons between the model and experiment for small aromatic species, large PAH, and soot for the ethylene/air flames. The model results track the experimental trends with equivalence ratio reasonably well for small aromatic species and large

PAH, but the trends in soot are not captured as well. For small aromatic species, the modeling results for the dominant one- and two-ring species, benzene and naphthalene, were combined. Benzene is much higher in concentration than naphthalene, but the naphthalene will fluoresce more strongly. In order to account for the stronger fluorescence of the naphthalene, its concentration was weighted by a factor of 14, which was determined to be the factor that best matched the Φ=2.34 experimental results. The factor of 14 was used for all other test conditions. The modeling predicts a much larger increase in small aromatic species as equivalence ratio increases than is observed in the experiments. For the large PAH the match between model and experiment is somewhat better; the large PAH predictions were obtained by summing all three-ring and larger aromatic species from the modeling results. The model predicts approximately a factor of two increase in large PAH species as equivalence ratio increases from Φ=2.34 to Φ=2.64, whereas the experiment showed a factor of three increase. The predictions for soot, which are made by postprocessing the premixed flame simulation results, show little increase in soot as equivalence ratio increases. The comparison at Φ=2.34 is reasonably good, but the soot model does not predict the increase of nearly a factor of three that occurs in the experiment when Φ is increased to 2.64.

Figure 3.1.5-7 shows the modeling results for all flames studies which are comparable to the experimental data in Figure 3.1.5-4. For small aromatic species and large PAH, the model results capture the general trend that increasing the amount of oxygen leads to greater reductions in aromatic species. Also the magnitudes of the reductions relative to the baseline match the data reasonably well for the aromatic species. The soot predictions for Φ=2.34 are reasonably consistent with the experimental data, although the volume fraction is underpredicted. For Φ=2.64, the comparison of the model and experiment are not good. The model predicts no effect of 5% oxygen at this condition.

The results from the modeling were used to determine the mechanism through which the ethanol leads to a reduction of aromatic species and soot. Since the modeling results matched the experimental results best at an equivalence ratio of 2.34, that condition was used as the basis for the analysis. The first step in the analysis was to track the main reaction pathways for the production of the aromatic species using XSenkplot. The results are summarized in Table 3.1.5-3 which presents the major reaction pathways from the fuel to aromatic species as well as competing oxidation reactions. The primary route for formation of the first aromatic ring is

predicted to occur through propargyl recombination; alternative routes involving C_4+C_2 species were not predicted to be important under the conditions of this study. The majority of naphthalene formation occurs through two consecutive Hydrogen-Abstraction-Acetylene-Addition (HACA) reactions via phenylacetylene (C_8H_6); the production via cyclopentadienyl is predicted to be relatively small. The recombination reaction of two cyclopentadienyl radicals (C_5H_5) makes a minor contribution to naphthalene formation at these conditions. A3, phenanthrene, is formed largely by ring-ring condensation reactions as opposed to formation through the HACA growth pathway from naphthalene. The production of pyrene ($C_{16}H_{10}$) is dominated by the HACA mechanism through phenanthryl radical ($C_{14}H_9$), which forms from phenanthrene by H abstraction.

The summary presented in Table 3.1.5-3 demonstrates that production of aromatic species is a complex, radical-driven process involving a competition between reactions that oxidize the carbon to CO and CO_2, and reactions that produce aromatic species and their precursors. The quantity of aromatic species formed will be the net result of the competition between the oxidation and aromatic production pathways. The addition of ethanol can change this balance in several ways including effects on temperature, radical concentrations, and the amount of carbon from the ethanol that contributes to aromatic production.

The thermocouple measurements showed that the addition of ethanol led to higher temperatures throughout the regions where aromatic species are formed. Modeling runs were performed for the ethylene/ethanol flames using the same temperature profile as the corresponding ethylene flame to obtain an indication of the effect of temperature on the production of aromatic species. The results, presented in Figure 3.1.5-8, show that the temperature is having only a small effect on aromatic species, PAH, and soot over most of the measurement region.

Other researchers have noted that changes in concentrations of radical species such as H, O, and OH can have a significant impact on the competition between oxidation pathways and pathways leading to aromatic species and soot. As an indication of the effect of the addition of ethanol on these key radicals, the changes in the predicted peak mole fractions caused by the addition of ethanol were determined relative to the base fuel. Table 3.1.5-4 presents a summary for Φ=2.34 and the two oxygen levels studied based on modeling using the measured temperature profiles and using the temperature profile of the corresponding ethylene flame. The

latter data can be used to judge the contributions of the increased temperature to changes in radical concentrations. Comparison of the two sets of results indicates that the temperature is contributing to the changes in radical concentrations. The increases in H atoms appear to be mostly caused by the temperature increase, and for the 5% oxygen case, temperature also appears to be the dominant factor in increasing O and OH. Increasing H will tend to enhance reactions leading to aromatic formation, and increasing O and OH will tend to enhance the competing oxidation reactions; therefore, the increases tend to offset each other to some degree. However, it would appear that the increases in the oxidizing radicals may be somewhat more significant than the increase in H and could account for some of the decrease in aromatic species observed in the experiments and the model.

The final effect that is contributing to the reduction of aromatic species is the contribution of ethanol to precursor species. In order to estimate this effect, the pathways through which the ethanol reacts were studied to determine their contributions to precursor species. A simplified reaction map is presented in Figure 3.1.5-9 showing its conversion to key products including CO. Ethanol can decompose via two reactions that break the C-O bond leading to ethylene and methyl, both of which can contribute to the formation of aromatic species. In addition ethanol can undergo hydrogen abstraction at three different sites, leading to three different radical species that subsequently undergo additional reactions eventually leading to precursor species and CO. Methyl undergoes additional reactions that can lead to various precursor species and CO. Due to the strength of the C=O bond, CO will not contribute to the production of aromatic species so any carbon from the ethanol that produces CO is considered to be removed from the reaction pathway leading to aromatic species and soot. This effect has been noted by many others including Curran et al [2001]. The carbon flow analysis revealed that only about one-half (54%) of the carbon in ethanol is converted to species that contribute to the production of aromatic species. The majority of this amount (49%) is converted to ethylene or ethane, which is quickly converted to ethylene, and the remainder (5%) contributes to propargyl formation. Thus, about half of that carbon in the ethanol is removed from pathways that can contribute to aromatic species and soot formation.

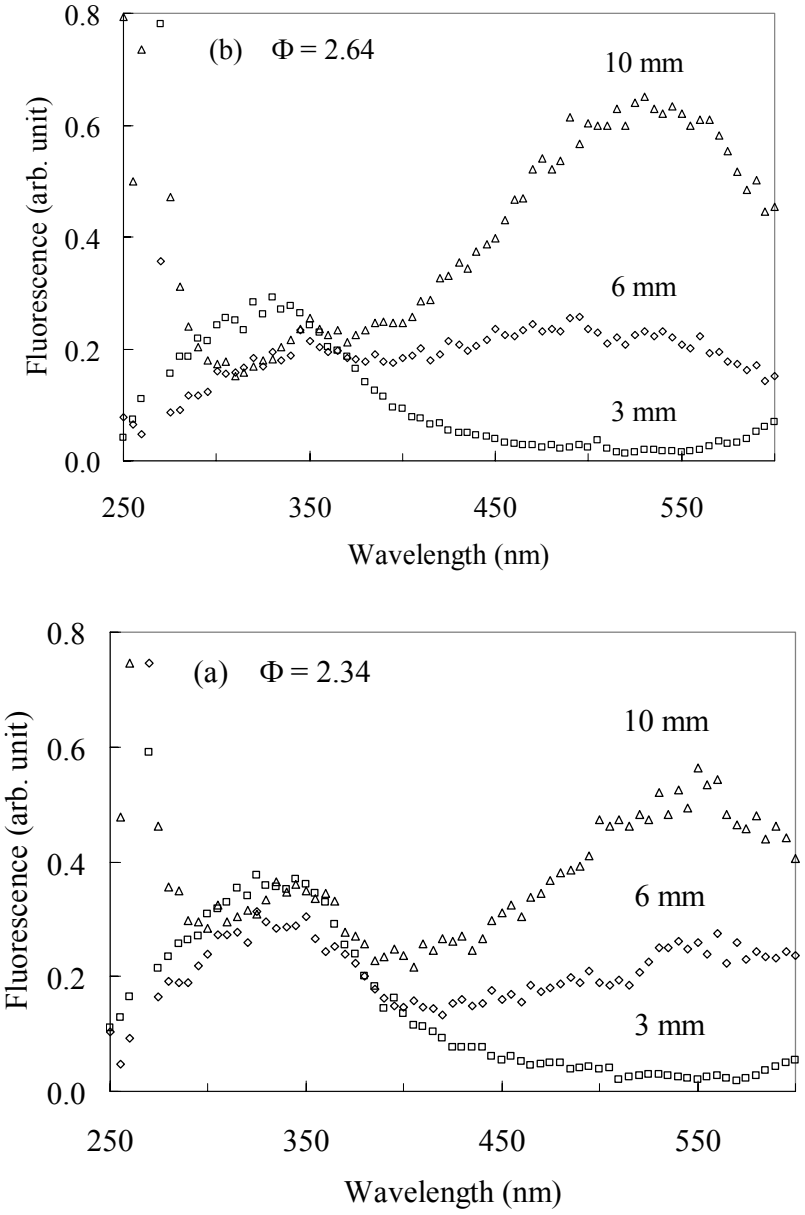

Figure 3.1.5-1. Fluorescence Spectra (a) Φ = 2.34; (b) Φ = 2.64.

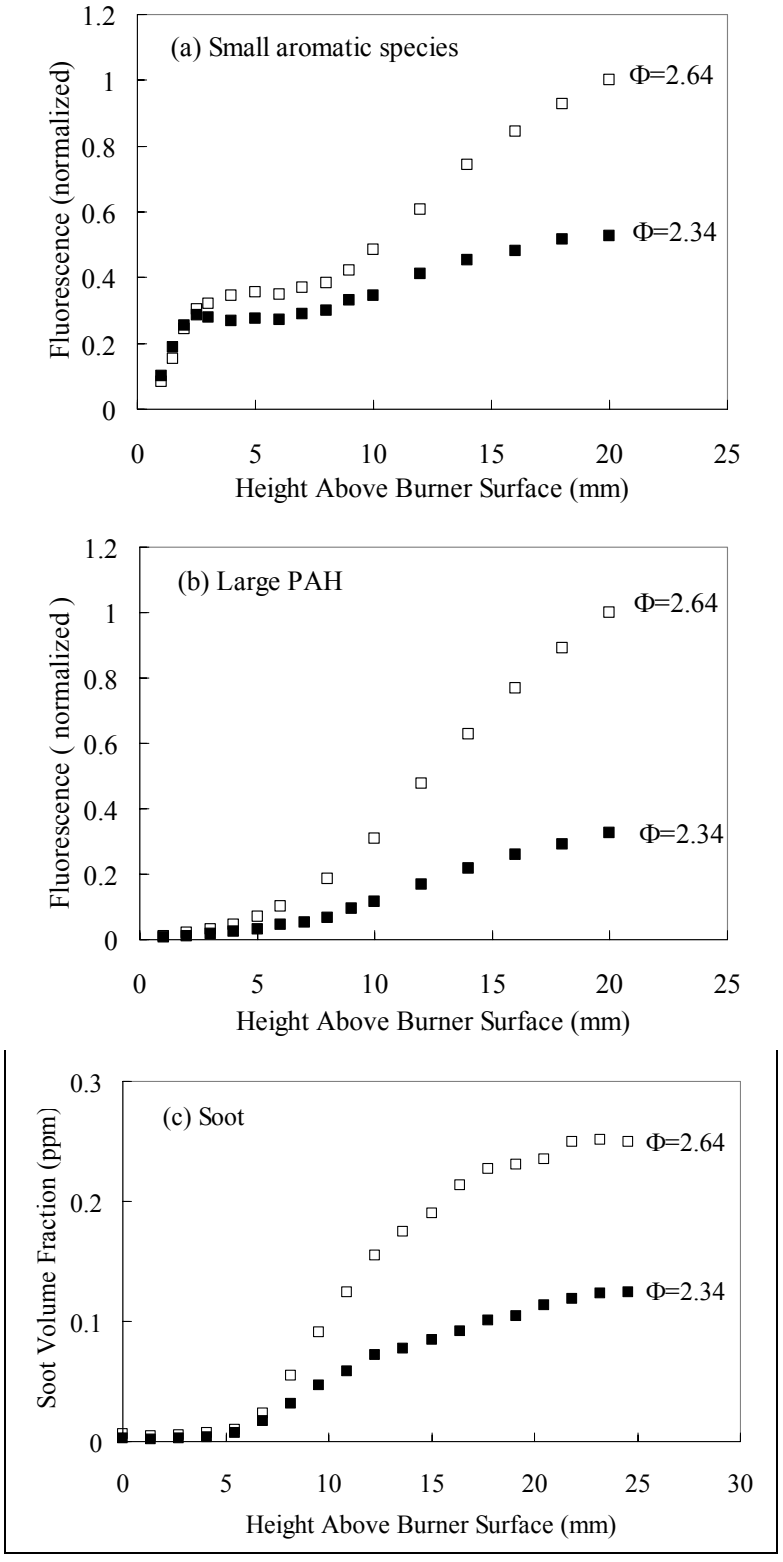

Figure 3.1.5-2 (a) Small Aromatic Species, (b) Large PAH, and (c) Soot for Ethylene/Air Flames. (Note that the PAH data are normalized by the maximum signal observed at Φ=2.64).

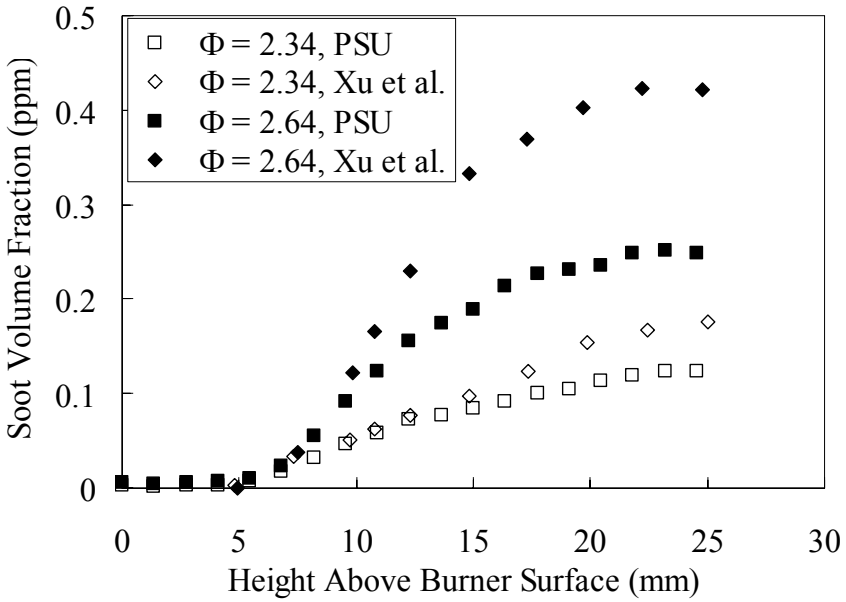

Figure 3.1.5-3. Comparison of Soot Volume Fraction Measurement Results to Those of Xu et al [1997].

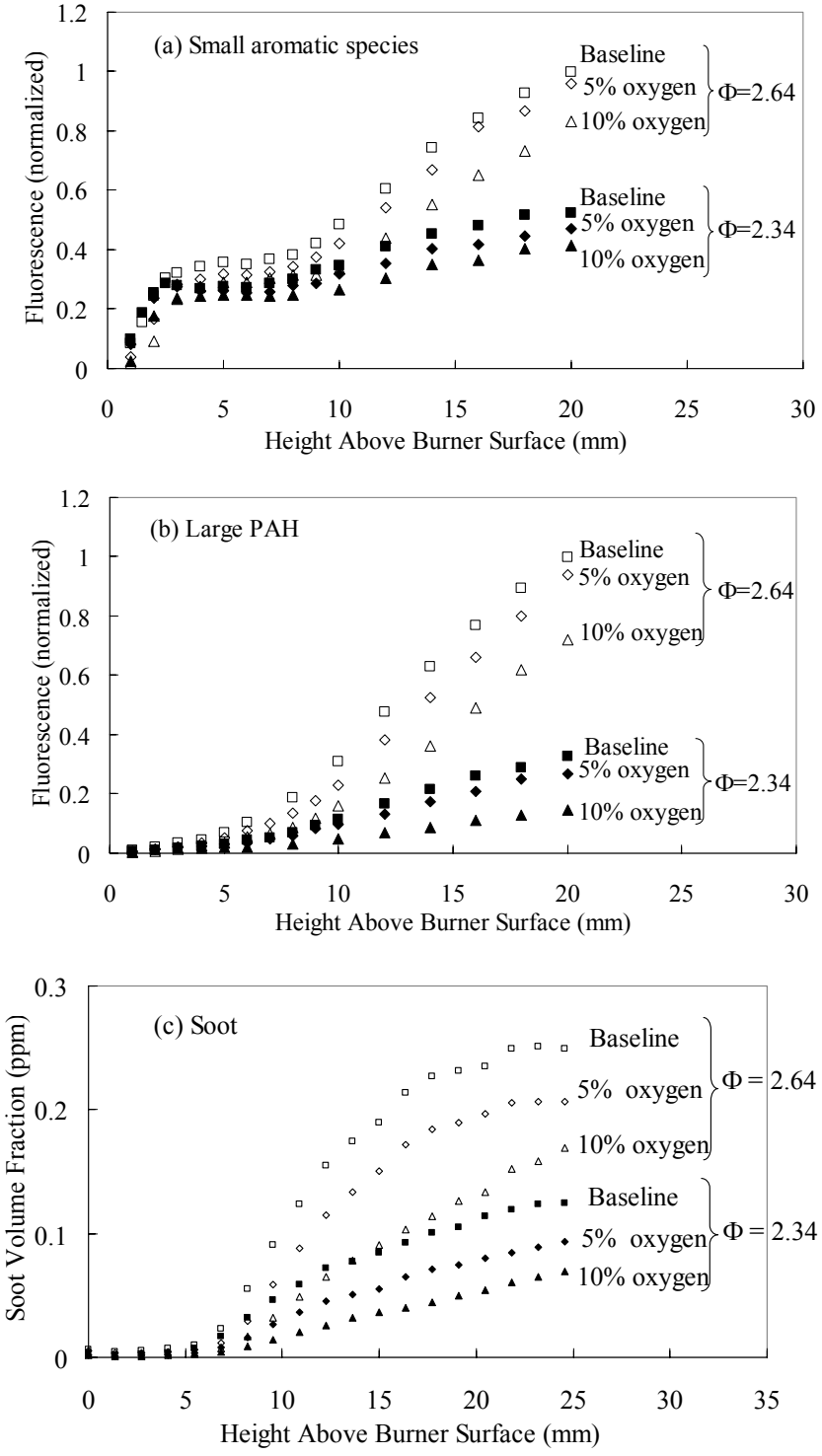

Figure 3.1.5-4. Effects of Ethanol on (a) Small Aromatic Species, (b) Large PAH, and (c) Soot for Ethylene-Air Flames. (Note that the PAH data are normalized by the maximum signal observed at ϕ=2.64).

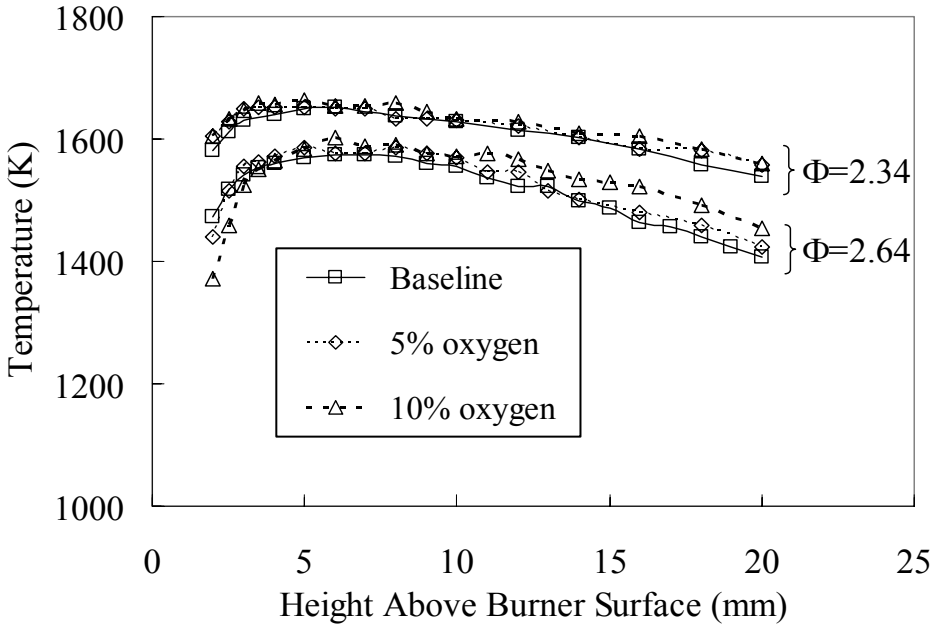

Figure 3.1.5-5. Measured Flame Temperature Profiles for Φ = 2.34 and 2.64.

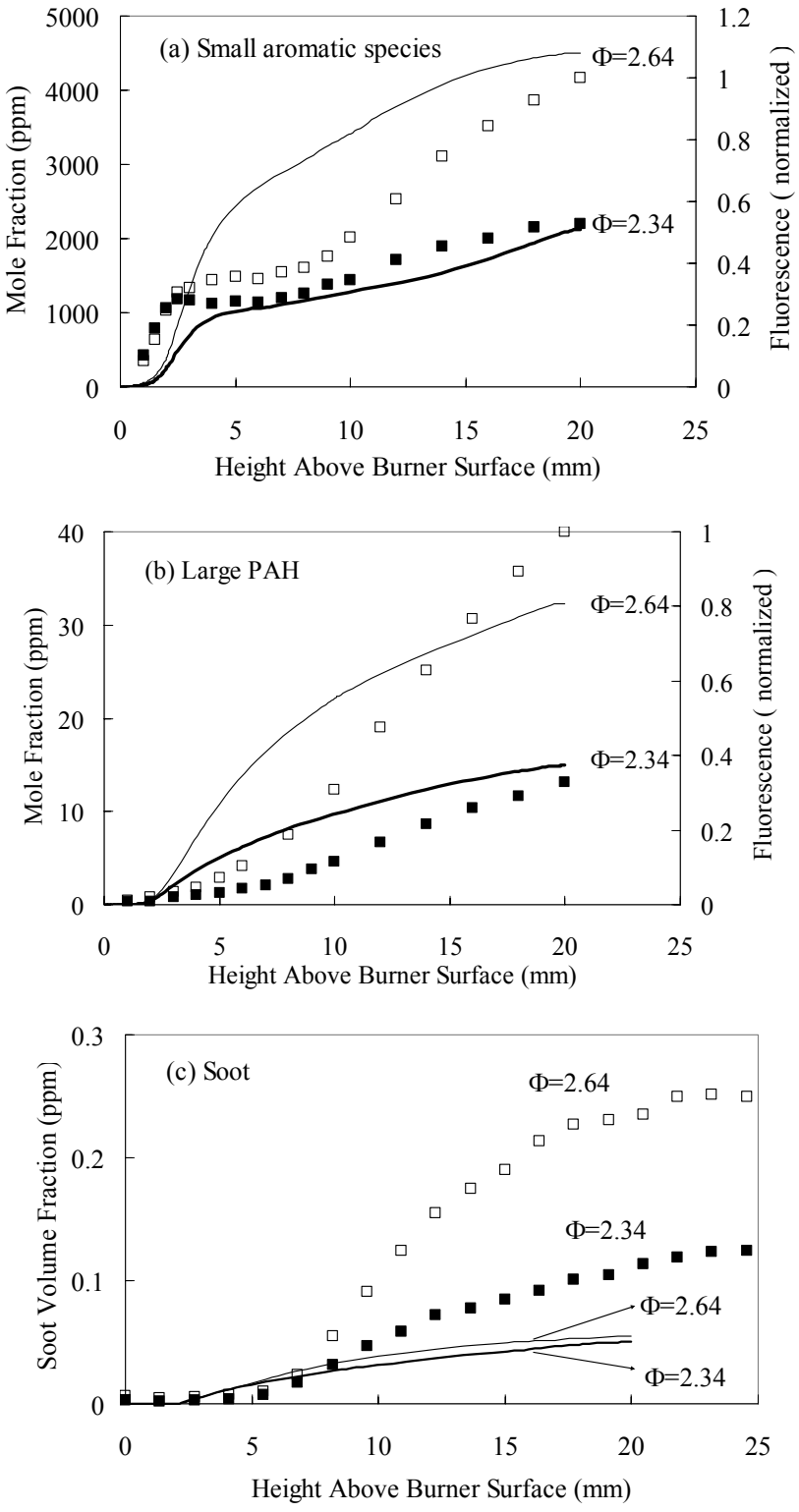

Figure 3.1.5-6. Comparison of Experiments (square symbols) and Model (solid lines) for (a) Small Aromatic Species, (b) Large PAH, and (c) Soot at Base Flames. (LIF data normalized by the maximum signal observed at Φ=2.64.)

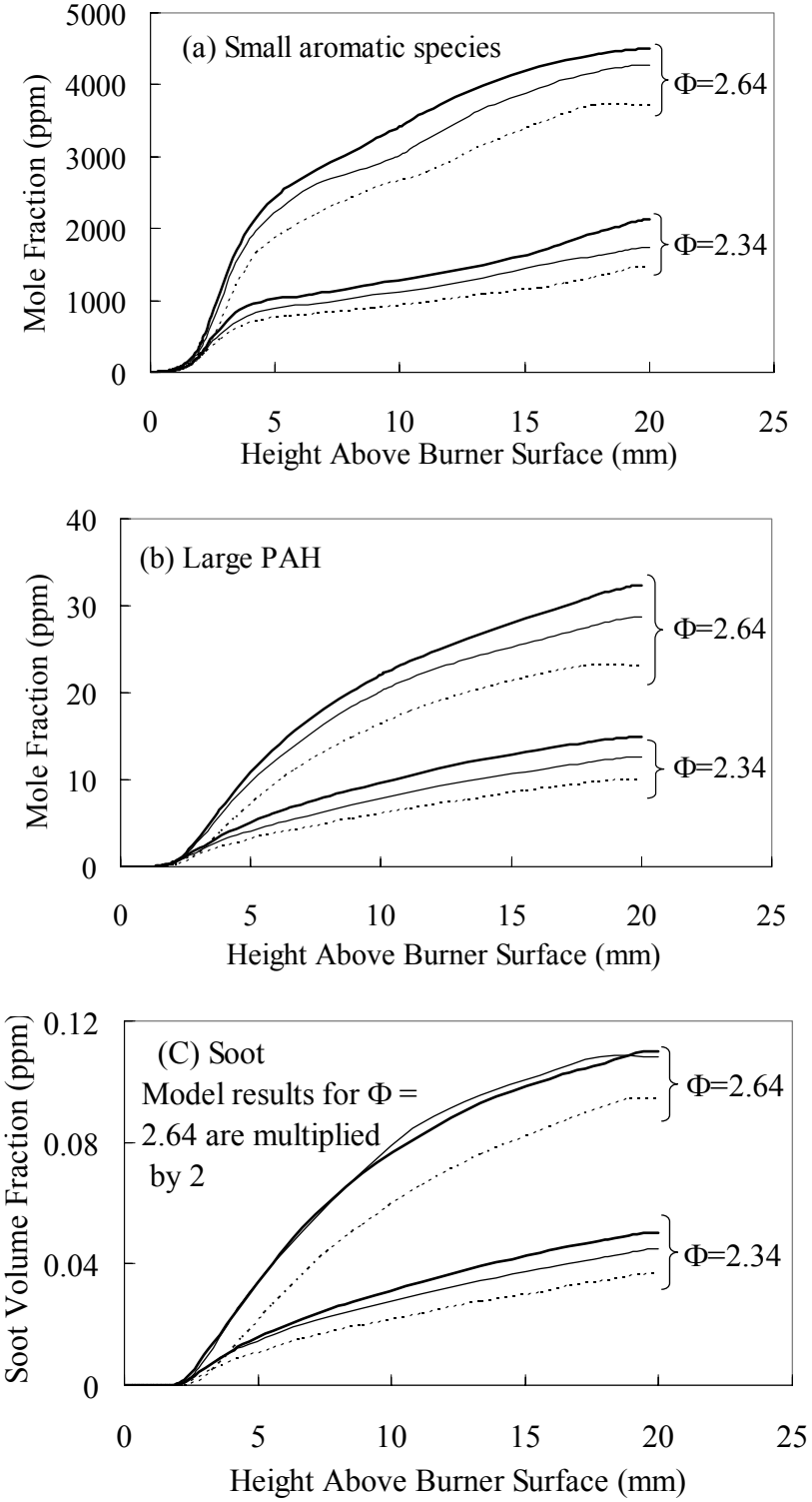

Figure 3.1.5-7. Model Predictions for Effects of Ethanol on (a) Small Aromatic Species, (b) Large PAH, and (c) Soot. Thick solid lines represent baseline, thin solid lines represent 5% oxygen and dotted lines represent 10% oxygen. (Note that model predictions of soot for Φ=2.64 case are multiplied by a factor of 2 to separate them from the Φ=2.34 results.)

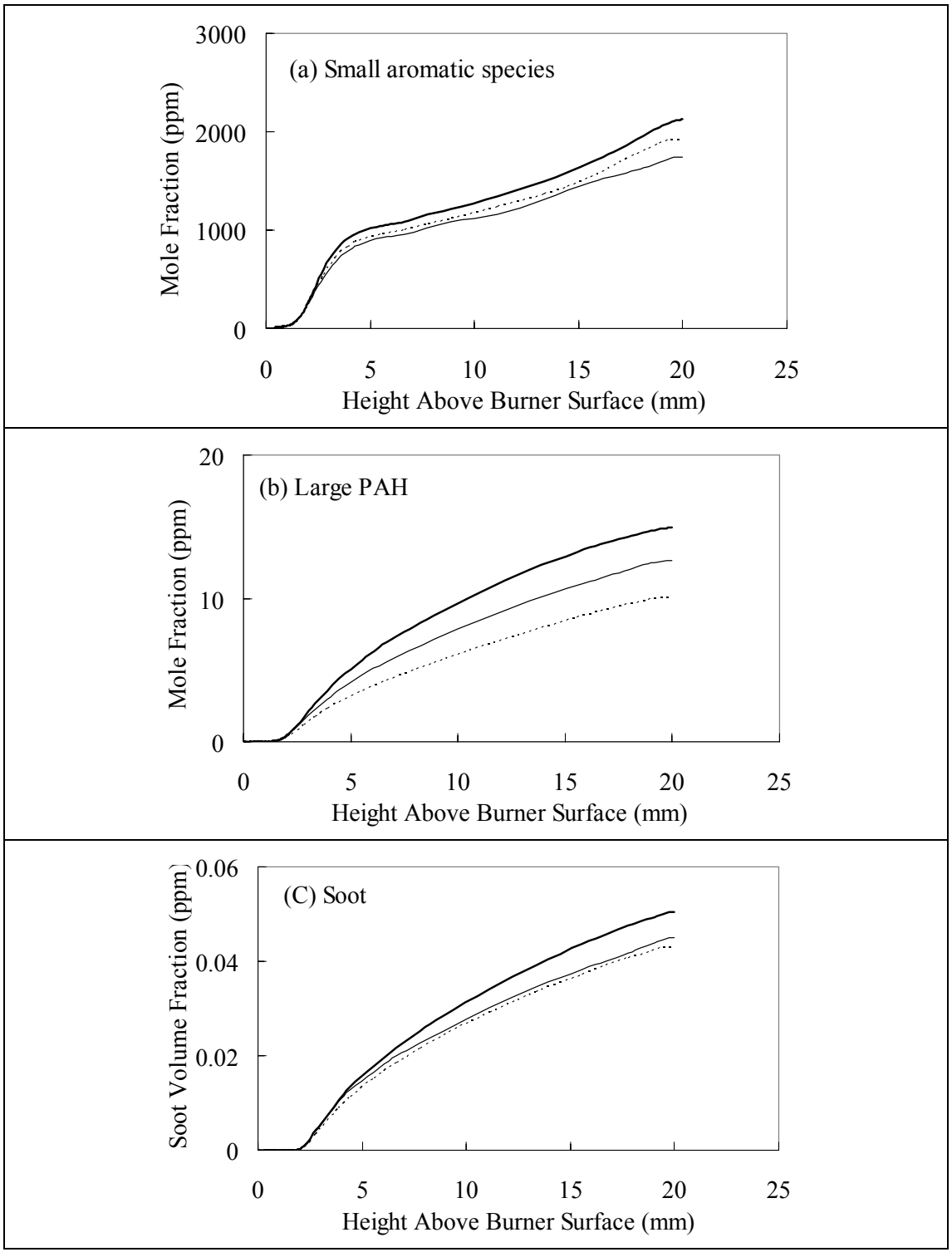

Figure 3.1.5-8. Effect of Temperature on (a) Small Aromatic Species, (b) Large PAH, and (c) Soot Predicted by Model at Φ=2.34. (Thick solid lines represent baseline cases, thin solid lines represent 5% oxygen cases with measured temperature profiles, and dashed lines represent 5% oxygen cases with same temperature profiles as the baseline cases.)

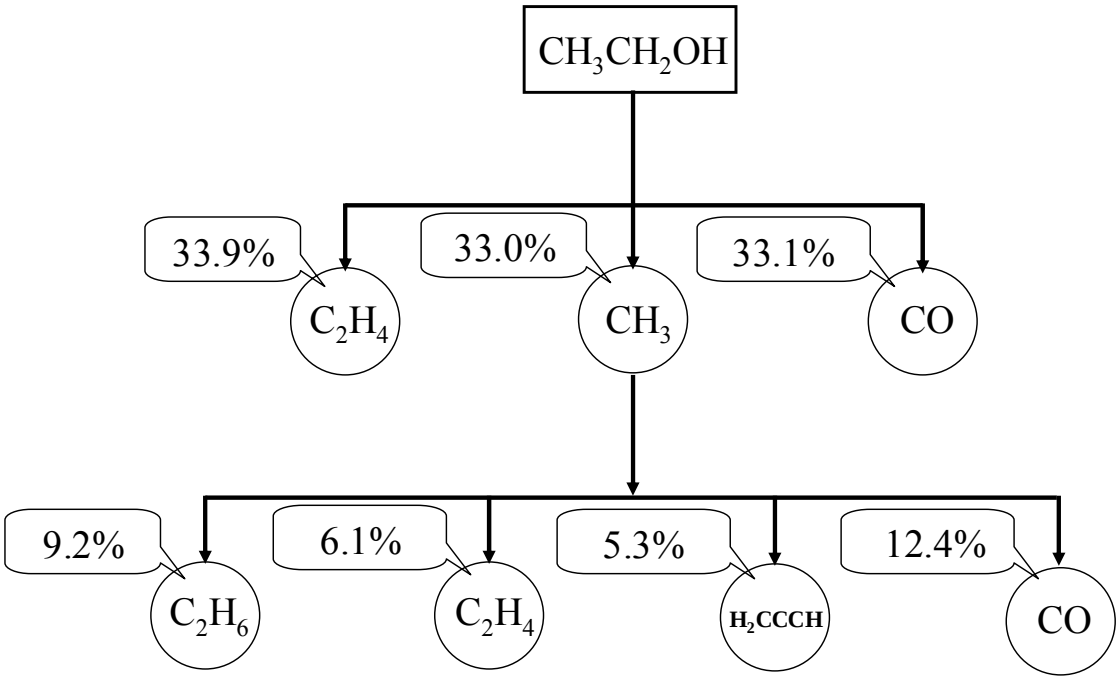

Figure 3.1.5-9. Carbon Flux Diagram for Ethanol at Φ=2.34. (Percentage indicates the fraction of carbon from ethanol passing through the species shown.)

Table 3.1.5-1. Experimental Conditions.

Mass flux of premixed ethylene/air flame (mg/s.cm^2)			
Equivalence ratio		2.34	2.64
W/O Additive	air	6.75	5.31
	ethylene (UHP)	1.07	0.95
% O in fuel	ethanol	0.16	0.14
	air	6.75	5.31
	ethylene (UHP)	0.97	0.86
10% O in fuel	ethanol	0.35	0.31
	air	6.75	5.31
	ethylene (UHP)	0.86	0.76

Table 3.1.5-2. Percentage Changes in Maximum Values of Aromatic Species and Soot Relative to the Baseline by Ethanol.

Φ	2.34		2.64	
oxygen content	5%	10%	5%	10%
small aromatic species	-10%	-21%	-4%	-17%
large PAH	-18%	-56%	-6%	-28%
soot	-25%	-44%	-17%	-32%

Table 3.1.5-3. Summary of Major Reactions in Pathway from Fuel to PAH at Φ=2.34.

Species	Modes	**Main Pathway to Soot Precursor**	**Competing Reaction**
C_2H_4	des	$C_2H_4+H<=>C_2H_3+H_2$ (49.0%) $C_2H_4+OH<=>C_2H_3+H_2O$ (13.1%) $C_2H_4+CH_3<=>C_2H_3+CH_4$ (9.5%) $C_2H_4+O<=>OH+C_2H_3$ (4.2%)	$C_2H_4+OH<=>CH_3+CH_2O$ (9.4%) $C_2H_4+O<=>CH_3+HCO$ (7.8%) $C_2H_4+O<=>CH_2O+CH_2$ (4.4%)
C_2H_3	prod	$C_2H_4+H<=>C_2H_3+H_2$ (63.3%) $C_2H_4+OH<=>C_2H_3+H_2O$ (16.9%) $C_2H_4+CH_3<=>C_2H_3+CH_4$ (12.2%) $C_2H_4+O<=>OH+C_2H_3$ (5.4%)	
	des	$C_2H_3<=>C_2H_2+H$ (71.2%) $C_2H_3+O_2<=>C_2H_2+HO_2$ (1.0%) $C_2H_3+H<=>C_2H_2+H_2$ (0.5%)	$C_2H_3+O_2<=>CH_2O+HCO$ (26.2%)
C_2H_2	prod	$C_2H_3<=>C_2H_2+H$ (78.9%) $C_3H_2+OH<=>C_2H_2+HCO$ (9.2%) $C_3H_2+O<=>C_2H_2+CO$ (2.4%)	
	des	$CH_2+C_2H_2<=>H_2CCCH+H$ (10.3%) $CH3+C_2H_2<=>C_3H_4P+H$ (7.6%) $C_3H_4+H<=>C_2H_2+CH_3$ (2.7%) $C_2H_3<=>C_2H_2+H$ (2.6%) $HCH+C_2H_2<=>H_2CCCH+H$ (2.6%)	$C_2H_2+O<=>HCCO+H$ (48.0%) $C_2H_2+O<=>HCH+CO$ (11.6%)
H_2CCCH	prod	$CH_2+C_2H_2<=>H_2CCCH+H$ (38.8%) $C_3H_4P+H<=>H_2CCCH+H_2$ (27.0%) $C_3H_4+H<=>H_2CCCH+H_2$ (10.8%) $HCH+C_2H_2<=>H_2CCCH+H$ (9.7%)	
	des	$H_2CCCH+H<=>C_3H_2+H_2$ (62.3%)	$H_2CCCH+OH<=>C_3H_2+H_2O$ (2.3%)
C_6H_6	prod	$2H_2CCCH<=>C_6H_6$ (66.7%) $C_6H_5+H<=>C_6H_6$ (20.5%) $OH+C_6H_6<=>C_6H_5OH+H$ (7.7%)	
	des	$C_6H_6+H<=>C_6H_5+H_2$ (80.4%) $C_6H_6+OH<=>C_6H_5+H_2O$ (13.3%)	$C_6H_6+O<=>C_6H_5O+H$ (2.5%) $OH+C_6H_6<=>C_6H_5OH+H$ (1.9%)

C_6H_5	prod	$C_6H_6+H<=>C_6H_5+H_2$ (79.0%) $C_6H_6+OH<=>C_6H_5+H_2O$ (13.1%)	
	des	$C_6H_5+C_2H_2<=>C_8H_6+H$ (27.6%) $C_6H_5+H<=>C_6H_6$ (23.8%)	$C_6H_5+O_2<=>C_6H_5O+O$ (16.9%) $C_6H_5+O_2<=>C_6H_4O_2+H$ (8.0%)
$C_{10}H_8$	prod	$C_{10}H_8+H<=>C_{10}H_7*1+H_2$ (45.1%) $C_{10}H_7*1+H<=>C_{10}H_8$ (25.6%) $C_{10}H_7*2+H<=>C_{10}H_8$ (13.4%) $C_{10}H_8+OH<=>C_{10}H_7*1+H_2O$ (6.8%) $2C_5H_5<=>C_{10}H_8+2H$ (2.4%)	
	des	$C_{10}H_8+H<=>C_{10}H_7*2+H_2$ (77.5%) $C_{10}H_8+OH<=>C_{10}H_7*2+H_2O$ (10.4%) $C_{10}H_8+OH<=>C_{10}H_7*1+H_2O$ (2.0%) $C_{10}H_8+H<=>C_{10}H_7*1+H_2$ (0.4%)	$C_{10}H_7OH\text{-}1+H<=>C_{10}H_8+OH$ (6.3%)
A_3	prod	$C_8H_6+C_6H_5<=>A_3+H$ (50.2%) $A_3L<=>A_3$ (11.8%) $A_1C_2H*2+C_6H_6<=>A_3+H$ (9.3%) $C_{12}H_9+C_2H_2<=>A_3+H$ (8.8%) $INDENE*+C_5H_5<=>A_3+H_2$ (7.0%)	
	des	$A_3+H<=>A_3*4+H_2$ (74.4%) $A_3+OH<=>A_3*4+H_2O$ (12.8%)	
PYRENE	prod	$A_3*4+C_2H_2<=>PYRENE+H$ (81.6%) $A_1C_2H*2+C_8H_6<=>PYRENE+H$ (5.5%) $PYRENE*4+H<=>PYRENE$ (4.9%)	
	des	$PYRENE+H<=>PYRENE*4+H_2$ (39.4%) $PYRENE+H<=>PYRENE*1+H_2$ (34.6%) $PYRENE+H<=>PYRENE*2+H_2$ (8.0%)	$PYRENE+OH<=>PYRENE*4+H_2O$ (5.8%) $PYRENE+OH<=>PYRENE*1+H_2O$ (5.0%)

Table 3.1.5-4. Changes in Computed Peak Radical Concentrations with Addition of Ethanol at Φ=2.34.

Temperature Profile	As Measured		From Ethylene Flame	
Oxygen level	5%	10%	5%	10%
H	4.2%	3.0%	0.6%	0.00%
OH	5.7%	7.4%	1.2%	6.0%
O	2.0%	2.3%	0.2%	2.4%

Dimethyl Ether

The work with dimethyl ether (DME), which has the same elemental composition as ethanol, was done to investigate the effect of oxygenate structure on soot reduction. The conditions of the study were identical to those used in the ethanol-ethylene experiments as were the experimental and modeling approaches. Therefore only main results will be presented here; complete results are reported in Wu et al [2006].

Flames with equivalence ratios of 2.34, 2.64, and two oxygen concentrations, 5 and 10 wt% in the ethylene/additive mixture, were studied. 5 wt% oxygen requires a 14.4% mass fraction of DME in the fuel stream, and 10 wt% requires approximately twice this amount. When the DME was introduced into the fuel line, the ethylene flow rate was reduced in appropriate proportion in order to keep the total carbon flow rate constant. Because of the fuel and oxygenate selected, the equivalence ratio was not affected by the introduction of the DME so adjustment of the air flow rate was not required to keep the equivalence ratio constant. The mass fluxes used in the experiments are summarized in Table 3.1.5-5; the designation UHP denotes ultrahigh purity and implies that the ethylene was 99.9% pure.

Table 3.1.5-6 presents a summary of the reductions in peak soot and PAH levels achieved through the addition of DME to the flames. Comparison of these reductions from the addition of ethanol under similar experimental conditions indicates that the DME is somewhat more effective than ethanol in reducing soot at phi=2.34 and about equivalent to it at phi-2.64. Modeling indicated that the effects of DME are similar to those identified for ethanol. The main effect of structure that was identified that can account for the somewhat greater effectiveness of

DME is that it has no decomposition path that involves the formation of C_2-species that can contribute directly to the formation of soot precursors. On the other hand, ethanol can undergo unimolecular decomposition to form an ethyl radical that can contribute to soot formation. Details of these differences are discussed in Song et al [2003].

Table 3.1.5-5. Experimental Conditions.

Mass flux of premixed ethylene/air flame (mg/s.cm^2)			
Equivalence ratio		2.34	2.64
W/O Additive	air	6.75	5.31
	ethylene (UHP)	1.07	0.95
5% O in fuel	DME	0.16	0.14
	air	6.75	5.31
	ethylene (UHP)	0.97	0.86
10% O in fuel	DME	0.35	0.31
	air	6.75	5.31
	ethylene (UHP)	0.86	0.76

Table 3.1.5-6. Percentage Changes in Maximum Values of Aromatic Species and Soot Relative to the Baseline by DME.

Φ	2.34		2.64	
oxygen content	5%	10%	5%	10%
small aromatic species	-19%	-49%	-6%	-19%
large PAH	-34%	-70%	-20%	-35%
soot	-34%	-62%	-13%	-32%

3.1.6 OPPOSED-JET DIFFUSION FLAME

Neat Ethylene/Air Opposed Flow Flames

Figure 3.1.6-1 shows a graph of calculated mole fraction profiles versus distance from the fuel duct for OH, C_2H_2, C_3H_3, A1 (benzene, C_6H_6) and A4 (pyrene, $C_{16}H_{10}$) for a neat ethylene/air opposed flow flame. Overlaid onto Figure 3.1.6-1 are values of pixel intensity along the centerline between the burner ducts, measured using the light scattering/PLIF technique, for the same flame. The calculation is in reasonable agreement with observation. The calculation predicts the separation of regions of maximum soot concentration (assuming A1 through A4 to be soot precursors in fuel-rich environments [Song 2003, Calcote 1981, Haynes 1981] and OH. The experimental data in this figure have been background corrected by subtracting the pixel dark current. To compare the data, the spatial location of the peak from OH fluorescence (relative to the fuel duct) measured in the flame was matched to the spatial location of the peak from OH predicted by the calculation. The measured light scatter from particles in the flame (and also possible broadband fluorescence from aromatics) is slightly closer to the fuel duct than the location of peak A1 and A4 concentrations predicted by the calculation. Because the soot particles in the flame are likely larger than A4, thermophoretic forces [Sung 1996] may be driving the larger particles towards cooler regions of the flame. Also shown in Figure 3.1.6-1 (dashed line) is an estimation of the location of the stagnation plane, based upon the calculations. We have given the stagnation plane a finite width defined by the point where the axial gas velocity goes to zero (approximately 0.375 cm from the fuel duct) and the point where the radial gas velocity is at a maximum (approximately 0.428 cm from the fuel duct). The initial fuel and oxidizer gas stream velocities (for experiment and calculation) were 41 and 55 cm/s, respectively.

To understand how adding ethanol vapor to the fuel or oxidizer gases will affect the concentrations of OH and particles, we begin by identifying the main chemical reactions in our mechanism responsible for the conversion of ethylene to A1 (benzene) in neat opposed flow flames. The approach we used takes advantage of the postprocessor utility available in CHEMKIN that allows calculation of the rates of production and destruction of each species in the mechanism by each reaction involving that species. Figure 3.1.6-2 shows the rate of production of A1 versus distance from the fuel duct for the top four contributing reactions in the

mechanism (out of 15 reactions in the mechanism involving A1). To assign a percent contribution to A1 formation to each reaction, the area under the curve (divided by the local gas velocity) for each reaction was integrated, and this area per reaction compared to the area for the total rate of production for A1 (not shown in Figure 3.1.6-2). According to this method, for A1 production in our neat ethylene/air opposed flow flame, the contribution of these four reactions is:

$C_3H_3 + C_3H_3 \rightarrow A1$	73%	(R4)
$n\text{-}C_4H_5 + C_2H_2 \rightarrow A1 + H$	12%	(R5)
$l\text{-}C_6H_6 + H \rightarrow A1 + H$	8%	(R6)
$n\text{-}C_6H_7 \rightarrow A1 + H$	6%	(R7)

It is worth noting that $l\text{-}C_6H_6$ and n-C6H7 are dependent upon reactions of $n\text{-}C_4H_5$ with acetylene. For radical species that are formed in one part(s) of the flame, and consumed in other parts of the flame, it is necessary to modify this approach by limiting the regions of integration.

This approach was used in the neat opposed flow ethylene/air flame to follow carbon as it passed from ethylene to A1. When the conversion from one species to another in the flame was near quantitative (such as the initial decomposition step of C_2H_4 to C_2H_3), tracing the reaction was straightforward. When the main path to A1 production was less than quantitative for destruction of a certain species (such as CH_2 conversion to C_3H_3), it was necessary to examine the contribution of all reactions to production and destruction rates for species participating in a given reaction. Using this method, the path to A1 from ethylene begins with the conversion of C_2H_4 to C_2H_3 (99%, via H and OH), followed by conversion of C_2H_3 to acetylene (C_2H_2) (90%). The formation of this acetylene "bath" is important to the chemistry of soot formation. However, as the initial ethylene/air mixture is fuel-rich, approximately 44% of the acetylene formed in this step remains unreacted. The mechanism contains 77 reactions in which acetylene is a participant. Approximately 34% of the acetylene is converted to methylene (CH_2) and singlet methylene (CH_2^*), of which approximately 4% is converted to propargyl (C_3H_3), of which approximately 6% is converted to A1. Although propargyl is the main source of A1 formation, only a small fraction of propargyl reacts directly to form A1.

Oxidizer Side Addition of Ethanol

In experiments and calculations, oxidizer side addition of ethanol vapor reduces soot and soot precursors. A graph of experimental measurements of peak light scatter and OH fluorescence and predictions of species maximum mole fraction based upon calculations, for oxidizer side addition of ethanol, is shown in Figure 3.1.6-3.

The error in the measured scattered laser intensity and OH fluorescence is estimated to be approximately 5%, based upon pixel to pixel noise in the individual images. Overall, the change with increasing ethanol addition of calculated peak mole fractions for the species C_2H_2, A1 and A4 is in reasonable agreement with peak experimental values (measured along the centerline between burner ducts) of light scatter, while the change with increasing ethanol addition of the calculated peak mole fraction of OH is in average agreement with peak measured values of OH fluorescence, with calculation and experiment predicting a small decrease in peak OH concentration with ethanol addition.

The slight increase in light scattering when ethanol vapor addition increases above 5% may be due to the transition from a diffusion flame to a partially premixed diffusion flame, and the onset of a secondary flame as the oxidizer mixture approaches premixed stoichiometry.
These results (decrease in soot, negligible change in peak OH concentration) at first seem contradictory. Soot reduction by addition of an oxygenated species is generally interpreted to be caused by an increase in local OH radical [Shaddix 1994] concentration, leading to increased soot oxidation:

$$C_xH_y\ (soot) + OH \rightarrow CO_2 + H_2O \qquad (R8)$$

However, examination of the individual experimental images (Figure 3.1.6-4) shows that as ethanol is added to the oxidizer (air) stream, the width of the OH region increases. We believe that the broadening of the OH region for this flame is the key to understanding the decrease in measured light scattering by particles. Figures 3.1.6-5 and 3.1.6-6 show calculated temperature and OH mole fraction as a function of distance from the fuel duct.

These figures show that the calculation predicts broadening of the OH and high temperature flame regions with increasing oxidizer side ethanol addition. Figure 3.1.6-7 shows the calculated rate of destruction of 4% ethanol vapor added to the oxidizer side of the opposed

flow flame, overlaid with the calculated temperature profile for this flame and for the neat flame. The region of ethanol destruction is shown to coincide in location with the onset of the broadened region of high temperature in the flame to which ethanol has been added. We believe this broadened region of high temperature is indicative of a secondary flame zone as the oxidizer gas gradually changes to a fuel/air gas mixture.

Qualitatively, addition of ethanol vapor to the air stream causes the flame to change from a diffusion flame towards a partially premixed diffusion flame. The broadening of the OH region and of the temperature profile moves the flame region (i.e., region of appreciable flame radical concentration and high temperature) closer to the stagnation plane, and therefore closer to the region of maximum soot concentration, thereby increasing the rate of soot oxidation (see Figures 3.1.6-5 and 3.1.6-6). Introduction of ethanol to the air stream moves the flame from a soot formation (SF) type towards a soot formation/oxidation (SFO) type, in which soot particles must travel a shorter distance into the oxidation region [Hwang 2001]. As more ethanol vapor is added to the air stream, the flame begins transition to a multiple flame structure due to partial premixing as has been studied with other fuel-rich oxidizer premixed flames [Lockett 1999].

Fuel Side Addition

In experiments and calculations, fuel side addition of ethanol increases soot and soot precursors, while peak OH concentrations remain approximately constant. A graph of experimental measurements of peak light scatter and OH fluorescence and predictions of species maximum mole fraction based upon calculations, for fuel side addition of ethanol, is shown in Figure 3.1.6-8. The calculated data have been normalized to the experimental data to allow comparisons of the trends shown by each. As in Figure 3.1.6-3, the error in the measured scattered laser intensity and OH fluorescence is estimated to be approximately 5%, based upon pixel to pixel noise in the individual images. Overall, the trend of the change (increasing), with increasing fuel side ethanol addition, of calculated peak mole fractions for the species A1 through A4 is in good agreement with peak experimental values (measured along the centerline between burner ducts) of light scatter. However, the change, with increasing fuel side ethanol addition, of the calculated peak mole fraction of OH is in reasonable agreement with peak measured values of OH fluorescence. Calculation and experimental measurement show peak OH concentration to remain nearly constant with increasing ethanol addition. For these flames, the calculation was able to reach convergence for all mole fractions of ethanol using an initial

grid of 60 points. Individual experimental images do not show apparent differences so are not reproduced here.

Calculations predict that addition of 8 mole percent ethanol to the fuel stream increases the integrated mole fraction of aromatic species A1 (C_6H_6), A2 ($C_{10}H_8$), A3 ($C_{14}H_{10}$), and A4 ($C_{16}H_{10}$) by approximately 3%, 19%, 23%, and 22%, respectively (see Figures 3.1.6-9 – 3.1.6-12). The peak increase in light scatter observed experimentally was approximately 19%. Temperature and OH concentration are predicted by calculation to remain approximately constant (see Figure 3.1.6-13). Acetylene is predicted to remain approximately constant while propargyl concentration is predicted to decrease approximately 9% when 8% ethanol is added to the fuel stream (Figure 3.1.6-14). In what follows, the production of soot precursors is divided into a discussion of A1 formation followed by a discussion of A2-A4 formation.

A1 Formation

Because the calculated change in propargyl mole fraction with ethanol addition was in the opposite direction of the change in A1 mole fraction for fuel side ethanol addition, a calculation of rate of formation of A1 by reaction was performed. The reactions contributing to A1 formation, and the change in A1 rate of formation per reaction, relative to the neat flame, when 8% ethanol was added to the fuel stream, are as follows:

Reaction	**Calculated Change in Rate of A1 Formation - 8% EtOH addition to Fuel (relative to neat flame)**	
$C_3H_3 + C_3H_3 \rightarrow A1$	-8%	(R4)
$n\text{-}C_4H_5 + C_2H_2 \rightarrow A1 + H$	+23%	(R5)
$l\text{-}C_6H_6 + H \rightarrow A1 + H$	+27%	(R6)
$n\text{-}C_6H_7 \rightarrow A1 + H$	+34%	(R7)

The calculation predicts that all of the increase in A1 produced by fuel side ethanol addition is caused by reactions other than propargyl recombination. The reactions of phenyl (A1·) influencing A1 formation

$$A1\cdot + H\,(+M) \rightarrow A1\,(+M) \qquad (R10)$$

$$A1 + OH \rightarrow A1\cdot + H_2O \qquad (R11)$$

are included in the mechanism but are not considered important here for A1 formation because the change in rate of each was less than 1% with fuel side ethanol addition.

To understand why propargyl is decreased, and why R5-R7 are enhanced, it is necessary to track the path of oxygen and carbon added, via ethanol, to the fuel gas. The initial decomposition reactions for ethanol when added on the fuel side of the flame differ from those for air side ethanol addition. For fuel side addition, in the absence of oxygen, ethanol decomposition occurs via a pyrolysis mechanism at approximately 1500K:

$$C_2H_5OH\,(+M) \rightarrow C_2H_4 + H_2O\,(+M) \qquad 58\% \qquad (R12)$$

$$C_2H_5OH\,(+M) \rightarrow CH_3 + CH_2OH\,(+M) \qquad 30\% \qquad (R13)$$

$$C_2H_5OH\,(+M) \rightarrow C_2H_5 + OH\,(+M) \qquad 8\% \qquad (R14)$$

The ethylene, water, ethyl radical, and OH radical formed from the initial decomposition have little additional effect on the chemistry as they are very slight perturbations on the concentrations of these species relative to the neat flame or are similar to fuel or initial fuel decomposition products. The bulk of the reactive oxygen (as CH_2OH) is stepwise converted to HCO, which then reacts with propargyl to yield CO and C_3H_4, which is then near-quantitatively reconverted to propargyl. The increase in other soot precursors [Richter 2000] predicted by the calculation may be ascribed to introduction of methyl radical (R13) into a relatively low temperature hydrocarbon/acetylene bath [Hwang 2001].

The methyl radicals formed in cooler regions of the flame (1400 K-1700 K) via ethanol pyrolysis react with propargyl (C_3H_3) to form C_4H_6 :

$$C_3H_3 + CH_3\,(+M) \rightarrow C_4H_6\,(+M) \qquad (R15)$$

This reaction shows a calculated increase in rate of production of C_4H_6 of 17% for the flame with 8% mole fraction ethanol compared to the neat ethylene/air flame. Mole fraction profiles (see Figure 3.1.6-13) of propargyl show a slight decrease in concentration over this temperature range (1400 K-1700 K). Approximately 85% of the C_4H_6 reacts with H to form C_4H_5, which then reacts in the acetylene bath to form A1 and aromatic precursors.

$C_4H_6 + H \rightarrow C_4H_5 + H_2$ (R16)

$C_4H_5 + C_2H_2 \rightarrow A1 + H$ (R17)

$C_4H_5 + C_2H_2 \rightarrow n\text{-}C_6H_7$ (R18)

Overall, the calculation predicts that the addition of ethanol to the fuel stream has a negative effect on integrated C_3H_3 concentration while enhancing alternate pathways, via C_4H_6 production, to formation of initial aromatic ring species (see Figure 3.1.6-14). This result was not anticipated prior to the experimental studies. However, it should be noted that other researchers [Alexiou 1996] have measured soot increases during combustion of ethanol/hydrocarbon mixtures, relative to neat ethylene combustion. Increases in soot precursor production have also been reported for methane addition to heptane/air flames [Roesler 2003].

A2-A4 Formation

For fuel side ethanol addition, the calculation predicts an increase in integrated mole fraction of benzene of 3% when 8% ethanol is added, relative to the neat flame. For the same comparison, the predicted increase in A2 (naphthalene), A3 (phenanthrene), and A4 (pyrene) is 19%, 23%, and 22%, respectively. However, the absolute change in mole fraction of A1 with 8% fuel side ethanol addition is greater than 10 times the absolute change in A2 addition. The change in mole fraction in going from the neat flame to the flame with 8% ethanol added to the fuel side for A1, A2, A3, and A4 is 5 $X10^{-7}$, 4.2 X 10^{-8}, 1.6 X 10^{-9}, and 4.8 X 10-^{10}, respectively. In contrast to the reaction path to A1 formation discussed above, the formation of A2-A4 follows the H-abstraction – C2H2-addition mechanism [Wang 1997]. For A1 conversion to A2, an example of one of the pathways may be summarized as follows:

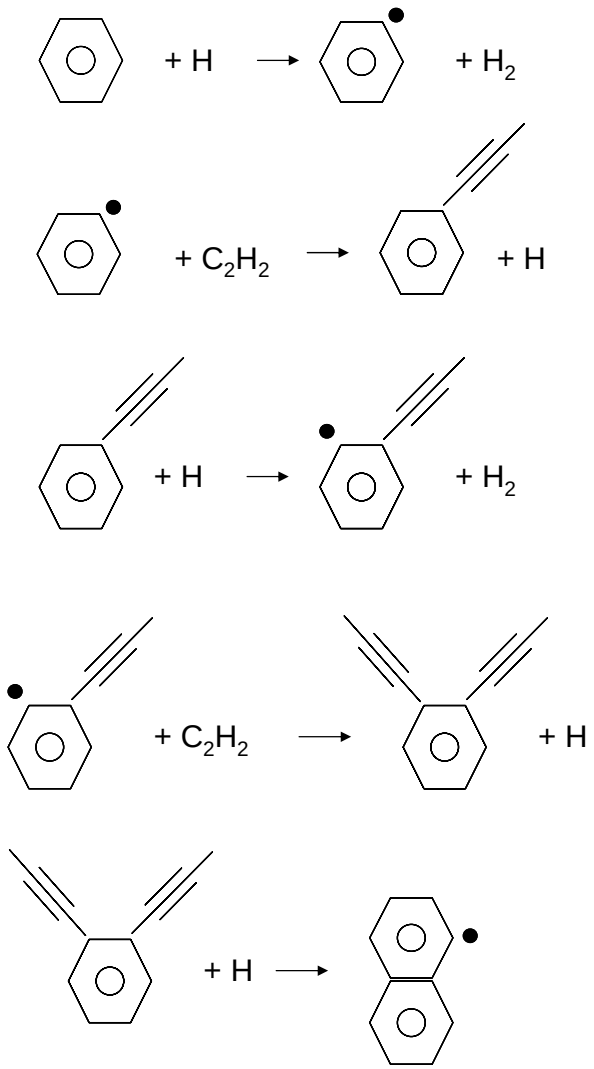

This study provides an example of how soot formation in opposed flow ethylene/air diffusion flames is dependent upon temperature, flame radical and bath gas compositions. Differing chemical behavior in opposed flow flames depending on fuel or air side addition of ethanol vapor has been observed experimentally and modeled, and shown to occur via different pathways within the context of a detailed chemical mechanism. In particular, ethanol introduced into the air side of the flame creates a premixed combustion (secondary flame zone) region prior to the main diffusion flame region. Hot gas products from this premixed flame region, including

OH, are convected into the diffusion flame zone, increasing peak temperature and broadening the OH concentration profile. The broadened OH concentration profile moves the oxidizing region of the flame closer to the stagnation plane and to the high soot concentration region of the flame. The increased temperature and integrated OH mole fraction cause an increase in soot and soot-precursor oxidation, leading to lower overall soot concentrations in ethylene/air diffusion flames with ethanol added to the air stream. It should be noted that the effect of radiation from soot in the experiment was not accounted for in the "particle-free" computational model. When ethanol is introduced into the fuel stream of the ethanol/air opposed flow diffusion flame, initial decomposition of ethanol occurs via pyrolysis reactions because of the lack of oxygen in the fuel stream. Methyl radical produced during the initial steps of decomposition of ethanol reacts with propargyl to produce C_4H_6, which leads to increased production of A1.

In summary, we believe addition of ethanol to the air side of the ethylene/air diffusion flame decreases soot concentration mainly through a thermal mechanism. This is supported by observation of the flame and the calculated increase in temperature (33K) and increase in OH concentration (142%) relative to the neat flame. Addition of ethanol to the fuel side of the ethylene/air diffusion flame increases soot mainly through a chemical mechanism involving introduction of methyl radical into an ethylene/acetylene bath. This is supported by observation of the flame and the calculated constant temperature and OH concentrations over the studied range of ethanol addition.

Heptane/Air and Heptane/Toluene/Air Opposed Flow Flames

Figure 3.1.6-15 shows an image of the heptane/air diffusion flame and PLIF/light scattering images on and off resonance with the OH absorption near 308 nm. We estimate the oxidizer strain rate for the heptane/air and heptane/toluene/air flames reported here to be approximately 38 sec^{-1}. The pressure generated by the vaporization of the liquid fuel in a confined environment was used to provide flow velocity into the burner ducts. PLIF/light scattering experiments for this flame were limited to fuel side addition of ethanol vapor. Figure 3.1.6-16 shows a graph of experimental results for light scattering by particles versus ethanol addition. Although the effect is minor, for this flame system addition of ethanol to the fuel side showed greater particle reduction compared to the increase observed for fuel side addition of

ethanol to ethylene/air opposed flow flames. For the heptane/air flames, we were unable to get the LLNL heptane mechanism to converge using the CHEMKIN OPPDIF code.

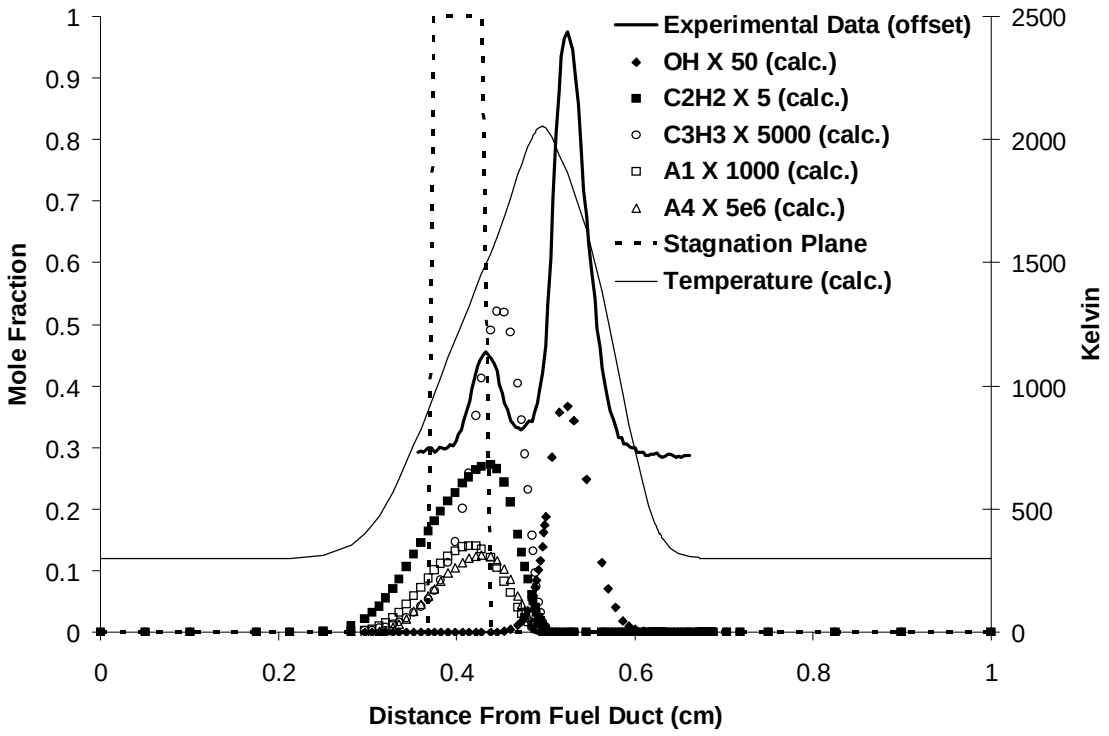

Figure 3.1.6-1. Results of Calculations Showing Temperature Profile and Separation of Soot Forming and Flame Radical Regions for an Undoped Ethylene/Air Opposed Flow Flame, with Overlay of Measured Centerline Pixel Intensities for Similar Flame. Also shown is calculated position of stagnation plane.

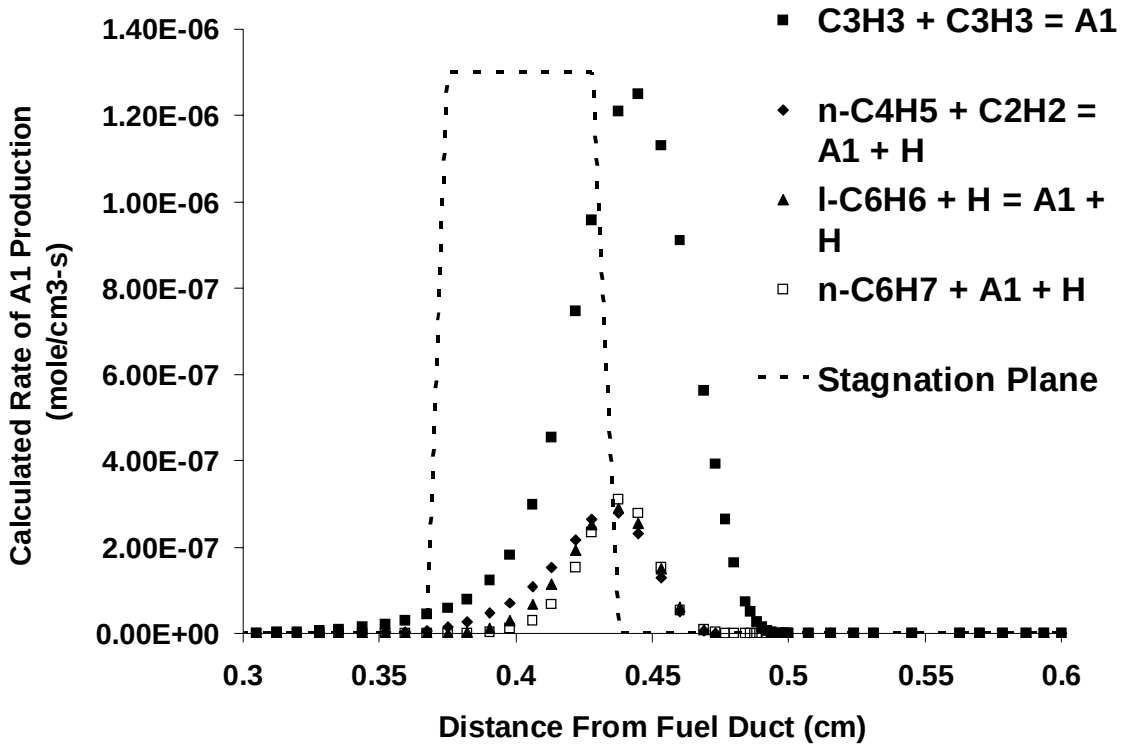

Figure 3.1.6-2**.** Calculated Rates of Production of A1 vs Distance from the Fuel Duct for the Top Four Contributing Reactions in the Mechanism (out of 15 reactions in the mechanism involving A1). Calculation is for the neat ethylene/air opposed flow diffusion flame. Also shown is calculated position of stagnation plane.

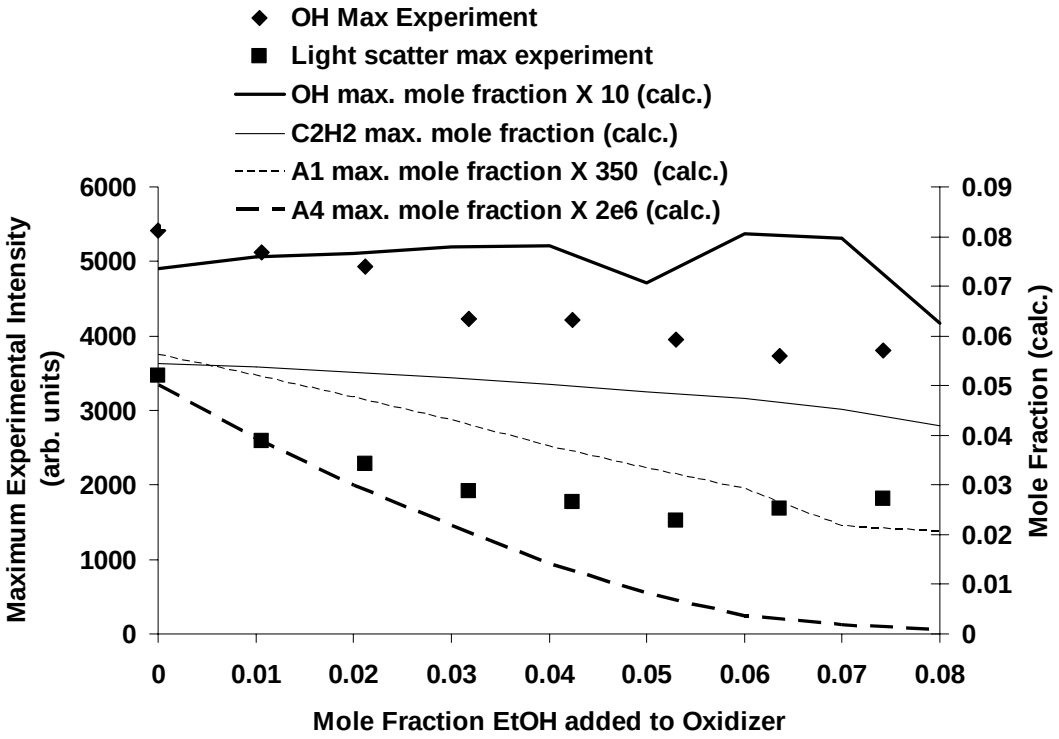

Figure 3.1.6-3. Graph of Experimental Measurements and Predictions Based Upon Calculations for OH, Soot and Soot Precursors, for Air Side Addition of Ethanol.

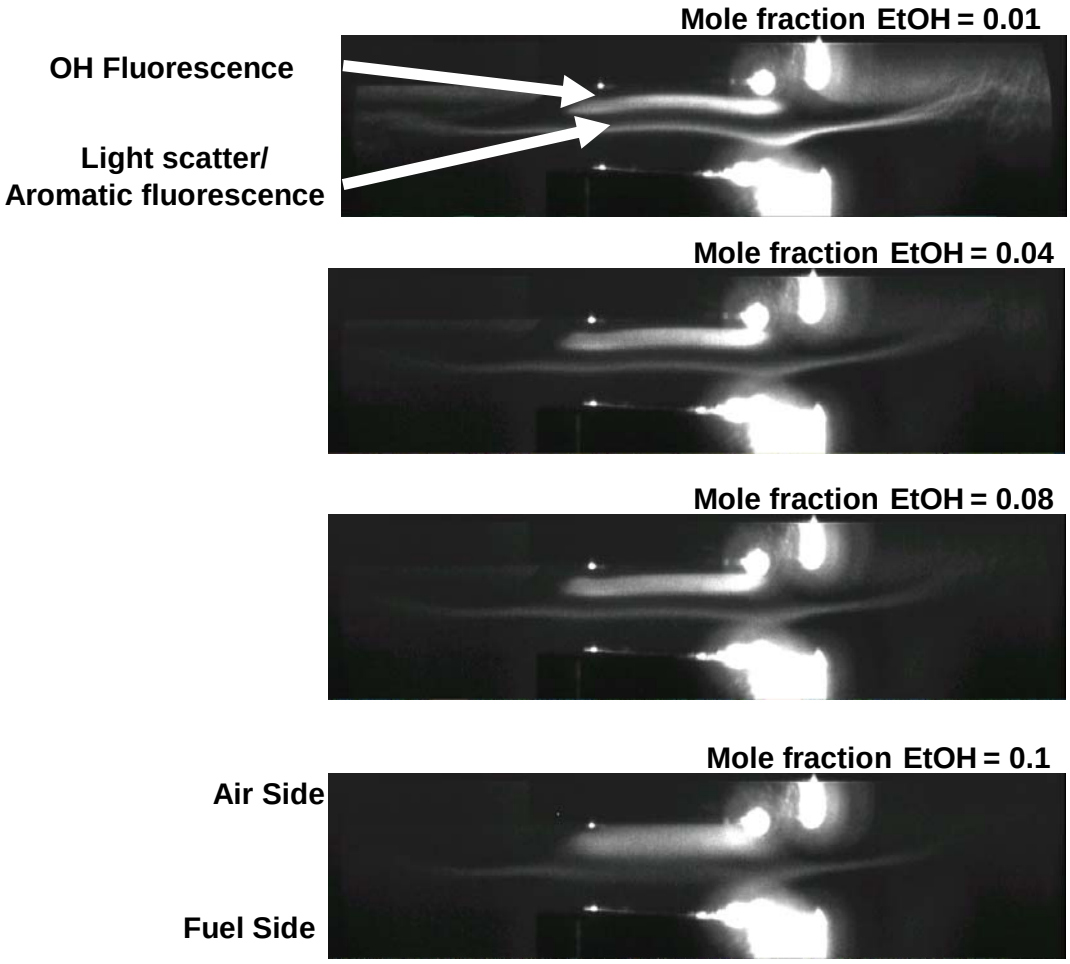

Figure 3.1.6-4. Images of OH PLIF and Light Scattering by Soot Particles as Increasing Amounts of Ethanol Vapor are Added to the Air Side. Note increasing width of OH region (upper feature) and decreasing intensity of light scatter from particles (lower feature).

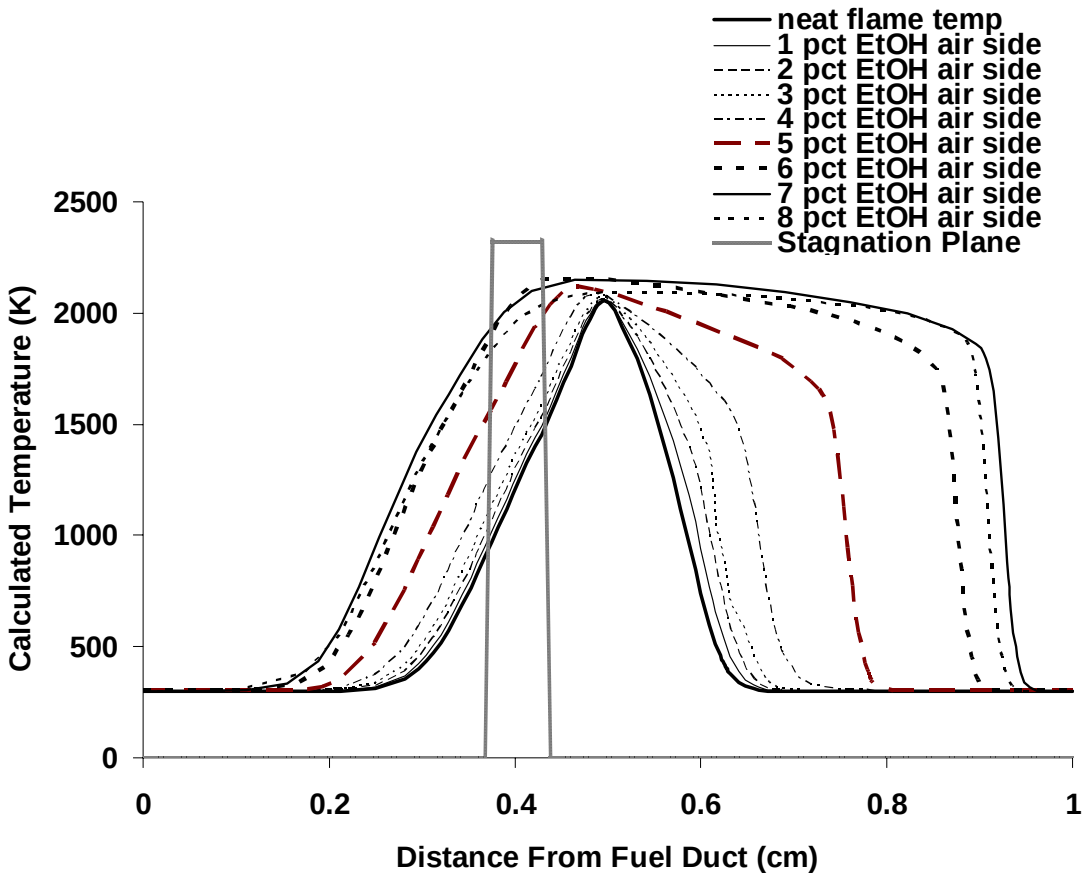

Figure 3.1.6-5. Calculated Temperature Profiles for Air Side Addition of Ethanol. Also shown is calculated position of stagnation plane.

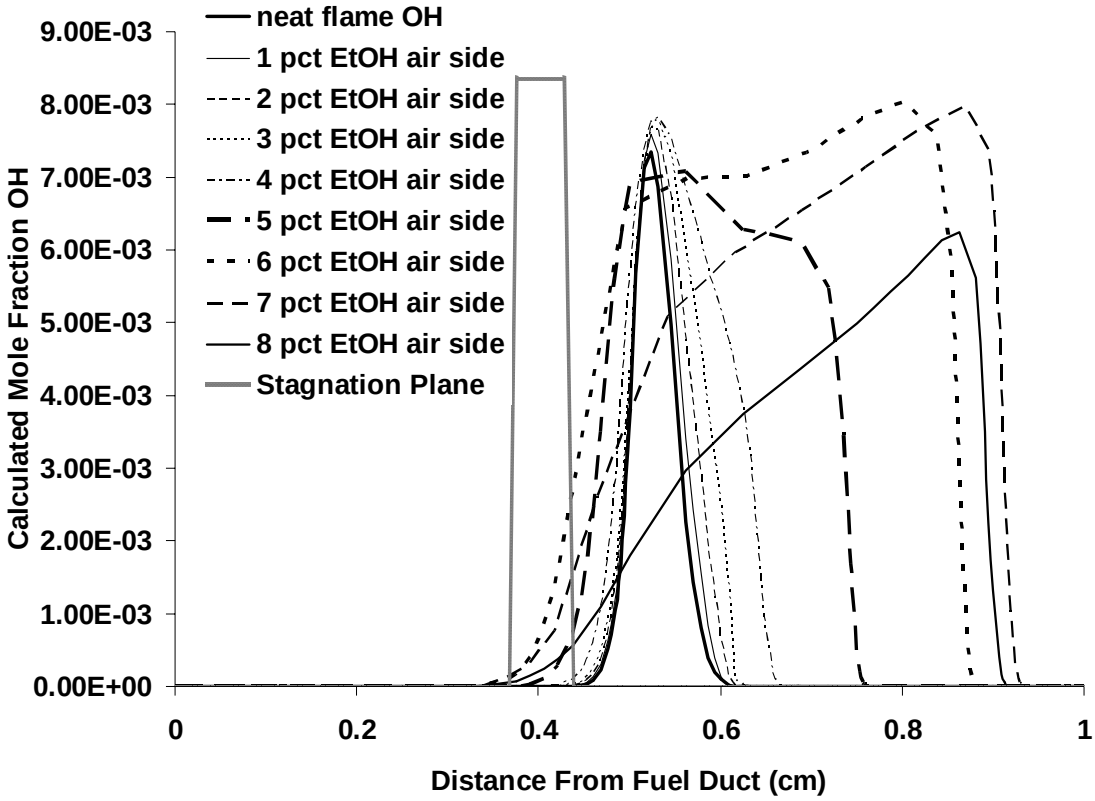

Figure 3.1.6-6. Calculated OH Profiles for Air Side Addition of Ethanol. Also shown is estimated position of stagnation plane.

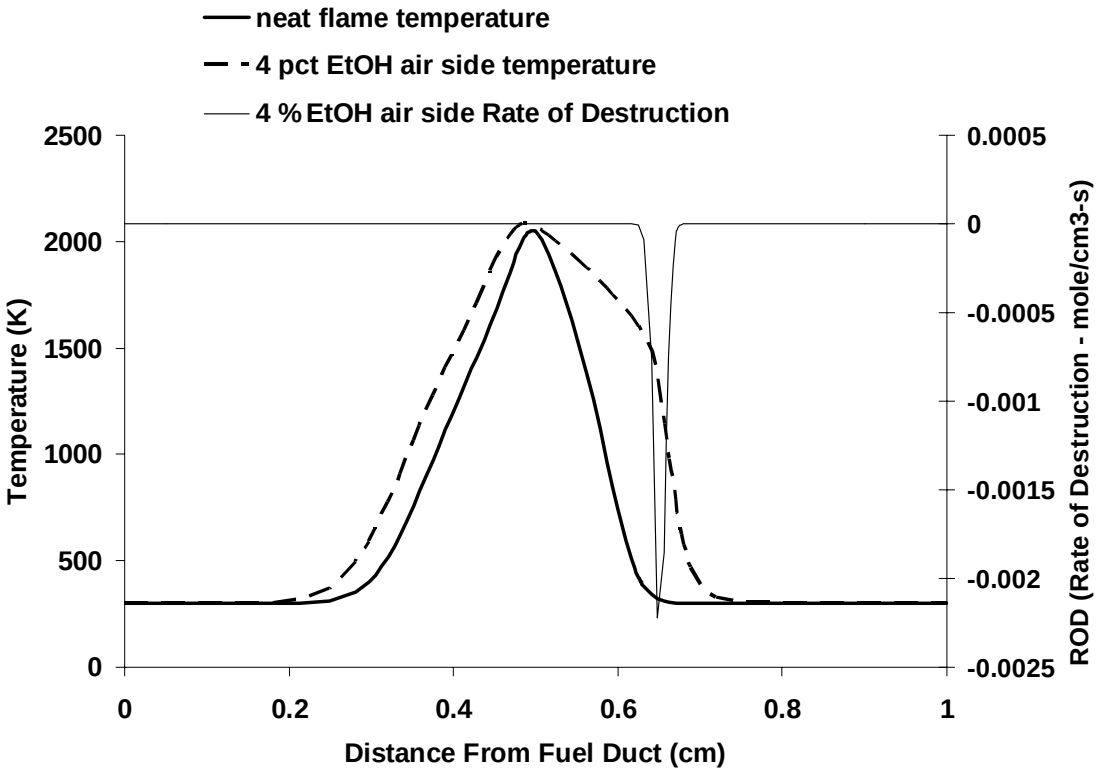

Figure 3.1.6-7**.** Calculated Temperature Profile for Air Side Addition of Ethanol, Overlaid with Overall Rate of Destruction of Ethanol Vapor (4% mole fraction fuel side). Note the coincidence of ethanol vapor combustion with edge of broadened temperature profile.

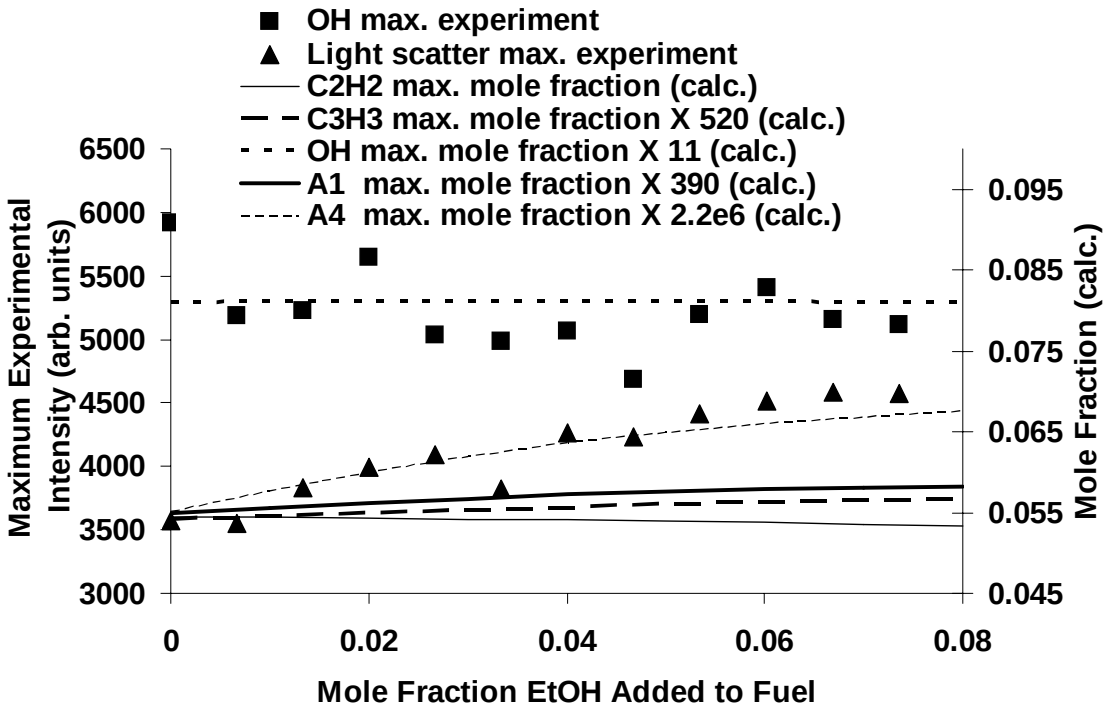

Figure 3.1.6-8**.** Graph of Experimental Measurements and Predictions Based Upon Calculations for OH, Soot and Soot Precursors, for Fuel Side Addition of Ethanol.

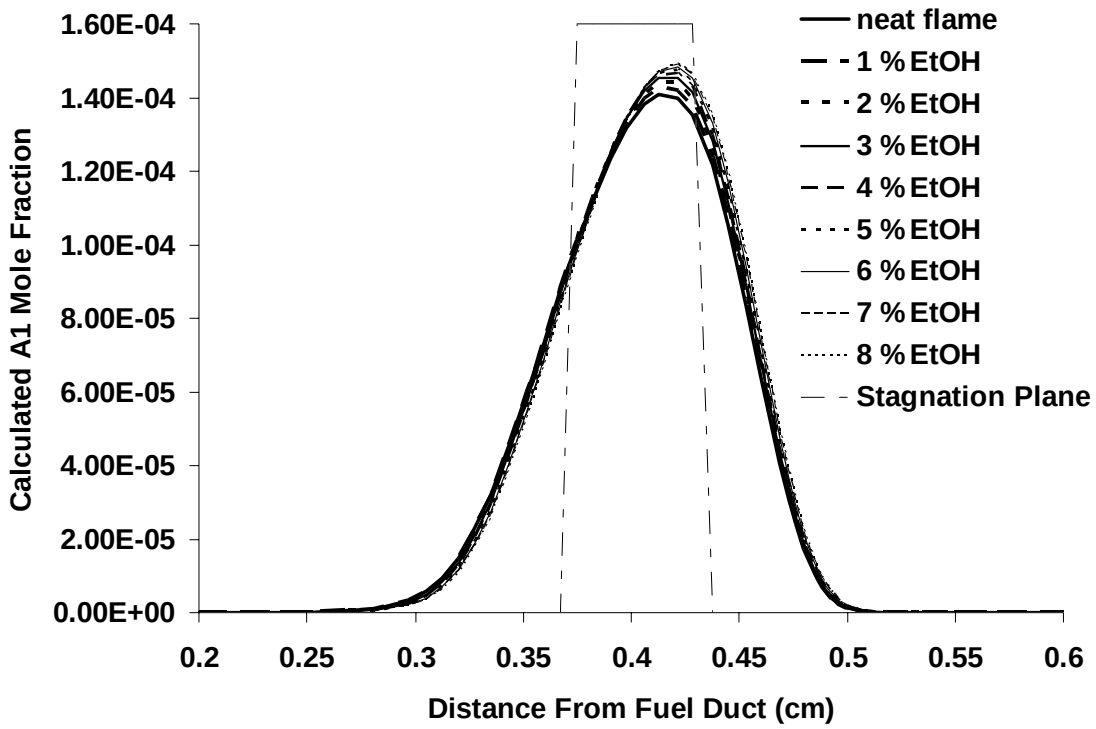

Figure 3.1.6-9. Calculated A1 Mole Fraction Profile for Increasing Amounts of Ethanol Vapor Added to the Fuel Stream.

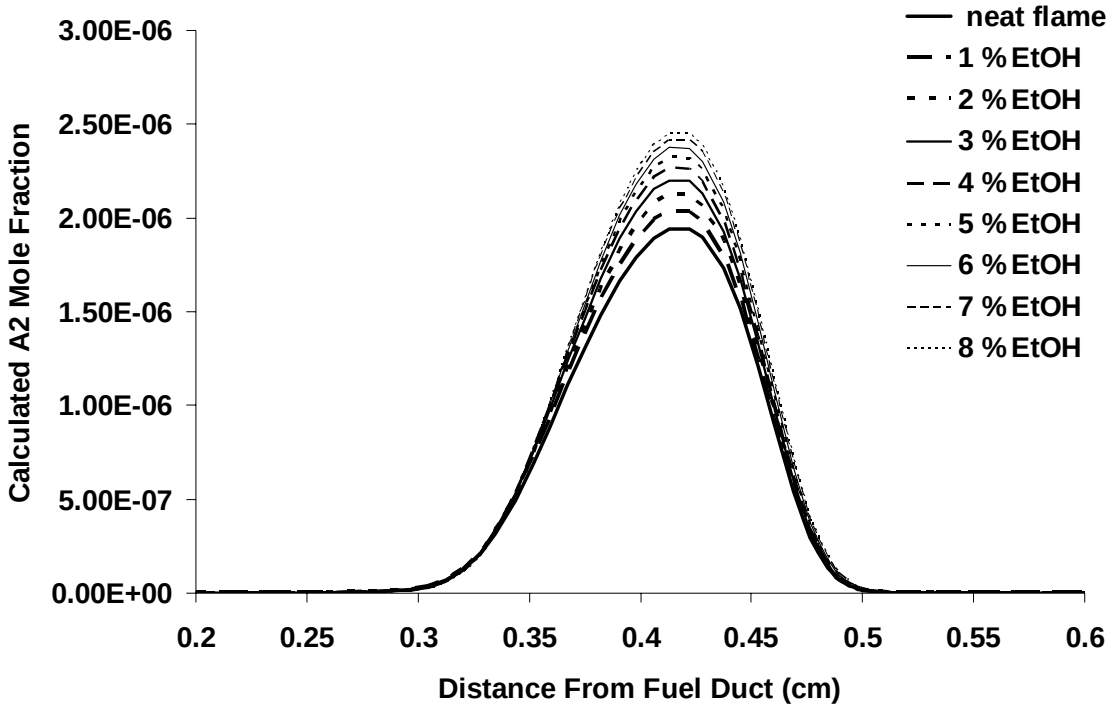

Figure 3.1.6-10. Calculated A2 Mole Fraction Profile for Increasing Amounts of Ethanol Vapor Added to the Fuel Stream.

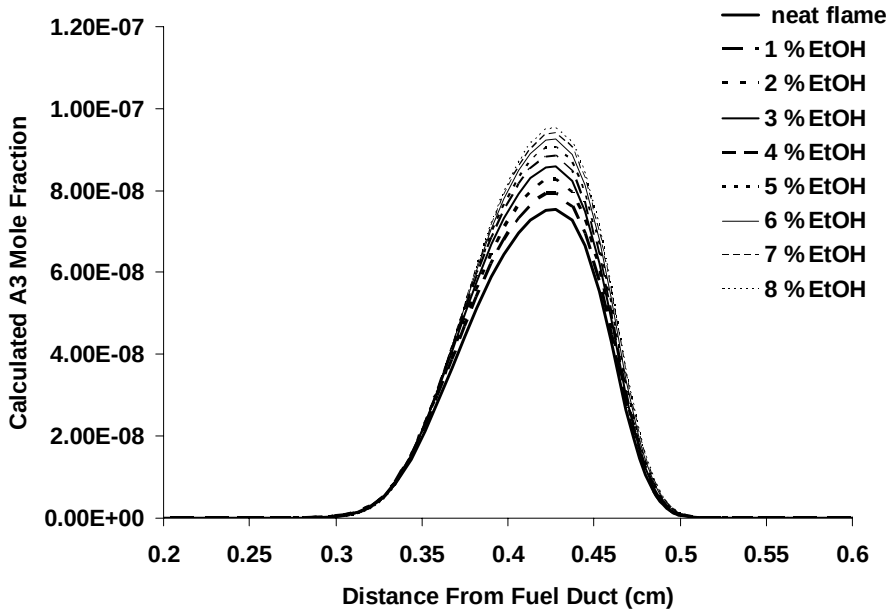

Figure 3.1.6-11. Calculated A3 Mole Fraction Profile for Increasing Amounts of Ethanol Vapor Added to the Fuel Stream.

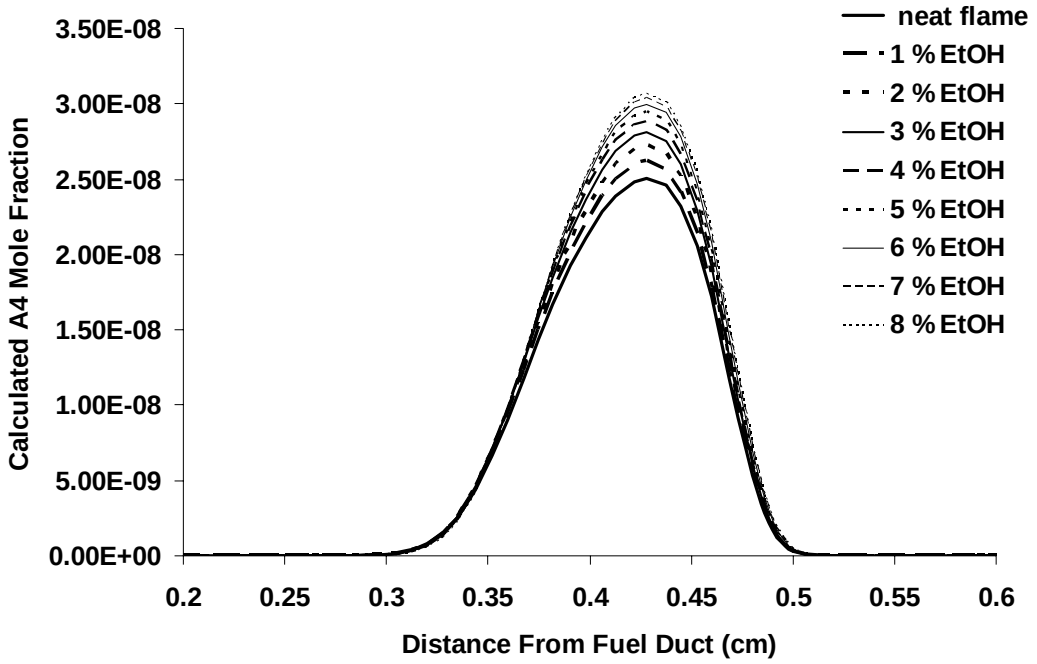

Figure 3.1-6-12. Calculated A4 Mole Fraction Profile for Increasing Amounts of Ethanol Vapor Added to the Fuel Stream.

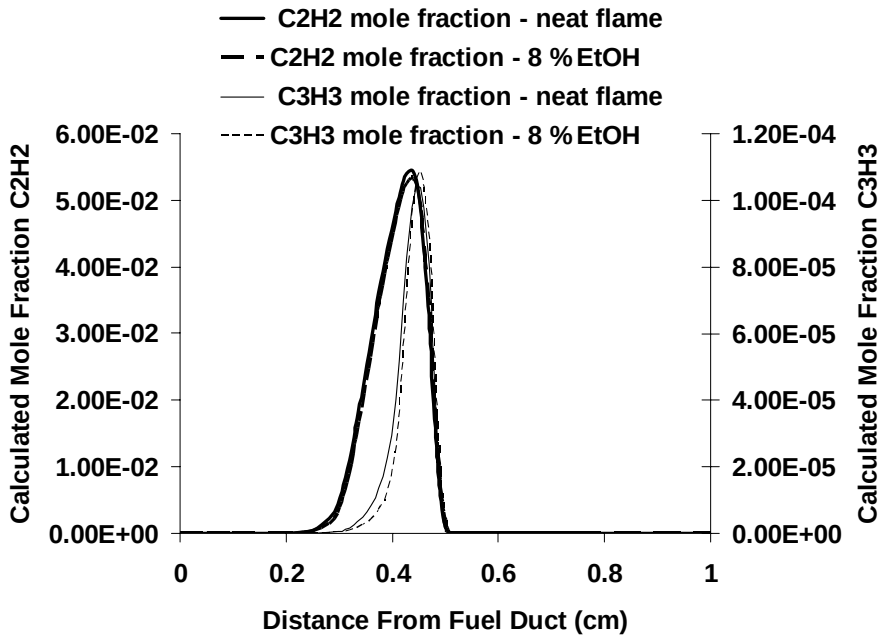

Figure 3.1.6-13. Calculated Acetylene (C_2H_2) and Propargyl (C_3H_3) Profiles for Neat Flames and for Flames with 8% Ethanol Vapor Added to the Fuel Stream. Intermediate values of ethanol addition yield C_2H_2 and C_3H_3 profiles between those for the extreme values. Note that the calculation predicts negligible change in C_2H_2 and C_3H_3 for fuel side addition of ethanol.

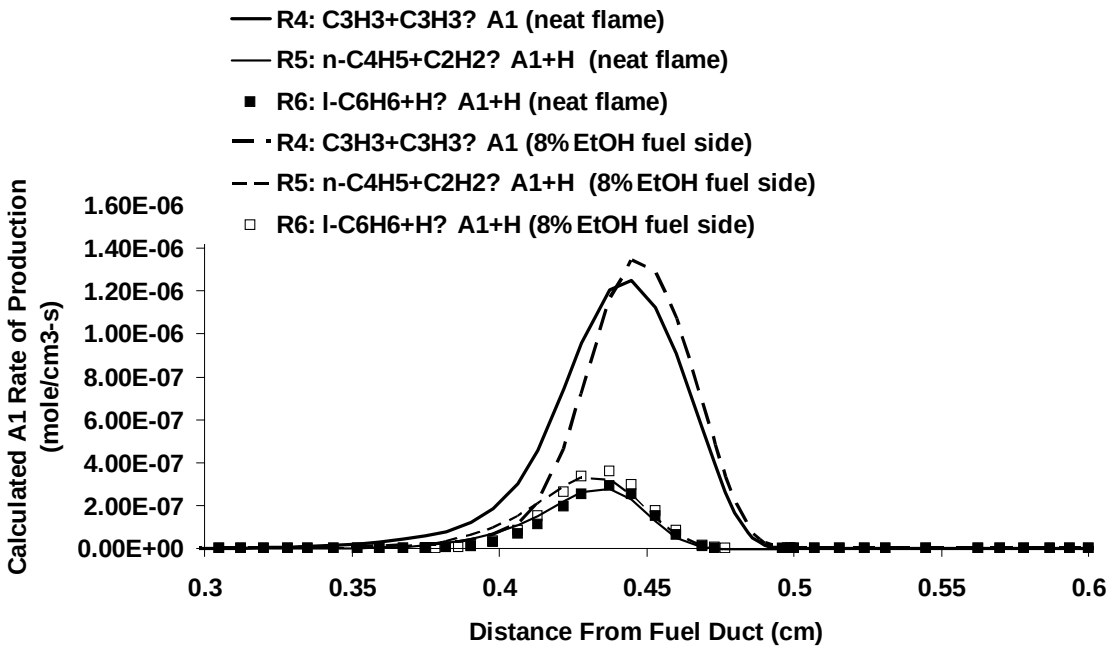

Figure 3.1.6-14**.** Rates of Production of A1 by the Three Most Important Reactions Contributing to A1 Production. Note the overall enhancement of rates of reactions that do not involve propargyl. The net rate of A1 production by propargyl combination is only slightly affected by the ethanol addition.

Burner Status

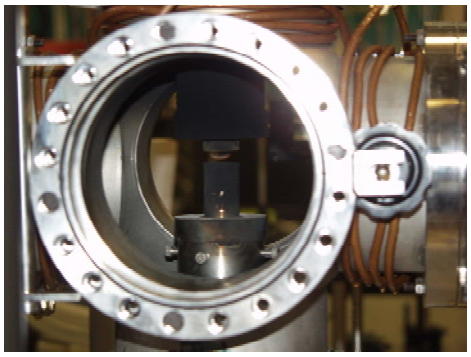

C_7H_{16}/air opposed flow flame (vaporized fuel from bottom, air from top), with 1% (vol.) EtOH addition to fuel.

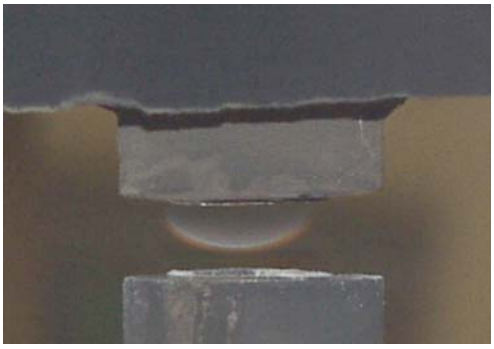

Detail of photograph at left. Note dual layer luminous region.

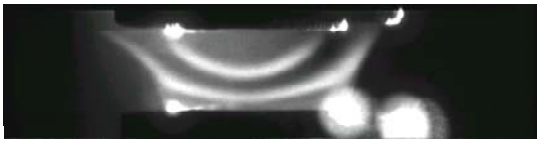

Planar laser induced fluorescence/light scattering excited At 309.587 nm. Upper feature is OH fluorescence, lower feature is scattering by particles. Of flame in photo.

Laser scattering at 309.5 nm. Note absence of OH fluorescence. Of flame in photo.

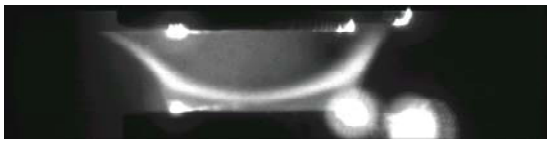

Figure 3.1.6-15. Normal and PLIF Images of the Heptane/Air Diffusion Flame.

Particle reduction at 5% EtOH fuel side addition to heptane is approximately 9%

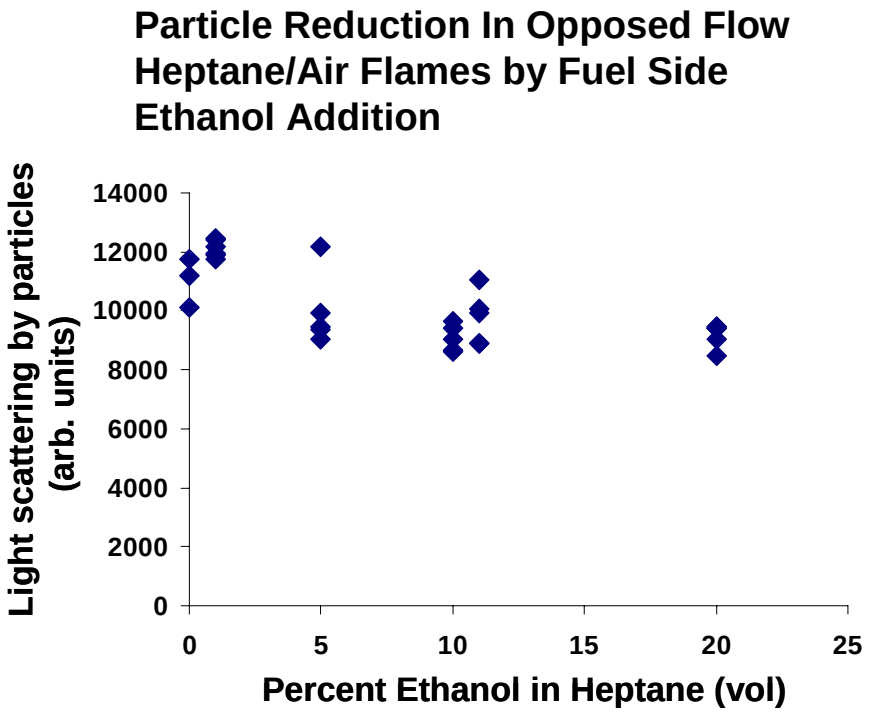

Figure 3.1.6-16. Light Scattering by Particles vs Fuel Side Ethanol Addition for Heptane/Air Opposed Flow Flames.

3.1.7 TURBULENT SPRAY FLAME

Heptane (99%) was the fuel for the initial studies in the turbulent spray flame. Several equivalence ratios were tested initially with ethanol as the additive, but most of them led to weak LII signals. After increasing the equivalence ratio to 2.76, relatively strong signals and good repeatability were achieved. The experimental conditions of the study are listed in Table 3.1.7-1. The amount of ethanol was set so that it introduced 5% oxygen by weight into the fuel (with fuel defined as heptane and ethanol) while keeping the total carbon flow and the equivalence ratio constant.

In the swirler-stabilized flame, Reynolds Number, along with the swirl number, is also a key factor for the onset of the vortex breakdown phenomenon [Syred and Beer 1974]. The

significant dimensions of the flame will be determined primarily by the airflow pattern for the pressure jet flames. Therefore, the Reynolds Number for the airflow is an important indicator of the onset of turbulence in the flame. This study used the Reynolds Number based on the cold air at the outlet of the swirler. The values of the Reynolds Number and the parameters, which determined the Reynolds Number, are listed in Table 3.1.7-2. Although the value is not in the highly turbulent range, the flame in this study is no doubt in the turbulent regime. Observations of the flame itself verified that it was indeed turbulent.

Examples of averaged and single shot LII images from this study are shown in Figure 3.1.7-1 and Figure 3.1.7-2, respectively. The regions of highest average LII signals are located towards the sides of the image, which is consistent with the flow field created by the swirler and hollow-cone spray formed by the nozzle. The asymmetry of the soot field is due somewhat to the fact that the beam is attenuated by the soot field, but there also appears to be some asymmetry inherent to the nozzle itself. The single shot image displays the intermittent eddy like soot structure whose location, shape, and volume fraction change with time in the turbulent flow.

Due to the low signal-to-noise ratio of LII in this experiment, it was important to remove the background noise before analyzing data. The first noise source, and the simplest form of noise to correct, is the background flame luminosity. It can be directly subtracted from data collected in a manner identical to that used for collecting the LII signal but with the laser beam blocked prior to entering the flame. Four hundred (400) accumulated images of the flame without laser illumination present were averaged to obtain the background signal. With the laser beam passing through the flame, the averages were taken over a series of 800 laser shots for pure heptane as the base fuel. A comparison of LII images before and after the background correction is shown in Figure 3.1.7-3 .

It was found that the portions of the two images that overlapped would often have different average intensity, even though nothing was changed but the camera position. The main reason is that individual pixels of the ICCD camera have variable responses to a given light intensity, as demonstrated by Quay [1998] using a similar camera. For quantitative LII measurements, it is desirable to be able to correct variation in pixel response. There are three options available for making the correction. The first is to take the average for the overlapped area, leaving the other part of images unchanged. The second method is to set one image as the base, and add or subtract the average intensity difference of the two overlapping regions from the

other images. The third method is similar to the second one except for using a ratio of the average intensity of the two overlapping regions to adjust for the different intensity. It was found, after testing, the third method had the best result when the image taken at the lower camera position was used as the base for correction.

ICCD camera has a field of view that is substantially smaller than the spray flame. Because the view field of ICCD camera cannot cover the entire spray and flame region, two overlapped images were collected at two heights, giving measured signals from the tip of the nozzle to a height of 6.3 inches above the nozzle, as shown in Figure 3.1.7-4.

The effects of ethanol on soot formation in the heptane spray flame were determined based on averages of 800 images for the two fields of view shown in Figure 3.1.7-4. Corrections were made for background luminosity and pixel-to-pixel variation as discussed above. The results were used to plot average intensity across the image as a function of height above the nozzle. The result is presented in Figure 3.1.7-5. The data in the figure have been filtered so show the overall trends more clearly. Overall, the addition of ethanol to heptane reduced soot in the order of 30%, similar to the results obtained for the addition of ethanol to ethylene in the premixed flame.

Table 3.1.7-1. Experimental Conditions for Heptane/Ethanol Study in Turbulent Spray Burner.

Base Fuel Formulation	Heptane
Additive	Ethanol
Base Fuel Supply (g/s)	0.32
Fuel with additive Supply (g/s)	0.34
Air Supply (g/s)	1.76
Equivalence Ratio	2.76

Table 3.1.7-2. Cold Flow Reynolds for Airflow.

Effective diameter	m	0.0176
Average exit velocity	m/s	6.13
Kinematic viscosity	MI/S	1.57e-5
Reynolds Number		6872

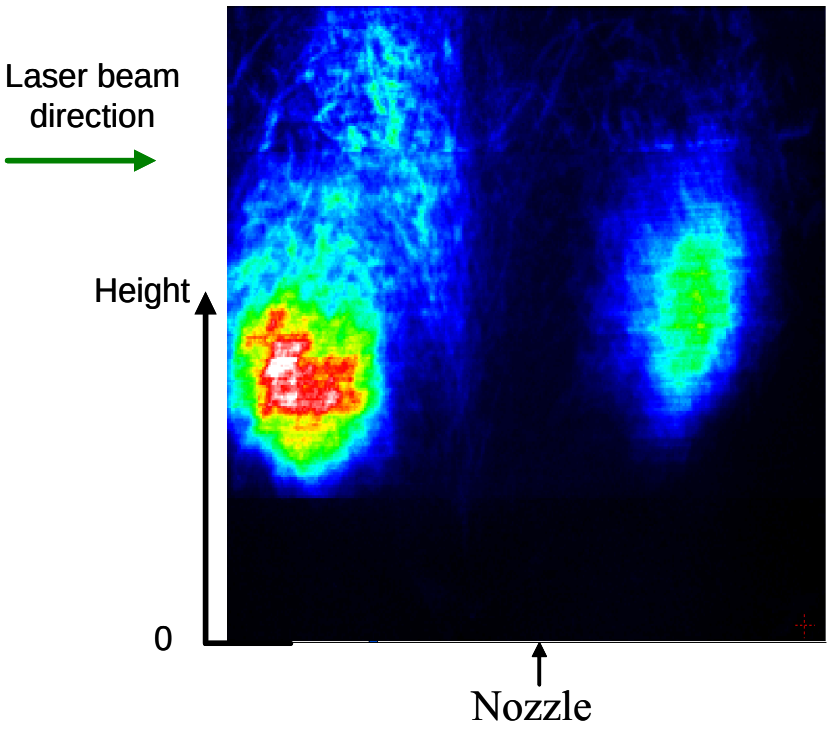

Figure 3.1.7-1. Sample Averaged LII Image from Heptane Spray Flame.

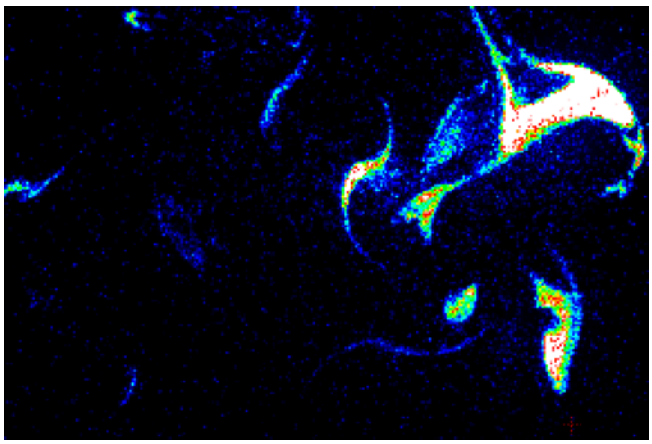

Figure 3.1.7-2. Sample Single Shot LII Image from Heptane Spray Flame.

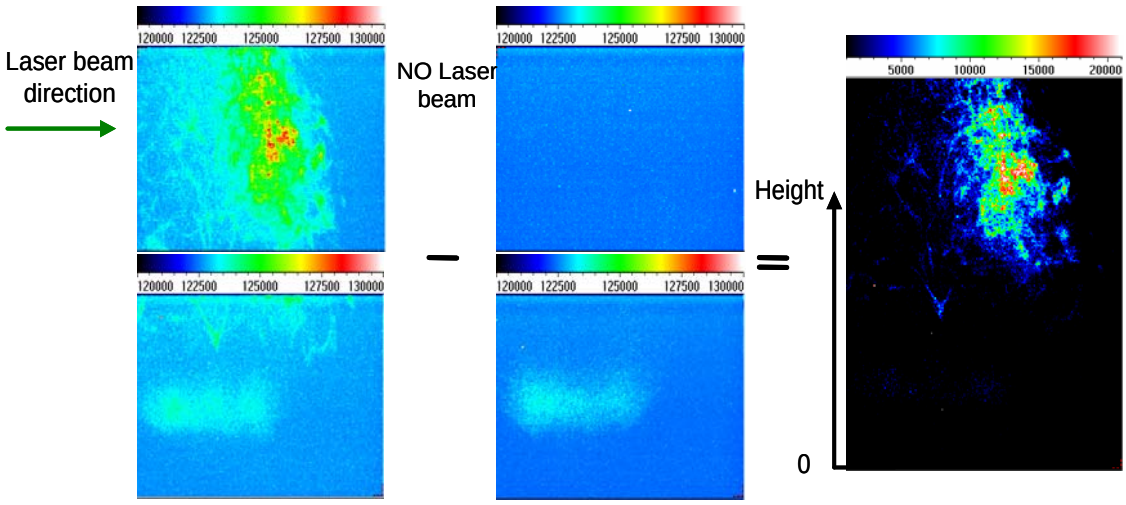

Figure 3.1.7-3. Comparison of LII images Before and After Background Correction.

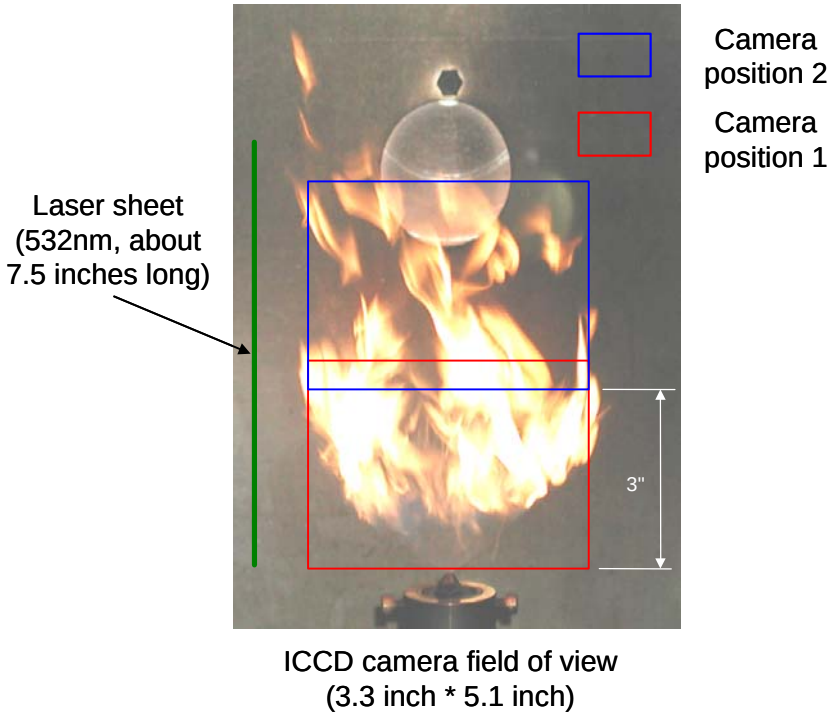

Figure 3.1.7-4. Overlapping of Fields of View Required to Cover Full Extent of the Flame.

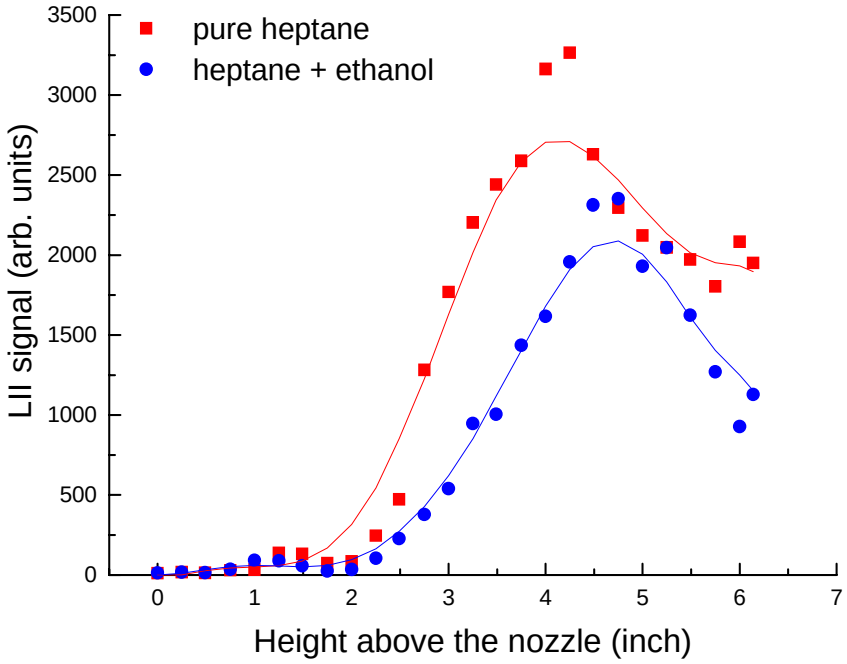

Figure 3.1.7-5. Effects of Ethanol Addition on Soot.

3.1.8 HIGH PRESSURE TURBULENT REACTOR

All tests with oxygenated additives in the high pressure turbulent combustor were run with JP-8 as the fuel, a major consideration being its reasonable cost compared to the heptane/toluene blend. The airflow for the tests was 32 gm/s and the equivalence ratio was 1.3. The inlet air temperature was 550 K and the chamber pressure was 0.5 MPa. Three oxygenated additives were investigated: ethanol, cyclohexanone, and methanol. The cyclohexanone was an oxygenate contained in a commercial additive that was also studied in the program. This additive also contained nitroalkanes for which the results appear in the next section. Methanol was studied as a comparison to the ethanol since it had shown good potential to reduce soot in prior work with sooting diffusion flames.

For cyclohexanone and ethanol, a range of concentration was investigated up to 10% by volume. Methanol was only studied at the highest concentration. Figure 3.1.8-1 presents a summary of the test results on soot volume fraction versus additive concentration. Ethanol was added to the fuel at concentrations ranging from approximately 2.5% to 10% by volume of the

JP-8. The extent of decrease in soot formation was found to increase with increase in additive concentration. The effect on soot formation ranged from about a 10% decrease at a concentration of 2.5% by volume to approximately 40% reduction in soot with an additive concentration of 10% by volume. The dump combustor adds spray processes, turbulence and elevated pressure to the phenomena that can affect the soot formation process beyond pure kinetics and molecular diffusion that are the key processes for the simpler devices used in this study. The fact that the magnitude of reduction is similar among all of these experiments suggests that the same processes are affecting the soot reduction, namely, chemical kinetic processes.

Although trends similar to ethanol were observed for cyclohexanone, the soot reduction effect was considerably lesser than both ethanol and methanol. The soot reduction ranged from approximately 10% at an additive concentration of about 2.5% by volume of JP-8 to about 20% reduction in soot at an additive concentration of 10% by volume of JP-8. Thus, the cyclohexanone appears to be less effective than the ethanol. Methanol was added to JP-8 in concentrations of approximately 10% by volume of JP-8 fuel; a decrease of approximately 50% was observed, larger than for ethanol. However, comparison on the basis of volume of additive is misleading since at the same volume percent the cyclohexanone will provide less oxygen in the fuel than ethanol and methanol will provide greater oxygen level in the fuel. Figure 3.1.8-2 presents the same results plotted against the percent oxygen in the fuel. It shows that the three oxygenates fall on essentially the same curve of soot reduction, which indicates that the soot reduction in each case is largely being driven by the same phenomena.

The levels of soot reduction are similar to those obtained in all of the other devices used in this program and suggests that the same mechanism is dominant in the reducing of soot. The one process common to all devices studied is chemical kinetics, so the results suggest that kinetic processes are dominating the reduction in soot.

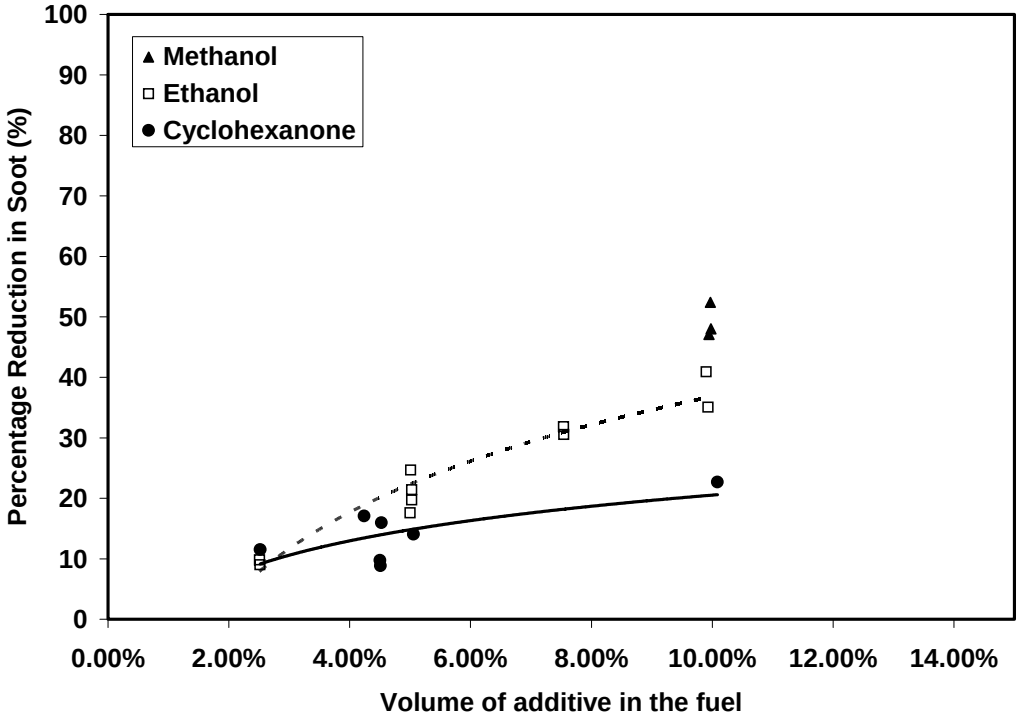

Figure 3.1.8-1. Effect of Oxygenated Additives on Soot Formation with JP-8.

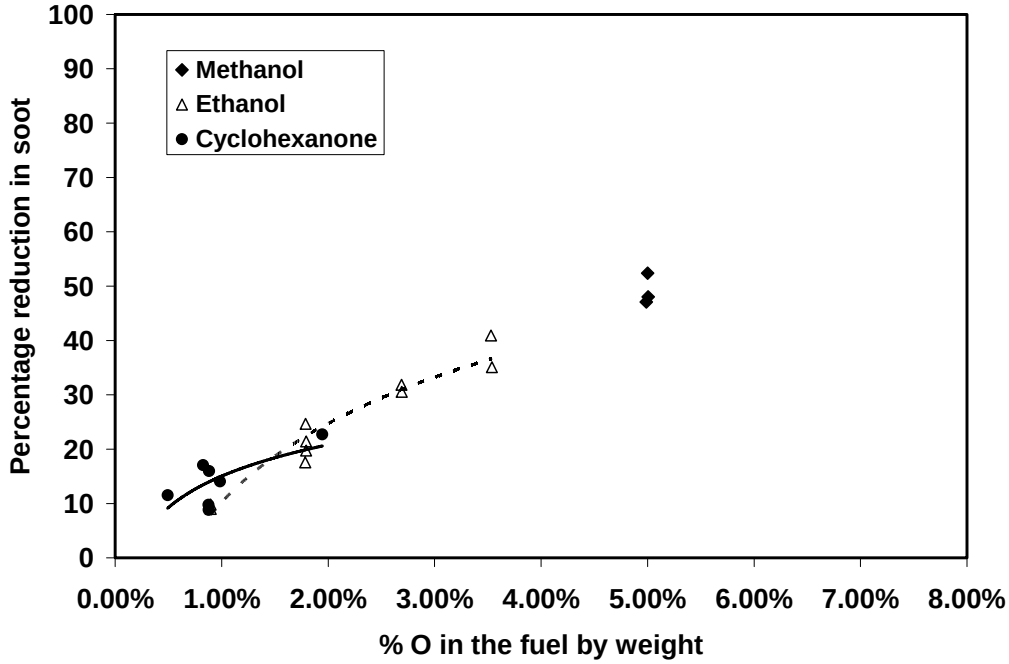

Figure 3.1.8-2. Effect of Oxygenated Additives on Soot Formation with JP-8.

3.2 NITROALKANES

3.2.1 SUMMARY OF MAJOR RESULTS

The study of nitroalkanes was motivated by testing of a commercial additive that showed promise in reducing soot. Analysis of the additive showed that its components that were most likely to be causing the soot reduction were nitroalkanes and cyclohexanone.

Table 3.2.1-1 presents a summary of the effects of various nitroalkanes across the suite of devices used in this study. The trends in the effects are much more complex than those observed for the oxygenated compounds. This complexity is most evident in the premixed flame results where the structure of the nitroalkane had a tremendous impact, leading to increases in soot for nitropropane and decreases in the other two compounds. For the shock tube and opposed-jet diffusion flame, soot was essentially unchanged; whereas, for the high pressure reactor, which most closely approximates a gas turbine combustor, large decreases in soot, up to approximately 70%, were observed with JP-8 as the fuel. Another important experimental result comes from the well-stirred reactor that established clearly that there are kinetic effects beyond those induced by changes in temperature caused by the additive.

Such a rich set of experimental results provides an excellent test for kinetic models of PAH and soot formation. In an effort to test a model for heptane/toluene combustion made available by the NIST SERDP team, kinetics related to nitromethane were added to the model. Unfortunately, it failed to model accurately even the shock tube data where kinetic processes must be dominant. Therefore, we were unable to establish whether the model supported conjectures on the mechanisms underlying the trends in the premixed flame data and the opposed-jet diffusion flame results.

Table 3.2.1-1. Summary of the Effects of Nitroalkanes on Soot.

	Additives	**Fuel**	**Effect on Soot**	**Comments**
Shock tube	Nitromethane	Heptane/ Toluene	Soot unchanged	
Well-stirred reactor	Nitromethane Nitroethane Nitropropane	Heptane/ Toluene	Decreased	Temperature plays a role but a chemical effect is present.
Premixed flame	Nitromethane Nitroethane	Heptane/ Toluene/ Ethylene	Decrease	The addition of ethylene was required to avoid instability on the flame.
	Nitropropane	Heptane/ Toluene/ Ethylene	**Increase**	2% oxygen level.
Opposed-jet flame	Nitromethane i-propyl nitrate	Heptane/ Toluene	**Small increase**	
Turbulent spray flame	Nitroethane Nitropropane	Heptane/ Toluene	Decrease	Nitromethane not run due to explosion hazard.
HP Turbulent reactor	Nitroethane Nitropropane	JP-8	Decrease	Nitromethane not run due to explosion hazard.

3.2.2 SHOCK TUBE

All nitroalkane additive experiments were conducted at a pressure of ~ 21 atm over a precombustion temperature range of 1100 K-1600 K (postcombustion temperature range of 1650 K-1950 K). The argon content in the test section was maintained at 93 vol% and the remainder comprised of oxygen and fuel. The experiments were conducted at an equivalence ratio of 3.0. The exothermic reactions of nitrocompounds can cause an increase in postcombustion temperature [Kahandawala 2005]. Therefore, to exclude any thermal effect, all product yields measured in this study were compared at postcombustion temperatures (the postcombustion temperature is the temperature after onset of ignition). Thus, any observation herein and associated conclusions are entirely due to the chemical effect from the additive.

For nitromethane experiments, 5 vol% of nitromethane was added to the base fuel mixture so that the oxygen content in the fuel mixture was 4 wt%. Both gaseous products and soot yields were measured and normalized with respect to the mass of carbon in the fuel to exclude any volumetric effect that may arise from normalization with respect to the mass of the fuel. Results from Leco carbon analysis of particle yields are shown in Figure 3.2.2-1. The solid lines indicate polynomial trend lines that were used to fit the experimental soot yields. The trend lines show that addition of nitromethane had no impact on soot yields. The experiments were done at close temperature intervals to cover the entire temperature range instead of repeating the same experiments at a fixed temperature.

As shown in Figure 3.2.2-1, the low carbon yields observed at the lower temperatures are due to the slower rate of particle formation, but as the temperature is increased, particle formation dominates and the soot yield goes through a maximum. However, further temperature increases cause the particle oxidation rate to dominate, which lowers the particle yields and thus generates a classical bell-shaped curve for soot yield as a function of temperature. Closer to the maxima where the soot formation is high, even a small difference in reaction times could cause a significant change. This is one of the reasons that a higher scatter is observed closer to the maxima.

The validity of any kinetic model dealing with the gas phase chemistry of particle formation depends on its ability to predict the correct order of magnitude of PAH yields and the order of PAH appearance. A valid model should have the ability to correctly predict profiles of

species that define soot particle nucleation and surface growth rates [Appel 2000]. For this study, the additive mechanism [Zhang 1997, Zhang 1999] was combined with the base fuel mechanism [Babushok 2004] which is a compendium of mechanistic work that takes into consideration both the HACA mechanism and the resonantly stabilized reaction pathways for molecular growth. The estimates for reaction rates for the growth to high molecular weight compounds for which no kinetic data is available are based on rates of similar reactions [Babushok 2004]. In an attempt to validate both the NIST base fuel (heptane/toluene) mechanism and the nitromethane mechanism and to better understand the observed soot yields, experimental yields of soot precursors obtained from volatile and semivolatile product analysis were compared against the yields predicted from the kinetic model (Figure 3.2.2-2). The product yields were obtained by using a point calibration of the internal standards for a similar class of compounds. The yields from both product analysis and modeling were normalized with respect to the mass of carbon in the fuel. The product yields are given as yield % per unit mass of carbon in fuel. For clarity, only a few selected species are shown here. Information on other observed species is available elsewhere [Kahandawala 2004]. A complete list of observed species is given in Table 3.2.2-1. The experimental yields of all volatile and semivolatile species identified in this study have been fitted with exponential trend lines and are shown as solid lines. The broken lines represent model yields and have been plotted using point plots. While comparing experimental and model yields, reader should be aware that axes showing experimental and model yields have different scales. As such, the difference observed from experimental yields with the additives may not be visible in product yields generated by kinetic model.

From the volatile compounds analyzed, only benzene data was quantified since the other compounds were only detected in trace levels and were close to the detection limit (the GC signal-to-noise ratio was <<2). The volatile and semivolatile species detected indicate that at the lower temperatures, the addition of nitromethane has a tendency to increase yield of every soot precursor yield except that of benzene, isomers of methyl naphthalene, and o-diethenylbenzene. However, the modeling results indicate that at lower temperatures, the yield of all volatile and semivolatile species decreases with the addition of nitromethane. Experimental scatter was higher for most species at lower temperatures although the scatter was less than the base fuel for nitromethane.

Figure 3.2.2-3 shows a comparison of experimental and modeling yields for selected nonvolatile organic compounds (NVOC). Again the model trends are shown by broken lines and the experimental yields are shown by solid lines. Both experimental and model yields are plotted using point plots. Unlike in the volatile and semivolatile product analysis, nonvolatile products were analyzed only at selected temperatures. Since similar results were obtained from thermal desorption and Soxhlet extraction, only thermal desorption data is shown in this paper. More information on other NVOCs detected using thermal desorption and the whole data set from Soxhlet extraction is given elsewhere [Kahandawala 2004].

From the NVOC data it can be seen that the PAH yields increase with the addition of nitromethane, although no significant difference in soot yield was observed. The effect of the additive that was predicted by the models did not match the observed experimental trends. For base fuel, the model was able to qualitatively predict experimental trends in species profiles (except for benzo[ghi]perylene and coronene), but the quantitative model overpredicted from a factor of two for benzene to two orders of magnitude for most other species. The model could overpredict the experimental yields for several reasons such as inaccurate thermodynamic or kinetic data, high production rate, low consumption rate or perhaps key species are missing from the reaction mechanism. Dibenzo[ah]anthracene is an example of missing specie as it was observed experimentally but was not present in the NIST mechanism.

To address the discrepancies due to missing species, an attempt was made to identify all species with significant yields, especially the nitrogenated compounds, in the hope that this information might help us better understand how nitromethane impacts the soot formation process. The following compounds were detected in this study when nitromethane was used as the additive: benzonitrile; benzonitrile, 2-methyl-; phenol, 4-methyl-2-nitro-; phenol, 5-methyl-2-nitro-; phenol, 2-nitro- (see Figure 3.2.2-4 for molecular structure and formula). However, none of these compounds were present in the model. As such, it is possible that some key species may have been omitted in the model, which could be one of the reasons why the other soot precursor yields were misrepresented in the model.

The yield for benzonitrile, the most abundant of these compounds observed, is plotted in Figure 3.2.2-5. The results for the yields of other nitro compounds detected are reported elsewhere [Kahandawala 2004]. Although no significant impact on soot yields were observed with the addition of nitromethane, its addition did cause a significant decrease in the measured

ignition delay times as observed in other studies where similar NO_x compounds were used as additives to enhance ignition. Addition of nitromethane reduced ignition delay thus increasing reaction time. This increase in reaction time in a fuel-rich zone may lead to an increase in soot production via surface growth reactions and could explain the experimental observations of higher PAH yields from the surface adsorbed NVOC for the additives.

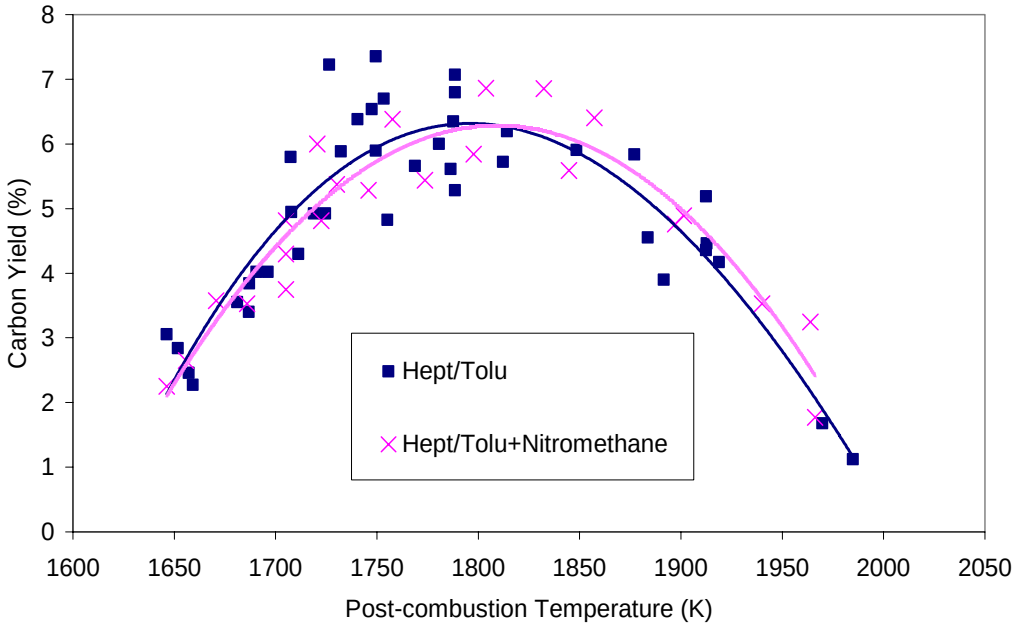

Figure 3.2.2-1. Carbon Yield from Combustion ($\Phi = 3$) of n-Heptane/Toluene and n-Heptane/Toluene + Nitromethane at 21 atm.

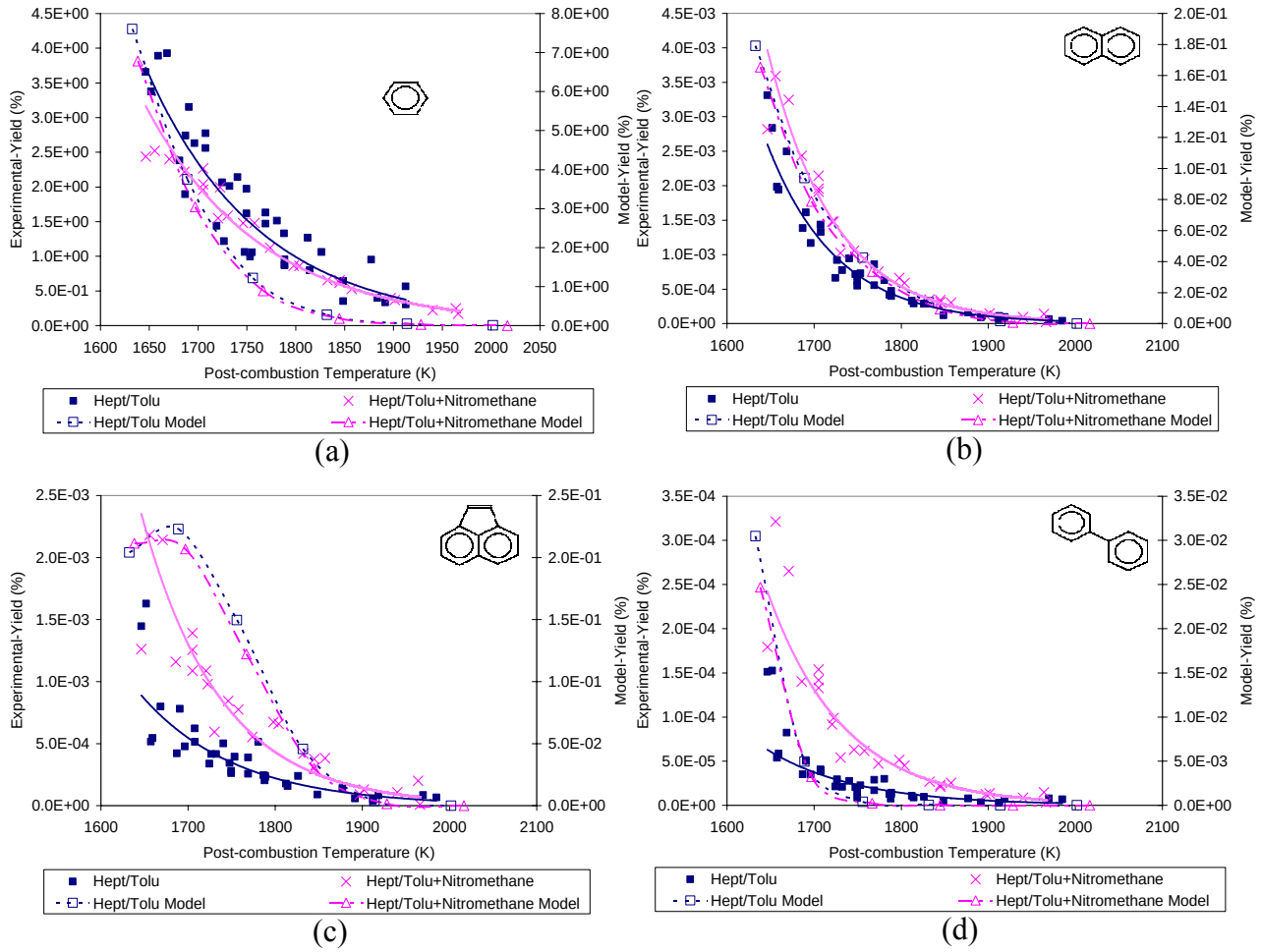

Figure 3.2.2-2. Yields of (a) Benzene, (b) Naphthalene, (c) Acenaphthylene, and (d) Biphenyl from Combustion of n-Heptane/Toluene and n-Heptane/Toluene + Nitromethane at 21 atm.

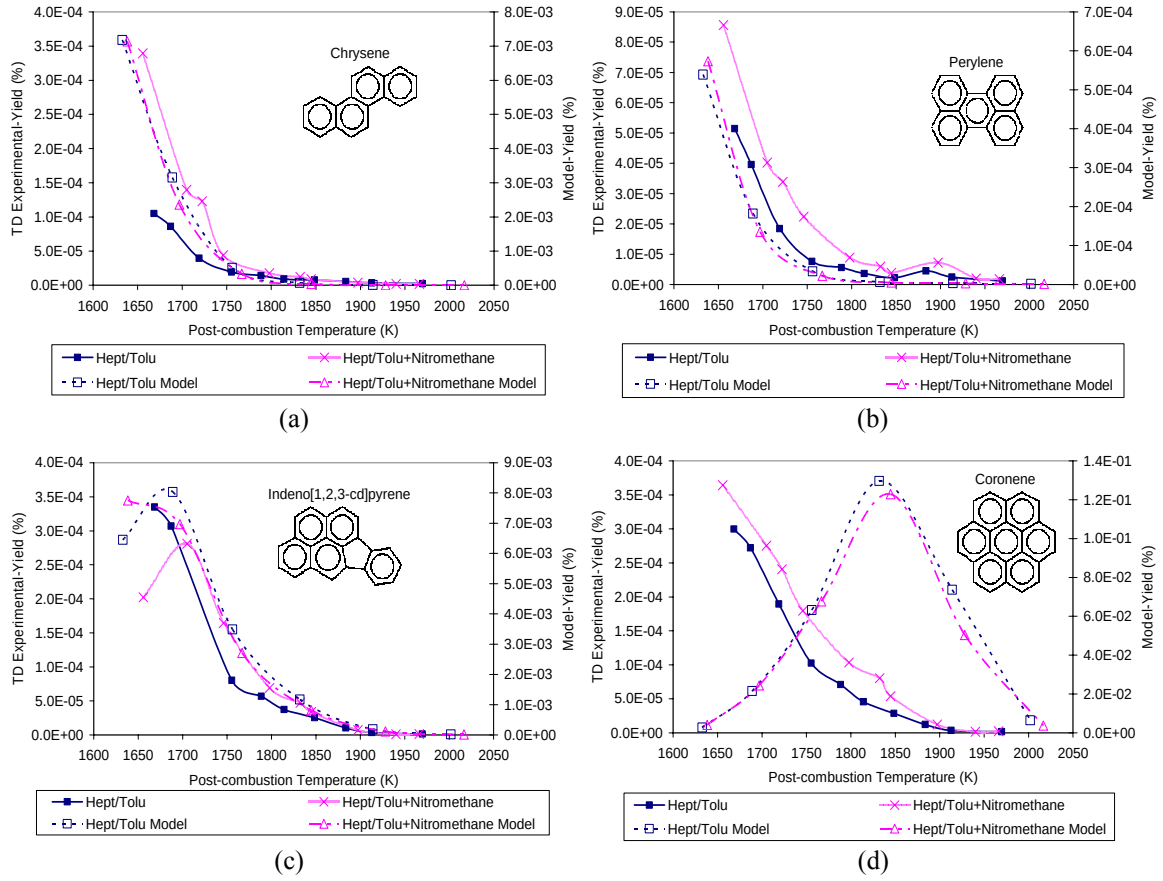

Figure 3.2.2-3. Yields of (a) Chrysene, (b) Perylene, (c) Indeno[1,2,3-cd]Pyrene, and (d) Coronene from Combustion of n-Heptane/Toluene and n-Heptane/Toluene + Nitromethane at 21 atm.

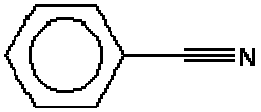

Benzonitrile- (C_7H_5N)

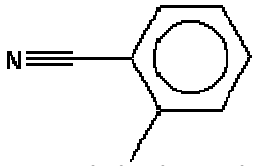

Benzonitrile, 2-methyl- (C_8H_7N)

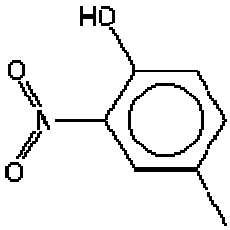

Phenol, 4-methyl-2-nitro- ($C_7H_7NO_3$)

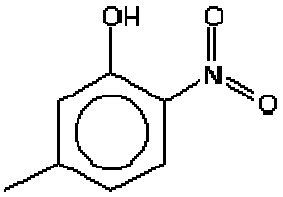

Phenol, 5-methyl-2-nitro- ($C_7H_7NO_3$)

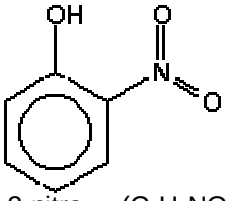

Phenol, 2-nitro- ($C_6H_5NO_3$)

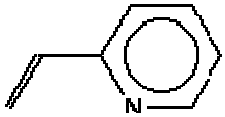

Pyridine, 2-ethenyl- (C_7H_7N)

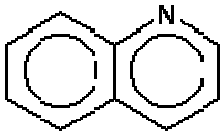

Quinoline (C_9H_7N)

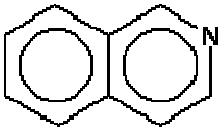

Isoquinoline (C_9H_7N)

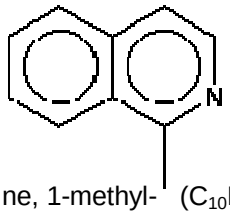

Isoquinoline, 1-methyl- ($C_{10}H_9N$)

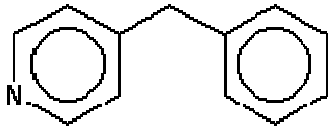

Pyridine, 4-(phenylmethyl)- ($C_{12}H_{11}N$)

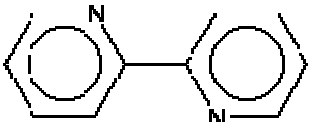

2,2'-Bipyridine $C_{10}H_8N_2$

Figure 3.2.2-4. Molecular Structure and Formulae of Semivolatile Nitrogenated Compounds Detected from Nitromethane, NO_2 and Pyridine Additives at 21 atm.

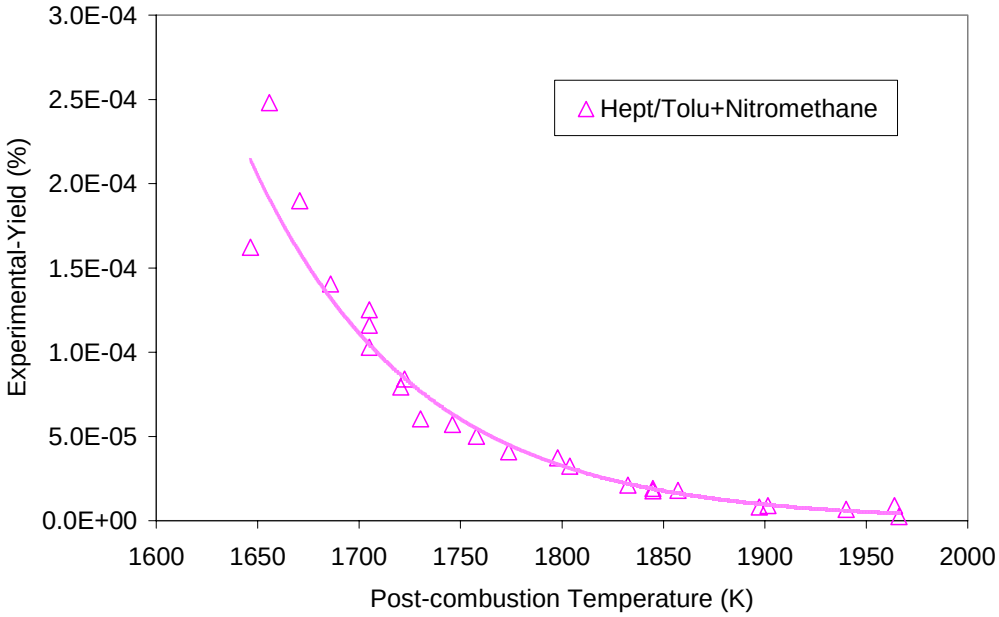

Figure 3.2.2-5. Benzonitrile Yield from Heptane/Toluene + Nitromethane at 21 atm.

Table 3.2.2-1. Species Quantified from Product Analysis.

ANALYSIS	SPECIES
Volatile	Benzene
Semivolatile	phenylacetylene m-diethenylbenzene p-diethenylbenzene o-diethynylbenzene naphthalene 2-methyl naphthalene 1-methyl naphthalene acenaphthylene biphenyl ethenylnaphthalene ethylnapthalene
Nonvolatile	phenanthrene anthracene fluoranthene pyrene chrysene benzo[b]fluoranthene benzo[k]fluoranthene benzo[a]pyrene perylene indeno[1,2,3-c,d]pyrene dibenzo[a,h]anthracene benzo[g,h,i]perylene coronene
Nitrogenated Products	benzonitrile methyl benzonitrile 4-methyl-2-nitrophenol 5-methyl-2-nitrophenol, 2-nitrophenol,

3.2.3 WELL-STIRRED REACTOR

The effectiveness of three nitroalkanes (nitromethane, nitroethane and nitropropane) was studied in the WSR. The results are discussed below and in Stouffer [2005a]. The neat fuel for the tests was 80% heptane/20% toluene by volume. The reactor material for the nitroalkane experiment was amorphous fused silica which minimized both cracking and heat loss and could

be used because the temperature in the reactor was less than the 1500°C melting point of the silica.

Equivalence ratios between 1.90 and 2.10 were studied. The WSR was limited to this equivalence ratio range on the low side by the melting point of the fused silica and on the high side by the rich blowout limit. However, as will be shown later, this range of equivalence ratios captures the peak along with the low temperature and high temperature sides of the so-called "soot bell". The airflow was held at a constant 240 g/s and the average residence time in the reactor was 10 +/- 0.4 ms. The reactor pressure was slightly (0.6-1.4 kPa) over the ambient atmospheric pressure for all of the tests.

The nitroalkane additives were added to the fuel in concentrations such that the oxygen mass fraction of the fuel was 0% (neat heptane/toluene mixture), 2% and 4%. The mass flows of the additive and the base fuel were adjusted to maintain the same equivalence ratio as the neat case. The additives concentrations used to achieve the desired oxygen levels are listed in Table 3.2.3-1. The indicated equivalence ratio was maintained to within +/- 0.006 of the target equivalence ratio, with most of the measurements occurring in an even tighter band of equivalence ratio.

It has been shown previously in this study and others that the effect of a temperature increase is to decrease soot produced for the high temperature side of the soot bell and increase soot produced for the low temperature side. Highly energetic nitroalkane additive compounds, such as nitromethane, will increase the combustion temperature at the same inlet temperature and equivalence ratio. This increase in temperature as a result of the additive raises the question of whether difference in the soot production is only due to the increased combustion temperature, or if the change is due to other chemical effects of the additive. For each of the nitroalkane additives, three test concentrations were considered with the same inlet fuel/air mixture temperature at each equivalence ratio: neat, additive with 2% oxygen weight in the fuel, and additive with 4% oxygen weight. To explore the effect of temperature on the soot formation, an additional test point was also considered where the combustion temperature of the neat case was adjusted to match that of one of the additive cases. The combustion temperature was increased by increasing the inlet temperature of the fuel/air mixture, and allowed differentiation between the thermal effect on the kinetic process and any chemical effect of the additive. The inlet fuel/air mixture temperature was adjusted by increasing the vaporizer, main air, and vaporizer air

and fuel temperatures. Due to the large thermal mass of the vaporizer and associated fluid path upstream of the jet ring, the process of matching the combustion temperatures required approximately 40-60 minutes between test points with matched temperatures. Note that over the range of conditions the increase in measured combustion temperature is less than the increase in the inlet temperature due to the difference in specific heats of the products and reactants. At the highest equivalence ratios tested ($\phi = 2.1$), the increase in the inlet temperature has a larger effect on the combustion temperature due to the increase in the combustion efficiency, as shown by decreased measured oxygen levels in the exhaust emissions.

The experimental results shown will be predominately from the carbon mass determined from carbon burn off from quartz filters and from FTIR measurements of gaseous emissions. Particulate mass samples were drawn through an oil-cooled probe at a location 16 cm downstream of the WSR in the plug flow reactor region. Smoke number was also determined during the study and was found to track well with the soot mass. Due to lack of instrument availability at the time of the experiments, particulate number densities and particle size distributions were not determined.

Experimental Results

Figure 3.2.3-1 shows the total particulate carbon mass data for experiments with the nitromethane additive plotted versus. temperature measured in the WSR. The curve shows a peak and a familiar soot bell shape. For the neat cases the peak is found for tests with $\phi = 2$. Above this equivalence ratio the carbon mass decreased as the temperature increased (as ϕ was lowered or inlet temperature was increased) and is commonly referred to as the high temperature side of the soot bell. On the opposite (low temperature) side of the soot bell, the carbon mass production increased as the temperature increased. For convenience of comparison, data at the same equivalence ratios is outlined within the ovals on the plots. The data clearly show that nitromethane decreases the total carbon particulate mass for $\phi < 2.05$. As the concentration of nitromethane increased the carbon mass dropped further. The reduction in carbon mass at $\phi = 1.95$ was over 47% for the 4% O case. To explore the effect of temperature, the inlet temperature for the neat elevated inlet temperature case was increased until the WSR flame temperature was approximately the same for both the 2% O and the neat case. For the low temperature side of the soot bell, the increased combustion temperature associated with the inlet temperature increased the soot mass production. On the high temperature side of the soot bell,

the soot produced for the neat case decreased as temperature was increased. However, the soot mass production for the nitromethane additive case at the same temperature was less than or equal to the neat case at the same combustion temperature. Therefore, it is apparent that the drop in soot production observed over most of the test points with the additive addition is not merely due to an increase in temperature caused by the additive, but rather by other features of the reaction mechanism associated with the additive. At the lowest equivalence ratio considered (ϕ =1.90), the additive case and the neat case had approximately the same total carbon mass. The carbonaceous carbon mass, which was determined from the carbon oxidized from the quartz filters at temperatures above 325°C, is shown in Figure 3.2.3-2 and exhibited the same general trends as the total carbon mass results.

During the early work with the nitromethane additive, an MKS 2030 FTIR multigas analyzer was used to determine the concentrations of several hydrocarbon species at neat and 28,460 ppm additive concentrations. This additive level corresponds to 2.3 weight % O in the fuel. Figure 3.2.3-3 shows that both the acetylene and methane concentrations increase as the equivalence ratio increased and decreased with the addition of nitromethane. The effect of nitromethane on the formaldehyde and ethylene is shown in Figure 3.2.3-4. Both the ethylene and the formaldehyde increase with an increase in f, and are reduced by the nitromethane. Figure 3.2.3-5 shows the effect of the nitromethane on the NOx and HCN. The NO and HCN were both below the detection limits for the neat case and were increased dramatically with the addition of nitromethane. No measurable quantities of NO_2 were detected for either the neat or additive case.

The effect of the nitroethane additive is shown in Figures 3.2.3-6 and 3.2.3-7. For the elevated inlet temperature neat cases, the inlet temperature was increased enough so that combustion temperatures were matched with the 4% O additive cases. Note that the combustion temperature increase for the nitroethane additive was less than the increase seen with the nitromethane, because nitroethane is a less energetic fuel. Decreases in the total carbon particulate mass and carbonaceous carbon similar to those shown for the nitromethane cases were seen with the addition of the nitroethane. At Φ=1.95, the total carbon mass is reduced by 50% for the 4% O case. The data plotted against temperature show that at all equivalence ratios, the high inlet temperature neat case produces more soot (as indicated by the total carbon mass) than the corresponding cases (same combustor temperature) with the additive. Therefore, it is apparent that the effect of the nitroethane additive is not merely caused by the increase in the

combustion temperature. Note that at Φ = 2.1, the additive slightly increases soot generated above the neat case; however, for the same combustion temperature with 4% O in the fuel, less soot is produced with the nitroethane additive than for the corresponding neat case.

The carbon particulate mass data for the nitropropane additive is shown in Figures 3.2.3-8 and 3.2.3-9. The trends are also similar to those shown previously for the nitromethane and nitroethane additives. The reduction in total carbon mass at Φ =1.95 was 48% for the 4 % O additive case. The results for the carbonaceous carbon mass show similar trends to the total carbon mass. As for the other two nitroalkane additives, the reduction of carbon mass is shown not to be only caused by an increase in the reaction temperature.

Summary

All three of the nitroalkane additives evaluated in the WSR showed a reduction in the amount of soot mass produced. While there is an effect of the additive on the flame temperature which will, in turn, affect the chemical kinetics, it has been shown that the effect of the additives is not merely a temperature effect.

The level of the reduction in carbon mass was similar for each of the additives as shown in Table 3.2.3-2 for three additives at oxygen levels of 4 % and an equivalence ratio of 1.95. Analysis of the gaseous emissions showed that nitromethane reduced acetylene, ethylene and formaldehyde while increasing hydrogen cyanide and nitric oxide.

Table 3.2.3-1. Additives and Concentration Levels (ppm by volume) Used in the Nitroalkane Experiments.

Additive	Formula	2% O in Fuel Additive Concentration	4% O in Fuel Additive Concentration
Nitromethane	CH_3NO_2	24,660 ppm	50,020 ppm
Nitroethane	$C_2H_5NO_2$	32,820 ppm	66,620 ppm
Nitropropane	$C_3H_7NO_2$	40,820 ppm	82,950 ppm

Table 3.2.3-2. Reduction in Carbon Mass with 4% O Addition.

Additive	Reduction in Carbon Mass
Nitromethane	48%
Nitroethane	50%
Nitropropane	48%

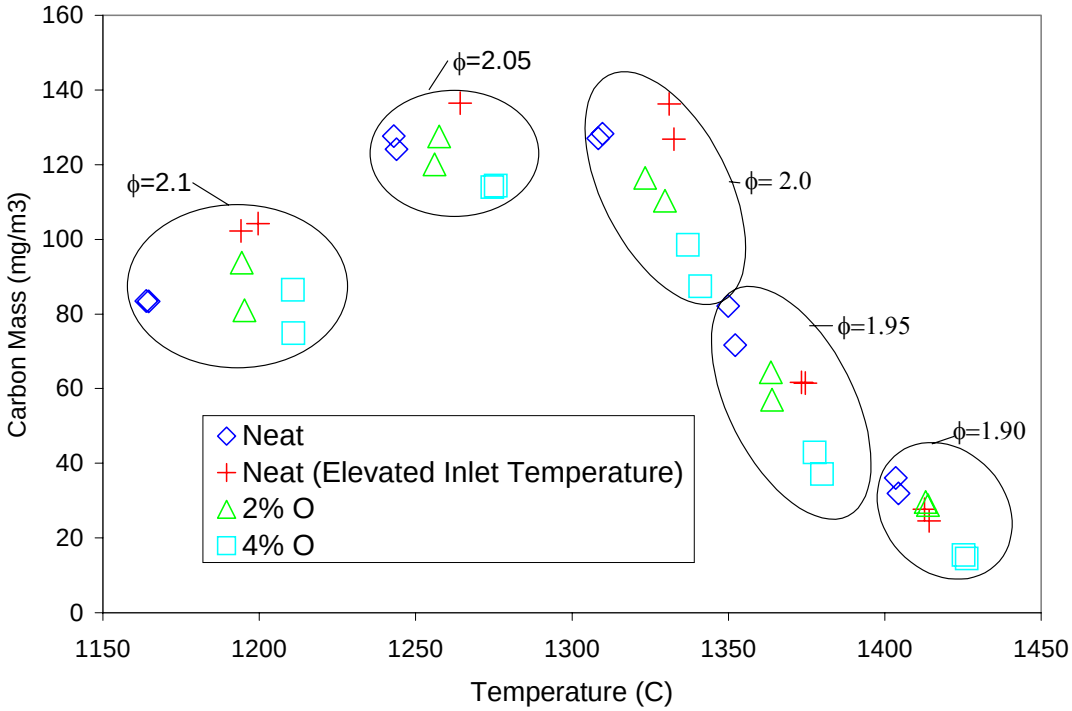

Figure 3.2.3-1. Total Carbon Mass for Nitromethane Additive Cases Studied in the WSR.

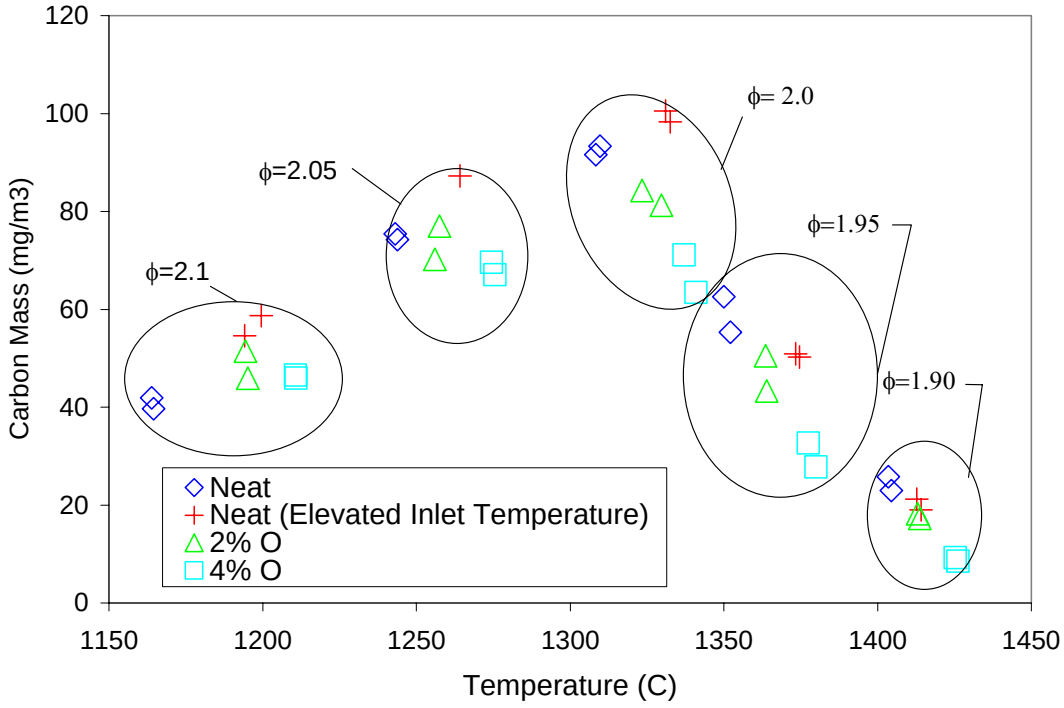

Figure 3.2.3-2. Carbonaceous Carbon Mass for the Nitromethane Additive Cases Studied in the WSR.

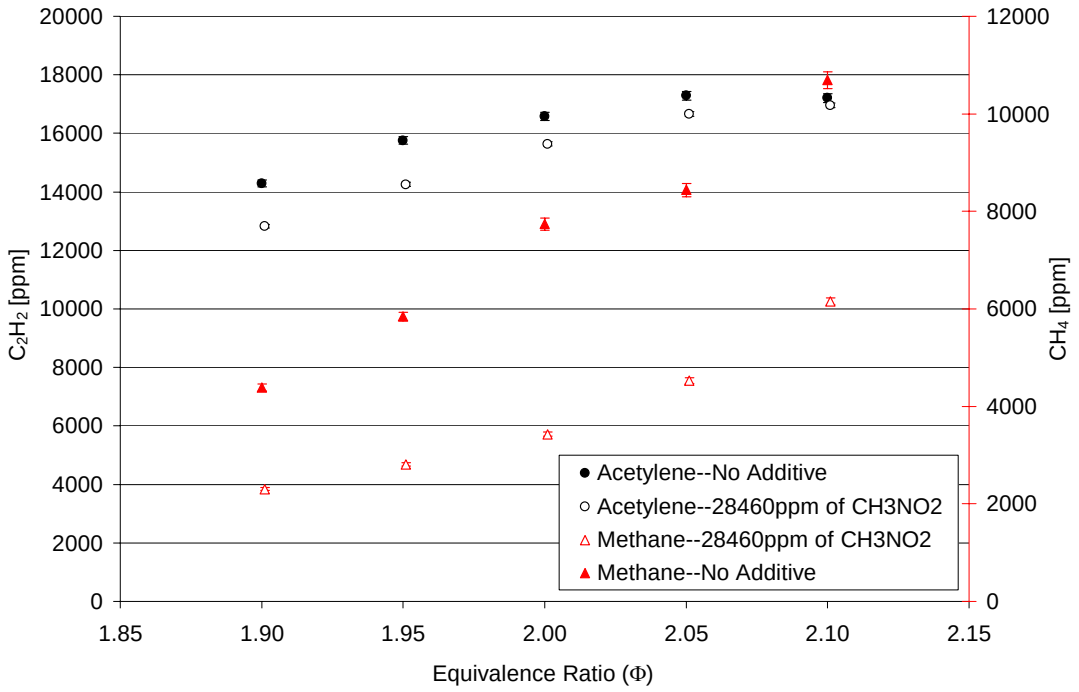

Figure 3.2.3-3. Effect of Nitromethane on Methane and Acetylene Emissions from the WSR.

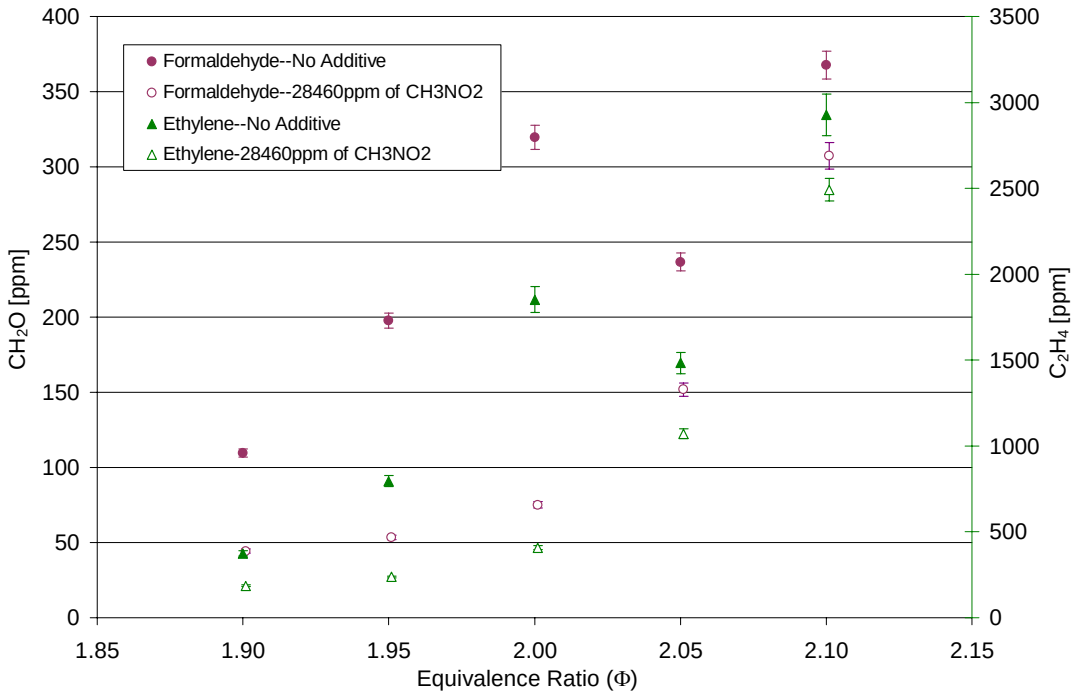

Figure 3.2.3-4. Effect of Nitromethane on Formaldehyde and Ethylene Emissions from the WSR.

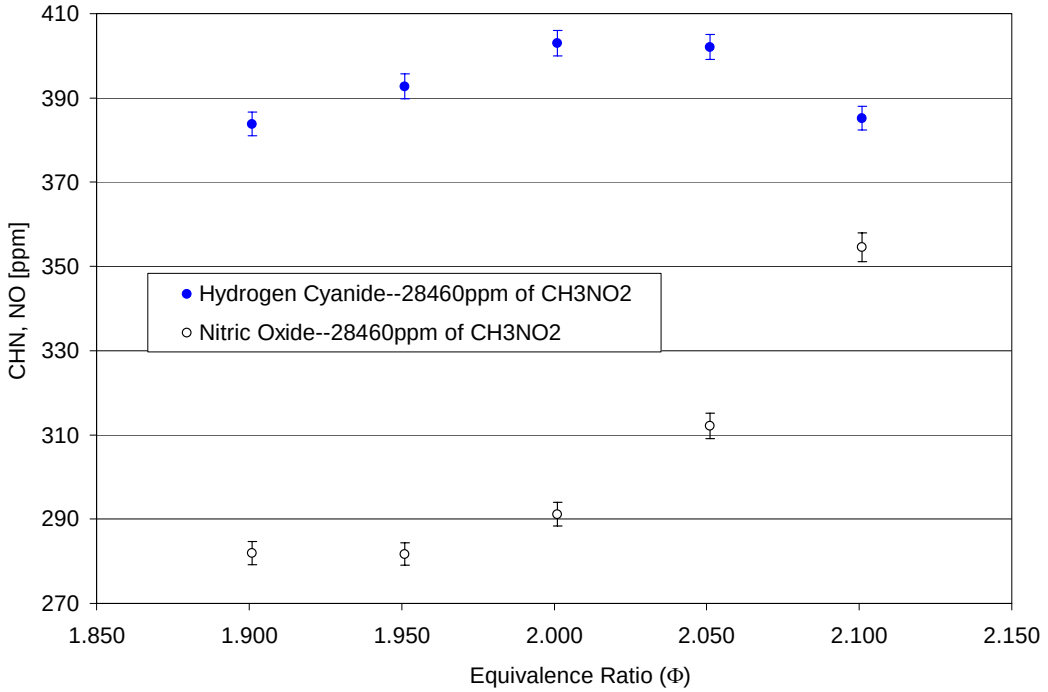

Figure 3.2.3-5. HCN and NO Emissions with Nitromethane Additive. (Neat case emissions were below detectable limits.)

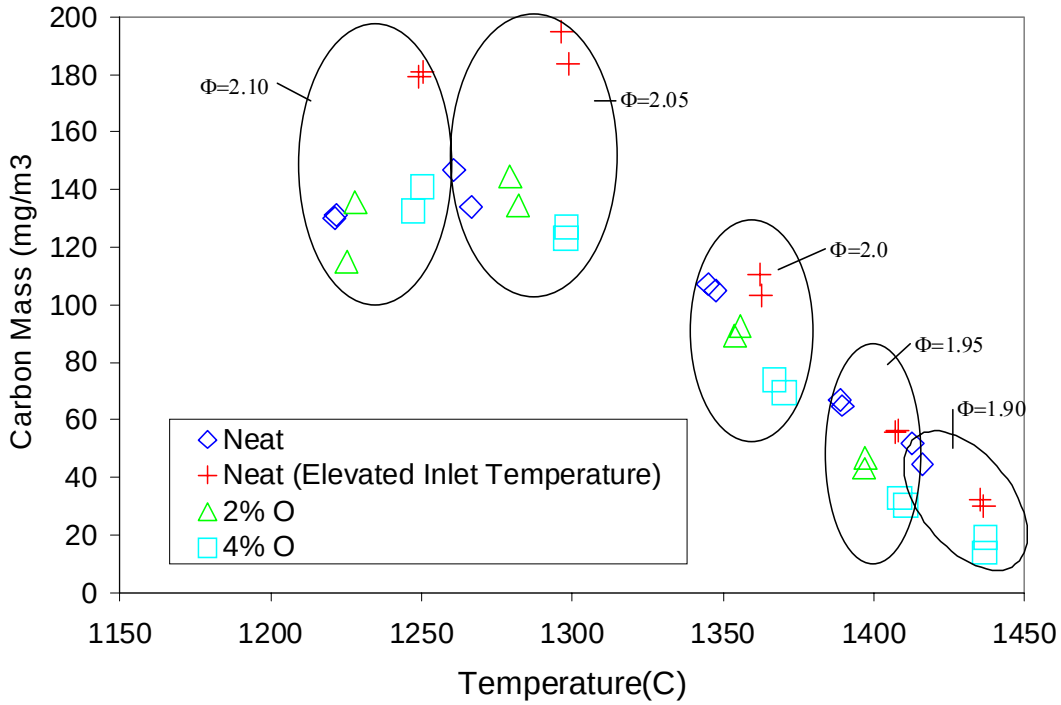

Figure 3.2.3-6. Total Carbon Mass for Nitroethane Additive Cases Studied in the WSR.

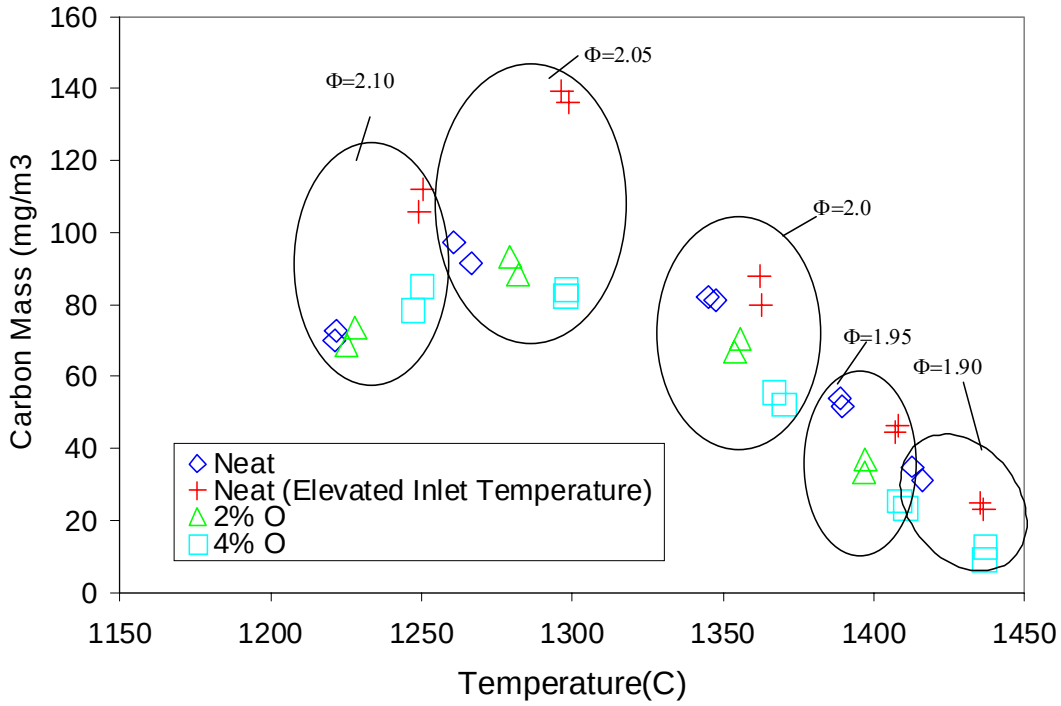

Figure 3.2.3-7. Carbonaceous Carbon Mass for the Nitroethane Additive Cases Studied in the WSR.

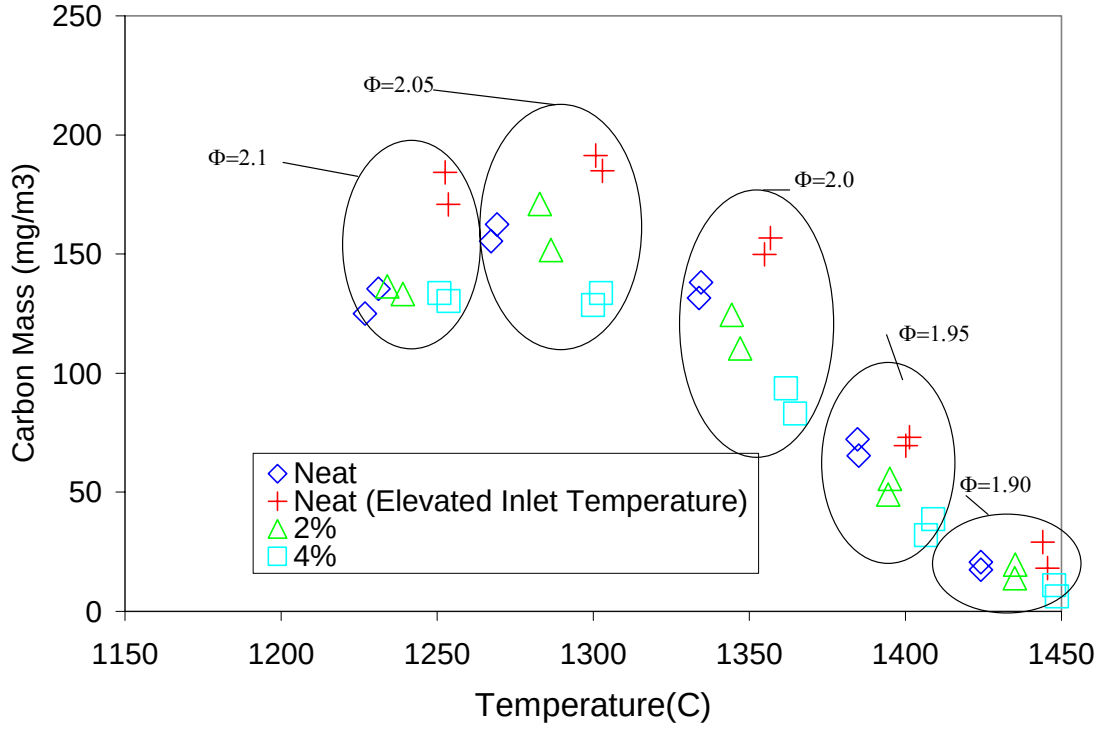

Figure 3.2.3-8. Total Carbon Mass for Nitropropane Additive Cases Studied in the WSR.

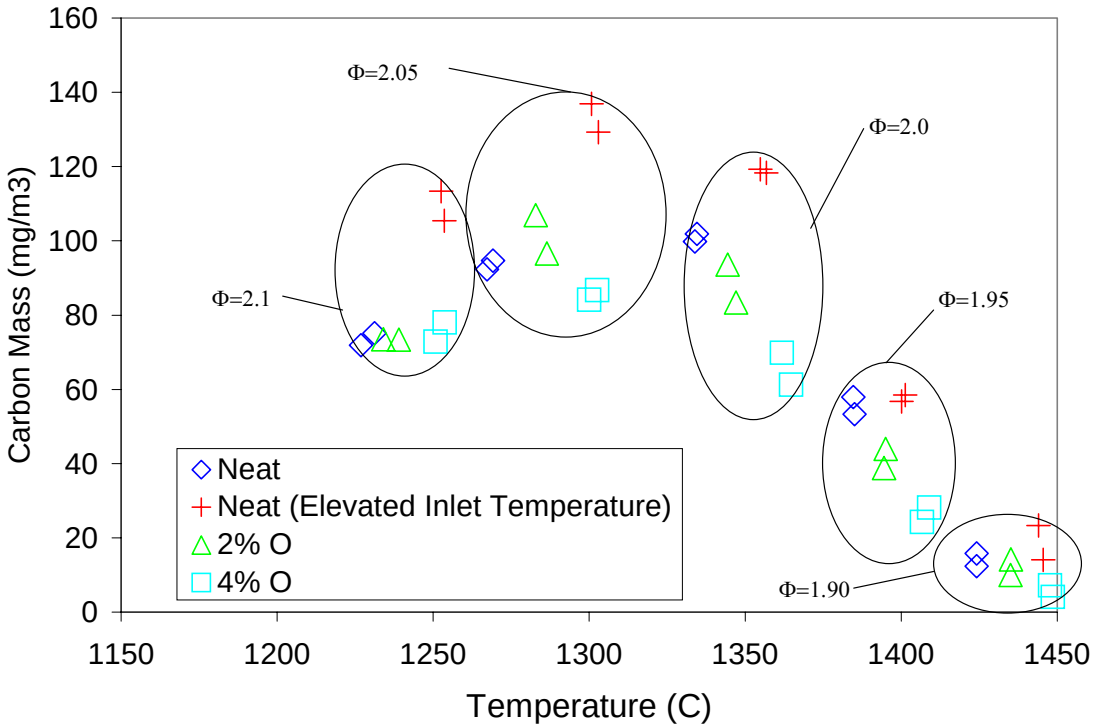

Figure 3.2.3-9. Carbonaceous Carbon Mass for the Nitroethane Additive Cases Studied in the WSR.

3.2.4 PREMIXED FLAME

Additive studies have been performed using nitromethane, nitroethane, and nitropropane, the primary components in the commercial additive which was found to have a relatively strong effect (see Table 3.2.4-1). Flame temperatures and soot volume fractions have been measured as a function of height above the burner surface. No discernable differences in flame temperatures were observed. At an additive loading of 4% by mass of oxygen, the most effective additives were nitromethane and nitroethane, with the former reducing the soot production by about 25% and the latter reducing soot production by more than 50%. For a flame with an equivalence ratio of 2.4, a comparison of the fractional reductions in soot as a function of additive levels is shown in Figure 3.2.4-1.

The most unusual feature of these data is the contrary effects of different levels of the additive, nitropropane. All of the results (and trends) have been confirmed by using a time

tracing method. In these tests, the flame height was kept constant and the make up of the inlet gases were altered in the following sequence: base flame, 4% oxygen (additive); base flame, 2% oxygen (additive). A typical time trace is shown in Figure 3.2.4-2 for the nitropropane results which exhibited the unusual results of increasing soot at the lower concentration, but a soot reduction effect at higher concentrations.

Our interpretation of these results in the laminar, premixed flames is that a C_3-hydrocarbon fragment (C_3H_5) from nitropropane enhances the propargyl radical (C_3H_3) concentration at low additive levels. Propargyl, in turn, is a known key intermediary to the formation of aromatic rings. We speculate that the formation of propargyl initially counterbalances any soot-reducing potential that the nitrate group provides. But at higher additive levels, the C_3 level is saturated, and the effect of the NO_2 component dominates, leading to reduced soot production. Nitromethane is a less active soot-reducing agent than is nitroethane since the former produces methyl radicals that add to C_2 hydrocarbons to form C_3 species. Nitroethane, on the other hand, is the most effective presumably because it barely perturbs the existing C_2 concentrations. Propargyl radicals are unaffected and there is no counterbalancing effect inhibiting the added NO_2 from reducing soot.

A schematic of the experimental setup with the particulate sampling probe is provided in the experimental section. This probes enables rapid high dilution rates ranging from several hundred to a hundred thousand. In this manner, the sample can be rapidly “frozen”, transported to the analyze, and particle coagulation and wall loss can be minimized.

Figure 3.2.4-3 depicts the problem with probe clogging in which particulate-laden samples are extracted from the flame and sent to a scanning mobility particle sizer (SMPS) and then to a condensation nuclei counter (CNC). Once the experiment is set up, an initial sample stream is collected (R28) and then after a few moments, a second sample (R29) is obtained. Significant degradation in the total particle count and in the particle distribution is observed. However, upon cleaning the probe orifice (mechanical insertion of a fine thermocouple wire into a 0.007” hole) and collecting another sample (R31), then the original count and distribution is recovered. Raw (i.e., highly diluted) samples of particle size distributions as a function of height above the burner are shown in Figure 3.2.4-4. As can be observed, there is a dramatic shift in the size distribution within only 2.5 mm within the flame. Absolute values of this distribution have not yet been determined, although the relative distributions should be valid.

The effectiveness of nitromethane, nitroethane, nitropropane and cyclohexanone in premixed laminar heptane/toluene/ethylene flames is described above using laser extinction to measure soot volume fraction. To further investigate those results, thermophoretic sampling was combined with scanning electron microscopy to measure particle size. A brief description of the sampling technique is provided in the experimental section.

The TEM grids onto which particles were collected via thermophoretic sampling were analyzed by scanning transmission electron microscopy (STEM) at a magnification of 40,000. Samples obtained at a height of 12.3 mm above the burner surface were compared for 3 different additives (nitromethane, nitroethane and nitropropane). The additive concentrations were set so that oxygen addition was 4%. The photomicrographs are compared in Figure 3.2.4-5 with the particle size statistics shown in the adjacent table. The results show that the nitroethane produced the smallest size particles. This observation is consistent with the laser extinction measurements indicating that nitroethane was the most effective additive in the premixed, flat flame studies.

Table 3.2.4-1. Particle Reduction Effectiveness of Commercial Additive Components (phi = 2.4).

Device		Nitromethane	Nitroethane	Nitropropane	Cyclohexanone
Premixed flame	4% Oxygen Heptane/toluene/ethylene	-25%	-60%	~15%	-12%
Premixed flame	2% Oxygen Heptane/toluene/ethylene	-15%	-20%	**~30% increase!**	-0%

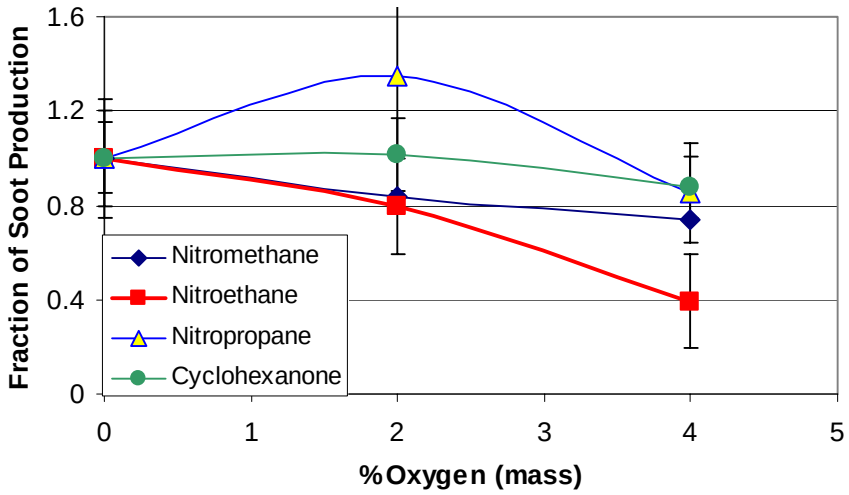

Figure 3.2.4-1. Relative Soot Production in Laminar Premixed Flame.

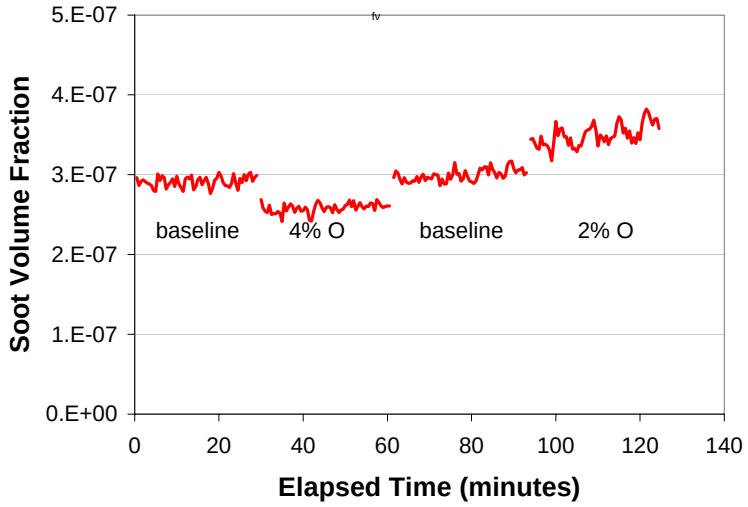

Figure 3.2.4-2. Time Trace Confirming Concentration Effect with Nitropropane.

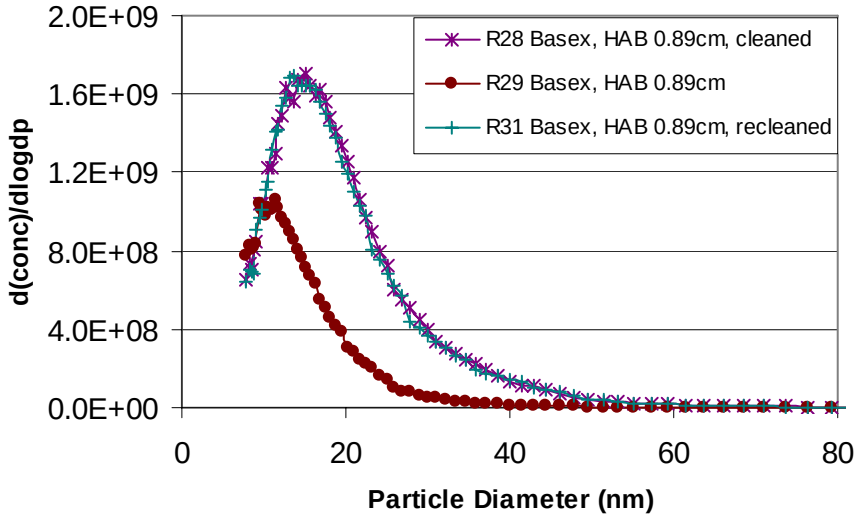

Figure 3.2.4-3. Degradation of Diluted Sample (Raw Signal) due to Orifice Clogging.

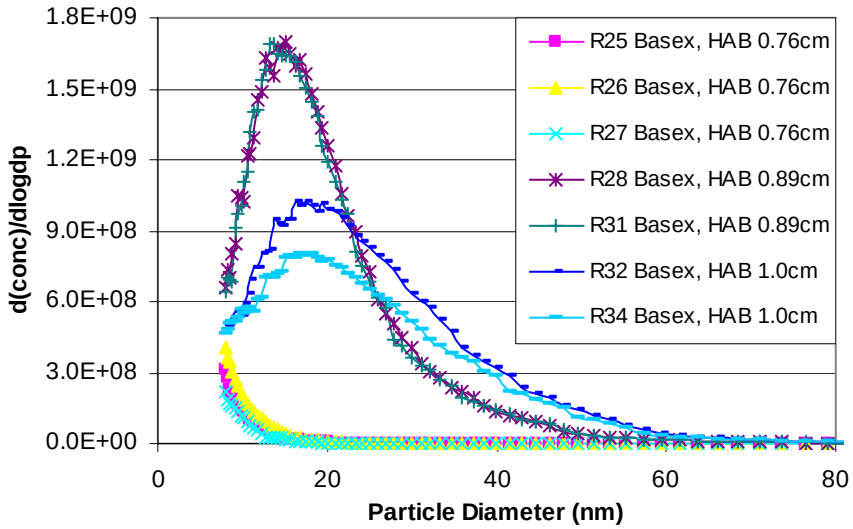

Figure 3.2.4-4. Particle Size Distributions in Diluted Samples.

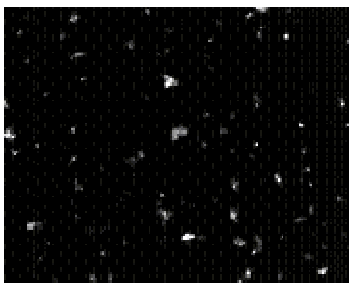

baseline

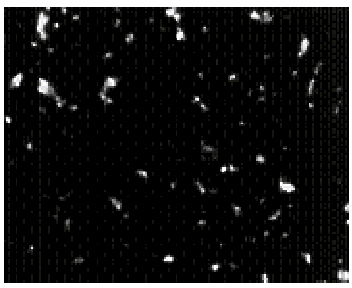

nitromethane

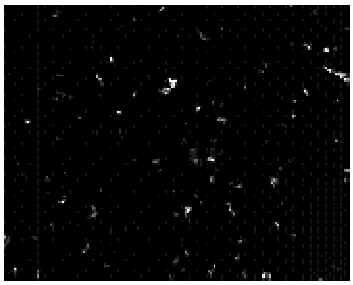

nitropropane

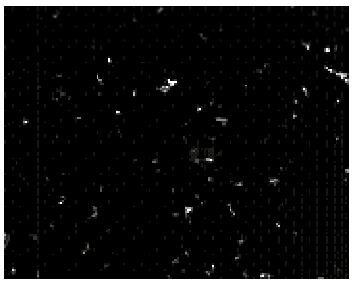

nitroethane

	average (nm)		standard deviation	
	major	minor	major	minor
Baseline	74.1	43.9	49.3	27.6
Nitromethane	77.9	52.0	62.1	31.9
Nitroethane (5%)	54.7	34.9	25.1	17.4
Nitropropane	51.0	27.4	31.8	19.2
Nitroethane	20.5	11.8	12.7	4.5

Figure 3.2.4-5. Photomicrographs of Particulates Collected from Premixed Flames Using Thermophortic Sampling.

3.2.5 OPPOSED-JET DIFFUSION FLAME

The primary experimental effort with nitroalkanes conducted in the opposed-jet diffusion flame was with nitromethane. However, in a parallel program at ARL, isopropyl nitrate was being studied as a fuel/air explosive. Given the expected similarity of IPN to the n-propyl nitrate that was a major constituent of the commercial additive, some work was done to investigate the effects of IPN on soot and to develop a kinetics model for it. The results with IPN and the kinetic are described at the end of this section after the results for nitromethane are discussed.

The data reported here is for flames to which nitromethane was added to the fuel side. Because of difficulties getting the nitromethane to completely dissolve in heptane, the base fuel was changed to an 80% heptane/20% toluene mixture by volume. This base flame was found to be much more soot producing than a neat heptane/air flame. Even with the heptane/toluene fuel mix, it was found that above an added oxygen component of approximately 2.4% by weight (about 3 ml of nitromethane added to 100 ml of heptane/toluene mix), some nitromethane would separate out if allowed to stand for a few minutes.

The experimental procedure was as follows. Fuel and airflow were initiated, and the flame ignited by placing a small torch between the burner ducts. Once the flame was established, a nitrogen shroud (heated) was used to prevent outside air from being entrained in the fuel flow. Approximately half of the contents of the injection pump (50 ml capacity) were dispensed into the flame when collection of data began. Each data point represents the average of the PLII signal produced by 100 laser shots. After every few data points the laser was blocked and an emission spectrum was recorded. The emission from the flame was typically 2.5 % of the PLII signal. Each charging of the injection pump yielded between 5 and 10 data points. Figures 3.2.5-1 and 3.2.5-2 show a PLII image of a heptane/air flame, and the resulting pixel intensities along the burner centerline of the PLII image, respectively.

Results

Figure 3.2.5-3 shows the peak pixel value of the raw PLII signal measured along the centerline of the burner for fuel side addition of nitromethane to heptane/toluene/air flames, up to an oxygen addition from nitromethane corresponding to 2.4% oxygen by weight. The data shown in Figure 3.2.5-3 is not corrected for emission. For each addition of nitromethane to the fuel stream, an increase in particle formation was observed. The amount of soot formation was

approximately proportional to the amount of nitromethane added to the fuel stream, and was independent of whether successive tests involved increases or decreases of the additive. The increase in soot reported here for small nitromethane addition to the fuel stream was also seen for small additions of ethanol and isopropyl nitrate to the fuel stream of heptane/air opposed flow flames, and for ethanol addition to the fuel stream of ethylene/air opposed flow flames. Modeling results suggest the increase in soot for the ethylene/air opposed flow flames upon addition of ethanol to the fuel stream may be attributed to introduction of hydrocarbon radicals in extremely fuel-rich areas near the stagnation plane. Currently, modeling efforts (OPPDIF, Reaction Design) are underway to help understand the increase in soot formation observed for the heptane/toluene/air flames with fuel side nitromethane addition. However, to date we have been unsuccessful in achieving a convergent solution. We believe the main difficulty to be the large size of the reaction mechanism used in the modeling calculations (1700 reactions).

Figures 3.2.5-4 and 3.2.5-5 show calculated temperature and A1 (benzene) formation for neat ethylene/air flames and ethylene/air flames to which 4 mole percent nitromethane has been added to the fuel side. The calculations predict that nitromethane addition to the fuel side of these flames should increase soot precursor formation. Although we have been unable to obtain convergence with the heptane/toluene/air mechanism, we believe the behavior may be similar.

The results from the experiment with nitromethane added to the fuel side of heptane/air flames (increased particle formation) and the results of calculations showing increases in soot precursor concentrations when nitromethane is added to the fuel side of ethylene/air flames suggest that the explanation provided earlier for observed increases in soot formation may apply here. That is, the increase in soot for opposed flow flames upon addition of nitromethane to the fuel stream may be attributed to introduction of hydrocarbon radicals in fuel-rich areas near the stagnation plane. Therefore, we believe that a preliminary result of this work is that in the diffusion flame region of the combustor, production of methyl radical in relatively cool, fuel-rich regions should be avoided.

This is supported by results of calculations that predict fuel side addition of methanol to decrease soot. The initial decomposition of methanol in the flame proceeds by the following two reactions:

$CH_3OH + H \rightarrow$ $CH_2OH + H_2$ ~70% (R1)

$CH_3O + H_2$ ~29 (R2)

Therefore, a main difference between ethanol and methanol decomposition when added to the fuel stream is that ethanol produces methyl and increases aromatics, while methanol produces no methyl and decreases aromatics. An intriguing result from this work is that aromatic production may be modified if the temperature at which CH_2OH is formed is forced to occur in hotter portions of the flame. This suggests that a possible route to particle suppressants involves tailoring species production to different flame regions.

Isopropyl nitrate

Figure 3.2.5-6 shows PLII images of heptane/toluene opposed flow flames with increasing amounts of IPN added to the fuel stream. Figure 3.2.5-7 shows a brief summary of results of these preliminary experiments. These initial experiments were encouraging, although the PLII measurements exhibited a fair amount of scatter. In order to fully evaluate the effectiveness of isopropyl nitrate as a soot reduction agent, we believed it was necessary to develop a chemical kinetic mechanism for the combustion of this additive in heptane/air flames.

Development of IPN Combustion Mechanism

With the help of Valeri Babushok at NIST, a combustion mechanism was developed for combustion of IPN in heptane/air flames, including nitrogen chemistry. This mechanism was assembled from mechanisms for heptane combustion posted on the Lawrence Livermore National Laboratory website. Unfortunately, by the conclusion of the project, transport files for all species in the mechanism were incomplete. Therefore, all calculations predicting combustion behavior used a closed homogeneous reactor as the combustor. Figure 3.2.5-8 summarizes the process of assembling the mechanism. We must also strongly emphasize that this mechanism is not yet validated by experiment.

Figure 3.2.5-9 shows a section of the mechanism (CHEMKIN format, including the main decomposition reaction for IPN). The full mechanism consists of 249 species and 2032 reactions. Figures 3.2.5-10 and 3.2.5-11 show the calculated thermal decomposition products of IPN at 1500 K and at 2500 K, respectively. The major decomposition product at each

temperature is predicted to be H2 gas. Figure 3.2.5-12 shows results of calculations (closed homogeneous reactor) that predict ignition delay when the IPN decomposition products encounter oxygen. These calculations were performed to investigate whether an additive could be used to provide decomposition products that could be temperature programmed to react in different combustor zones. The calculations show that ignition delays of up to tens of milliseconds may be achieved within a narrow temperature range.

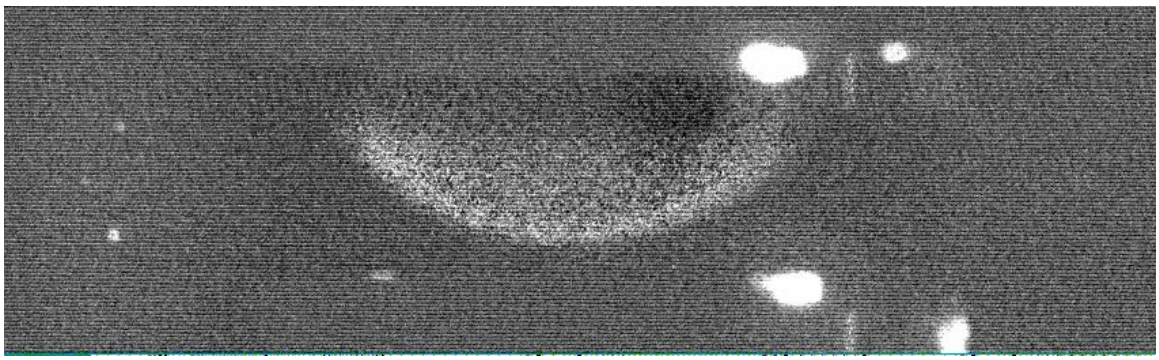

Figure 3.2.5-1. A PLII Image of a Heptane/Air Flame.

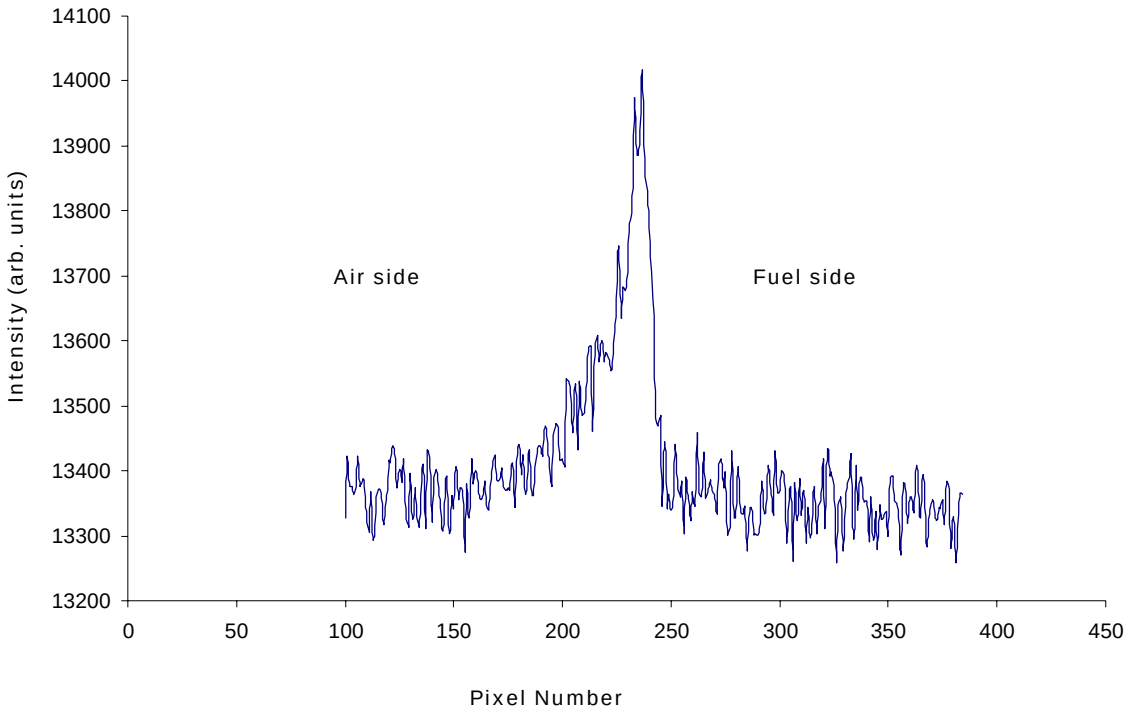

Figure 3.2.5-2. Pixel Intensities Along the Burner Centerline of the PLII Image of a Heptane/Air Opposed Flow Flame.

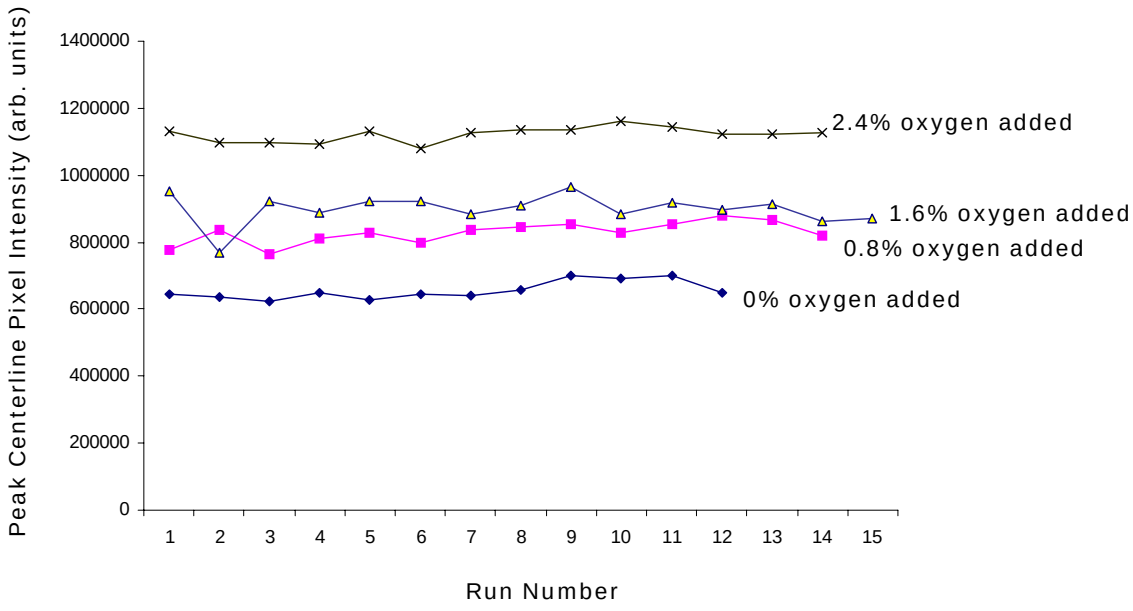

Figure 3.2.5-3. The Peak Pixel Value of the Raw PLII Signal Measured Along the Centerline of the Burner for Fuel Side Addition of Nitromethane to Heptane/Toluene/Air Flames. (Up to an oxygen addition from nitromethane corresponding to 2.4% oxygen by weight.)

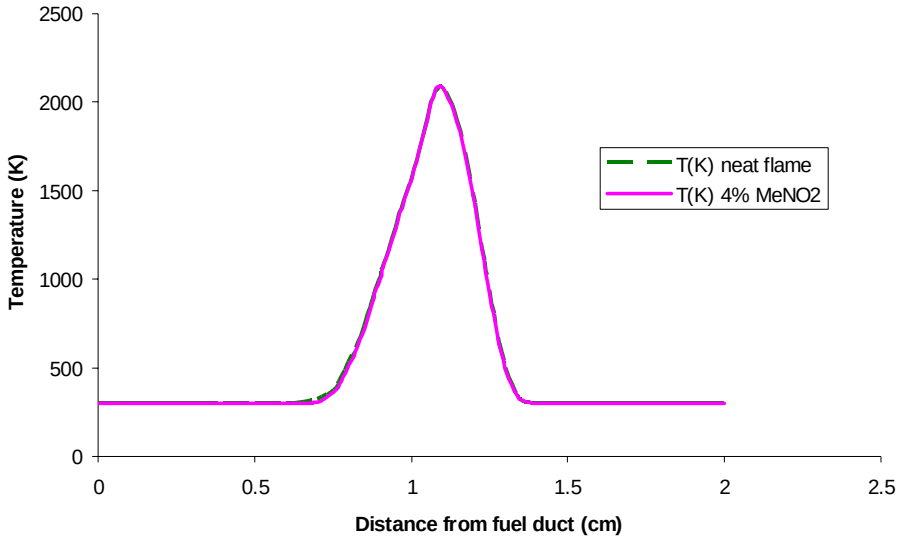

Figure 3.2.5-4. Calculated Temperature for Neat Ethylene/Air Flames and Ethylene/Air Flames to which 4 Mole Percent Nitromethane has been Added to the Fuel Side.

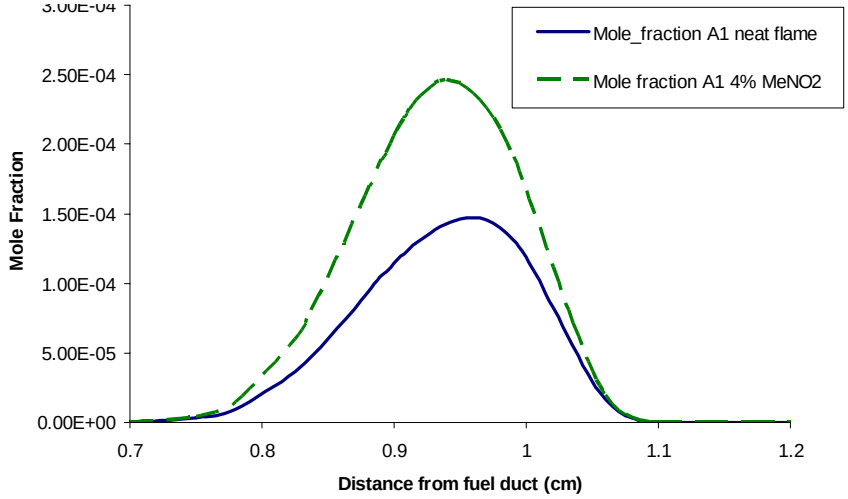

Figure 3.2.5-5 Calculated A1 Concentrations for Neat Ethylene/Air Flames and Ethylene/Air Flames to which 4 Mole Percent Nitromethane has been Added to the Fuel Side.

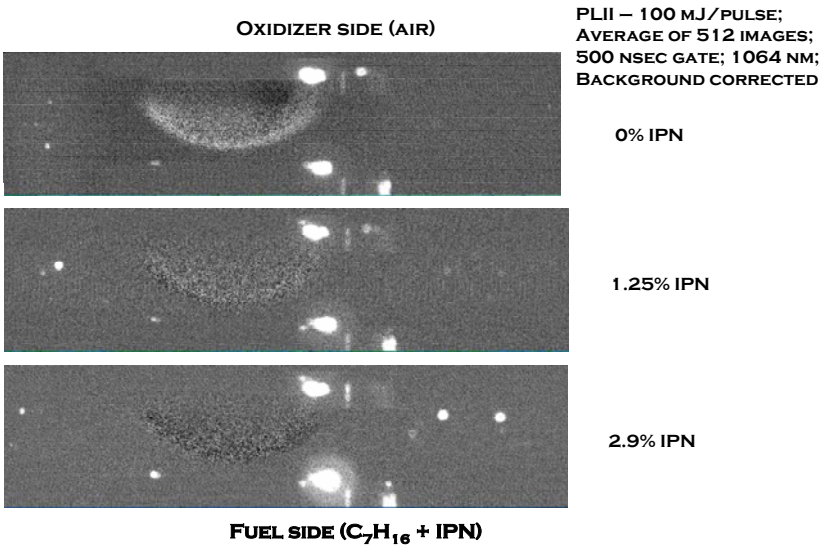

Figure 3.2.5-6. PLII Images of Heptane/Air Flames to which Isopropylnitrate has been Added on the Fuel Side.

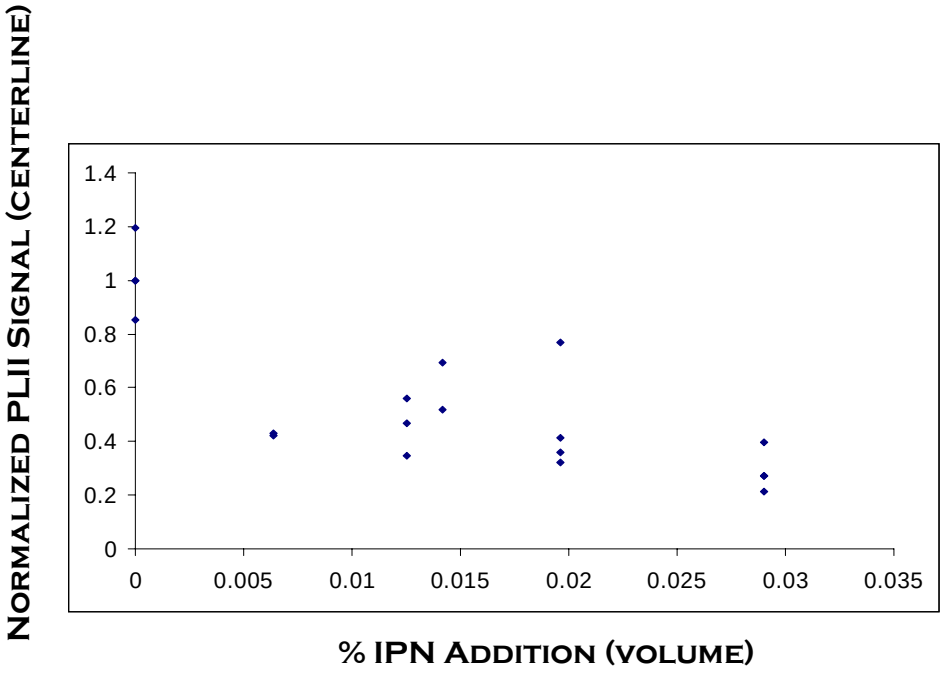

Figure 3.2.5-7. PLII Signal (peak centerline) vs IPN Addition to the Fuel Stream of Opposed Flow Heptane/Air Flames.

Calculations of IPN ($C_3H_7ONO_2$) Decomposition in Heptane/Air

model sources:

a) NO/NO_2/ - C1-C3 - Westbrook et al;
b) b) heptane-reduced - Seiser, Curran et al
c) c) N-reactions from Gri-mech.
d) decomposition of isopropylnitrate (Babushok)

249 species
2032 reactions

Closed
Homogeneous
Reactor

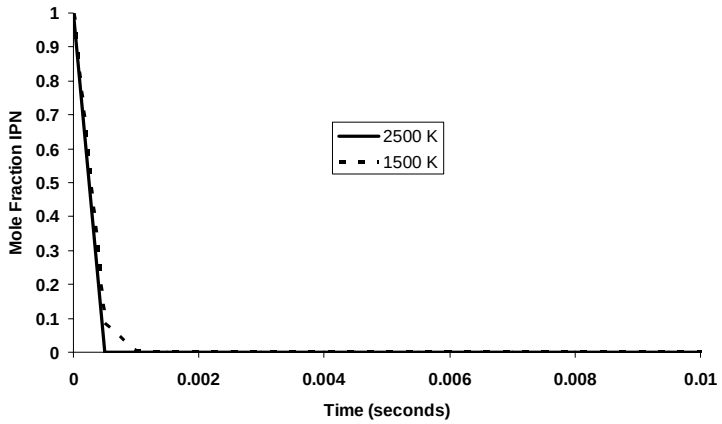

IPN Decomposition in < 1ms at T > 1500K

Figure 3.2.5-8. Overview of the Chemical Kinetic Mechanism Used to Describe Combustion of IPN in Heptane/Air Flames.

```
                                                    Pre-exp  Temp Exp  Act Energy
489. ch2chch2o+no2=ch2chcho+hono                    2.70E+12    0.0      105.0
490. c2coj+no2=acetone+hono                         2.70E+12    0.0      105.0
491. cccoj+no2=cccho+hono                           2.70E+12    0.0      105.0
492. ic3h7ono2(+m)=ic3h7o+no2(+m)                   3.80E+13    0.0    32600.0
     Low pressure limit:  0.12600E+18  0.00000E+00  0.42000E+05
493. ch3+h(+M)=>ch4(+M)                             2.14E+15   -0.4        0.0
     h2              Enhanced by    2.000E+00
     h2o             Enhanced by    5.000E+00
     co              Enhanced by    2.000E+00
     co2             Enhanced by    3.000E+00
     Low pressure limit:  0.33100E+31 -0.40000E+01  0.21080E+04
     TROE centering:      0.00000E+00  0.10000E-14  0.10000E-14  0.40000E+02
494. ch4(+M)=>ch3+h(+M)                             1.05E+21   -1.4   107900.1
     h2              Enhanced by    2.000E+00
     h2o             Enhanced by    5.000E+00
     co              Enhanced by    2.000E+00
     co2             Enhanced by    3.000E+00
     Low pressure limit:  0.16300E+37 -0.50000E+01  0.11001E+06
     TROE centering:      0.00000E+00  0.10000E-14  0.10000E-14  0.40000E+02
495. ch4+h=>ch3+h2                                  1.73E+04    3.0     8224.0
496. ch3+h2=>ch4+h                                  6.61E+02    3.0     7744.0
497. ch4+oh=>ch3+h2o                                1.93E+05    2.4     2106.1
498. ch3+h2o=>ch4+oh                                4.82E+02    2.9    14859.9
```

Figure 3.2.5-9**.** A Portion of the Chemical Mechanism for IPN Burning in Heptane/Air. The initial decomposition reaction of IPN is shown in bold.

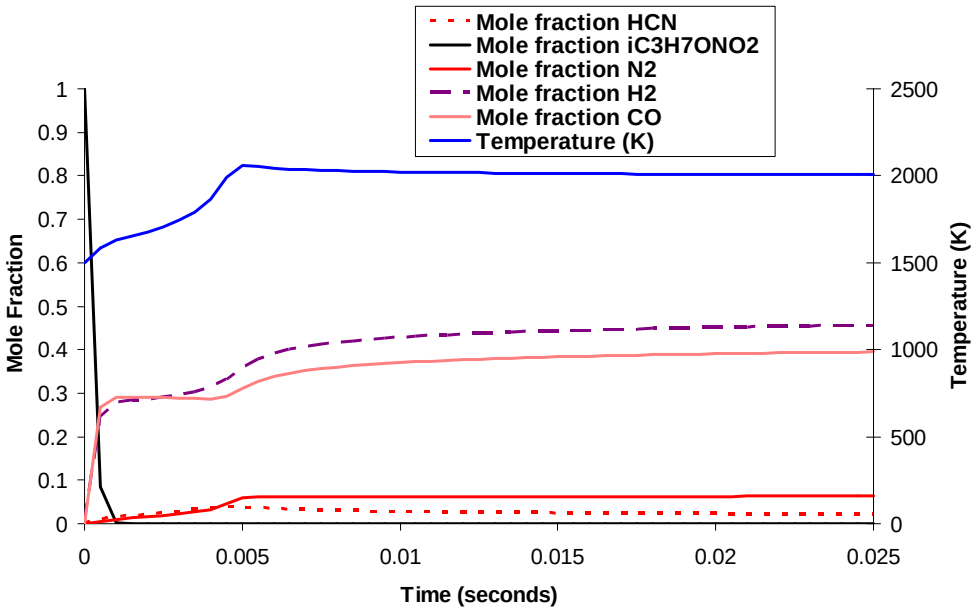

Figure 3.2.5-10. Calculated Thermal Decomposition of Neat Isopropyl Nitrate at 1500 K in a Closed Homogeneous Reactor. Major decomposition products are H2, CO, N2, HCN.

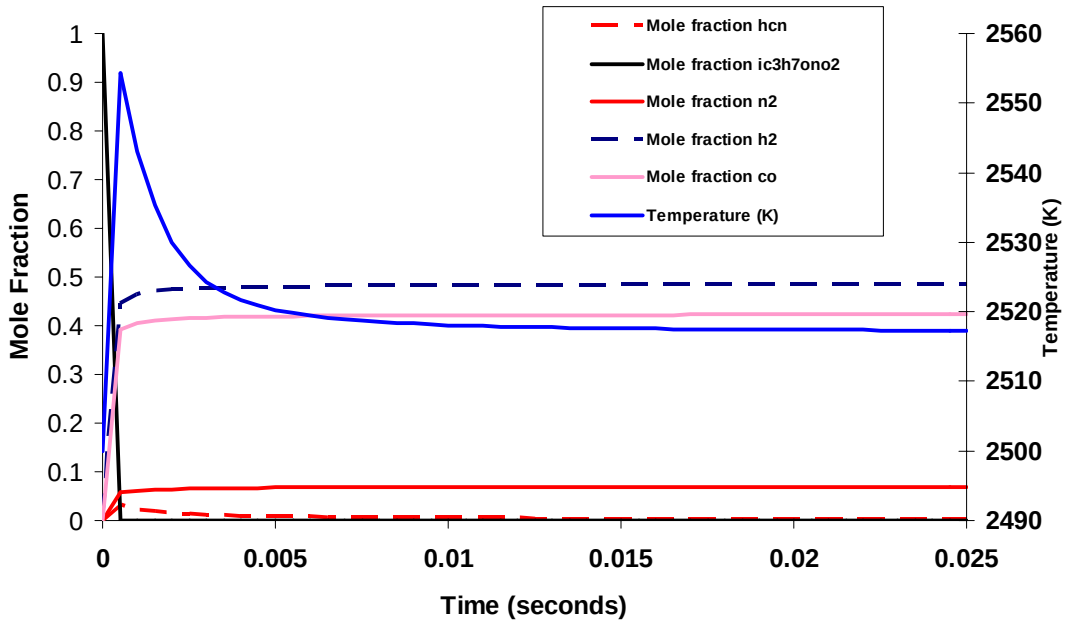

Figure 3.2.5-11. Calculated Thermal Decomposition of Neat Isopropyl Nitrate at 2500 K in a Closed Homogeneous Reactor. Major decomposition products are H2, CO, N2, HCN.

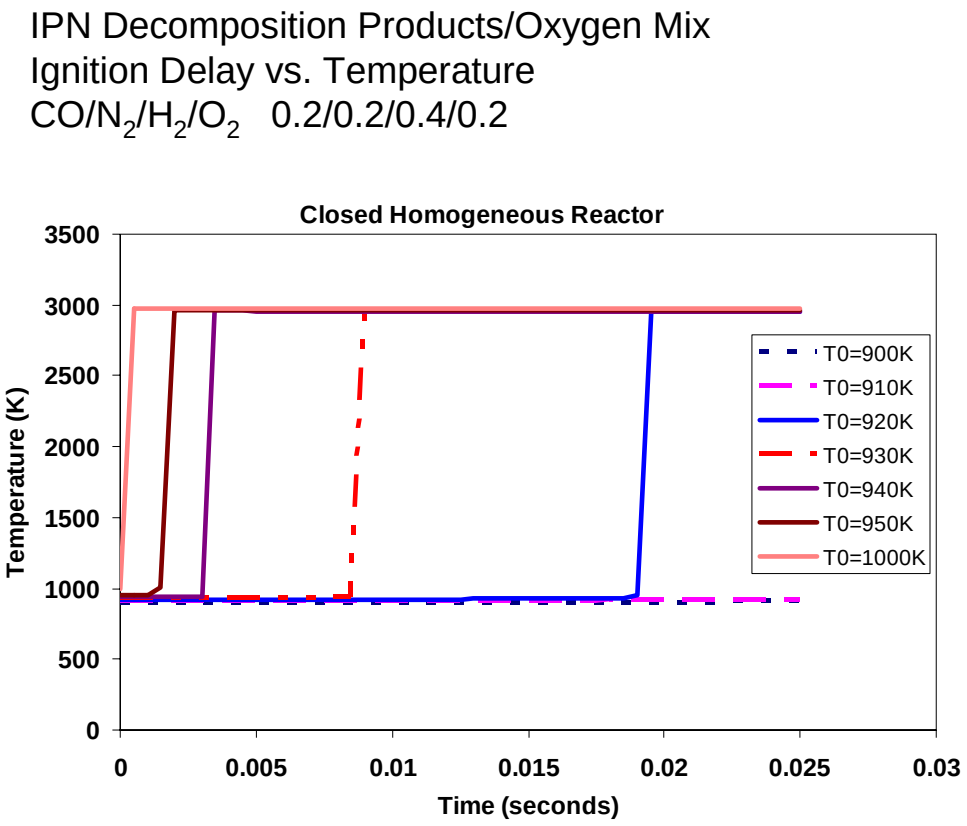

Figure 3.2.5-12. Results of Calculations (closed homogeneous reactor) that Predict Ignition Delay when the IPN Decomposition Products Encounter Oxygen. These calculations were performed to investigate whether an additive could be used to provide decomposition products that could be temperature programmed to react in different combustor zones.

3.2.6 TURBULENT SPRAY FLAME

Experimental Conditions

A mixture of 20% toluene/80% heptane was used as the base fuel for these experiments to better approximate the composition of JP-8 relative to pure heptane. Due to the greater tendency of this fuel to soot compared to pure heptane, the experiments were run at a leaner equivalence ratio of 2.37 versus 2.76 for heptane. The airflow rate was the same as that for the heptane/ethanol experiments so the cold flow Reynolds number was identical for the two sets of tests. The commercial additive was added at 5% by volume. At the time of the initial experiments with the commercial additive, its chemical constituents and properties were not

available. Therefore, the fuel flow rates with and without the commercial additive were not corrected, but adopted the same value. The experimental conditions of the study are listed in Table 3.2.6-1.

Subsequent to the initial experiments with the commercial additive, its basic composition was determined and the main components with a potential to reduce soot were identified as cyclohexanone, nitromethane, nitroethane, and nitropropane. These components were run individually in the turbulent spray flame to determine their effectiveness in reducing soot under conditions similar to those listed in Table 3.2.6-1. Nitromethane was not run in these experiments because of the possibility that it could explode upon compression. The tests were done at two levels of oxygen addition, 2% and 4% of the fuel by mass.

Experimental Results

The commercial additive showed very interesting time dependent behavior in these experiments. After it was first introduced, the amount of soot decreased slowly to a steady state level; when the additive was removed, the soot increased slowly toward the initial baseline level. This behavior is illustrated in Figure 3.2.6-1. A number of experiments were run to determine the cause of this slow time response. Unfortunately, difficulty getting good repeatability in these experiments due to nozzle fouling made it impossible to determine the cause of the time dependent behavior.

Data to determine the effect of the additive on soot were collected during the steady periods of behavior. Three hundred (300) shot averages were used and the results were background corrected and also corrected for pixel-to-pixel variation. Figure 3.2.6-2 presents a plot of the average LII intensity for the flame with and without the commercial additive. The results for the commercial additive show that it has a greater effectiveness than ethanol. Soot yields decreased by about 40%, even though its volume fraction is significantly less than that used for ethanol.

Following this work, experiments were performed to test the effective individual components in the commercial additive. Figure 3.2.6-3 presents summaries of the effect of the nitroethane and nitropropane on soot formation in the turbulent spray flame. The effectiveness of ethanol and cyclohexanone are also presented for comparison purposes. The nitroalkanes are both more effective than ethanol at equivalent oxygen levels, and the cyclohexanone leads to soot reductions on the order of those for ethanol.

Table 3.2.6-1: Experimental Conditions for Heptane/Toluene Fuel and Commercial Additive

Base Fuel Formulation	80% Heptane, 20% Toluene by volume
Additive	Commercial Additive
Base Fuel Supply (g/s)	0.28
Fuel with Additive Supply (g/s)	0.28
Air Supply (g/s)	1.76
Equivalence Ratio for Bseline Test	2.37

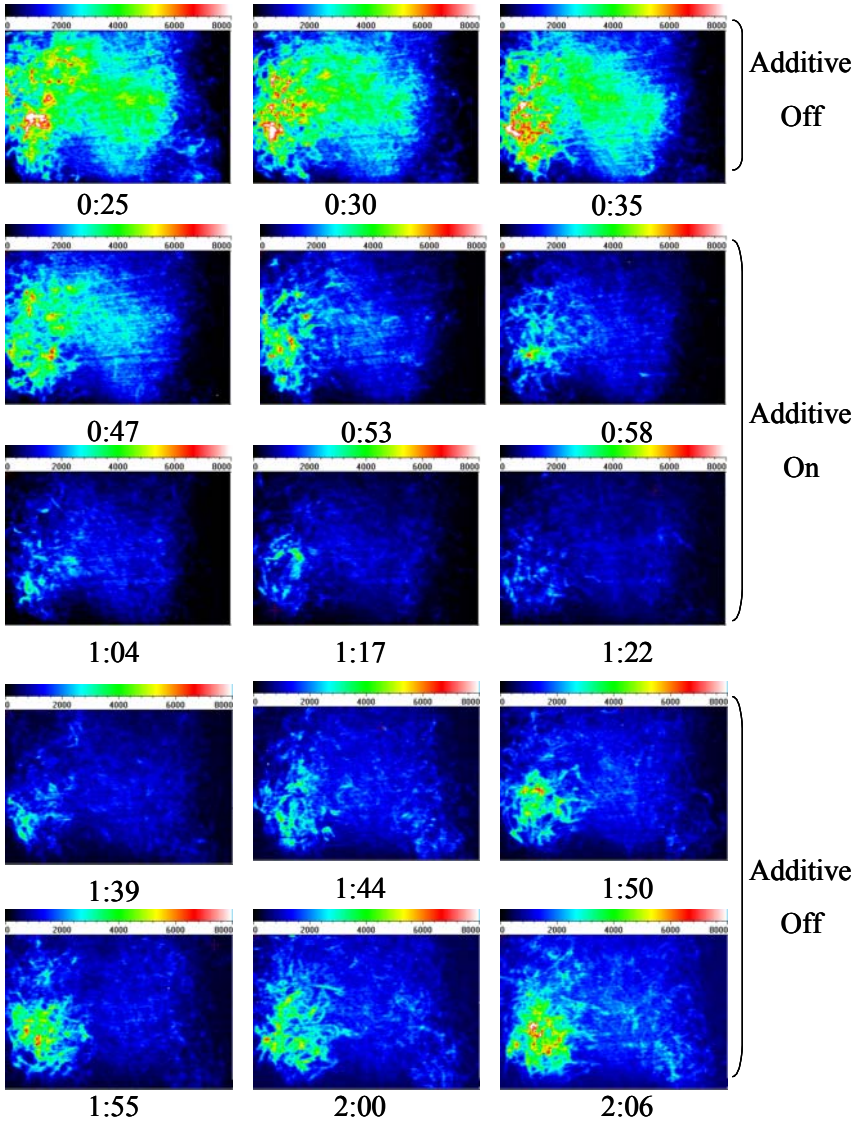

Figure 3.2.6-1. Series of LII Images Illustrating the Time Dependent Behavior of the Commercial Additive.

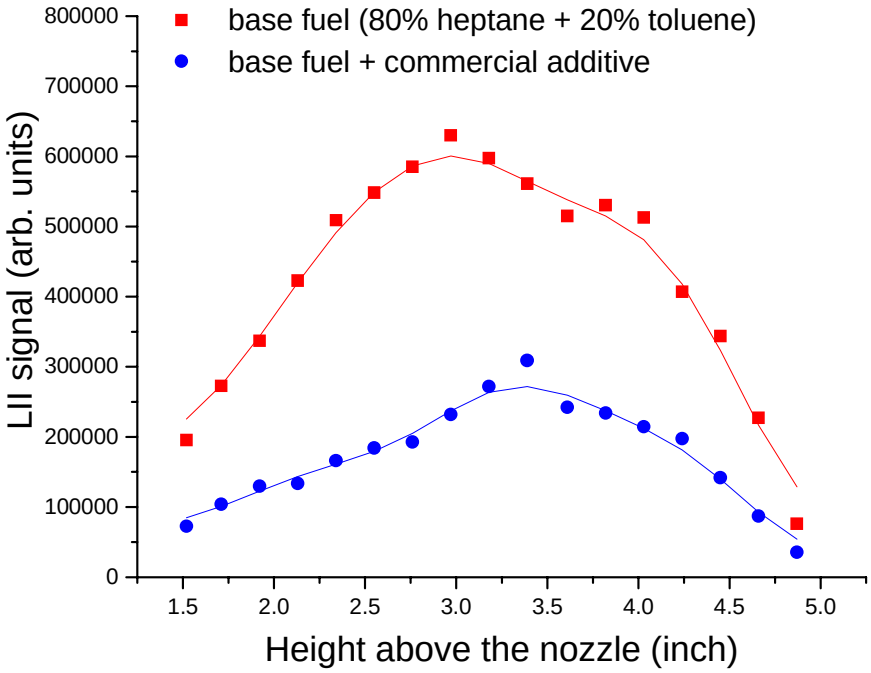

Figure 3.2.6-2. Effects of Commercial Additive on Soot.

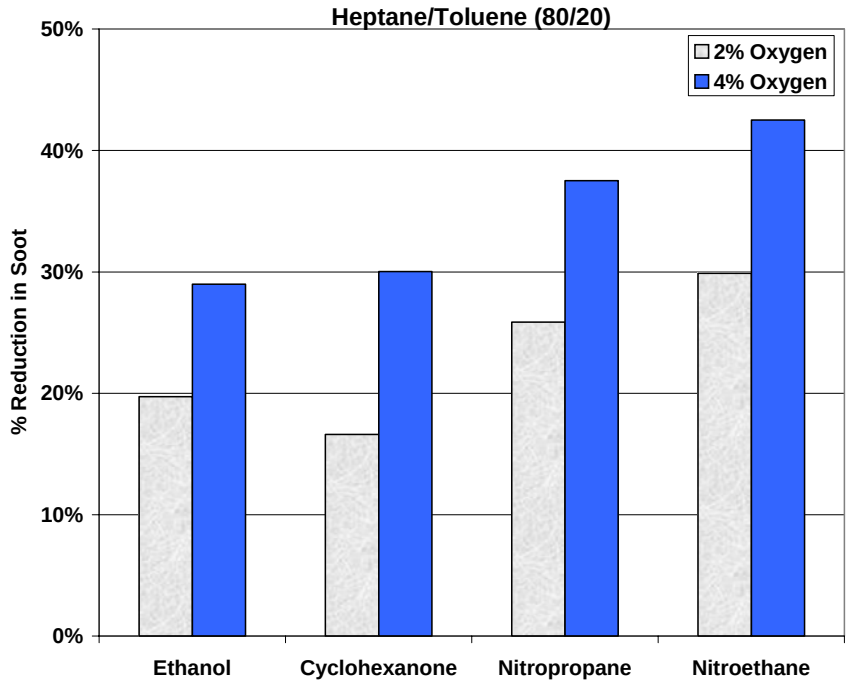

Figure 3.2.6-3. Effect of Individual Components of the Commercial Additive on Soot (ethanol included for comparison purposes).

3.2.7 HIGH PRESSURE TURBULENT REACTOR

All tests with nitroalkane additives in the high pressure turbulent combustor were run with JP-8 as the fuel, a major consideration being its reasonable cost compared to the heptane/toluene blend. The airflow for the tests was 32 gm/s and the equivalence ratio was 1.3. The inlet air temperature was 550 K and the chamber pressure was 0.5 MPa. Only two of the three nitroalkanes from the commercial additive were studied, nitroethane and nitropropane. The third, nitromethane, can detonate due to compression so it was not run in these experiments.

Experimental Results

Figure 3.2.7-1 presents a summary of the test results on soot volume fraction versus additive concentration. Nitroethane was added to JP-8 in concentrations ranging from approximately 2.5% to 10% by volume of the fuel. It was found that the nitroethane reduced soot at all concentrations. The soot suppression effect was found to increase with increase in the additive concentrations. At the lowest concentration of about 2.5%, the soot reduction was roughly 20%; at an additive concentration of 10% by volume in the fuel, the reduction was ~70%. Similar trends were observed with the addition of nitropropane. Although the reduction in soot was approximately the same as with nitropropane at the lowest additive concentrations, the reduction was slightly lower than nitroethane at higher additive concentrations. At an additive concentration of about 10% by volume of JP-8, nitropropane reduced soot by approximately 60%.

These levels of reduction were substantially greater than those obtained with ethanol. Modeling of the experiments could not be performed with standard tools in CHEMKIN due to the complexity of the flowfield, so the reasons for the greater effectiveness observed could not be identified through modeling.

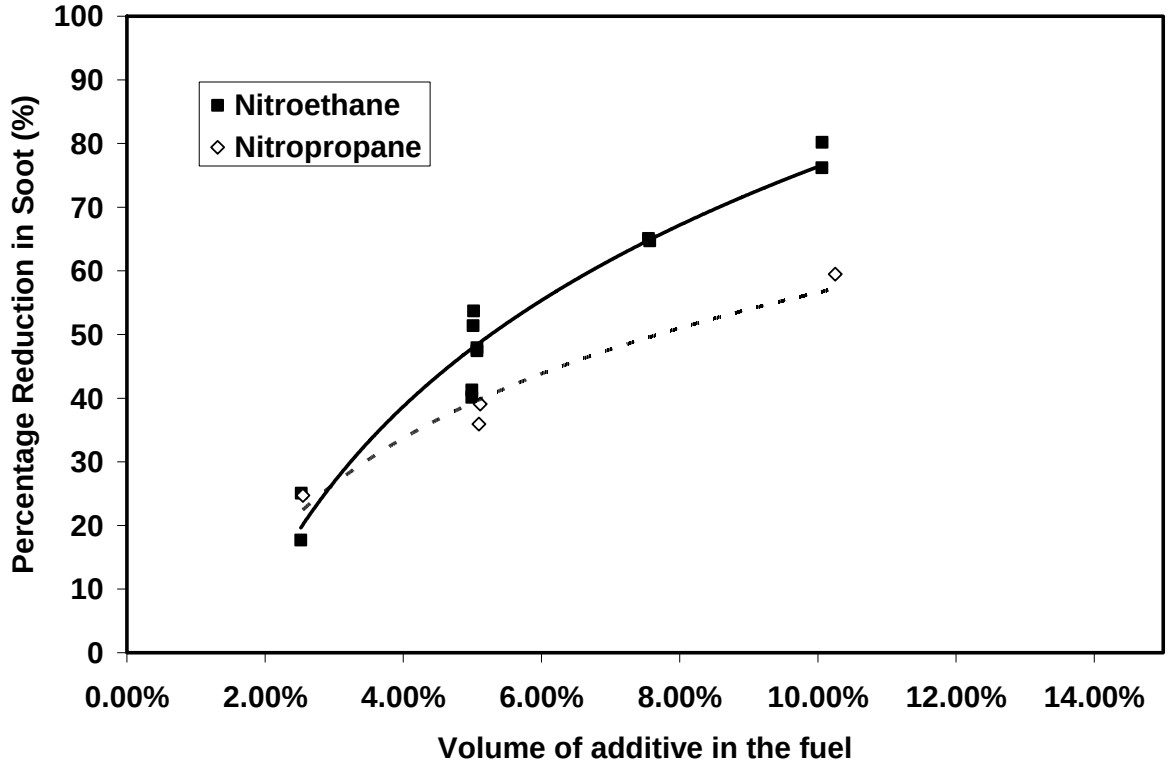

Figure 3.2.7-1. Effect of Nitroalkanes on Soot Formation in the Dump Combustor with JP-8.

3.2.8 MODELING STUDY: NITROMETHANE IN JET DIFFUSION FLAME

Calculations were performed for a jet diffusion flame for understanding the effects of nitromethane on soot formation. The fuel jet and coflow air velocities used are 0.05 m/s and 0.2 m/s, respectively. The fuel jet diameter is 1 cm. Pure fuel (100% heptane) and blended fuel (80% heptane + 20% toluene) are used as fuels. Effect of nitromethane on soot formation in these flames is studied by adding various amounts of nitromethane to the fuel jet. Two-dimensional calculations are performed using a grid system with 151 x 101 mm nodes on a physical domain of 150 x 50 mm.

Results obtained for 100% heptane flame are shown in Figure 3.2.8-1. Distributions of soot mass fraction in these flames are shown. Peak value corresponding to white color is ~ 3% of the total gas mass. Regions shaded with white represent flame locations where soot mass fraction has increased beyond 3% level. As seen from Figure 3.2.8-1 soot is increasing with the addition

of nitromethane. However, addition of nitromethane is also reducing the flame height and flame diameter. Consequently, increase in local soot concentration may not necessarily result into an increase in total soot generated in these flames. For finding this possibility, flame structures in radial and axial directions are shown in Figures 3.2.8-2, 3.2.8-3, and 3.2.8-4. The axial velocity and temperature profiles obtained at a height of 60 mm (Figure 3.2.8-2) indicate that the flame diameter decreases with the addition of nitromethane. Flame is also accelerating at the centerline due to volumetric expansion resulting from higher temperature. As seen from Figure 3.2.8-3(a, heptane is more rapidly consumed in the presence of nitromethane. While heptane in the 80% fuel case depleted to 1.5% heptane in the 100% fuel case depleted only to 6%. Consistent with the increase in soot mass fraction, peak concentrations of benzene, acetylene and biphenyl are increasing with the addition of nitromethane (Figure 3.2.8-3(b)).

In order to assess the overall effect of nitromethane in these jet flames, mass fractions of heptane, benzene, acetylene and biphenyl are integrated over the flame cross section at different flame heights. The results are shown in Figures 3.2.8-4(a) and 3.2.8-4(b). Interestingly, net mass fractions of benzene, acetylene and biphenyl are decreasing with the addition of nitromethane. This suggests that even though nitromethane increases the local concentrations of PAH species and soot in a jet flame, the overall production of these species is actually decreased.

Results obtained for 80% heptane+20% toluene fuel blend are shown in Figures 3.2.8-5(a) and 3.2.8-5(b). Even though addition of nitromethane flame up to 18% yielded stable flames, addition of 20% nitromethane destabilized the flame base and the flame became extinguished in time. The data shown in Figures 3.2.8-5(a) and 3.2.8-5(b) for the 20% nitromethane case was obtained from the instantaneous solution obtained during the blowout process. Similar to the pure heptane flames, local soot mass fraction increased with the addition of nitromethane in the blend-fuel case also. Due to the reduction in the flame size, the net production of benzene, acetylene and biphenyl are decreased with the addition of nitromethane.

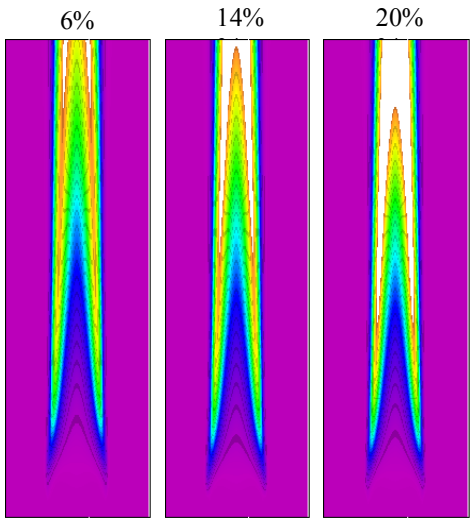

Figure 3.2.8-1. Soot Distribution in a Jet Diffusion Flame with Different Levels of Nitromethane Added to Heptane Fuel Jet. Each image represents 120 mm height. Excess soot is marked in white.

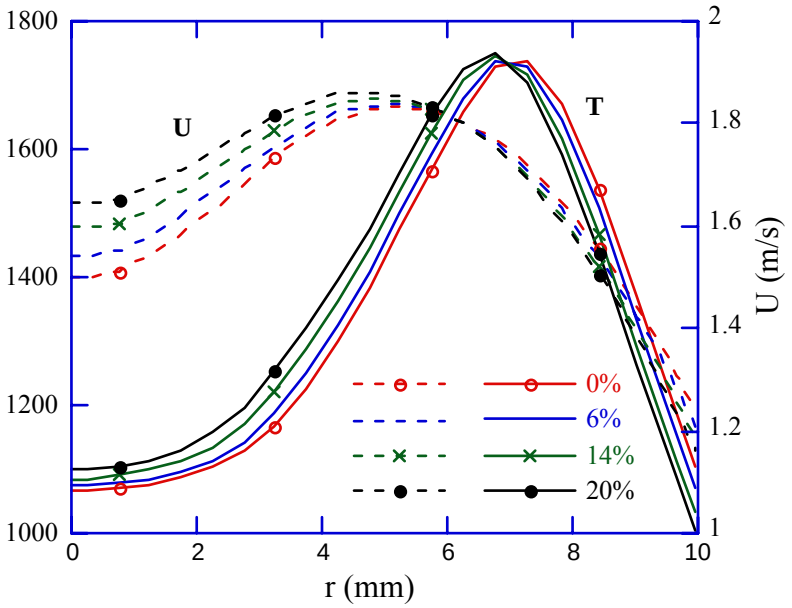

Figure 3.2.8-2. Distributions of Axial Velocity and Temperature at a Height of 60 mm Above the Burner.

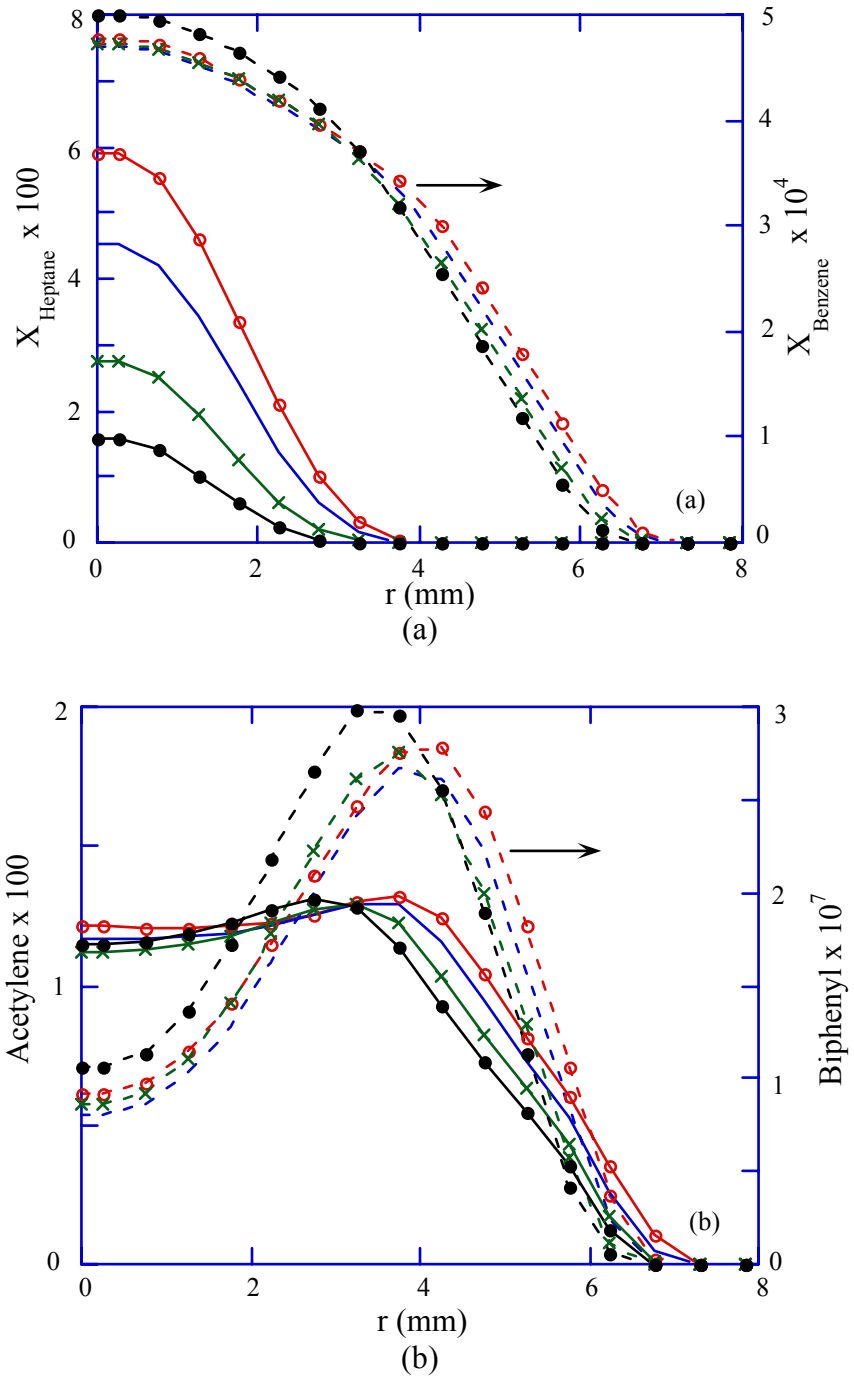

Figure 3.2.8-3. Concentration Distributions of (a) Heptane and Benzene and (b) Acetylene and Biphenyl at a Height of 60 mm Above the Burner.

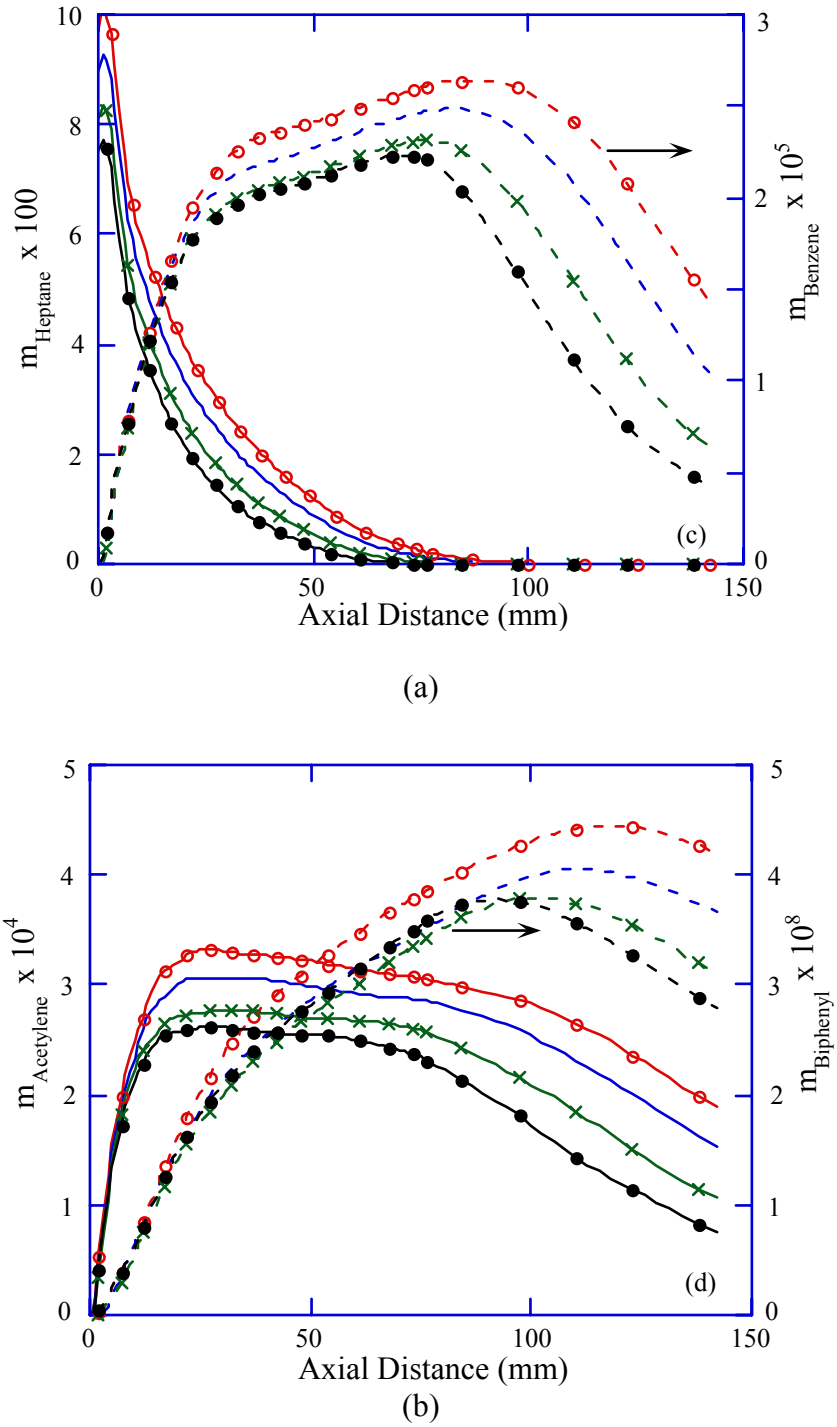

Figure 3.2.8-4. Total Mass Fractions of (a) Heptane and Benzene and (b) Acetylene and Biphenyl at Different Heights in the Flame for Various Concentrations of Nitromethane. Lines with open circles, no symbols, crosses, and solid circles represent 0, 6, 14, and 20 % nitromethane, respectively.

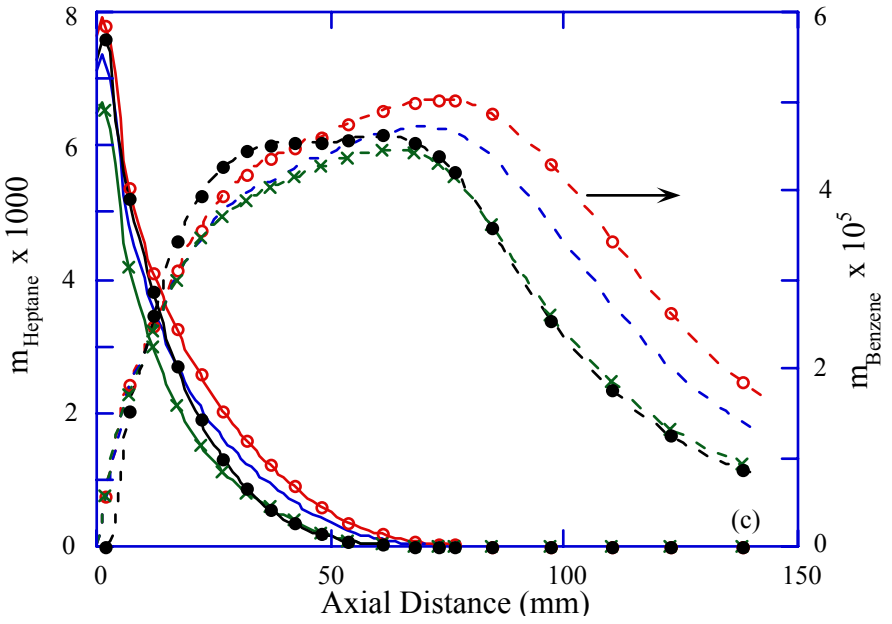

(a)

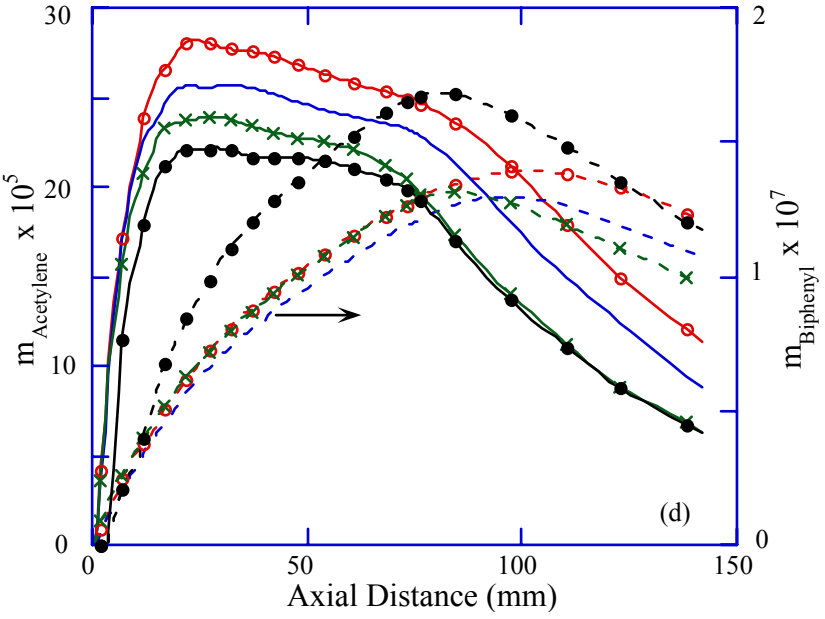

(b)

Figure 3.2.8-5. Total Mass Fractions of (a) Heptane and Benzene, and (b) Acetylene and Biphenyl at Different Heights in 80/20 Heptane/Toluene Jet Diffusion Flame for Various Concentrations of Nitromethane. Lines with open circles, no symbols, crosses, and solid circles represent 0, 6, 14, and 20 % nitromethane, respectively.

3.3 NITROGEN DIOXIDE

Due to the fact that NO_2 was identified as a major intermediate in the reduction of soot by the nitroalkane species, experiments were run with NO_2 addition to understand its direct effect on soot. Experiments with NO_2 addition were performed in the shock tube at UDRI and in a premixed flame at Penn State. Since the Penn State premixed flame facility was not set up to utilize prevaporized liquid fuels, those experiments were performed with ethylene as the fuel.

3.3.1 SUMMARY OF MAJOR RESULTS

The study of NO_2 addition in the shock tube was directed at checking the hypothesis that the methyl radical formed when nitromethane decomposes could offset the tendency of the NO_2 to reduce soot. The experimental results did not confirm this hypothesis; they showed a small decrease in soot at lower temperatures and a small increase at higher temperatures. Therefore, the results were not significantly different than those for nitromethane. Modeling was then undertaken to investigate the effect, but the study did not yield conclusive answers, potentially due to difficulties with the kinetic model.

The study of NO_2 addition to the ethylene flame was conducted in order to determine the relative contributions of temperature changes and direct kinetic effects on reducing soot. The study yielded the very unusual result that soot decreased, but the polycyclic aromatic hydrocarbons increased. Modeling of the flames with and without the addition of NO_2 was used to understand the reason for the increased PAH, which appears to be linked to higher yield of acetylene when NO_2 is added.

3.3.2 SHOCK TUBE

When results of an earlier nitroalkane study showed that addition of nitromethane did not decrease soot or PAH yields, it was hypothesized that perhaps the presence of the methyl radical (CH_3) negated any soot reduction that may have occurred due to generation of oxidative radicals by the NO_2 group of nitromethane. Therefore, to test this hypothesis, another set of experiments was performed where NO_2 was used as an additive. The NO_2 molar concentration in these experiments was the same as the available NO_2 molar concentration in the nitromethane experiments. Figure 3.3.2-1 shows the normalized soot yield curve for this set of experiments. The addition of NO_2 causes a slight reduction in soot yields at the lower temperature range and

an increase in soot yields at the higher temperatures. Thus, it is possible, as shown in previous studies, that the addition of NO_x compounds could reduce soot yields [Ray 1964, Ai-Rubaie 1991]. Engine manufacturers observe large reductions in soot yields when the NO_x emitted from engines is converted to NO_2 using catalyst which is then recirculated into the engine. This is one of the methods utilized by diesel engine manufacturers to control particle emissions. However, since large amounts of NO_2 are used during exhaust gas recirculation, it is possible that more reductions in soot yields than that observed here with the addition of NO_2 may be observed if a higher concentration of NO_2 is used, especially in the lower temperature range. The results of this study show only qualitatively that the addition of NO_2 may decrease soot at lower temperatures because quantitatively the observed impact of NO_2 on soot yield is within the experimental scatter.

Product analysis showed that NO_2 additive experiments generated products similar to those observed in nitromethane experiments. Figures 3.3.2-2 and 3.3.2-3 show normalized yields of a few selected soot precursors from analysis of gaseous products and from thermal desorption of soot filters. In these figures, the solid lines also indicate experimental trends and dashed lines indicate model trends. Similar to the nitromethane study, benzene was the only volatile product that was quantified for NO_2 experiments. The soot precursor results from the analysis of both gaseous and soot samples are similar to those observed in nitromethane, except for i-ethenyl naphthalene. The addition of nitromethane increased the yields of ethenyl naphthalene over the base fuel at the lower temperature, but the addition of NO_2 decreased its yields at the lower temperature. This difference is perhaps due to the presence of the methyl radical in nitromethane. Results of a study conducted by Senkan and Castaldi [Senkan 1996], and later verified by Roesler et al [2001], suggest that the presence of methyl radical promotes the formation of hydrocarbon species containing an odd number of carbon atoms, which would then increase the production of benzene and naphthalene through resonantly stabilized radical pathways and could lead to higher PAH and soot yields. To verify this hypothesis, the benzene and naphthalene yields for nitromethane and NO_2 experiments were compared, and it was found that nitromethane had higher yields at the lower temperature. This suggests that presence of methyl radical (a possible soot precursor) may have negated any impact the NO_2 in nitromethane had on reducing the soot yields. Nitrogenated compounds observed in NO_2 experiments were similar to those observed in nitromethane experiments except for 2-nitro phenol, which had

higher yields for NO_2 experiments. It has been hypothesized that because of their high thermal stability, nonvolatile PAH (NPAH) do not form soot, which suggests that carbon that has been used for NPAH formation is no longer available for soot formation [Yu 1999].

Results from these experiments show that NO_2 and nitromethane reaction systems share many similarities. This suggests that perhaps all NO_x additives behave in a similar fashion. However, the observations made for PAH yields from results of this NO_x additive study are not consistent with the results of the Ray and Long study [1964]. In their study with the NO_x additives, Ray and Long observed a reduction in soluble organic content (referred to as NVOC in this study) and no change in elemental carbon. In this study, all the measured nonvolatile PAHs from the additives had higher yields. These different observations could be due to a difference in the solvent, extraction procedure and analytical techniques. Even though we observed an increase in nonvolatile PAHs, it is possible that the lower soot yields in NO_2 experiments were primarily due to reduced elemental carbon yield. If this was the case, Ray and Long [1964] in the final conclusions state that such an observation would conflict with the hypothesis that elemental carbon is formed from PAHs as intermediates. However, in a study on soot and PAH formation from spray combustion of heptane and other hydrocarbons under pyrolytic conditions, Cadman and Wang [1998] observed the same PAHs as observed in this study. They also observed an increase in PAH yields with the addition of oxygen. They hypothesized that the addition of oxygen enhanced hydrocarbon breakdown to smaller radicals which in turn enhanced growth to PAHs and that in an inert atmosphere, polymerization of PAH type radicals to form soot may predominate. Thus, it is possible that at lower temperatures, an increase in the oxidative radical pool due to the addition of NO_2 enhanced PAH formation and inhibited polymerization of PAH type radicals to soot.

Although the addition of nitromethane or NO_2 failed to make a significant impact on soot yield, their addition caused a significant decrease in the measured ignition delay times (see Figure 3.3.2-4). These results are consistent with results of other studies where NO_x compounds were used as additives to enhance ignition [Clothier 1993a, Clothier 1993b, Toland 2003, Inomata 1990, Higgins 1998, Suppes 1996]. In Figure 3.3.2-4, the ignition delays times are plotted against preignition temperatures that have been corrected using a chemical thermometer calibration to account for possible nonideal gas dynamic effects behind the reflected shock. The correction was required due to the high sensitivity of ignition delay to changes in temperature.

As Figure 3.3.2-4 shows, nitromethane had a lower ignition delay than NO_2. Thus it is possible that the hydrocarbon radicals (e.g., methyl) produced from the initial dissociation of nitromethane were able to increase the radical pool which caused a reduction in ignition delay. In a fuel-rich reaction system (Φ =3; conditions of this study), a decrease in ignition delay means that more time is available for molecular growth reaction which will increase PAH yields; this perhaps is a reason for higher PAH yields in additive experiments. In brief, based on the lower temperature results, we can propose that the addition of NO_2 significantly increases the oxidative radical pool which reduces ignition delay times and causes breakdown of the fuel to the smaller reactive species needed for molecular growth reactions. Both of these factors cause an increase in PAH formation. However, an increase in the oxidative radical pool is perhaps also inhibiting or slowing the polymerization of PAH type radicals into soot. At higher temperatures, fuel decomposition rates are already high and the addition of NO_2 does not cause a significant increase in the reactive radical pool. This is the reason that at higher temperatures ignition delay times and PAH yields are very similar for both base fuel and additive experiments.

To better understand the impact of NO_x additives on ignition, the experimental trends in ignition delay times were compared to calculated values from the models. The rise time of the temperature profile from shock simulation was interpreted to indicate the onset of sustained ignition. Also, the ignition delay times from the model were verified through comparison with the peak rise time of CH and OH radicals which are also good indicators of sustained ignition. Global activation energies for the base fuel + additive mixtures are shown in Table 3.3.2-1.

The model results indicated significantly higher activation energies than the experimentally determined values. Also, the activation energy in the model for NO_2 was higher than that for the base fuel. This indicates inaccuracies in the kinetic or thermodynamic data or perhaps that some key reactions involving initial species from additive decomposition are not present or correctly accounted for and need to be revisited. To further investigate the impact of additives on ignition chemistry, the temporal profiles of CH, OH, O, HO_2 and H were examined. Figure 3.3.2-5 shows the profiles of OH and HO_2 as yield % per unit mass of carbon in the fuel at three precombustion temperatures. Similar data at other temperatures and for other species is reported elsewhere [Kahandawala 2004]. These profiles show that at the lower temperature (1100 K) the peak time for these species is longer for NO_2 experiments than the base fuel experiments. But at the higher temperatures, the O, OH and HO_2 peaks from NO_2 experiments

are between the base fuel and nitromethane experiments. The order of evolution of these species at the lower temperature is contrary to experimental observations since the rise times (start of peak yield point in the profiles) of radicals such as OH and CH are good indicators of sustained ignition. This suggests that initial NO_2/fuel interactions at lower temperatures are not accurately represented in the model. This is the reason why activation energy calculated by the model for NO_2 system is higher than the base fuel because model predicts longer ignition delays for NO_2 experiments at lower temperatures, but at higher temperature model predictions are accurate; i.e., evolution of these species in the order of nitromethane $\rightarrow$ NO_2 $\rightarrow$base fuel. Another interesting thing to note is that for additive experiments, the model predicts lower yields of HO_2 at lower temperatures when compared to the base fuel experiments.

To better understand the difference between experimental and model PAH yields, a model was used to generate temporal profiles of some species that are known PAH precursors in dominant soot forming pathways. This was done because any discrepancy in PAH precursor species could accumulate and manifest as significant errors in the overall predictive capability of the model for higher molecular weight PAHs. The model profiles of C_2H_2, C_3H_3 and C_2H_3 as well as the top ten generation/consumption reactions and their sensitivity was calculated at pre-combustion temperatures of 1100, 1300, and 1500 K for the base fuel and for nitromethane experiments.

This analysis showed that the same reactions were important for generation/consumption of soot precursors for both the base fuel and nitromethane experiments. However, the predicted temporal species profiles were different, especially at lower temperatures. All these species appear to evolve earlier for nitromethane than the base fuel which probably gave nitromethane a head start in PAH formation process at the lower temperatures. This effect is reduced at the higher temperatures.

Since experimental evidence (evidence from this study as well as from other studies [Litzinger 2004] suggested that NO_2 has a tendency to reduce soot yields, the profiles of NO_2 and NO were plotted (see Figure 3.3.2-6) and the top 10 reaction sensitivities for NO were examined (reactions 1 to 11) to understand the main reaction pathway through which NO_2 impacted the soot yields. The profiles of NO_2 and NO indicate that at lower temperatures they are both available for a longer time. Although the mechanism indicated problems (incorrect ignition delay times) at 1100 K with NO_2 reactions, it showed the proper ignition delay trend for nitromethane

and also the correct trend at the other two temperatures for NO_2. As a result, we decided to use the mechanism to help understand the impact of NO_2. The top 10 reactions for NO generation/consumption and these temporal profiles indicate a probable regenerative cycle involving both NO_2 and NO. The most dominant reaction in producing NO was reaction 3 (due to the additive nitromethane) and 6, and the most important reaction in consuming NO was reaction 5. Both reactions 5 and 6 indicate an interconversion of NO and NO_2. The observation made previously that HO_2 yield decreases with addition of NO_x additives is perhaps due to this NO and NO_2 regenerative process that converts the relatively unreactive oxidative radical HO_2 into reactive oxidative radical OH. Therefore, it is possible that the NO_2 in other NO_x compounds may also in a similar manner generate more reactive oxidative radicals.

CH3+NO2<=>CH3O+NO	(Rxn1)
HCO+NO<=>CO+HNO	(Rxn2)
HNO2+M<=>NO+OH+M	(Rxn3)
C2H5+NO2<=>CH3+CH2O+NO	(Rxn4)
HO2+NO<=>NO2+OH	(Rxn5)
NO2+H<=>NO+OH	(Rxn6)
NH+NO<=>N2O+H	(Rxn7)
H+NO+M<=>HNO+M	(Rxn8)
HNO+O2<=>HO2+NO	(Rxn9)
CH2+NO<=>H+HNCO	(Rxn10)
HCCO+NO<=>HCNO+CO	(Rxn11)

A similar observation was made following sensitivity analysis of an ethylene flame [Litzinger 2004] where reductions in soot yields were observed with the addition of NO_2 under fuel-rich conditions. The most important reactions related to OH generation from the flame study were reactions 5 and 6. This set of reactions represents a pseudocatalytic cycle that converts H and HO_2 into 2 OH. Converting the H to OH converts a radical important for soot formation into one that is important for the oxidation of precursor species. Similarly, the conversion of HO_2 to OH enhances oxidation of precursor species because OH is much more reactive than HO_2.

An interesting observation from this study is that similar products were observed as major products with both additives. Thus, regardless of what the initial composition of the fuel may be, the final growth of PAH and, later on, soot formation process appears to be the same. Also, most of the PAHs observed from analysis of the combustions products are in the list of 16 priority pollutant PAHs classified by the US Environmental Protection Agency [Wang 1998]. It should also be noted that these nitroadditives will potentially increase emissions of other undesirable pollutants such as NO_x. Although it is possible that results similar to those obtained in this study may not be observed in more practical combustion systems, the value of this study is that soot formation was studied under well defined conditions and that the results provide insights into the hypothesized mechanisms by which the proposed additives function. Thus, it would be unwise to view the results from this study as an additive evaluation study. They should be considered a contribution to the existing fundamental knowledge base on these additives.

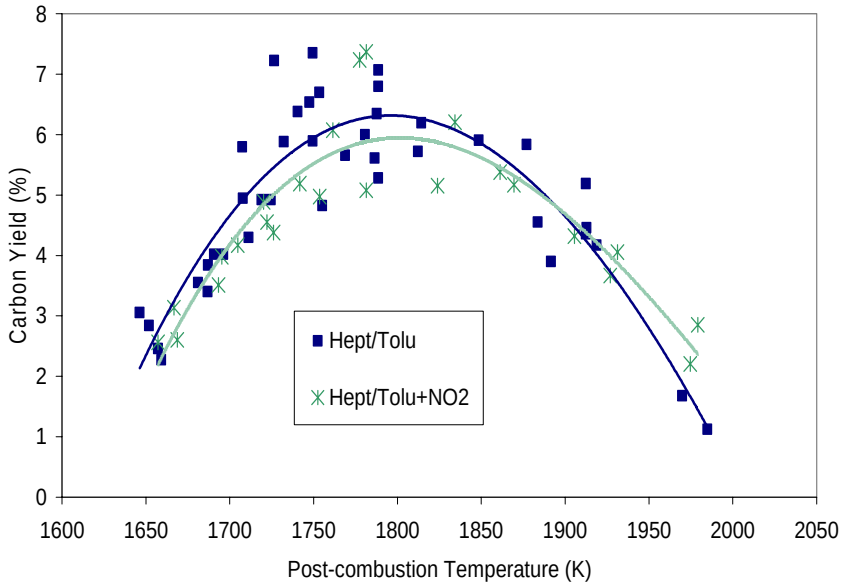

Figure 3.3.2-1. Carbon Yield from Combustion of n-Heptane/Toluene and n-Heptane/Toluene + NO_2 at 21 atm.

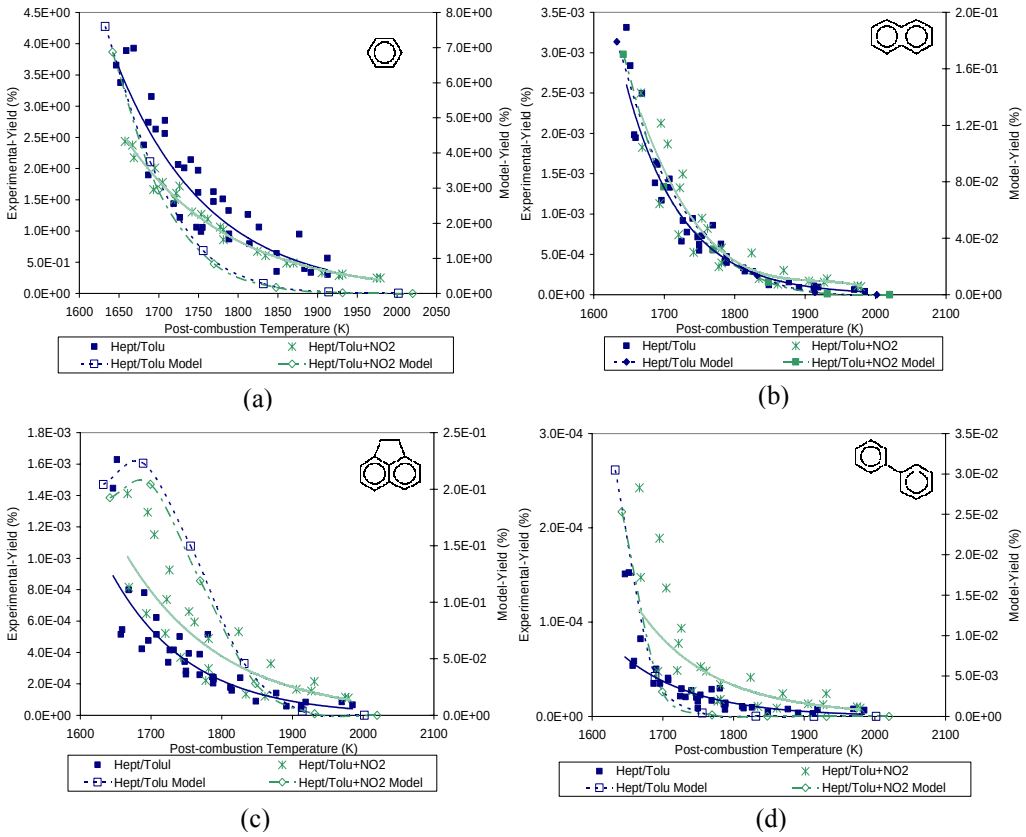

Figure 3.3.2-2. Yields of (a) Benzene, (b) Naphthalene, (c) Acenaphthylene, and (d) Biphenyl from Combustion of n-Heptane/Toluene and n-Heptane/Toluene + NO_2 at 21 atm.

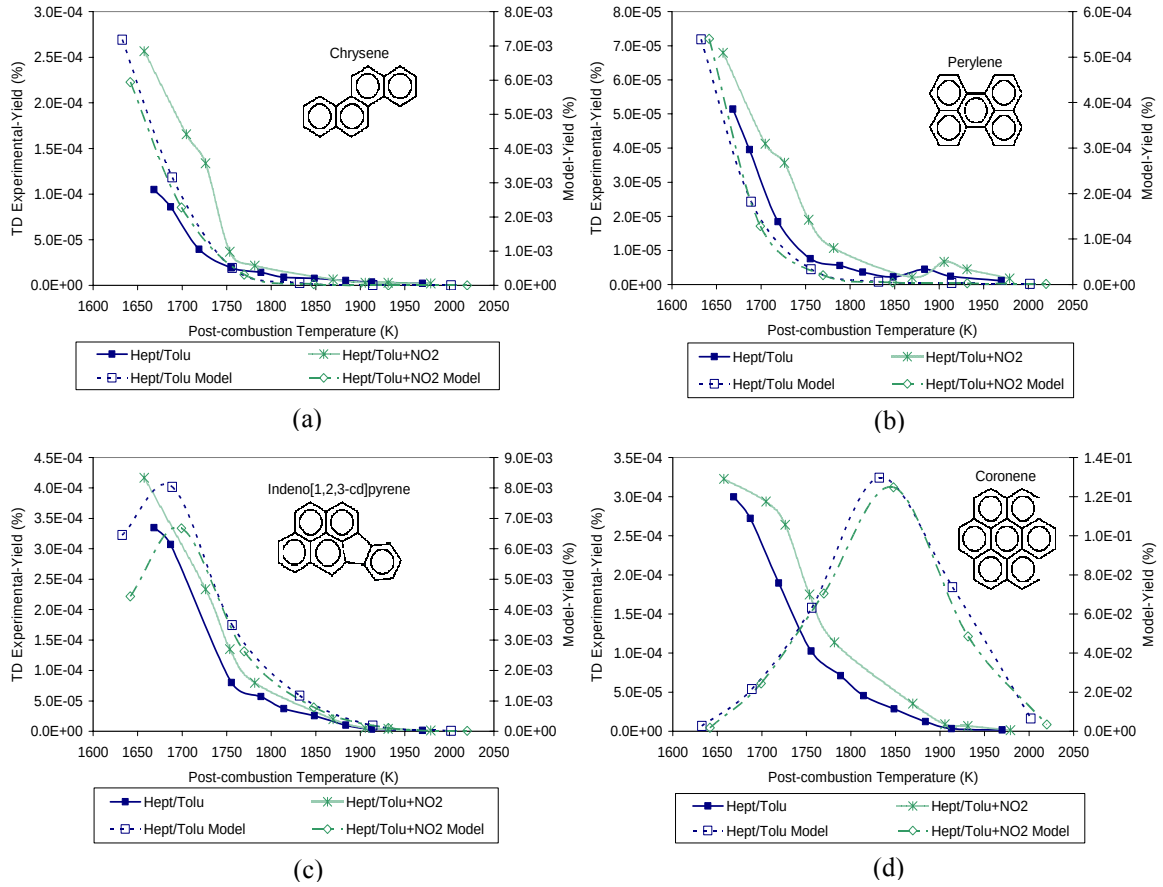

Figure 3.3.2-3. Yields of (a) Chrysene, (b) Perylene, (c) Indeno[1,2,3-cd]Pyrene, and (d) Coronene from Combustion of n-Heptane/Toluene and n-Heptane/Toluene + NO_2 at 21 atm.

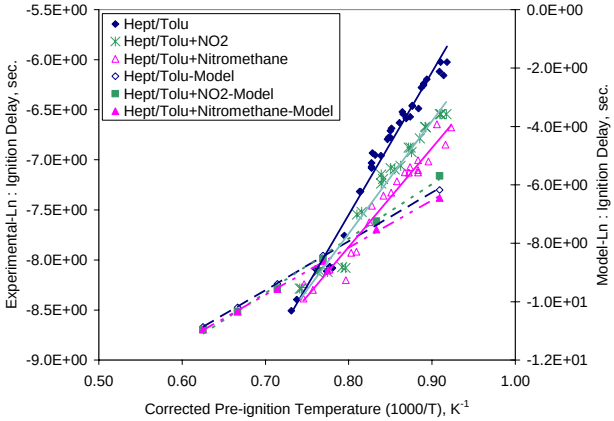

Figure 3.3.2-4. Ignition Delay from Combustion of n-Heptane/Toluene + NO_x Additives at 21 atm.

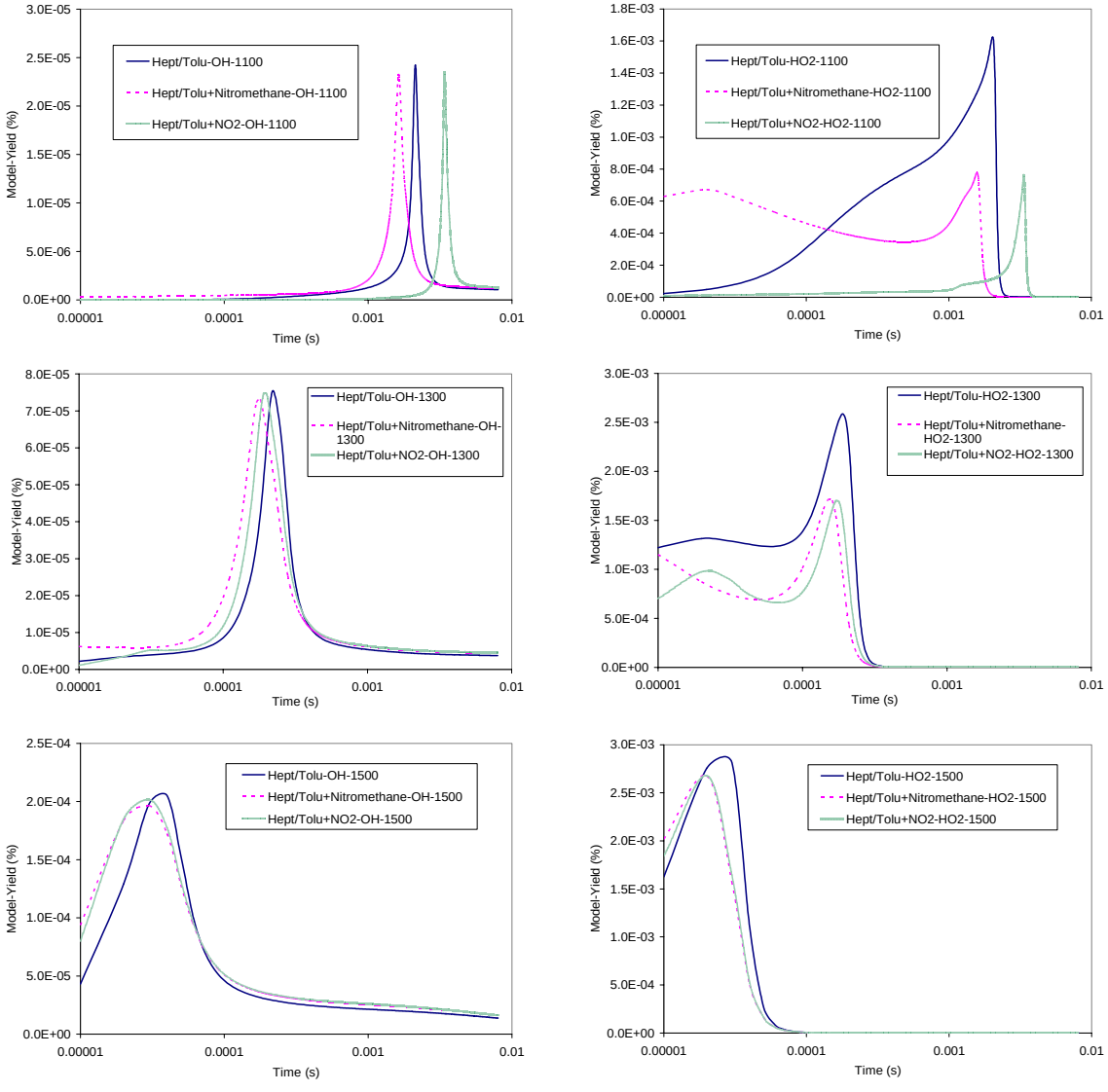

(a) (b)

Figure 3.3.2-5. Model Profiles of (a) OH and (b) HO_2 for Combustion of n-Heptane/Toluene + NO_x Additives at 21 atm and 1100, 1300, 150 K.

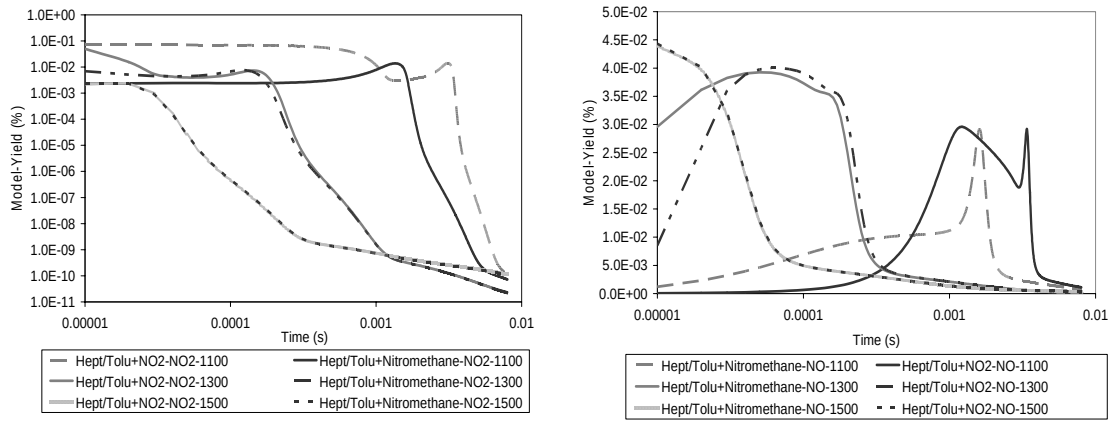

(a) (b)

Figure 3.3.2-6. Temporal Profiles (a) NO and (b) NO_2 from Combustion of n-Heptane/Toluene + NO_x-Additives at 21 atm and 1100, 1300, 1500 K.

Table 3.3.2-1. Activation Energy Calculated from Experimental vs Model Values.

Fuel Mixture	Ea, kcal/mol-K	
	Experimental	Model
Heptane/Toluene	28.3	33.3
Heptane/Toluene + Nitromethane	19.7	32.1
Heptane/Toluene+NO_2	22.1	37.0

3.3.3 PREMIXED FLAME (PSU)

Experimental Conditions

A premixed flame of ethylene (99.9%) and air at 1 atm was stabilized on a 60 mm stainless steel water-cooled porous plate, surrounded by a 6 mm wide porous annulus to provide a shroud of nitrogen (99.5%) to help shield the flame from the surroundings. The flame was stabilized using a 125 mm diameter circular aluminum plate with a 30 mm hole in the center that was mounted 32 mm above the burner surface. This setup, which yielded a very stable flame, matched those used by Xu et al [1997]. The entire assembly was mounted on a two-dimensional linear translation stage controlled by stepper motors (±0.0254mm). All reactant flows were controlled using mass flowmeters (±0.1% at full scale) and all secondary flows such as cooling

water and coflow nitrogen were controlled using calibrated rotameters. A mixture of NO_2 at a concentration of ~10,000 ppm in air was then added to additional air and ethylene streams that were passed into a mixer which consisted of a 10 mm inner diameter, 1m long stainless steel pipe with stainless steel washers placed every 20 mm to enhance mixing.

The flow conditions for these laminar premixed ethylene/air and ethylene/air/NO_2 flames for the two equivalence ratios studied are tabulated in Table 3.3.3-1. The C/O ratio and mass flux across the burner were maintained constant for both the baseline and the flames with NO_2 added. The adiabatic flame temperature as calculated from the CEA chemical equilibrium code [McBride and Gordon 1996] was maintained constant for the baseline flame and the flames with NO_2 added, by adding a small quantity of nitrogen to the flow.

Experimental Results

Figure 3.3.3-1 shows the profiles of soot volume fraction, temperature and normalized CH* emission for the baseline (BL) flames and flames with NO_2 added at the equivalence ratios of 2.34 and 2.64 as a function of the height above the burner (HAB) surface. For both equivalence ratios, a reduction in the soot volume fraction, fv, is observed when NO_2 is added. For the Φ=2.34 flame, a reduction of about 15% is observed at the final measurement point of 22.5 mm HAB. For Φ=2.64, the fv profiles exhibit a similar trend as seen in the Φ=2.34 flame, however, the reduction in soot with the addition of NO_2 is seen to be significantly greater. In the baseline flame at Φ=2.64 the maximum fv is observed to be around 1.1 ppm at 22.5 mm HAB, while the peak value observed with the addition of NO_2 is about 0.8 ppm, a decrease of roughly 30%. It is interesting to note that an increased reduction in fv is seen in the Φ=2.64 flame as compared to the Φ=2.34 flame when NO_2 is added.

The temperature measurements are shown in Figure 3.3.3-1(b). All measured baseline temperatures fall below the adiabatic flame temperature of 1728 K for Φ=2.34 and 1578 K for Φ=2.64 calculated from the chemical equilibrium code [McBride and Gordon 1996]. The temperature increases sharply until about 6 mm HAB where it plateaus until approximately 12 mm HAB, after which a gradual decrease in the temperature is observed. For both equivalence ratios, the peak temperatures and its axial location are nearly identical for both the baseline flame and the flame where NO_2 is added. For both equivalence ratios, the measured temperatures for the

flame where NO_2 is added are slightly lower (10 to 25 K) than for the baseline flame below 12 mm HAB. However, higher up in the regions that contain soot particles, temperatures of the flames with NO_2 added are slightly higher than for baseline flames ($\pm$25K). These measurements confirm that the temperature profiles change very little in location or peak temperatures as intended in the selection of the flow conditions. These temperature profiles are used as the input data for the modeling analysis.

The axial location of the reaction zone was also determined from the CH* chemiluminescence emission at 431 nm using the same optical setup as used in the line reversal method. As shown in Figure 3.3.3-1(c) the location of the peak in the CH* profile remains unchanged with the addition of NO_2 for both equivalence ratios. The axial location of the CH* peak also corresponds to the region of maximum gradient in the temperature profiles shown in Figure 3.3.3-1(b), another indicator of the location of the reaction zone.

Figure 3.3.3-2 shows the measurements of Qvv, Qhv and Qf profiles at the two equivalence ratios for the baseline flame and the flame where NO_2 is added. This figure yields a broad overview of the evolution of the soot particle field starting with the fuel molecules. Examination of Qvv profiles for the baseline flame at Φ=2.64 shows that the light scattering measurement, Qvv, is significantly greater than the Qhv and Qf measurements very near the burner surface until a height of approximately 3 mm HAB. This result is due to the relatively strong Rayleigh scattering by the gases in the region comprised of the initial by-products of fuel pyrolysis and oxidation processes. Between approximately 3 mm and 6 mm above the burner, Qvv, Qhv and Qf are observed to be comparable in magnitude. A sharp rise in Qvv is observed at a height of approximately 6 mm HAB, possibly corresponding to the point of inception of soot particles, given the magnitude of the observed increase. It should be noted that in this region and up to a height of approximately 7.5 mm, Qhv and Qf are approximately equal in magnitude, indicating that both signals have a common source, i.e., both are due to fluorescence which is depolarized. Above 7.5 mm HAB, a clear separation of Qhv from Qf is observed, indicating a departure from the Rayleigh theory of light scattering from small particles since Qhv = 0 at a 90º angle in the Rayleigh limit. The source of such a departure from Rayleigh theory could be due to the occurrence of nonspherical particles resulting from the agglomeration of incipient soot particles formed lower in the flame.

In the flames to which NO_2 is added, light scattering near the burner surface is equal to that observed in the baseline case up to a height of approximately 2 mm HAB. However, Qvv remains higher than both Qf and Qhv in the flames that contain NO_2 until 4 mm HAB when compared to the baseline case. This result indicates that the formation of the species which contribute to the fluorescence in this region has been delayed by approximately 2 mm. The same shift is seen in the location where Qvv increases above the depolarization, Qhv, and fluorescence, Qf, profiles, and for the location where Qhv rises above the Qf.

Figure 3.3.3-2(c) shows specifically the fluorescence signals shown in Figures 3.3.3-2(a) and 3.3.3-2(b) to provide additional clarity. Broadband fluorescence identical to that observed in these flames is widely considered to be an indicator of the presence of PAH species in hydrocarbon flames [Naegeli 1998, Bomse 1992]. Although fluorescence originates from a wide range of aromatic species, these are two very similar flames as indicated by the measured temperature profiles. Thus, the relative difference in the intensities of the fluorescence signal of the baseline flame and the flame with NO_2 added is argued to be due to a change in the concentrations of the aromatic species under these particular conditions. For the Φ=2.34 flame, it is seen that the fluorescence signal with the addition of NO_2 is lower than the baseline case earlier in the flame until about 5 mm HAB, but for HAB greater than 5 mm, the fluorescence signal in the flame with NO_2 added is higher than in the baseline flame. This crossover point is also seen in the Φ=2.64 case at an HAB of approximately 9 mm. The wavelength of the fluorescence signal from PAH is dependent on the number of aromatic rings present in the excited species [Bomse 1992]. The fluorescence signal at 514.5 nm used in the present study is indicative of the presence of aromatic species of four rings or greater [Kohse-Höinghaus and Jeffries 2002].

Modeling Results

To gain further insight into these observations, the chemical kinetic modeling results must be discussed. There are two key factors to be noted about the modeling results that are presented and their analysis: 1) The reactions in this mechanism and the corresponding rate constants are pertinent to the interpretations of the chemical pathways and possible explanations of the observed experimental results. 2) The model captures the kinetics of the flame only through the formation of PAH species and does not consider soot formation or growth. However,

since PAH are widely regarded as the precursors of soot, a study of the formation of PAH will give insight into the soot inception process. The modeling results for Φ=2.64 are discussed.

With the aid of Xsenkplot, the integrated carbon flux from C2H4 to C6H6 was analyzed using the rates of production of the intermediate species such as C2H3 (vinyl), C2H2 (acetylene) and H2CCCH (propargyl). This analysis follows the method outlined by Song et al [2004]. Competing oxidation and other "non-soot" reactions were also considered for each species. This carbon flux diagram is shown in Figure 3.3.3-3; the numbers indicate the percentage flow of carbon to each species relative to the fuel concentration with the NO_2 case shown on the right. The soot path is shown with bold arrows and bold lettering. The oxidation pathways are considered relative to the parent species and not to the fuel. Considering the formation of the vinyl radical, it is seen that 72.8% of C2H4 is converted to C2H3 in the flame where NO_2 is added in comparison to the 73.0% conversion in the baseline flame. Following the path to soot, in the baseline case, 41.3% of the fuel is converted into acetylene, while 39.4% of the fuel is converted to acetylene with the addition of NO_2. Similarly for the propargyl radical, the fuel conversions are 3.8% and 3.3% for the baseline flame and the flame with NO_2 added, respectively. At the final step in the path to soot precursors, 2.0% of the C2H4 goes to forming benzene in the baseline case, whereas in the flame with NO_2 added the conversion drops slightly to 1.9%. Thus in the flame with NO_2 added, key intermediates in the reaction pathway from the fuel to benzene and benzene itself are reduced relative to the baseline flame in the presoot inception region. Interestingly, however, the acetylene concentration shifts to being higher for the flame with NO_2 added, at approximately 2.5 mm HAB (see Figure 3.3.3-5).

Analysis of the modeling results was undertaken to explain these trends. The first species that were investigated were key chain-carrying radicals, H, OH, and O. The H atom concentrations shown in Figure 3.3.3-4 are lower for the flame with NO_2 added until 2.5 mm HAB. The initially lower levels of H atoms appear to be due to the reaction NO2+H=NO+OH in the flame where NO_2 was added and the lower temperatures of this flame (approximately 25 K lower near the burner) that led to lower rates of production of H atoms via decomposition of C2H3. At lower HAB, the hydroperoxy (HO2) radical concentrations are also considerably lower with the addition of NO_2, the major route of depletion being the reaction NO+HO2= NO2+OH [Mueller et al 1999]. The decrease in H and HO2 concentrations in the flame with NO_2 added is reflected in a similar decrease in the OH concentrations, by way of the reactions HO2+H=2OH

and H+O2=OH+O. The lower reaction rate of C2H3 decomposition also leads to lower formation rate of acetylene at low HAB. However, near 2.5 mm the concentrations of H and OH radicals for the flame where NO_2 is present become higher, leading to increased formation of vinyl radicals that subsequently form acetylene.

The lower acetylene concentration at lower HAB leads to lower propargyl concentrations and subsequently lower benzene concentrations as shown in Figure 3.3.3-5. On the other hand, the higher concentration of C2H2 downstream of the soot inception zone is instrumental in yielding the higher concentrations of the large PAH in that region. For instance, pyrene (C16H10), a four-ringed aromatic compound, is formed predominantly by a C2H2 addition reaction involving the phenanthrene radical (C14H9), C14H9+C2H2= C16H10 +H. The increase in C2H2 higher in the flame corresponds to an increase in the concentrations of pyrene as seen in Figure 3.3.3-5. Similarly the formation of coronene (C24H12) involves the addition of acetylene to benzo[ghi]perylene (C22H12) by the reaction C22H12 +C2H2=C24H12. A lower concentration of coronene near the burner surface and a subsequent increase higher up in the flame correlates with the trend seen in the C2H2 profile.

The major route for the formation of phenanthrene (A3, C14H10) is through the reaction of the indenyl radical (C9H7) with cyclopentadienyl (C5H5) radical, C9H7+C5H5= C14H10+H2. The indenyl radical is formed from indene (C9H8) primarily by the reaction C9H8+H=C9H7+H2. However, indene is formed from acetylene and the benzyl radical (C7H7) by the reaction C7H7+C2H2= C9H8+H. The major reaction for the formation of C5H5 is the dehydrogenation of cyclopentadiene via C5H6+H=C5H5+H2. The lower acetylene concentrations in the presoot inception region slow down the formation of indene and, in turn, the formation of the indenyl radical. In addition, the lower H atom concentrations slow the formation of the cyclopentadienyl radical. These result in a lower concentration of phenanthrene in the pre-soot inception region. Moreover, as can be seen from Figures 3.3.3-4 and 3.3.3-5, when the C2H2 concentrations in the flame with NO_2 added become higher than in the baseline case, a corresponding rise is seen in the A3 (phenanthrene) profiles for the flame with NO_2 added. Thus, when provided with the experimentally measured temperature profiles, the model produces trends in aromatic species that are consistent with the crossover that is observed in the fluorescence signals (see Figure 3.3.3-2(c) and Figure 3.3.3-5 (top)). The modeling also predicts

lower levels of soot precursor species in the region prior to soot inception that are consistent with the observations of lower soot levels in the flame with NO_2 added.

Table 3.3.3-1. Experimental Conditions.

Φ		2.34		2.64	
Condition		Base flame	5% NO_2	Base Flame	5% NO_2
C/O Ratio		0.78	0.78	0.88	0.88
Air Flow rate	(mg/s)	194.3	39.0	190.9	19.1
Air/NO_2 Flow rate	(mg/s)	0.0	149.7	0.0	166.1
Nitrogen Flow rate	(mg/s)	0.0	5.8	0.0	5.8
Fuel Flow rate	(mg/s)	30.8	30.7	34.1	34.0
Coflow Nitrogen Flow rate	(mg/s)	557.0	557.0	557.0	557.0
		Mole fractions			
C_2H_4		0.1408	0.1410	0.1560	0.1567
O_2		0.1805	0.1734	0.1773	0.1698
N_2		0.6787	0.6782	0.6667	0.6652
NO_2		-	0.0074	-	0.0083

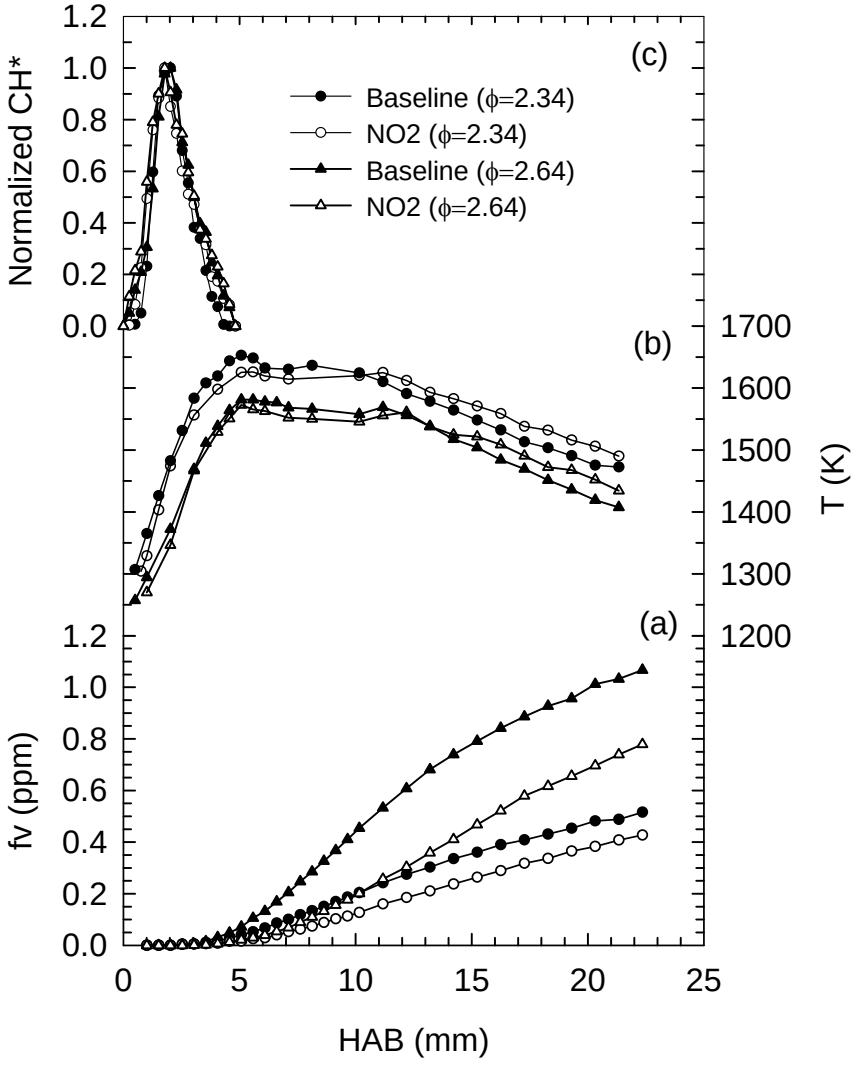

Figure 3.3.3-1. The Axial Profiles of (a) fv, (b) Temperature and (c) Normalized CH* Emissions for Two Equivalence Ratio of 2.34 and 2.64. Solid symbol: baseline; open symbol: NO_2 addition.

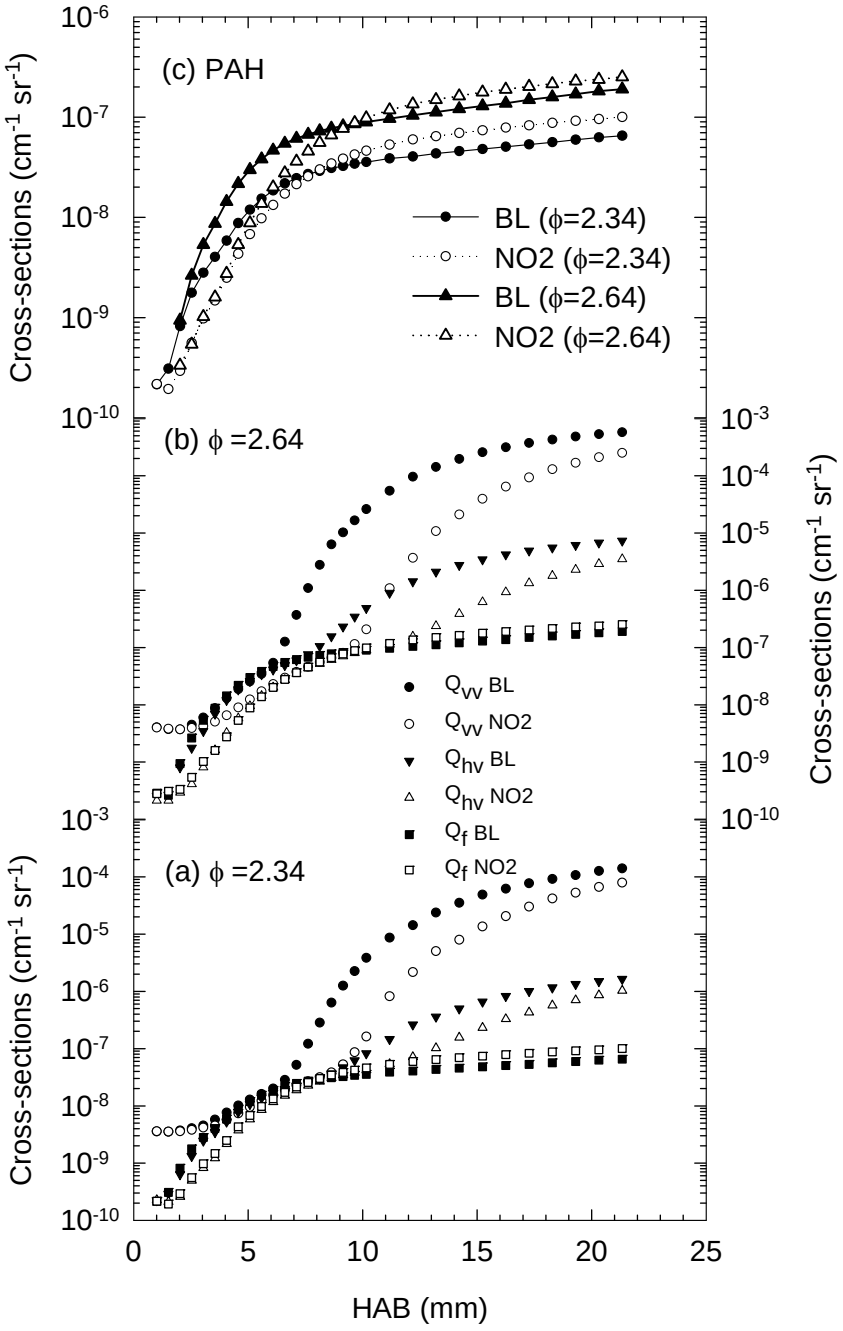

Figure 3.3.3-2. Polarized (Q_{vv}), Depolarized (Q_{hv}) Scattering and Fluorescence (Q_f) Signals for (a) Φ=2.34, (b) Φ=2.64 and (c) PAH vs HAB. Solid symbol: baseline; open symbol: NO_2 addition.

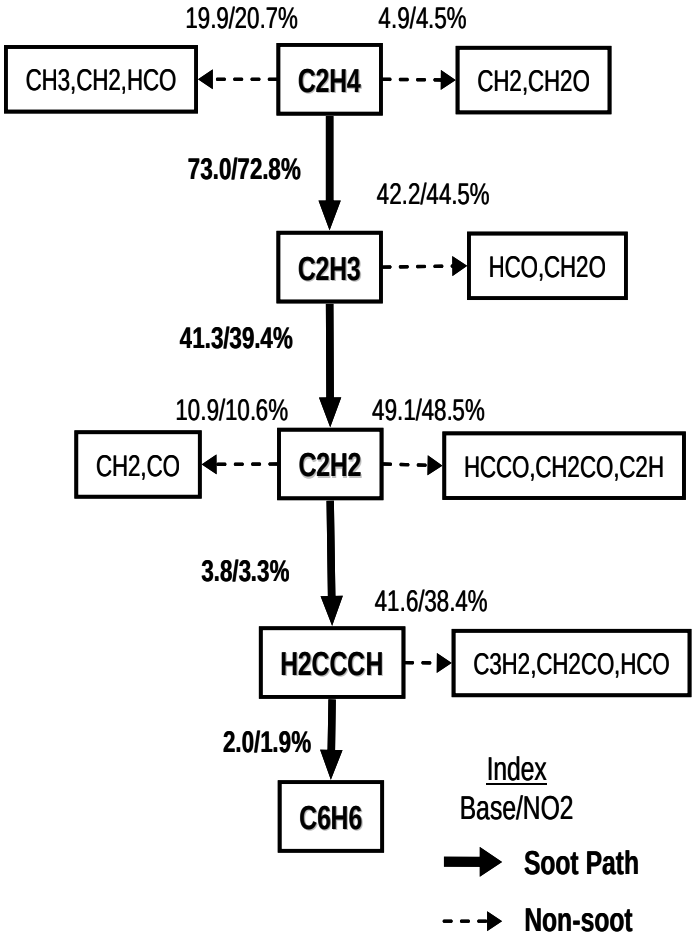

Figure 3.3.3-3. Absolute Carbon Flux Map Comparing Baseline and NO_2 Addition for Φ=2.64.

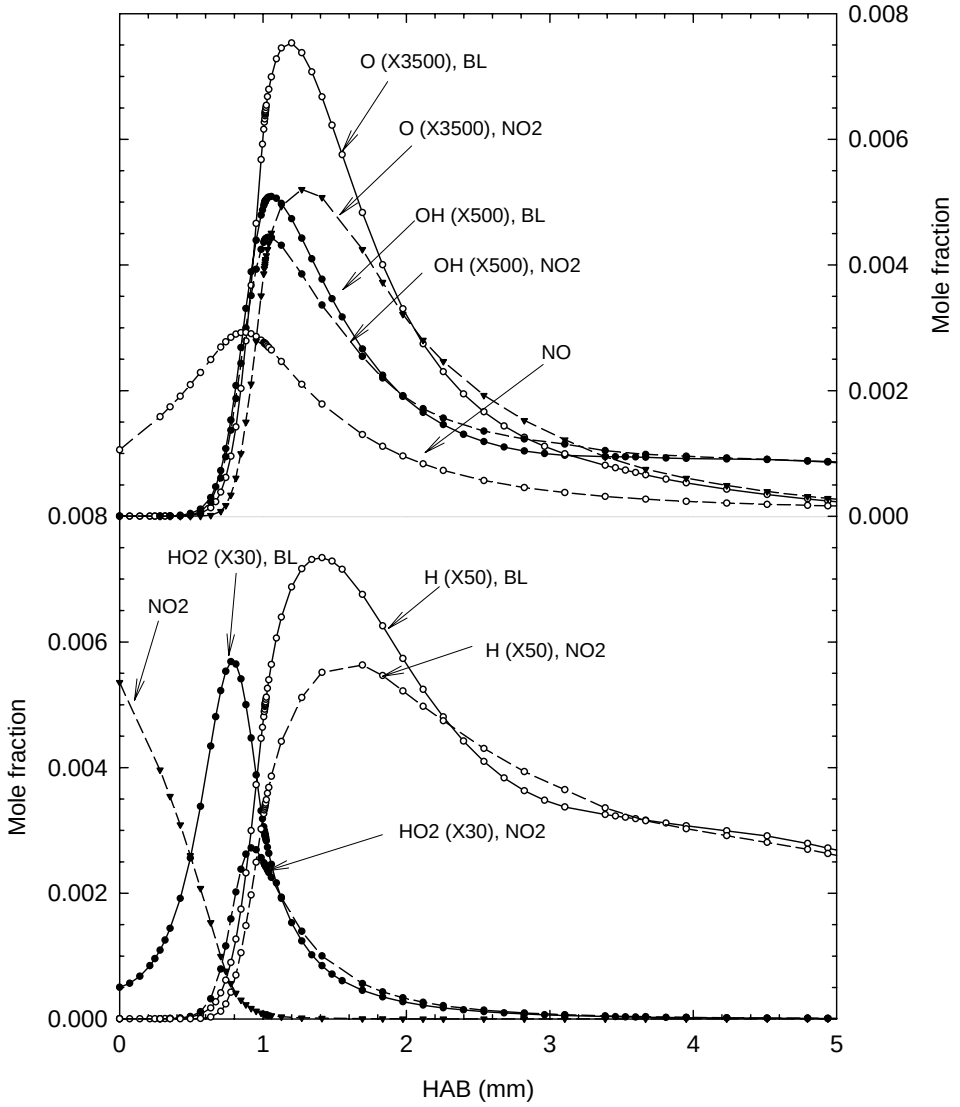

Figure 3.3.3-4 . Minor Species at Φ=2.64. Solid line: baseline; open line: NO_2 addition.

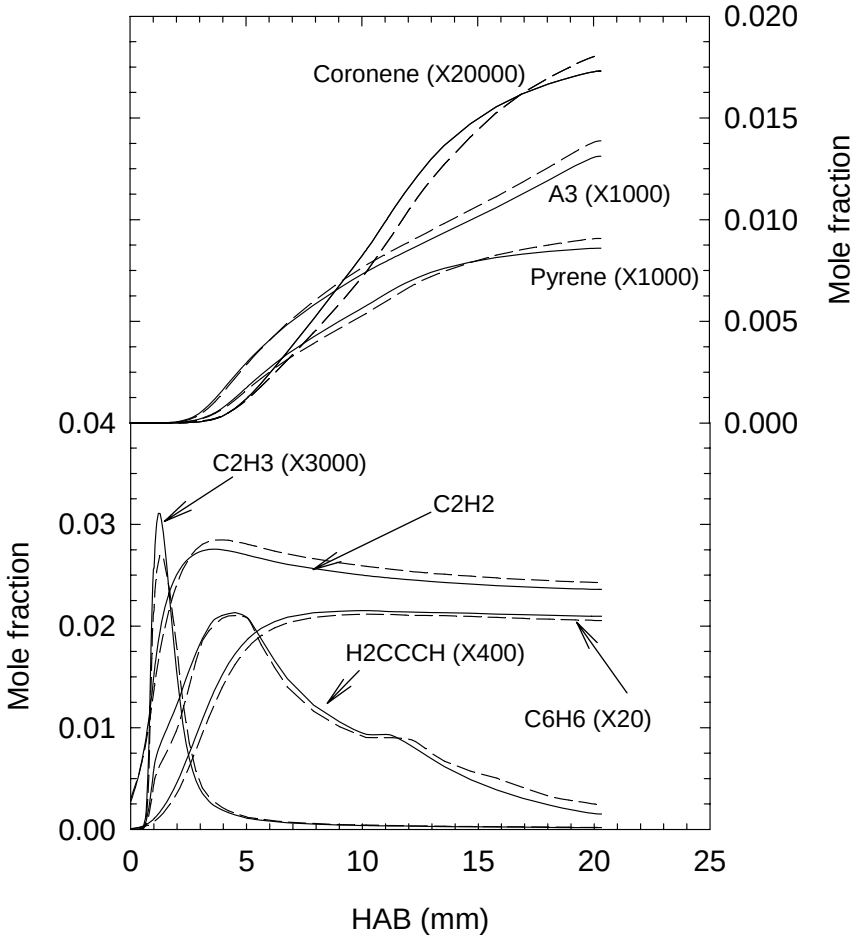

Figure 3.3.3-5. Carbon Species (bottom) and Aromatic Species (top).

3.4 PYRIDINE

3.4.1 SUMMARY OF MAJOR FINDINGS

The study of nitroalkanes triggered a thought process that led the team to consider other species containing heteroatoms that might reduce soot, which eventually led to testing of pyridine. Pyridine, a six-membered ring containing five carbons and one nitrogen, is known to pyrolyze without forming soot. Initial studies in a premixed flame showed substantial reductions in soot and led to the study in the full suite of devices.

Table 3.4.1-1 presents a summary of the effects of pyridine across the suite of devices used in this study; quinoline, a two-ring heteroatomic species, was also tested in the WSR. The pyridine results show fairly complex behavior from variation on the effectiveness with temperature in the shock tube and WSR to the complete lack of an effect in the HP Turbulent Reactor. Only the premixed flame and the turbulent spray flame showed decreases. A possible explanation for the trends that were observed is that there are two competing effects: an inhibiting effect caused by the presence of the nitrogen in the ring that slows ring growth, and an accelerating effect resulting from the reaction of the ring producing products that contribute to soot formation. The inhibiting effect requires the ring to remain intact and would be more important at lower temperatures.

In order to check this hypothesis, a chemical kinetic mechanism was created based on available pyridine chemistry, which was added to the heptane/toluene mechanism. Modeling was undertaken for the shock tube and the premixed flame. The results showed that there were significant deficiencies in the model, so it was not possible to confirm or refute the hypothesis. So the data set stands as a challenge for future research after an improved mechanism can be formulated.

Table 3.4.1-1. Summary of the Effects of Pyridine on Soot.

	Additive	**Fuel**	**Effect on Soot**	**Comments**
Shock tube	Pyridine	Heptane/ Toluene	Varies: no change to increase	Variation occurs as reaction temperature increases.
Well-stirred reactor	Pyridine	Heptane/ Toluene	Varies: decrease to increase	Temperature of reactor appears to be key factor.
	Quinoline	Heptane/ Toluene	Increase	
Premixed flame	Pyridine	Heptane/ Toluene/ Ethylene	Decrease	
Opposed-jet flame	*Pyridine*	*Heptane/ Toluene*		*No data due to experimental difficulties.*
Turbulent spray flame	Pyridine	Heptane/ Toluene	Decrease	
HP Turbulent Reactor	Pyridine	JP-8	No Effect	
		Heptane/ Toluene	No effect	Run to determine if the lack of an effect was due to use of JP-8.

3.4.2 SHOCK TUBE

The experiments were conducted at a pressure of ~ 21 atm over a preignition temperature range of 1100 K -1600 K (postcombustion temperature range of 1650 K-1950 K). The argon content in the test section was maintained at 93 vol% with the remainder comprised of fuel and oxygen. The experiments were conducted at an equivalence ratio of 3.0. The exothermic or endothermic nature of fuels could result in an increase or decrease in postcombustion temperature [Kahandawala 2005]. Therefore, to exclude any thermal effect that may arise by comparing combustion products from this study at precombustion temperatures, all products measured in this study were compared at postcombustion temperatures (the postcombustion temperature is the temperature after onset of ignition). Thus, any observation herein and associated conclusions are entirely due to the chemical effect from the additive.

A set of experiments performed with the base fuel (n-heptane-80 vol% + toluene-20 vol%) was compared against a set of experiments performed using pyridine (5 vol%) as an additive to the base fuel mixture. Pyridine experiments were performed to test the hypothesis that the presence of N-atom in the ring will hinder growth to more rings by preventing ring closure. Thus, pyridine was expected to stop one of the main pathways of ring growth, the HACA mechanism. The following reaction product distribution was assumed when calculating the equivalence ratio with pyridine:

$$nC_7H_{16} + C_7H_8 + C_5H_5N + O_2 \rightarrow CO_2 + H_2O + N_2 \qquad \text{(Rxn 1)}$$

Both gaseous products and soot yields were measured and normalized with respect to the mass of carbon in the fuel to exclude any volumetric effect that may arise from normalization with respect to the mass of the fuel. Results from Leco carbon analysis of particle yields are shown in Figure 3.4.2-1. The solid lines are polynomial trend lines used to fit the experimental observations of soot yields. Experiments with pyridine showed no noticeable decrease in soot yield. Instead, it showed a small increase in soot yields at the higher temperatures. The experiments were conducted at close temperature intervals to cover the entire temperature range instead of repeating the same experiments so that a better experimental trend could be obtained.

As shown in Figure 3.4.2-1, the low carbon yields observed at the lower temperatures are due to the slower rate of particle formation, but as the temperature is increased, particle formation dominates and a maxima in the soot yields is observed. However, further increases in

temperature causes the oxidation rate to dominate and thereby lowers the particle yields and thus gives the observed classical bell shape trends in soot yields as a function of temperature. Closer to the maxima where the soot formation is high, even a small difference in reaction times could cause a significant change. This could be one of the reasons that a higher scatter is observed closer to the maxima.

The ignition delay data shows that pyridine had no impact on the ignition delay, but none was expected since pyridine was not expected to dissociate to give ignition enhancing radicals. In order to validate the kinetic models, the experimental trends in ignition delay times were compared to calculated values from the models. The model predicted an activation energy of ~33 kcal/mol-K versus an experimentally determined activation energy of ~29 kcal with pyridine. Since the validity of any kinetic model dealing with the gas phase chemistry of particle formation depends on its ability to predict the correct order of magnitude levels of PAH concentrations and the order of PAH appearance, the species profiles that define soot particle nucleation and surface growth rates should first be verified [Appel 2000]. Thus, in an attempt to validate both the NIST mechanism and the pyridine mechanism used for this study and to better understand the observed soot yields, experimental yields of soot precursors obtained from product analysis were compared against the yields predicted from the kinetic models. The yields from both product analysis and modeling were normalized with respect to the mass of carbon in the fuel. The yields are given as yield % per unit mass of carbon in fuel. To validate the mechanisms, the additive mechanism was combined with the base fuel mechanism which is a compendium of mechanistic work that takes into consideration both the HACA mechanism and the resonantly stabilized reaction pathways for species molecular growth. The reaction rates for the growth to high molecular weight compounds for which no kinetic data is available are based on analogy to similar reactions [Babushok 2004]. The kinetic mechanism for pyridine oxidation [Ikeda 2000] incorporates the GRIMech submechanism [Bowman] for oxidation of N, O, H and small hydrocarbons and the pyridine pyrolysis mechanism proposed by Mackie et al [Mackie 1990]. When combining the pyridine mechanism, care was taken to verify the kinetic information from GRIMech submechanism with the data already available in the NIST mechanism. The NIST mechanism contained similar reactions with identical rate constants as in the GRIMech submechanism part incorporated in the pyridine oxidation mechanism. In prior studies both the pyrolytic and oxidation mechanisms of pyridine were validated against the major

products observed from pyrolysis (C_2H_2, C_4H_2, HCN and HCCCN) [Mackie 1990] and from oxidation (CO_2, CO, N_2, NO and decomposition of pyridine and O_2) [Ikeda 2000].

Figure 3.4.2-2 shows a comparison of modeling and experimental yields for volatile, semivolatile and nonvolatile compounds. For clarity, only a few selected species are shown here. Information on other species detected and data reduction is available elsewhere [Kahandawala 2004a]. The experimental yields of all volatile and semivolatile species identified in this study were fitted with exponential trend lines and are shown as solid lines. The broken lines represent model yields and were plotted using point plots. An exponential fit was chosen for the experimental yields, since kinetically, the yields are exponentially dependent on temperature. From the volatile compounds analyzed, only benzene data was quantified, since the other compounds were only detected in trace levels and were at the detection limit (the GC signal-to-noise ratio was <<2). The volatile and semivolatile species detected indicate that at the lower temperatures, the addition of pyridine has a tendency to increase every soot precursor yield except benzene, isomers of methyl naphthalene and o-diethenylbenzene.

Unlike in the volatile and semivolatile product analysis, nonvolatile products were analyzed only at selected temperatures. From the experimental yields of nonvolatiles detected, it was observed that the PAH yields increased with the addition of pyridine. Since no difference in ignition delays was observed (see Figure 3.4.2-3), the increased PAH yields could be attributed to the increase in the rate of PAH production due to the additive. The only plausible explanation, for increased PAH yields at lower temperatures where no reductions in particle yields were observed, is that the higher PAH yields at the lower temperature may be the reason that no reductions in soot yields were observed. This follows since the PAHs may not have completely reacted and undergone rearrangement to form elemental carbon. At the higher temperatures a faster conversion of PAHs to soot particles may be occurring and would also be competing with the increased oxidation rates at these temperatures. Modeling results obtained using the detailed kinetic model for the base fuel combined with the detailed kinetic model for pyridine showed no significant difference with the addition of pyridine. A closer look at the pyridine model reveals that this is perhaps because besides a few major known soot precursor species, the model doesn't really contain pyridine or pyridine-product reactions that could impact the yield of soot precursors. Also, the model could inaccurately predict the experimental yields for several reasons. One reason could be that due to inaccurate thermodynamic or kinetic data, the rate of

production is high or rate of consumption is low; another could be due to species that are missing from the reaction mechanism. From the observed compounds, dibenzo[ah]anthracene was not found in the species list of the NIST mechanism.

To obtain a better understanding of how pyridine impacts the soot formation process and also identify any compounds that may not have been accounted for in the model, an attempt was made to identify and measure the nitrogenated compounds that were formed. The following compounds were detected when pyridine was used as the additive: quinoline; isoquinoline; isoquinoline,1-methyl-; pyridine,2-ethenyl-; benzonitrile; benzonitrile,2-methyl-; pyridine,4-(phenylmethyl)-; 2,2'-bipyridine. However, from the compounds identified, only 2,2'-bipyridine was present in the model. As such, it is possible that some key species may have been omitted from the model, which could be one of the reasons that the model miscalculated the yields of soot precursors. For 2,2'-bipyridin, the model was able to predict the trend of 2,2'-bipyridine qualitatively, but quantitatively the model predicted significantly lower yields. Benzonitrile was the most abundant of the NPAHs observed and has yields similar in magnitude to other PAHs observed in this study. The yields of the NPAHs identified are given elsewhere [Kahandawala 2004a]. Another possibility for not observing higher soot yields at the lower temperature with the addition of pyridine could be due to the higher NPAH yields, which prevents the ring formation that leads to soot. However, with increasing temperature, reactions that lead to PAHs that are soot precursors may become dominant and may compete with the formation of NPAHs and thereby reduce any impact the additive may have in reducing the soot yields. Also, at these higher temperatures, the C-N bond may dissociate and contribute to the soot yields. Hore and Russell [1998] proposed a reaction scheme for pyridine pyrolysis at low temperatures where they identified two major pathways, one that leads to cyanoacetylene or acrylonitrile, and a second that leads to diacetylene or vinylacetylene that could serve as soot precursors. Major by-products were acetylene for the first route and HCN for the second route. Although this mechanism was meant for low temperatures, it is possible that it occurs even at higher temperatures where other studies have reported that the dominant product observed at the lower temperatures (<1450 K) was cyanoacetylene, and that with increasing temperature (>1450 K), yields of HCN predominated [Mackie 1990]. The species profiles for HCN and C_2H_2 indicate higher yields for both with increasing temperature. Thus, at higher temperatures pyridine may not behave as

hypothesized (molecular growth inhibitor), but dissociates to give HCN and soot precursors like acetylene.

To further elucidate the probable effects of pyridine, a computational analysis was performed with neat pyridine under pyrolytic and oxidative conditions (Φ=3.0) at a pressure of 21 atm over a preignition temperature range of 1100 K - 1600 K. The argon content was maintained at 93 vol%. Despite the computational observation in this study which indicated flaws in the kinetic mechanism for pyridine, the model was considered adequate to perform the computational analysis because it was validated previously under pyrolytic and oxidative conditions with neat pyridine and found to predict experimental trends of major products reasonably well. The product yields obtained from modeling are listed in Table 3.4.2-1 and are normalized with respect to the mass of carbon in pyridine. Table 3.4.2-1 compares the yields of the top 10 most abundant nitro compounds together with a few selected soot precursor species for pyrolytic and oxidative conditions (Φ=3.0) at three temperatures. Table 3.4.2-1 shows that the major products under oxidation were HCN and N_2 at all temperatures while H_2CCHCN and cyanoacetylene were dominant under pyrolytic conditions. For oxidative conditions the yields of cyanoacetylene decreased with increasing temperature, but under pyrolytic conditions cyanoacetylene yields increased with an increase in temperature. Table 3.4.2-1 shows that yields of all C_3 to C_5 nitrogen containing species increased with increase in temperatures under pyrolytic conditions. As the temperature increases, pyridine dissociation also increases. Therefore, all the species yields increase with increasing temperatures under pyrolytic conditions. It was evident that under pyrolytic conditions, even at the highest temperature simulated (1600 K), the amount of pyridine consumed was <45%; whereas, under oxidation almost the entire amount of pyridine was consumed even at the lowest temperature. The presence of HCN and N_2, which are the two dominant nitrogen-containing species under oxidative conditions, suggests that nitrogen is no longer bound to a carbon chain of any significant length (or ring) to inhibit carbon from making PAH and soot. This perhaps explains the observed increase in soot yields at higher temperatures in this study. Although pyridine failed to hinder the growth process to soot, the results of this study showed that only an additive that is thermally stable enough to exist as itself or as its significant fragment until molecular growth phase can hinder PAH growth process to soot.

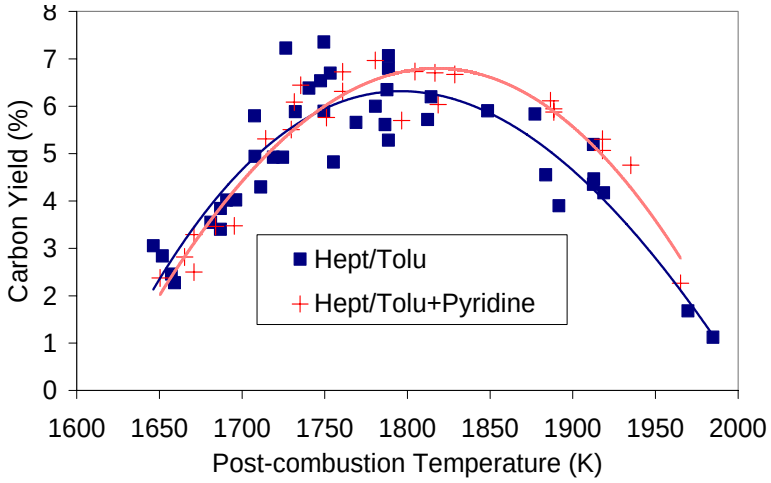

Figure 3.4.2-1. Carbon Yield from Combustion of n-Heptane/Toluene and n-Heptane/Toluene + Pyridine at 21 atm.

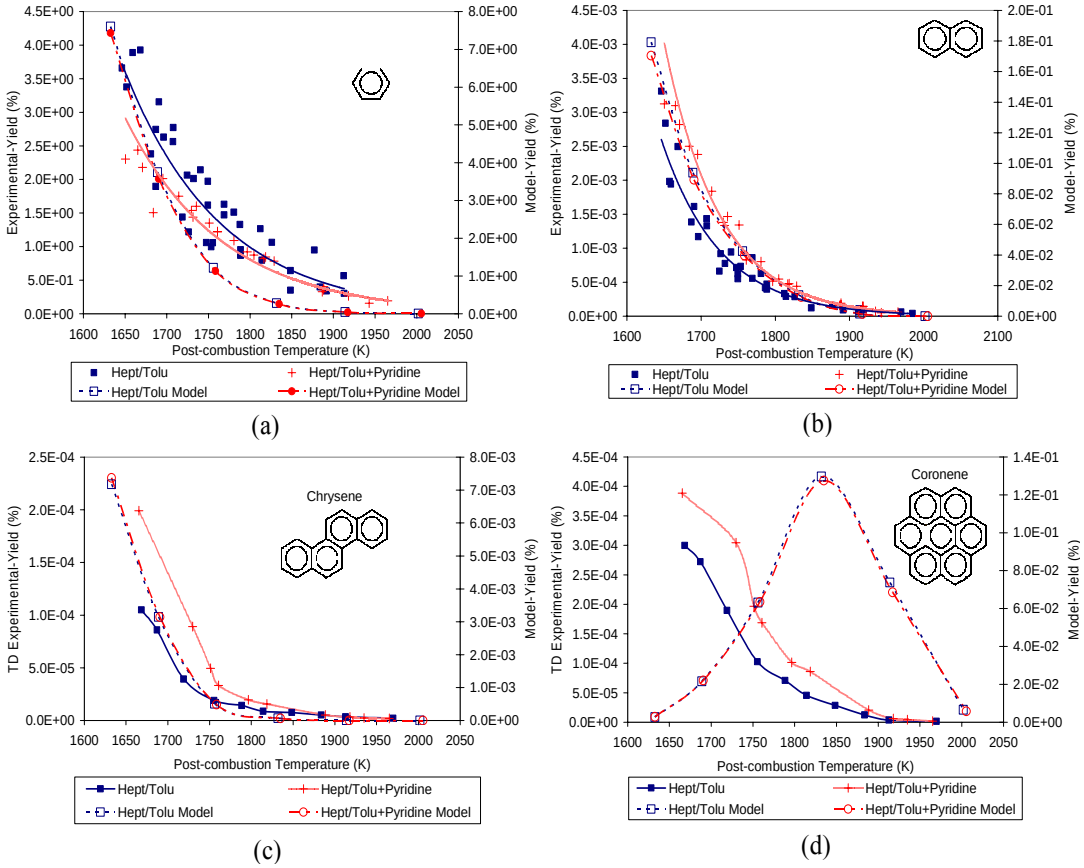

Figure 3.4.2-2. Modeling and Experimental Yields of Volatile, Semivolatile, Nonvolatile Compounds from Combustion of n-Heptane/Toluene and n-Heptane/Toluene + Pyridine at 21 atm.

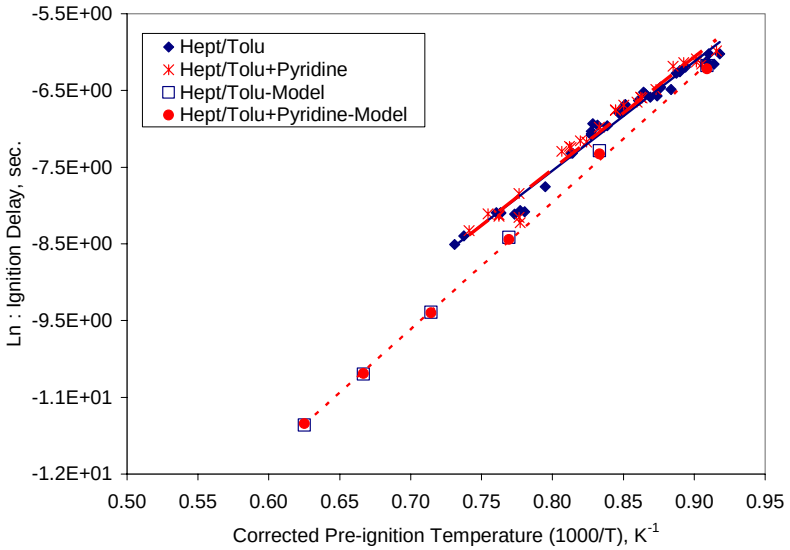

Figure 3.4.2-3. Ignition Delay from Combustion of Heptane/Toluene + Pyridine at 21 atm.

Table 3.4.2-1. Top 10 Nitro Compounds and Selected Soot Precursor Yields.

Yield% from modeling neat pyridine oxidation			
Temperature, K	1100	1300	1500
HCN	1.58E+01	1.74E+01	1.59E+01
N2	7.88E-01	2.16E+00	6.10E+00
NH3	5.29E+00	4.58E+00	2.10E+00
HNCO	2.00E+00	1.24E+00	5.67E-01
HCCCN	2.43E+00	1.12E+00	5.05E-01
NO	4.39E-02	1.21E-01	1.25E-01
C2N2	1.09E-01	8.14E-02	4.91E-02
CH3CN	5.41E-02	1.06E-01	3.50E-02
NH2	2.64E-03	7.81E-03	1.03E-02
H2CCHCN	1.91E-01	6.24E-02	1.87E-02
C2H2	8.33E+00	1.21E+01	1.13E+01
C6H6	2.42E+00	1.98E-01	7.38E-03
C10H8	5.77E-02	6.49E-03	1.26E-04
Phenanthrene	5.16E-02	1.26E-03	1.44E-05
Chrysene	5.56E-03	9.99E-05	1.17E-07

Yield% from modeling neat pyridine pyrolysis			
Temperature, K	1100	1300	1500
H2CCHCN	1.84E-06	3.62E-01	9.36E+00
HCCCN	6.88E-04	1.20E+00	9.29E+00
HCN	5.05E-06	4.47E-02	2.14E+00
2,2'-Bipyridine	3.43E-04	3.97E-01	2.08E+00
C5H3N	3.53E-06	2.43E-02	6.35E-01
C2N2	1.21E-06	3.92E-03	5.61E-02
A-C5H4N	1.66E-04	6.41E-03	2.41E-02
A-C4H4CN	2.22E-06	4.60E-04	2.52E-03
HCCHCN	2.69E-05	1.27E-03	2.04E-03
C4H4CN	1.70E-08	5.17E-06	3.09E-05
C2H2	3.76E-04	8.46E-01	1.03E+01
C6H6	5.31E-11	8.49E-04	4.93E-01
C10H8	1.28E-13	2.60E-06	9.25E-03
Phenanthrene	0.00E+00	1.38E-07	5.54E-03
Chrysene	0.00E+00	6.79E-12	9.90E-07

3.4.3 WELL-STIRRED REACTOR

The effectiveness of pyridine and quinoline as additives were studied in the WSR using a neat fuel of 80% heptane/20% toluene by volume. The results are discussed below and in Stouffer [2005a]. The reactor material used for the experiment was amorphous fused silica, which minimized both cracking and heat loss and could be used because the temperature in the reactor was less than the 1500°C melting point of the silica. It should be noted that the structure of pyridine and quinoline resembles that of benzene and naphthalene, with the addition of a nitrogen atom on the ring structure. It was proposed that presence of the nitrogen atoms in the pyridine and quinoline would inhibit closure of additional aromatic ring structures and thus trap soot precursors such as acetylene, preventing formation of soot.

Experimental Conditions

Equivalence ratios between 1.90 and 2.10 were studied. The WSR was limited to this equivalence ratio range on the low side by the melting point of the fused silica and on the high side by the rich blowout limit. However, this range of equivalence ratios captures the peak along with the low temperature and high temperature sides of the so-called "soot bell". The airflow was held at a constant 240 g/s and the average residence time in the reactor was 10 +/- 0.4 ms. The reactor pressure was slightly (0.6-1.4 kPa) over the ambient atmospheric pressure for all of the tests. The fuel additive levels were neat (0%), 10,000 ppm, and 50,000 ppm. During each of the tests with additive, the fuel equivalence ratio was held at a constant level by adjusting the total fuel flow rate to match the corresponding equivalence ratio for the neat cases.

The results for total carbon mass collected on quartz filters for the pyridine additive tests are shown in Figure 3.4.3-1. The carbon mass curve versus equivalence ratio shows a bell shaped curve with a peak between ϕ =2 and ϕ = 2.05 for the neat case. Below this equivalence ratio the carbon mass decreased as the temperature increased (as ϕ was lowered or inlet temperature was increased) and is commonly referred to as the high temperature side of the soot bell. On the opposite (low temperature) side of the soot bell, the carbon mass production increased as the temperature increased (as ϕ decreases). With the additive concentration at 10,000 ppm, the effect on the soot is shown to be minimal over the entire range of equivalence ratios. In contrast, the pyridine additive at the 50,000 ppm level reduced carbon mass on the high temperature side

of the soot bell, showed little effect near the peak, and increased the carbon mass produced on the low temperature side of the soot bell. The reduction in total carbon mass with the 50,000 ppm additive is most pronounced (-32%) at $\Phi = 1.9$, which is the highest temperature case considered. The plot of the total carbon mass versus WSR temperature in Figure 3.4.3-2 shows that the reduction of mass at the high temperature side of the curve is strongly related to the temperature. The volatile (oxidized from filters at temperatures below 325°C) and carbonaceous (oxidized from filters at temperatures above 325°C) carbon mass from the filters is shown in Figures 3.4.3-3 and 3.4.3-4, respectively. The volatile content of the carbon mass was shown to increase along with increases in the equivalence ratio for the neat and the additive cases while the trends for the carbonaceous carbon resemble those for the total carbon.

Quartz filters were analyzed using the Chromatoprobe and GC/MS to monitor the Polycyclic Aromatic Hydrocarbon (PAH) contents of the soot. The results for two most concentrated species observed, fluoranthene and pyrene, are shown in Figure 3.4.3-5. It can be seen that the two species decrease with the addition of the pyridine.

For the tests with the pyridine additive, the acetylene concentration was of particular interest because of the proposed mechanism of trapping acetylene within the pyridine ring. The acetylene concentration inside the WSR was measured using the FTIR MGA, and the results shown in Figure 3.4.3-6 show decrease at some equivalence ratios and increase in others. It is hard to explain this behavior, and more important, it is not consistent with what was observed during other additive studies. Methane decreases with the addition of pyridine at all equivalence ratios observed. As shown in Figure 3.4.3-7, at high equivalence ratios light hydrocarbons and aromatics decreased with addition of pyridine.

Figure 3.4.3-8 shows the concentration of hydrogen cyanide (HCN) as an effect of pyridine addition. For the neat case, both the HCN and NO were below detectable limits. The addition of the pyridine did not increase the NO; however, the increase in the HCN was significant.

The particulate carbon mass results for quinoline additive are shown in Figures 3.4.3-9 and 3.4.3-10 for the volatile and carbonaceous fractions of the carbon mass, respectively. Both the volatile and the carbonaceous fractions of particulate carbon mass increased with the quinoline addition over the entire range of equivalence ratios. Similar to the results for the pyridine, the volatile carbon content increased as the equivalence ratio increased for each of the

concentrations. The carbonaceous carbon mass was shown to increase dramatically as a result of the 50,000 ppm quinoline addition, increasing from 31% at ϕ =1.9 to 91% at ϕ =2.1. The effect of the quinoline on the combustion temperature was found to be small (less than 9°C) at each equivalence ratio, therefore, the effect of the quinoline is thought to be predominately chemical rather than by the effect of a temperature shift on the chemical kinetics. Certainly the quinoline is a poor additive. Recall that quinoline has a single nitrogen atom on only one of its aromatic rings. It is thought that while the presence of nitrogen on one of the aromatic rings may inhibit subsequent ring addition to that ring, the presence of the nitrogen on one ring does not significantly effect addition to the other aromatic ring.

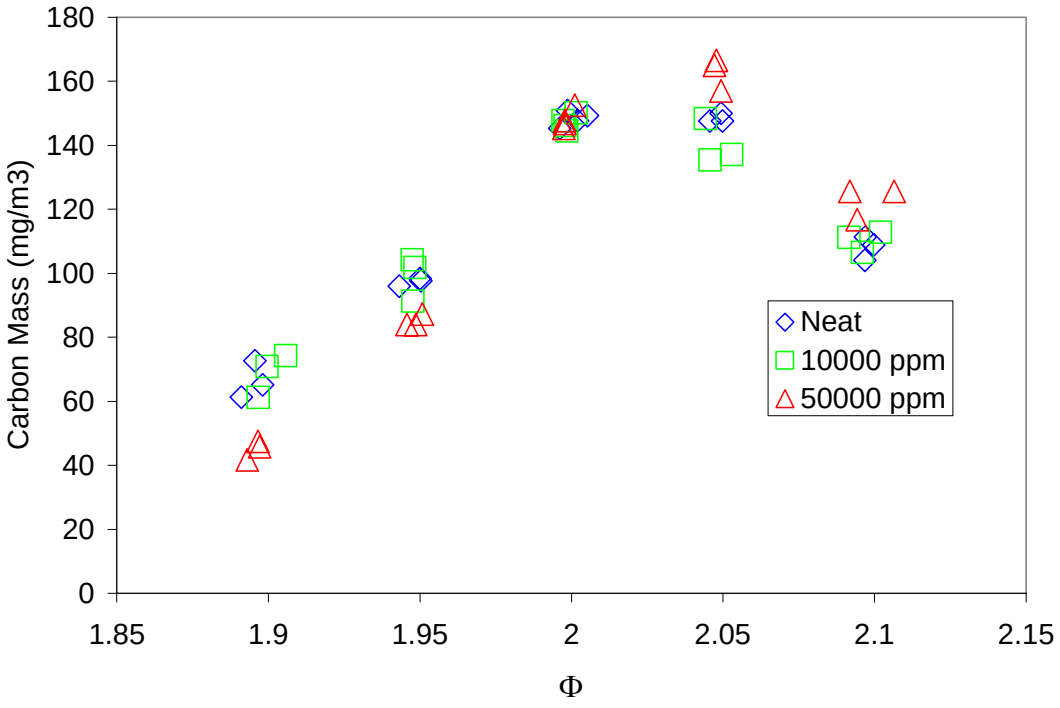

Figure 3.4.3-1. Total Carbon Particulate Mass vs ϕ for Pyridine Additive Cases.

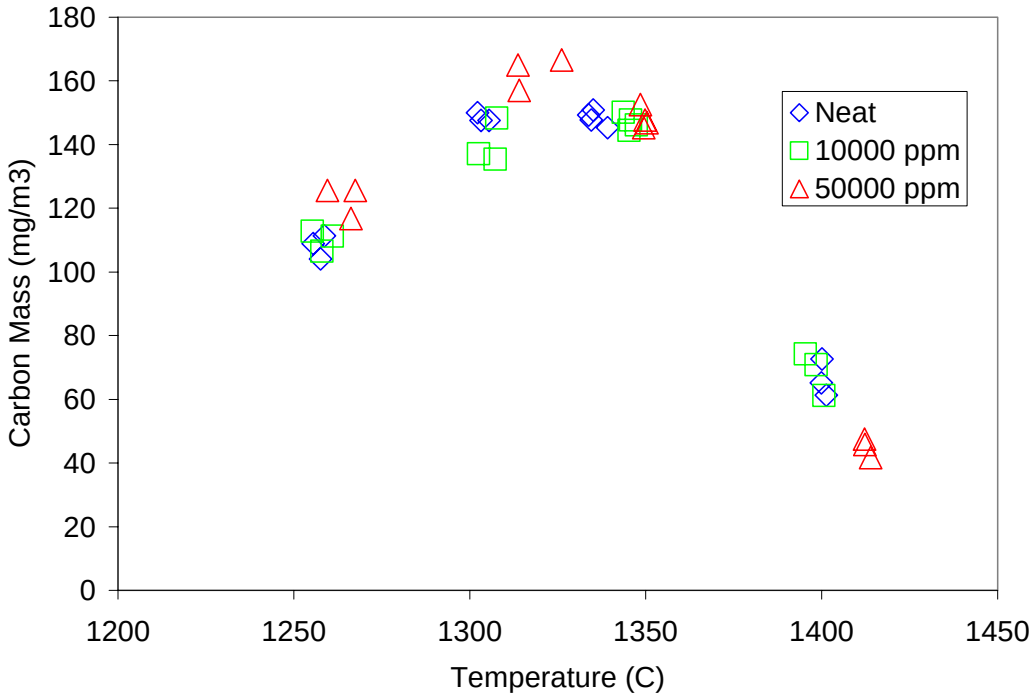

Figure 3.4.3-2**.** Total Carbon Particulate Mass vs WSR Temperature for Pyridine Additive Cases.

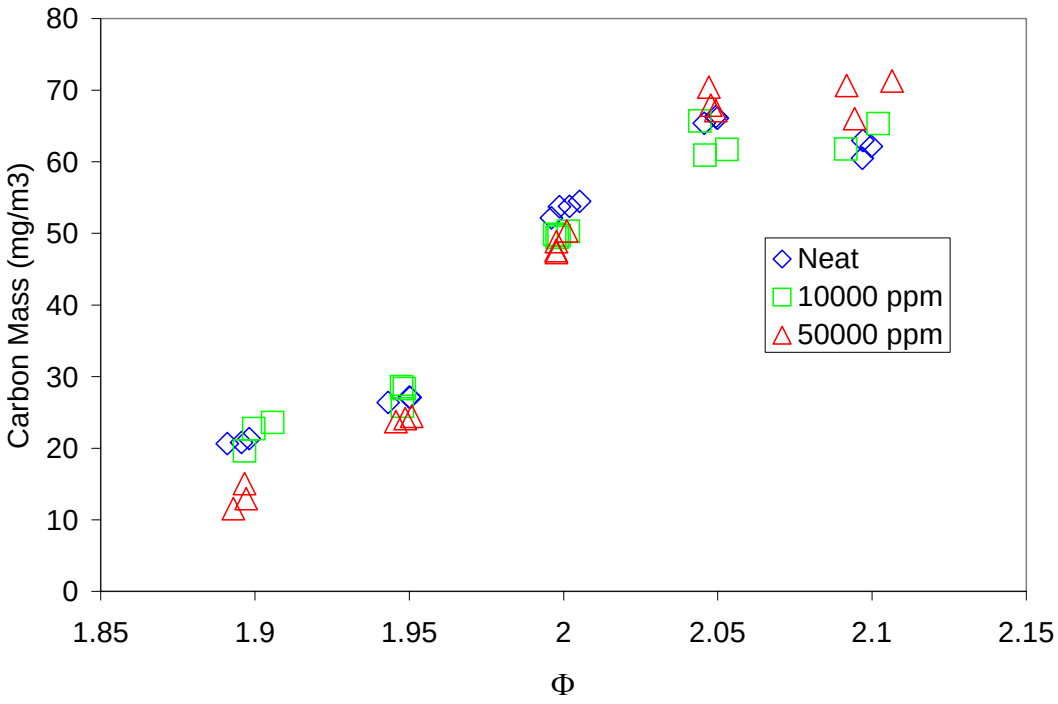

Figure 3.4.3-3. Volatile Carbon Mass for Pyridine in the WSR.

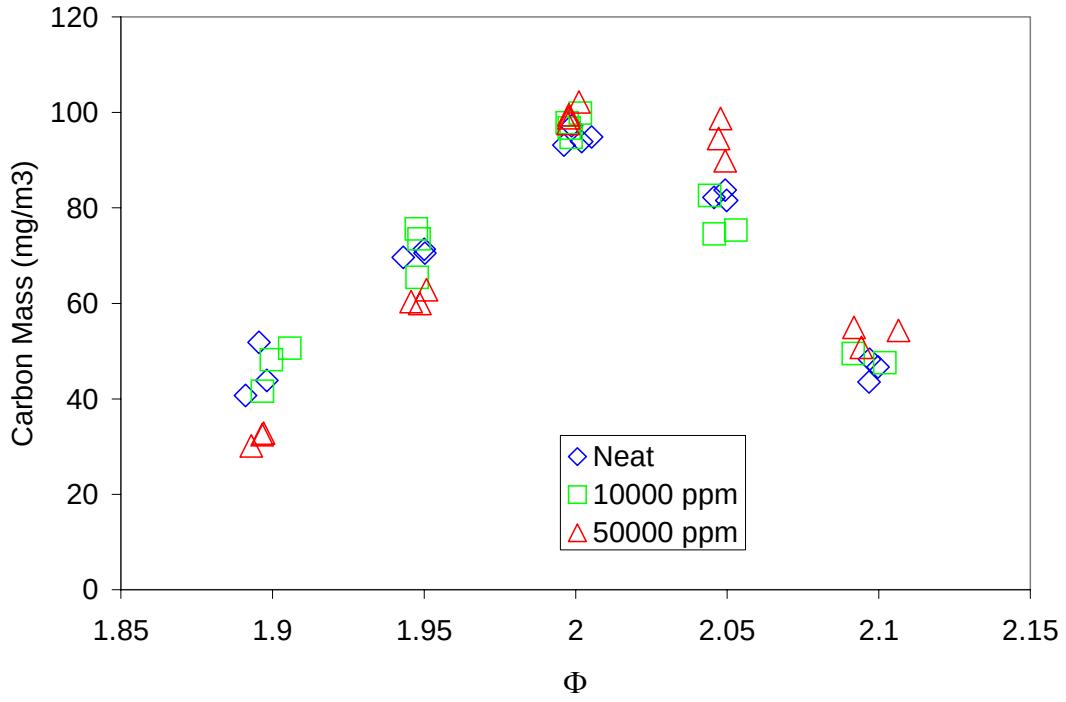

Figure 3.4.3-4. Carbonaceous Carbon Content Measured in the WSR for Pyridine Additive Tests.

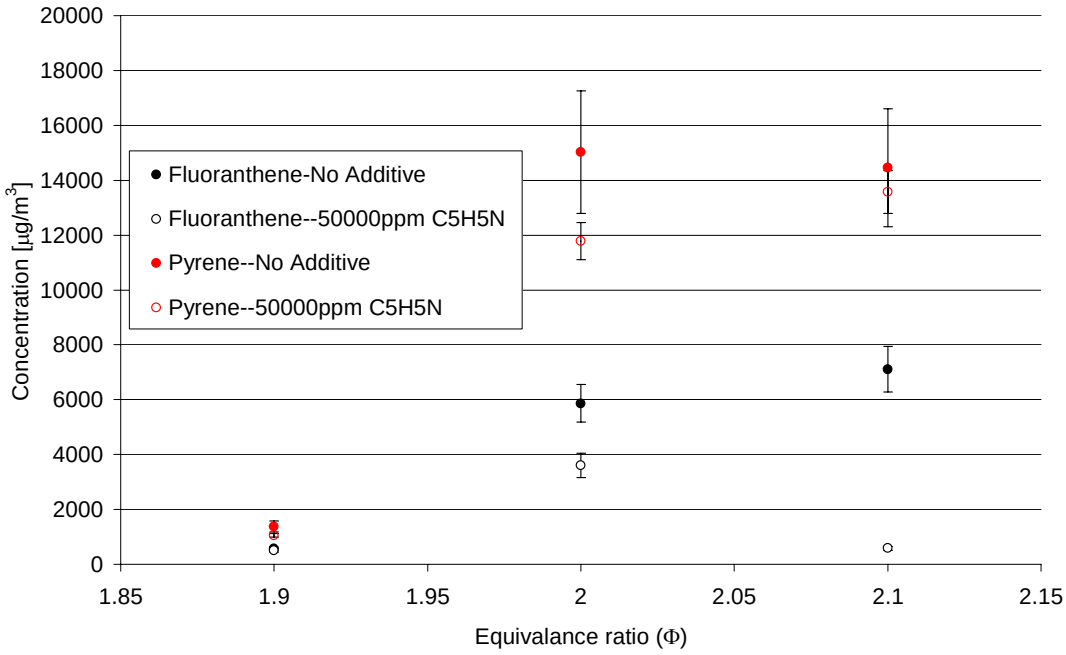

Figure 3.4.3-5. Effect of Pyridine on Fluoranthene and Pyrene.

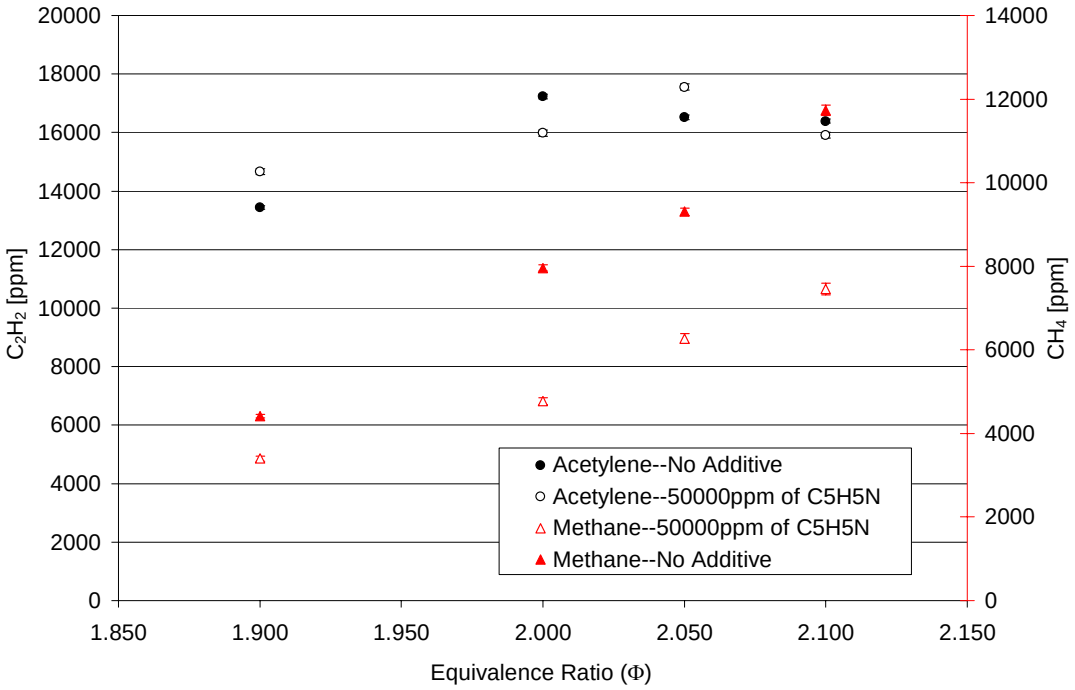

Figure 3.4.3-6. Effect of Pyridine on the Acetylene Concentrations.

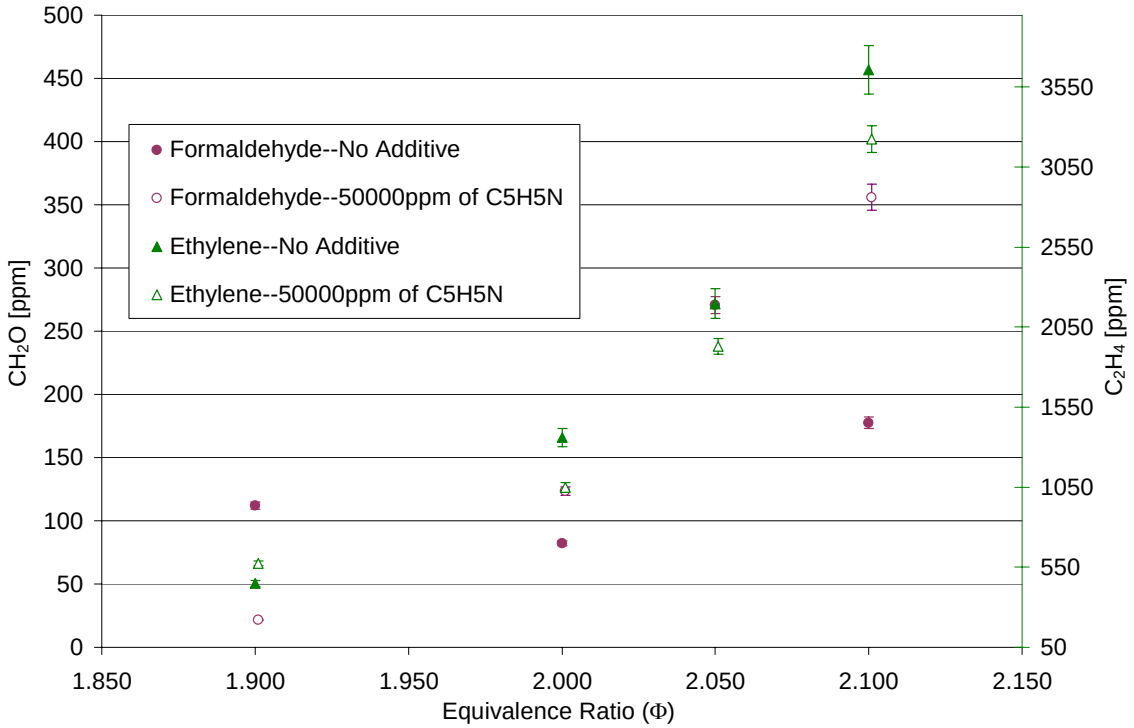

Figure 3.4.3-7. Effect of Pyridine on Formaldehyde and Ethylene Concentrations.

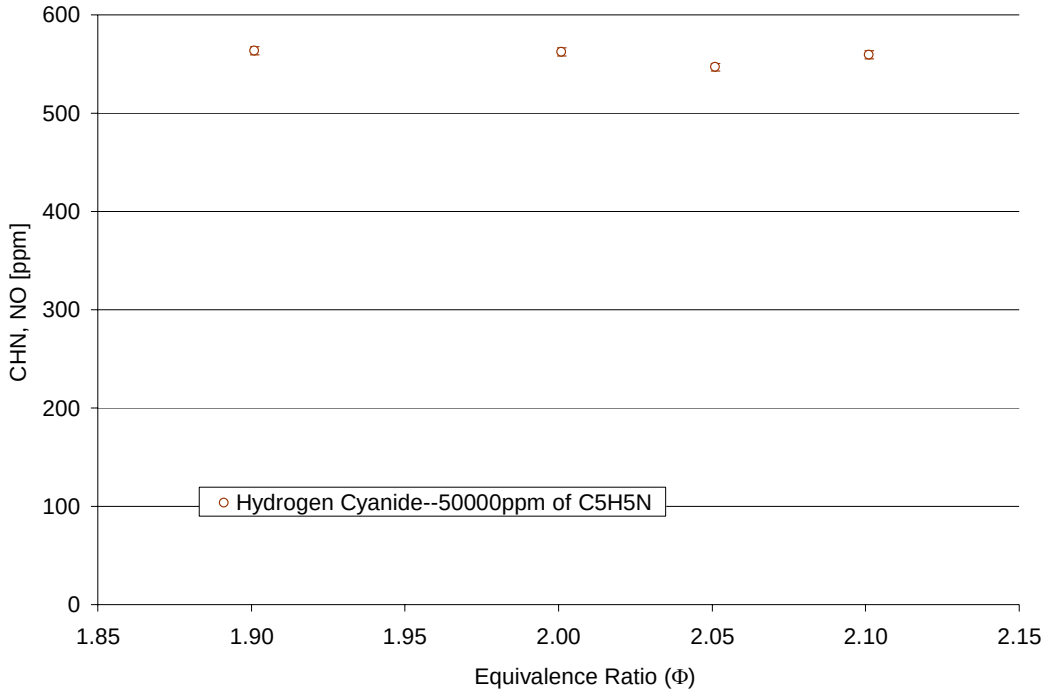

Figure 3.4.3-8. Hydrogen Cyanide Concentration with Pyridine as an Additive (neat concentrations were below detectable limits).

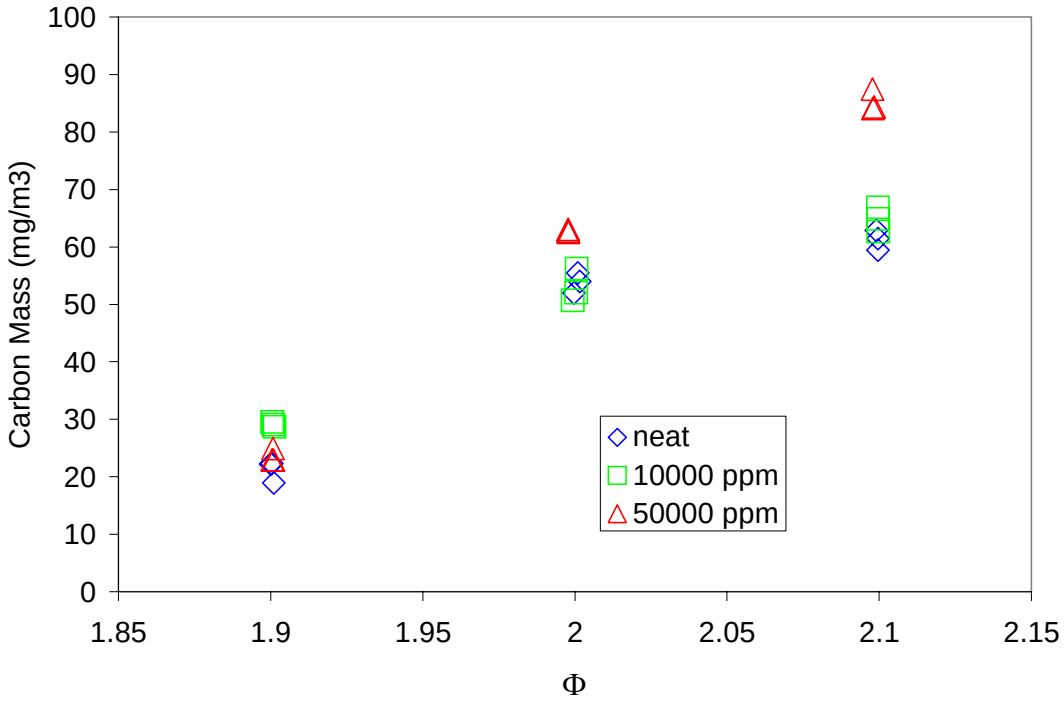

Figure 3.4.3-9. Volatile Carbon Mass for Quinoline Additive Tests in the WSR.

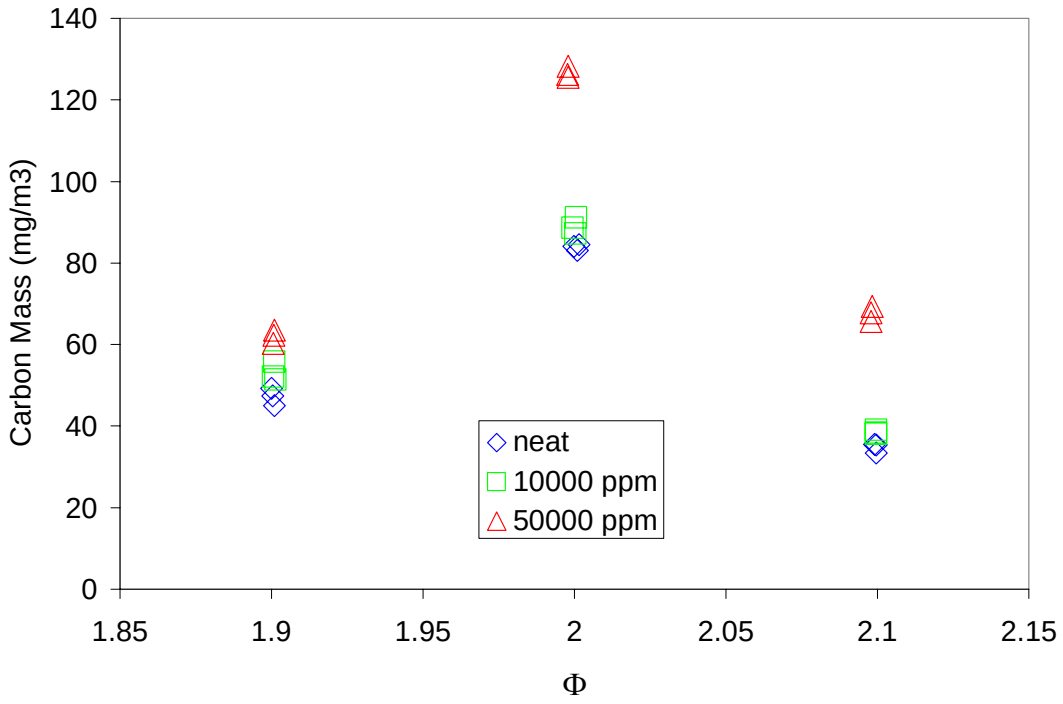

Figure 3.4.3-10. Carbonaceous Carbon Content Measured in the WSR for Quinoline Additive Tests.

3.4.4 PREMIXED FLAME

Due to uncertainty in the measurements, changes in the observed soot volume fraction less than 10% imply minimum impact by the additive. Pyridine was one of the more effective additives for reducing soot volume fraction in the premixed flame experiments. Additional data for this additive are provided in Figure 3.4.4-1, and demonstrate increasing soot reduction with increasing additive levels.

Despite the very encouraging results with pyridine, soot samples extracted from the flame and analyzed by Scanning Electron Microscopy (SEM) indicate that primary particle diameter with pyridine added to the fuel are 10% higher than those produced in the baseline flame. The lower soot volume fraction, yet larger particle diameters, is consistent with the proposed mechanism by which pyridine reduces soot in the flames.

Due to the expected dependence of surface oxidation rates on surface area, it is assumed that the lower soot volume fractions in the fuel-rich flames with added pyridine may not proportionally translate to the same factional soot reductions from a combustor that includes soot oxidation.

In the work described above, the flame structure was not uniform as the flame front had a cellular structure. Initially, we believed the structure was a result of the geometry of the perforated plate flame holder, which had been utilized to avoid condensation of the high molecular weight reactants (of interest in this work) within a cooled porous plug burner, which is conventionally used for flat flame burner studies. In an attempt to correct for this nonuniform flame front, we designed and constructed an uncooled porous plug burner made of hastalloy (see experimental section). We tested the new burner and found cellular flame structures nearly identical to those observed with the perforated plate. Hence, we performed a literature review and were reminded of a well-known phenomenon for fuel-rich, premixed flames for fuels with high molecular weight [Strehlow 1968]. Apparently, this structure is due to large differential between thermal conductivity and species transport and/or differential species diffusion. The problem did not arise in the (previously-studied) ethylene flames, but became apparent for fuel-rich, premixed flames. The effect was aggravated by the increased molecular weight of the parent fuel. In this case, heptane and 20% toluene was the initial fuel. The cellular structure of the flame was mitigated by use of a porous plug burner and by addition of ethylene 25% by mass of the fuel.

The temperatures of the heptane/toluene burner-stabilized, premixed flames with and without pyridine were determined to assess whether the reduction in soot with added pyridine was due to a temperature shift. Several flames were investigated. Details of the flows are provided in Table 3.4.4-1, to facilitate modeling of these flames. As described previously, ethylene was added to avoid cellular flame structure with 25% ethylene and 75% primary fuel liquid on a mass basis The primary fuel liquid comprises either 10% toluene/90% heptane or 20% toluene/80% heptane on a volumetric basis. Pyridine added 4% by mass of the fuel and the flow rates were 0.00820 grams/sec/cm^2.

The measured temperature profiles from thermocouple particle densitometry (TPD) are shown in Figure 3.4.4-2 and demonstrate that the pyridine additive does not affect the temperature profile significantly, although a slight increase of as much as 20 K is possible high

in the flame. (The baseline flames have no pyridine additives.) In contrast, the 10% toluene flame(s) have flame temperatures about 60 K lower than the 20% toluene flames. Equilibrium (adiabatic) temperatures for these all of these flames are identical.

Soot measurements were also determined for the 10% toluene flames using laser extinction. They are shown in Figure 3.4.4-3 with and without the pyridine additive. Pyridine reduces soot in this flame by about 20%, slightly less than that observed previously for a similar additive level. Modeling of these flames has been attempted, but is challenging due to the size of the mechanism and the requirement for the coupled transport and kinetics for the flame solutions. Note that recent suggestions [Krishnan et al 2001, Williams et al 2005] for the extinction coefficient of soot indicate that the actual levels of soot may be about 2 to 2 ½ lower than those reported in Figure 3.4.4-3, as we have used an earlier preferred value for this coefficient.

A second experimental problem was associated with obtaining repeatable results with the new dilution probe (see Experimental Section). Careful control and monitoring of operating conditions are critical. In addition, the probe orifice through which the sample is collected must be cleaned frequently. Furthermore, the clogging process is so severe, that medium and heavily sooting environments cannot be examined.

Modeling of Pyridine Effect in Premixed Flames

Predictions using the revised kinetic set were performed to assess the effect of pyridine on modifying the gas-phase chemistry and the precursors to soot. Initially, isothermal conditions at one atmosphere were assumed just to assess the reaction chemistry. The equivalence ratio of the mixture was assumed to be two. Computations were performed at 1400 K and 1600 K with no pyridine added and with 1% pyridine added to the fuel, heptane. In addition, a separate set of computations was performed without the reactions speculated to inhibit aromatic growth. Computed values of naphthalene are shown in Figure 3.4.4-4, and indicate only a small decrease (~5%) in the naphthalene concentration with 1% pyridine added. The decrease in pyrene was as much as 10% through addition of pyridine.

Recently, the complete chemical kinetic mechanism has been utilized to predict chemical kinetic effects occurring within a premixed flame when pyridine is added. Two flames were studied. The first is a heptane/toluene/ethylene fuel-rich flame. As discovered earlier in the project, fuel-rich flames with high molecular weight fuels (such as heptane and/or toluene) are

subject to cellular formation due to differential diffusion between the oxidizer and fuel. Ethylene mitigates the effect. For the second flame, about 3% of the fuel was replaced with added pyridine. The overall equivalence ratio for the two flames was 2.39. Computations were performed with Sandia's CHEMKIN Premix code using flow rates matched to experimental conditions and using a previously measured temperature profile (same assumed for both flames). Obtaining converged solutions was challenging, but eventually we modified an approach developed by colleagues (Litzinger) at PSU to get converged flame solutions. Comparisons of profiles of benzene, naphthalene, phenanthrene, and pyrene for the nonseeded and the pyridine-seeded flames are shown in Figure 3.4.4-5.

Clearly the differences are virtually negligible. To accentuate the differences, the mole fractions from the pyridine-seeded flame were normalized by those from the nonseeded flame. The results are plotted in Figure 3.4.4-6. The odd shapes low in the flame (~ 0.15 cm) can be ignored as this is the preheat portion of the flame and little chemistry is occurring. The early values of the normalized benzene concentration are about 3% lower than the neat values (those with no pyridine added). This reduction is directly in line with the fact that the initial value of toluene (the primary source of benzene) is diluted by 3%. The initial concentration of naphthalene is reduced by more than 5%, consistent with arguments that have been previously proposed for why pyridine should suppress soot production. However, the relative suppression of phenanthrene formation is not as great, and the pyrene concentrations are affected by only 1%. Hence, the predictions leave open some questions and uncertainties regarding the effectiveness of pyridine as a soot-reducing agent. Note that while the trend observed in the modeling was the same as observed in limited experiments, the level of decrease was sufficiently small that further modeling work in this area is not warranted without additional experimental confirmation of the effectiveness of this molecule.

Table 3.4.4-1. Mixture Mole Fractions and Fuel Mass Fractions for Premixed Flames.

Mixture Mole Fractions				
	10% Toluene	10% Toluene/ 4% Pyridine	20% Toluene	20% Toluene/ 4% Pyridine
C7H16	0.02846	0.02758	0.02481	0.02758
C7H8	0.00435	0.00421	0.00853	0.00421
C2H4	0.03864	0.03746	0.03888	0.03746
C5H5N	0.00000	0.00225	0.00000	0.00225
O2	0.19453	0.19452	0.19437	0.19452
N2	0.73402	0.73398	0.73341	0.73398

Fuel Mass Fractions				
	10% Toluene	10% Toluene/ 4% Pyridine	20% Toluene	20% Toluene/ 4% Pyridine
C7H16	0.657599	0.6309	0.569842	0.6309
C7H8	0.092401	0.08865	0.180158	0.08865
C2H4	0.25	0.23985	0.25	0.23985
C5H5N	0	0.0406	0	0.0406

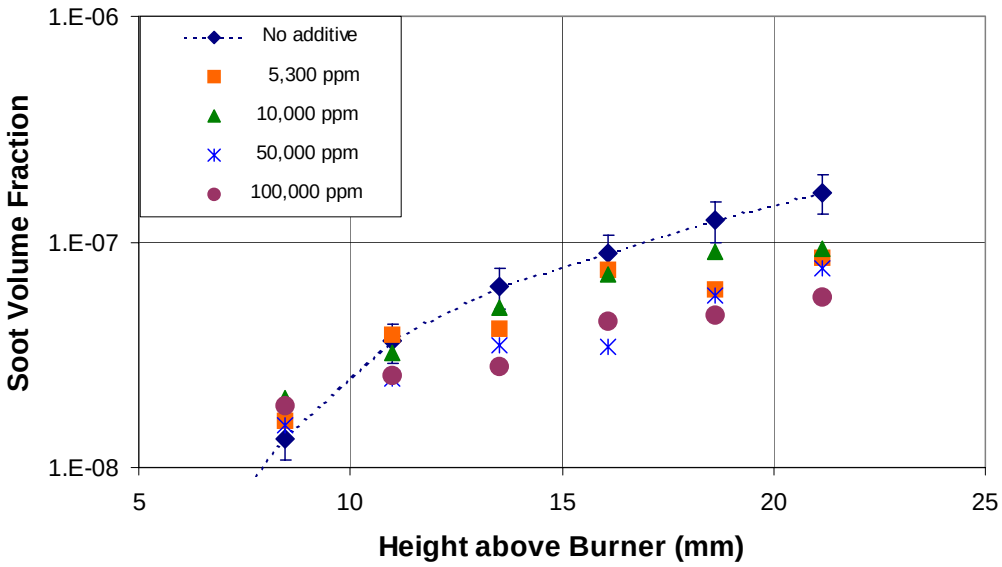

Figure 3.4.4-1. Reduction of Soot in Premixed Flame with Various Levels of Added Pyridine (as ppm in fuel).

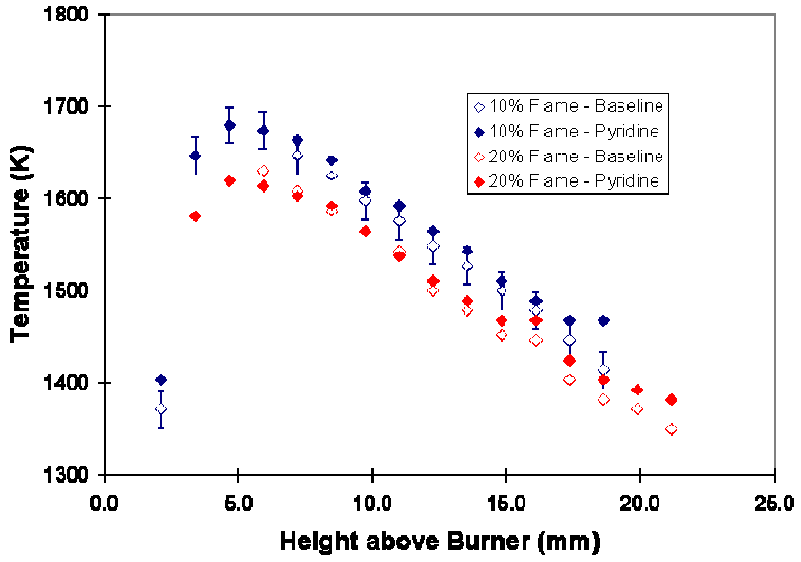

Figure 3.4.4-2. Measured Temperature Profiles for Several Premixed Flames.

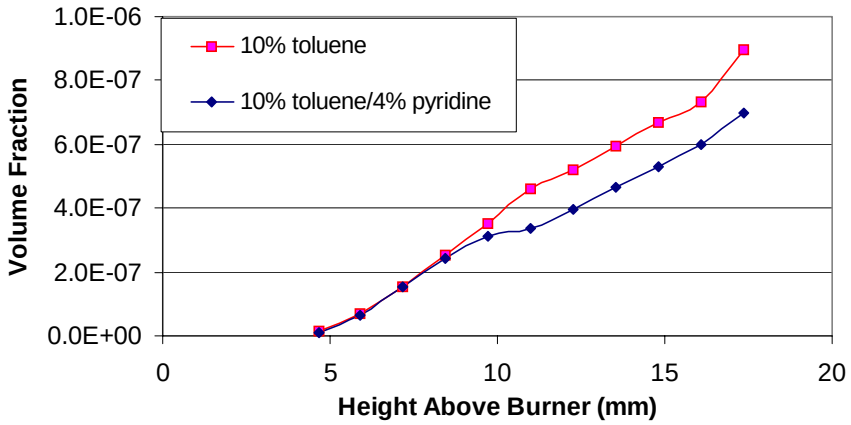

Figure 3.4.4-3. Comparison of Soot Volume Fractions (laser extinction) for Heptane/10% Toluene Flames.

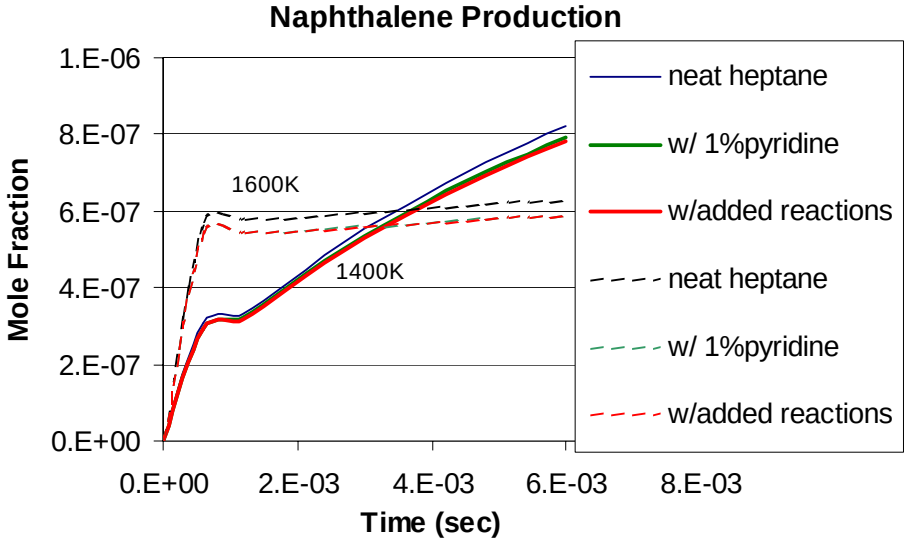

Figure 3.4.4-4. Comparison of Predicted Naphthalene With and Without Added Pyridine.

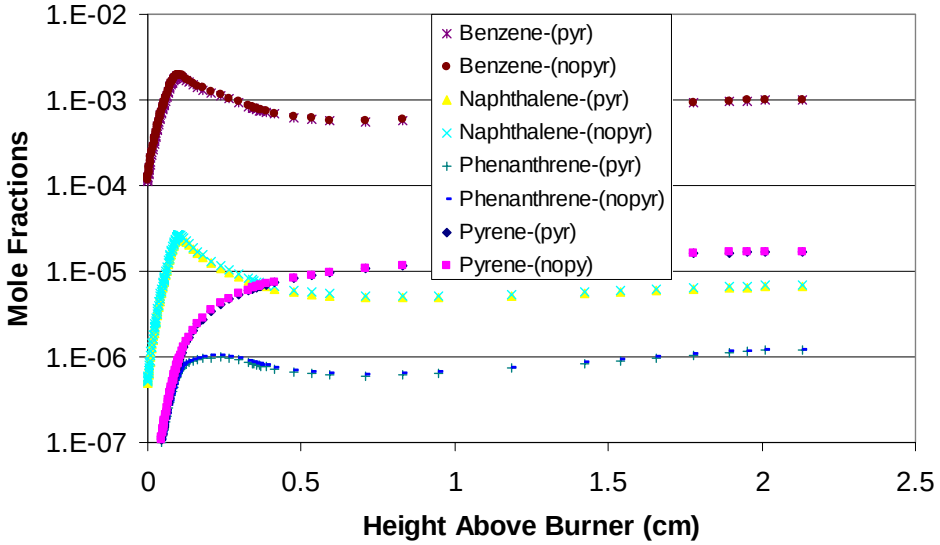

Figure 3.4.4-5. Comparison of Computed Mole Fractions for Several Species as a Function of Height Above the Burner for Fuel-Rich, Premixed Flames With and Without Added Pyridine.

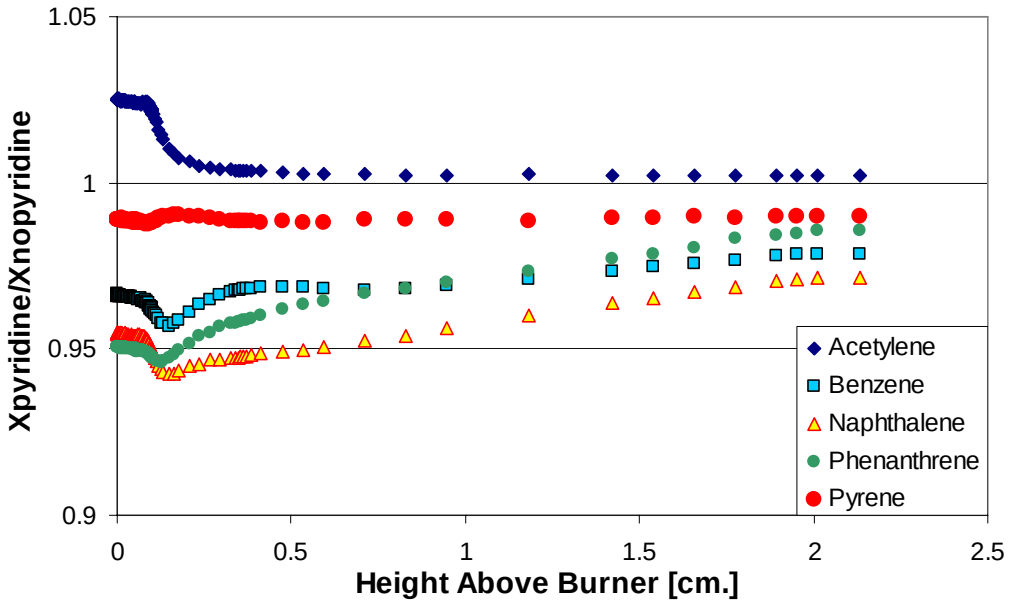

Figure 3.4.4-6. Normalized Concentrations of Key Species in Fuel-Rich Premixed Flames with Added Pyridine.

3.4.5 TURBULENT SPRAY FLAME

Experimental Conditions

In spite of the difficulties in getting repeatable results in the spray flame, it was still useful in obtaining results on the effects of additives. After discovery of the problem with repeatability, experimental procedures were modified to allow for real-time addition of the additive so that day-to-day repeatability was not an issue. It was in this mode that the burner was used to investigate the effectiveness of pyridine on soot. The experimental conditions were similar to those used for the commercial additive tests. Precisely equivalent conditions could not be established due to problems with nozzle fouling and subsequent cleaning which modified flow characteristics. Pyridine was added at 10% by volume to ensure that any effect from the additive would be clear in the measurements.

Experimental Results

Figure 3.4.5-1 presents the time dependent plot of the LII signal with and without the pyridine additive for the heptane/toluene fuel. The results show a substantial reduction, on the order of 40%, for this level of pyridine addition.

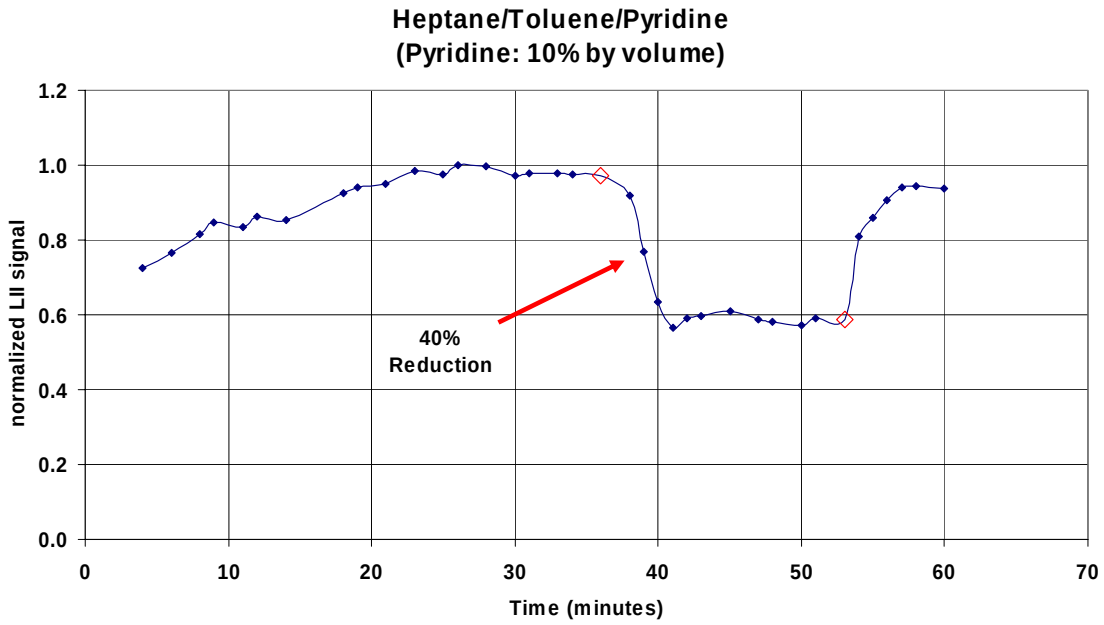

Figure 3.4.5-1. Effect of Pyridine on Soot in the Turbulent Spray Flame.

3.4.6 HIGH PRESSURE TURBULENT REACTOR

Experimental Conditions

Initial tests with pyridine were run with JP-8 as the fuel. The airflow for the tests was 32 gm/s and the equivalence ratio was 1.3. The inlet air temperature was 550 K and the chamber pressure was 0.5 MPa. The results showed little effect of pyridine in contrast to the results from the turbulent spray burner and premixed flame results. At the annual IPR in 2005, a suggestion was made that experiments be performed with heptane/toluene to investigate the effect of fuel composition on the results. Consequently, runs with pyridine in heptane/toluene were performed under similar experimental conditions to the JP-8 experiments.

Experimental Results

Figure 3.4.6-1 presents a summary of the test results on soot volume fraction versus additive concentration for JP-8 and heptane/toluene. Pyridine was added at 5 and 10% by volume. The measured soot volume fractions with and without pyridine in the fuel stream indicate that there was a small reduction in soot by the additive. For JP-8, the decrease in soot concentrations was approximately 3% at an additive concentration of 5% by volume and approximately 10% at an additive concentration of 10% by volume, both of which are within the measurement uncertainty for the extinction method used. The experiments with heptane/toluene showed even smaller reductions in soot levels when pyridine is added. The results led to two conclusions: first, that pyridine is not effective in reducing soot under conditions which simulate actual combustor conditions; and secondly, that the fuel composition does not account for the lack of an effect on soot.

It appears then that the pyridine is not effective at the higher pressure conditions in this reactor compared to the atmospheric pressure spray flame. The reason for this effect could not be determined from modeling because the chemical mechanism for the pyridine/heptane/toluene mixture proved to be inadequate, even for the shock tube experiments.

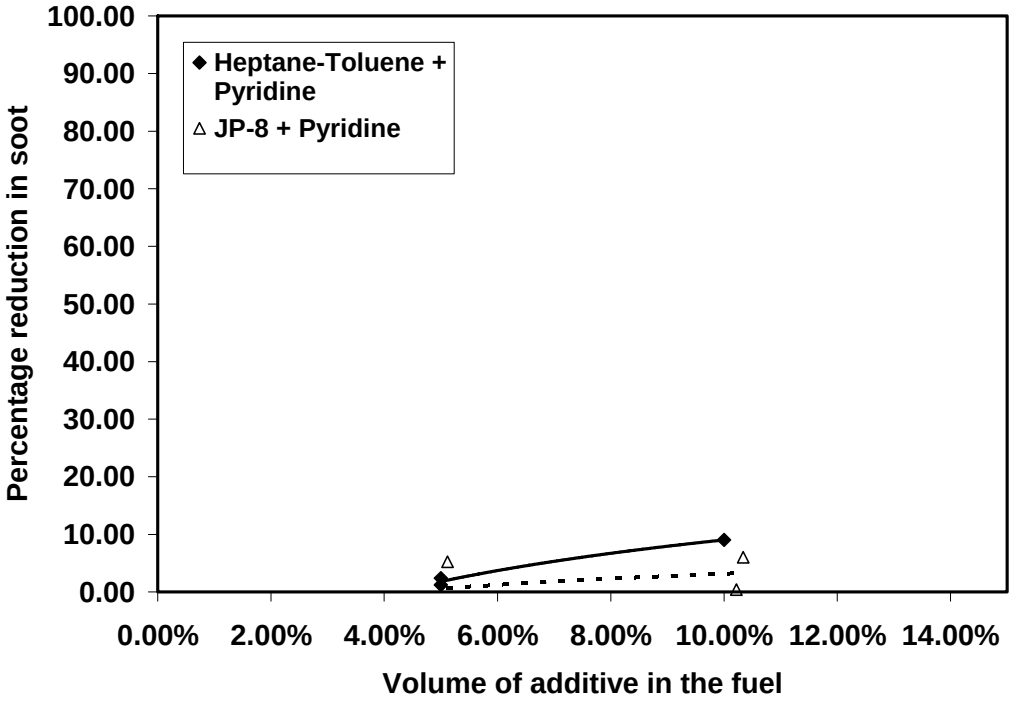

Figure 3.4.6-1. Effect of Pyridine on Soot Formation in the Dump Combustor with JP-8.

3.5 PHOSPHORUS

The studies of the effects of phosphorus were done under supplemental funding for the program; therefore, the work performed was essentially screening studies to determine if the phosphorus showed sufficient reductions in soot to merit more detailed testing. Experiments were performed in the shock tube, theWSR, the premixed flame and a combustor. In addition tests were performed in a coflow diffusion flame because this type of flame was used in the prior study at NBS that motivated the investigation.

3.5.1 SUMMARY OF MAJOR FINDINGS

Table 3.5.1-1 presents a summary of the effects of the phosphorus compounds tested. The use of different molecules to deliver the phosphorus resulted from a problem with MSDS data on the compound that was originally chosen. As a consequence, each lab took it upon itself to locate alternatives suitable for the device to be used. Past work in the literature indicates that the molecule used to deliver the phosphorus has little or no effect on the results for flame inhibition. Overall the results from the various experiments are not encouraging. Depending upon the device, and in some cases the experimental conditions, the phosphorus often had no effect; in the test of a device that is closest to an actual combustor, it increased soot emissions.

An important and unexpected result, however, came out of the modeling work that was part of this study. The modeling results indicated that the addition of phosphorus would lower NOx emissions. As far as we can ascertain, this result has not been reported in the literature to date. This effect on NOx emissions was predicted prior to the studies in the CFM combustor, so those studies were modified to include measurements of NOx emissions. The measurements show that NOx decreases with the addition of phosphorus under certain test conditions, so the predictions were partially verified by the experimental data.

Table 3.5.1-1. Summary of the Effects of Pyridine on Soot.

	Additive	**Fuel**	**Effect on Soot**	**Comments**
Shock tube	Trimethyl phosphite	Heptane/ Toluene	Varies: decrease to increase	Variation with reaction temperature
Well-stirred reactor	Diethyl allyl phosphate	Heptane/ Toluene	Varies: no effect & reduction	Depends on temperature and treatment level. Experimental problems led to early termination of the test series.
Premixed flame	Trimethyl phosphate	Ethylene	No effect	
Coflow Diffusion Flame	Trimethyl phosphate	Ethylene	Decrease	
	Trimethyl phosphate	Propane	Decrease	
	Trimethyl phosphate	Ethane	No effect	
Opposed-jet flame	Demethyl methyl phosphonate	Ethylene	No effect	
CFM Combustor	Diethyl allyl phophate	Heptane/ Toluene	Increases soot	Decreases particle size, but increases number density

3.5.2 SHOCK TUBE

Organophosphorus (OPC) compounds have been investigated as potential flame suppressants and their catalytic cycles that involve recombination of key flame radicals have been identified [Jayaweera 2004, Korobeinichev 2004]. In this study, the effects of OPCs and their flame inhibiting catalytic cycles on soot formation was investigated. Premixed gas phase experiments were conducted using a single pulse shock tube. An OPC, trimethyl phosphite with an adequate vapor pressure (17 torr at 760 mmHg), was selected as the phosphorus additive for this study. For all phosphorus additive experiments 1.73 vol% (2.5wt%) of trimethyl phosphite was added to base fuel mixture (80 vol% heptane + 20 vol% toluene). Experiments were conducted over a temperature range of 1600 K – 1900 K at a pressure of ~21 atm, an equivalence

ratio of 3.0, and dwell times (fuel exposure times) of ~7.5 ms. The product distribution assumed when calculating the equivalence ratio was CO_2, H_2O, and $HOPO_2$. Fuel mixture composition was verified using GC-MS.

Both gaseous products and soot yields were measured and normalized with respect to the mass of carbon in the fuel to exclude any volumetric effect that may arise from normalization with respect to the mass of the fuel. Results from Leco carbon analysis of particle yields are shown in Figure 3.5.2-1. The solid lines indicate polynomial trend lines that were used to fit the experimental soot yields. The trend lines show that addition of trimethyl phosphate decreased soot yields at lower temperatures and increased soot yields at higher temperatures. The experiments were done at close temperature intervals to cover the entire temperature range instead of repeating the same experiments at a fixed temperature. The measured ignition delay data shows (see Figure 3.5.2-2) addition of trimethyl phosphite reduced the ignition delay over the entire temperature range.

The lower ignition delay under fuel-rich conditions at the lower temperature region indicates a possible chemical effect in reducing the soot yields from reactions of the type $HOPO_2+H=PO_2+H_2O$ [Jayaweera 2004] that consume the H radicals. At the higher temperatures this effect is negated due to dissociation of $HOPO_2$.

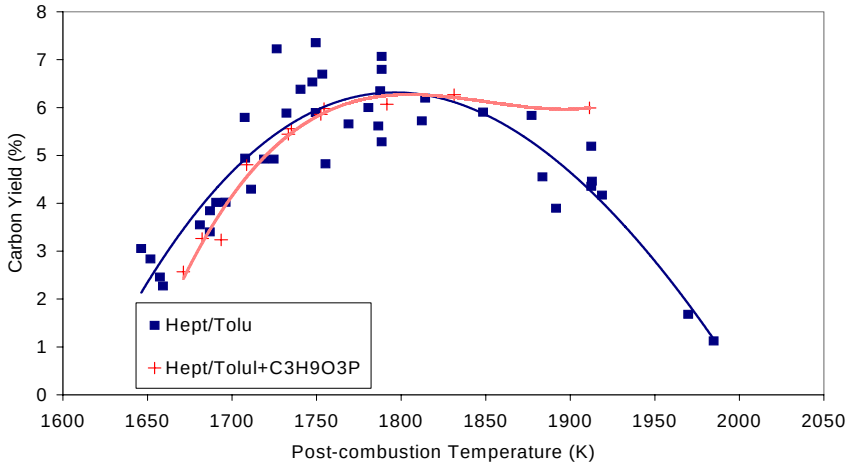

Figure 3.5.2-1. Carbon Yield from Combustion of Heptane/Toluene and Heptane/Toluene+(25K ppm) Trimethyl Phosphite.

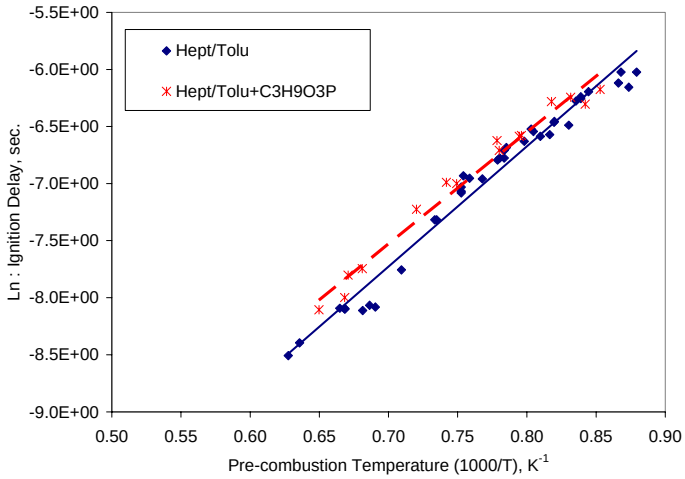

Figure 3.5.2-2. Ignition Delay from Combustion of Heptane/Toluene and Heptane/Toluene+(25K ppm) Trimethyl Phosphite.

3.5.3 WELL-STIRRED REACTOR

Diethyl allyl phosphate at concentrations of 2500 ppm and 1000 ppm was tested as a soot reduction additive in the WSR using a 80% heptane/20% toluene mixture as the neat fuel. The air mass flow rate for the WSR was 240 g/min, and the equivalence ratio, ϕ, was set to 1.92 or 2.0. The vapor pressure of this additive was much lower than had been advertised in the manufacturers literature, however, we estimate that at $\phi = 2.0$ and 2500 ppm, the additive needs to have a vapor pressure of only 0.125 Torr to remain in the vapor phase. To enhance vaporization the fuel was heated to a temperature of 160°C, and the air to 200°C before entering the vaporizer, leading to a final inlet temperature 175°C. In contrast to studies of lean to slightly fuel-rich studies in the CFM56 combustor, no visual effect was observed on the exhaust plume when the additive was added. Soot mass samples were acquired from a probe located at a distance of 16 cm from the exit of the WSR in the plug flow region.

The results of carbon mass collected on quartz filters and determined by carbon burnoff in the LECO analyzer are shown in Figure 3.5.3-1. Most of the results obtained with the 1000 ppm additive concentration were compromised by a problem with the LECO apparatus. At the concentration levels studied, the additive was shown to reduce total measured carbon at $\phi = 2.0$ by approximately 20% and to have little effect on the total measured carbon mass at equivalence

ratios of ϕ = 1.92. The total carbon mass measured was divided into a volatile component, that was obtained by measuring the carbon burned off from the filter at temperatures below 330°C, and a carbonaceous component, obtained by the carbon mass burned off from the filter at temperatures above 330°C. The results are shown in Figures 3.5.3-2 and 3.5.3-3. For ϕ = 2.0 the greatest reduction in the carbon mass with the addition of the additive occurred in the volatile component, while the carbonaceous fraction of the carbon mass changed little for the cases with the additive.

Methane, acetylene, ethylene, formaldehyde and benzene were monitored using the FTIR multigas analyzer; the results are shown in Figures 3.5.3-4 and 3.5.3-5. All of these gaseous species increased in concentration as the equivalence ratio changed from ϕ=1.92 to ϕ= 2.0, but their concentrations increased further when the additive was used. These data suggest the concentrations of these soot precursors increase in association with the decrease in volatile carbon mass, associated with the use of the additive.

The results of the gas analysis show no measurable increase or decrease in the already low NO_x values. Reactor temperature was measured for the ϕ = 2.0 case and showed a slight difference (less than 5 °K) between the additive and nonadditive cases. The reactor thermocouple broke during the second day of testing and no temperatures were measured for the ϕ = 1.92 cases.

Testing was halted early because of observed pressure increases in the reactor jet ring which are thought to be indicative of accumulation of deposits caused by the additive in the hot jet ring.

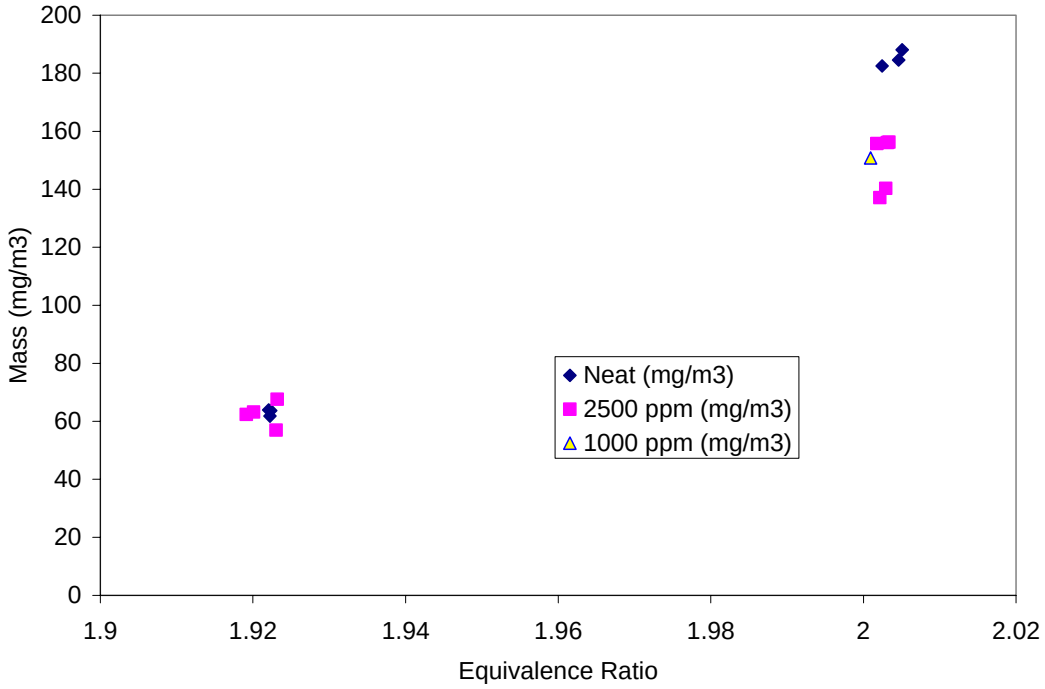

Figure 3.5.3-1. The Effect of Diethyl Allyl Phosphate on Measured Carbon Mass from Samples in the WSR.

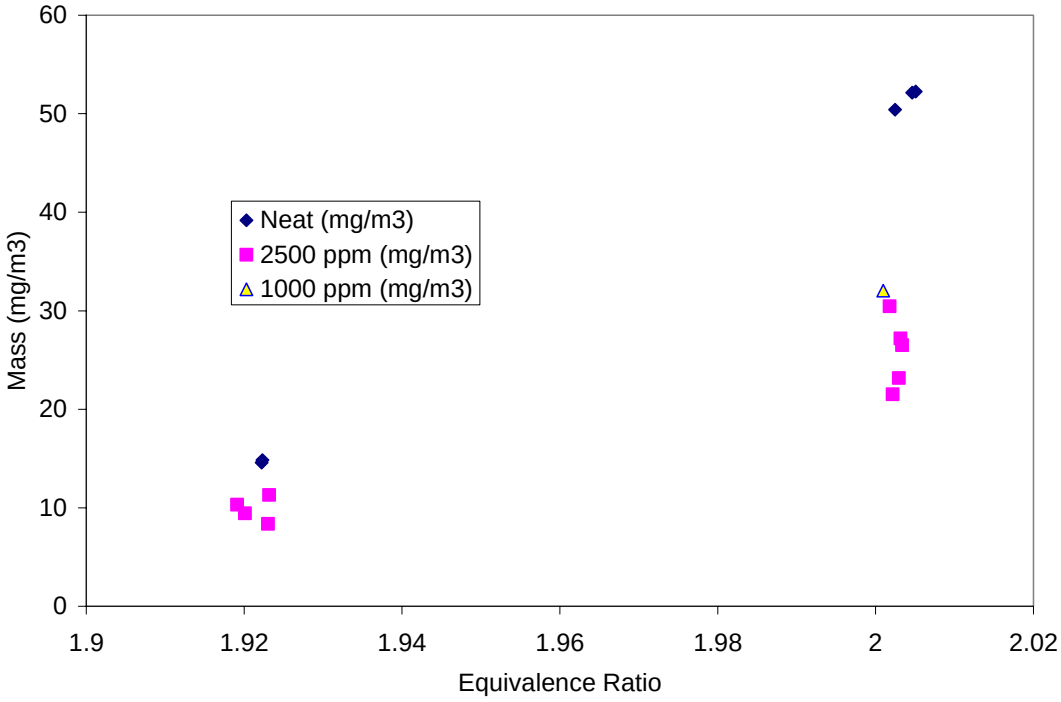

Figure 3.5.3-2. The Effect of Diethyl Allyl Phosphate on the Volatile Carbon Mass from Samples in the WSR.

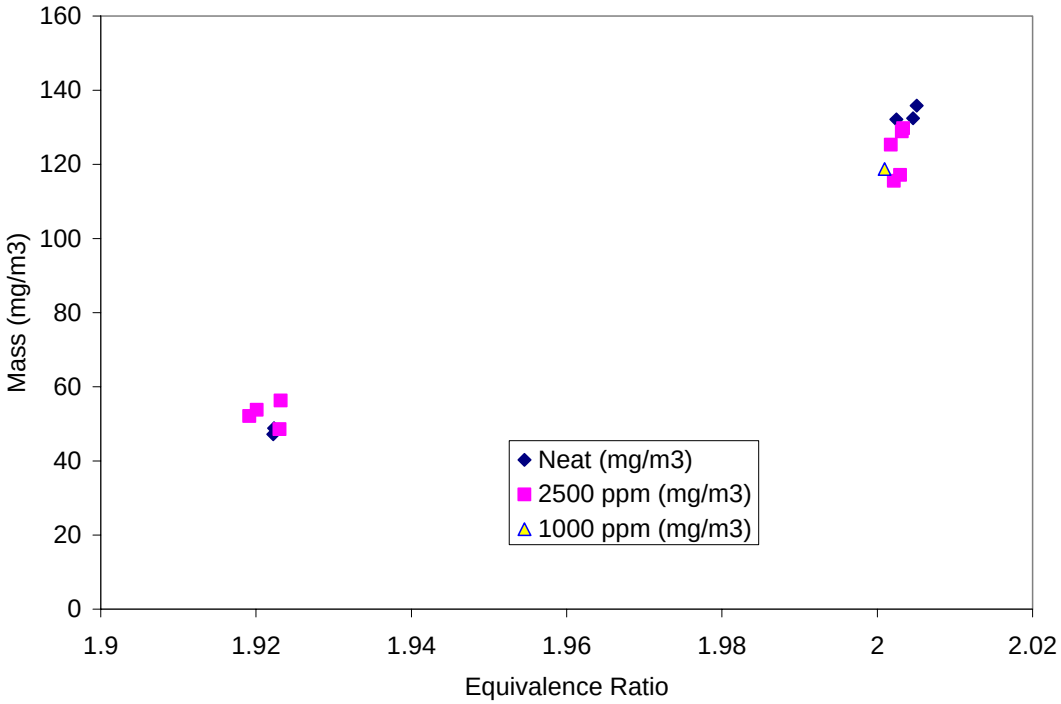

Figure 3.5.3-3. The Effect of Diethyl Allyl Phosphate on the Carbonaceous Carbon Mass from Samples in the WSR.

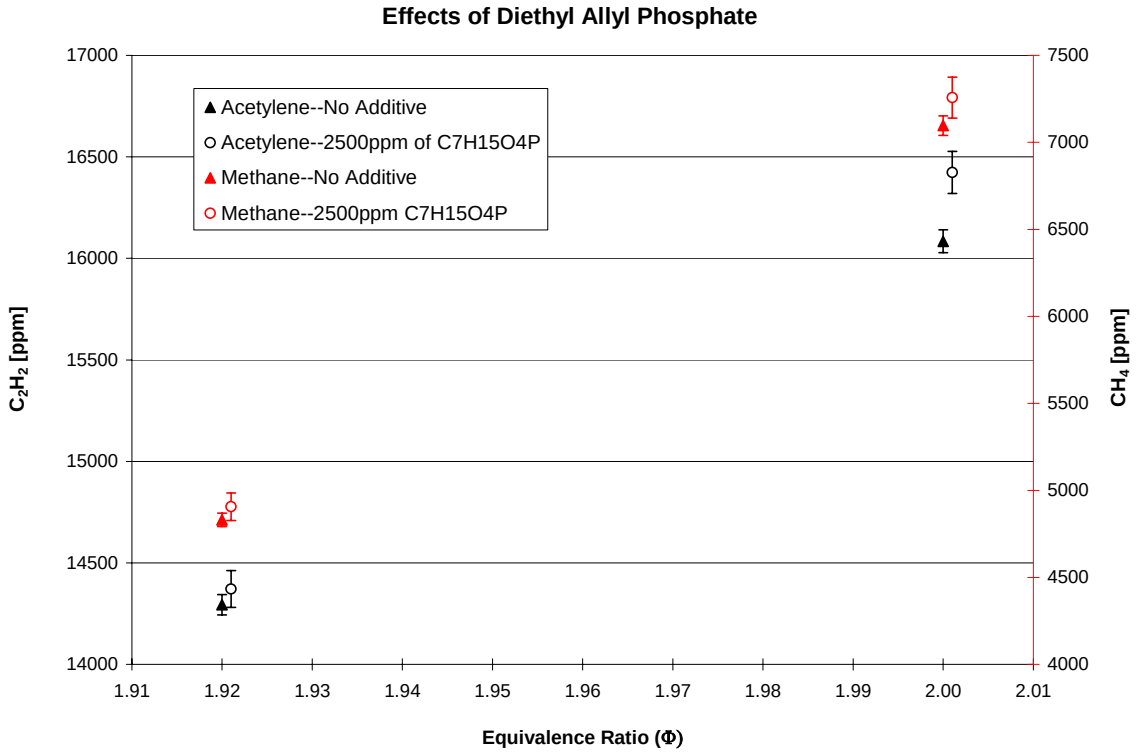

Figure 3.5.3-4. Effect of Diethyl Allyl Phosphate on Acetylene and Methane.

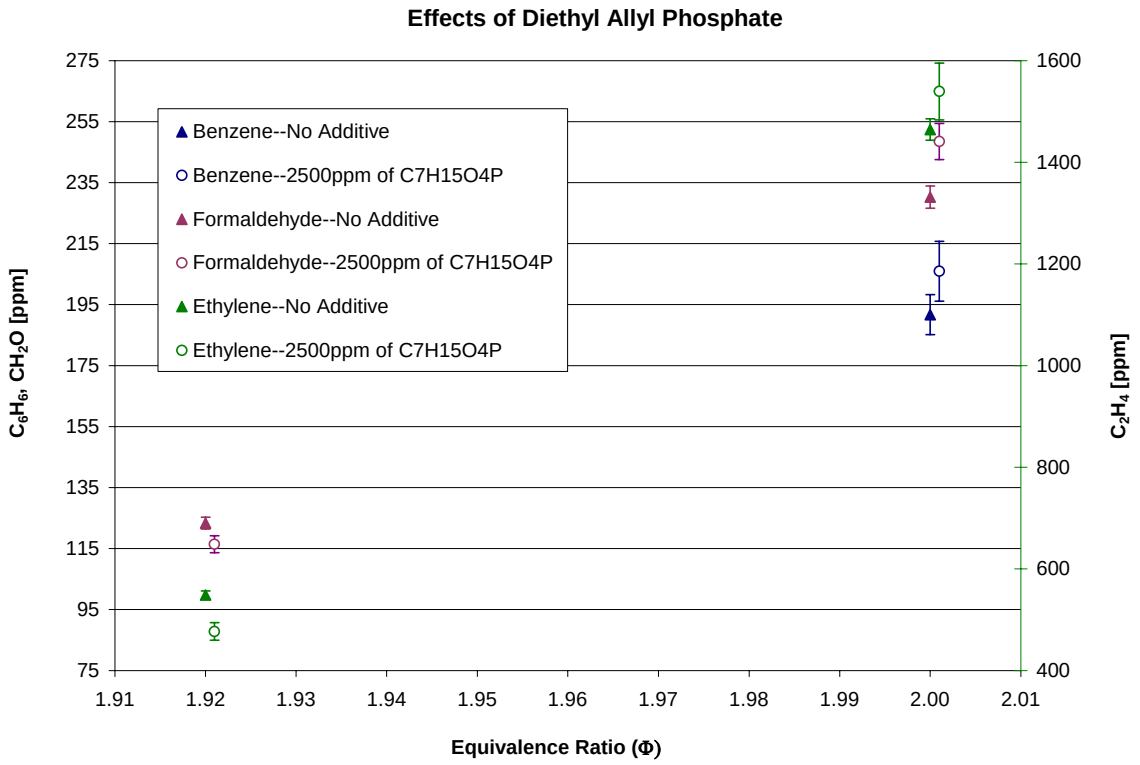

Figure 3.5.3-5. Gas Analysis of Light Hydrocarbons from WSR.

3.5.4 PREMIXED FLAME

Experimental Conditions

The experiments were conducted on a laminar premixed flat flame burner using ethylene (C_2H_4) as the fuel and air as the oxidizer. The flame was shielded from the surrounding air using a shroud of nitrogen supplied through an annulus 11 mm thick, concentric to the burner, which was 60.3 mm in diameter. The soot volume fraction was measured using laser extinction, using the 514.5 nm line of an argon-ion laser (Coherent Innova 70).

The total mass flow rate of the fuel/air mixture was approximately 225 mg/s. The additive was introduced into the reactant stream by passing the reactant's flow through a bed of glass beads ~4 mm in diameter and filled with trimethyl phosphate (TMP). Using the vapor pressure of TMP, it was estimated that the concentration of TMP in the reactant stream was approximately 0.1% by volume of the reactant stream or 0.7% by mass of the reactant stream. The experiment was conducted for equivalence ratios of 2.34 and 2.64, conditions used in all of

the other premixed flame experiments conducted at Penn State. The flow conditions for the experiment are presented in Table 3.5.4-1.

Experiments were also attempted with propane in order to allow direct comparison to the work of Hastie and Bonnell [1980]. However, the flame was just beginning to produce soot at the higher equivalence ratio of 2.64, and at those conditions it was beginning to become unstable. Consequently, no data could be collected for propane with and without TMP added. The difference between the present experiments and those of Hastie and Bonnell is the type of burner used. They used a small diameter premixed jet flame that could be stabilized at much richer conditions than the flat flame used in this study. The flat flame burner is necessary to allow optical diagnostics to be used.

Results

The soot volume fractions for the baseline and the flame with TMP added for an equivalence ratio of 2.34 is shown in Figure 3.5.4-1. It is seen that the soot volume fractions for the flame with TMP added are slightly higher than the baseline flame, the increase in soot at the last measurement point being approximately 3%, which is within the uncertainty of error for the technique. The same trend is seen at an equivalence ratio of 2.64 in Figure 3.5.4-2; but the increase in soot is slightly higher than the leaner flame, with an increase of approximately 6.5% at the final measurement point of 20 mm HAB.

Within this program, an increase of soot was observed when ethanol was added to ethylene/air opposed flow diffusion flames due to similar effects. Analysis of modeling results showed that the increase was due to the methyl radicals formed from the ethanol which increased the rate of formation of the first aromatic ring via a 4-carbon intermediate. The increase of soot with the addition of TMP may be a result of a similar effect.

Table 3.5.4-1. Flow Conditions for Premixed Ethylene Flames with TMP.

Flame	Baseline	Additive	Baseline	Additive
Equivalence Ratio	2.34	2.34	2.64	2.64
C/O ratio	0.78	0.78	0.88	0.88
Fuel mass flow rate (C_2H_4), mg/s,(cc/s)[a]	30.8 (26.45)	30.8 (26.45)	34.1 (29.28)	34.1 (29.28)
Air mass flow rate mg/s,(cc/s)[a]	194.3 (161.93)	194.3 (161.93)	190.9 (159.09)	190.9 (159.09)
TMP mass flow rate mg/s,(cc/s)[b]	0	1.19 (0.20)	0	1.19 (0.20)
Coflow N_2 mass flow rate mg/s,(cc/s)[a]	557 (478.28)	557 (478.28)	557 (478.28)	557 (478.28)
Pressure (atm)	1	1	1	1
Temperature (K)	295	295	295	295
Fuel	Ethylene (99.5%)	Ethylene (99.5%)	Ethylene (99.5%)	Ethylene (99.5%)

a: volumetric flow rate calculated based on T=293K

b: TMP mass flow rate calculated based on T=293K and vapor pressure (110Pa at 293K)

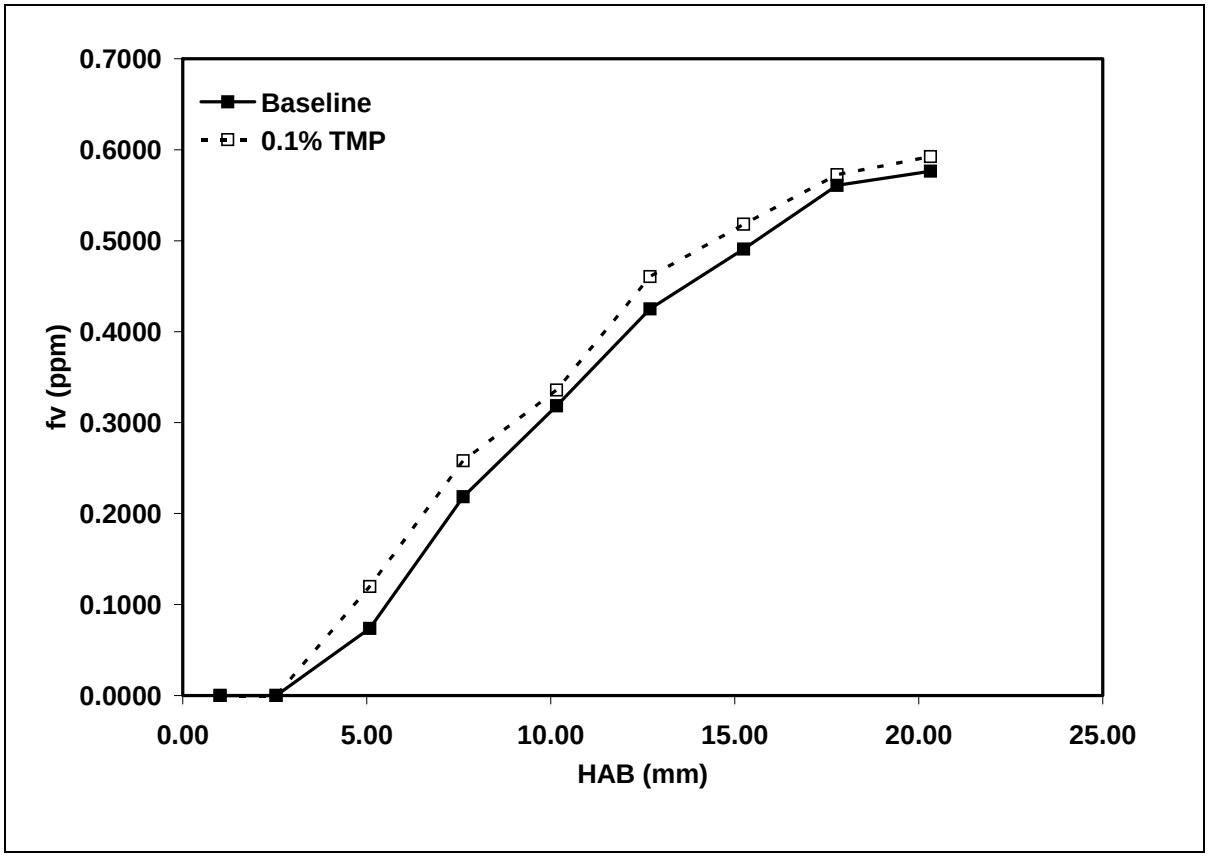

Figure 3.5.4-1. Effect of TMP on Soot Volume Fractions for Phi = 2.34 Premixed C_2H_4 Flame.

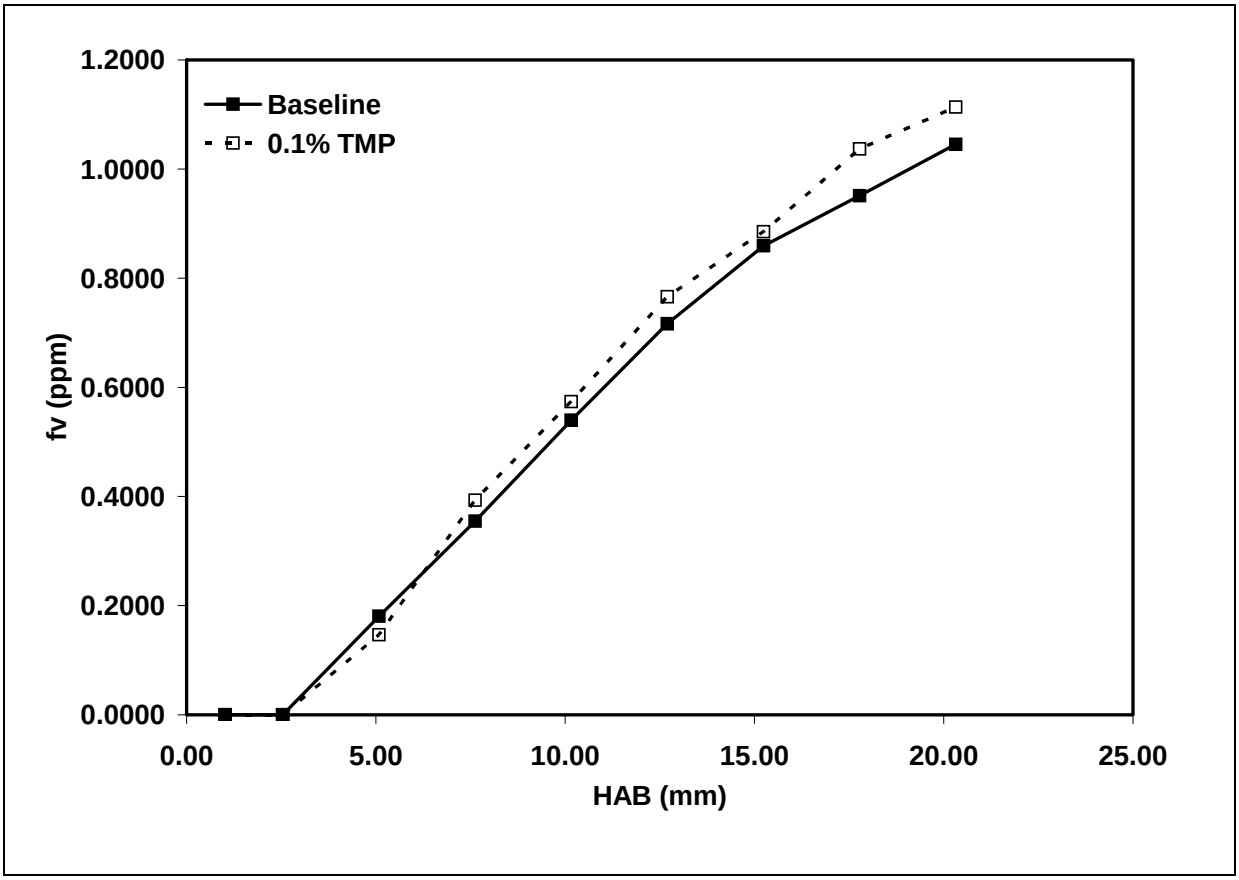

Figure 3.5.4-2. Effect of TMP on Soot Volume Fractions for Phi = 2.64 Premixed C_2H_4 Flame.

3.5.5 COFLOW DIFFUSION FLAME

Experimental Conditions

The fuels used in the study were ethylene (purity 99.5%), propane (purity 99.9%) and ethane (purity 99.5%). Coflow air was supplied from a laboratory compressor. The volumetric flow rates of ethylene, propane and ethane were 3.85, 2.5 and 4.13 cc/s, while air flow rate was fixed at 713.3 cc/s for each fuel. The TMP (purity ≥ 99%), supplied by Sigma-Aldrich Corp., and known as a chemically active flame inhibitor is liquid at room temperature with low vapor pressure (less than 1 torr at ambient temperature). Due to higher boiling point (~197 °C) of TMP, it is impractical to make a vaporizer system. Instead, a glass aspirator was fabricated to convey the TMP vapor by the fuel volumetric flow. The volumetric percentage of TMP was

approximately 0.1% of fuel volumetric flow rate based on vapor pressure of TMP. Flame running conditions are shown in Table 3.5.5-1.

Results

Figure 3.5.5-1 shows "false-color" images of the three flames with and without TMP added. The most obvious effects are visible for ethylene and propane in which the TMP delays the appearance of soot increasing the height above the burner at which soot is first observed. For ethane the soot concentration is so low that no differences are visible.

Decreases in soot concentration do occur when TMP is added to the ethylene and propane flames, but they are difficult to see from the images. Therefore, radial soot concentration profiles at various heights in the flames are presented in Figures 3.5.5-2, 3.5.5-3 and 3.5.5-4 to show the differences more clearly. (In these figures the solid symbols represent the baseline flame and the open symbols the flame with TMP.) In general, differences are most clear at the lowest flame heights. Finally, to give an overall sense of the effects on soot, volume fraction was integrated radially at each height according to the equation:

$$F_v(z) = \pi\left(\int_0^R f_v(z,r)rdr + \int_{-R}^0 f_v(z,r)rdr\right)$$

Figure 3.5.5-5 presents the overall trends showing that phosphorus leads to a decrease in soot for in the ethylene and propane flames. The reduction in soot with the addition of TMP to the propane flame is consistent with the original work of Hastie and Bonnell with this fuel.

Table 3.5.5-1. Experimental Conditions for Coflow Diffusion Flame Studies with TMP.

	Ethylene		Propane		Ethane	
	Baseline	Additive	Baseline	Additive	Baseline	Additive
Fuel flow rate (cc/s)	3.85	3.85	2.5	2.5	4.13	4.13
Coflow air flow rate (cc/s)[a]	713.3	713.3	713.3	713.3	713.3	713.3
TMP flow rate (cc/s)[b]	0	0.00418	0	0.00271	0	0.00448
Ambient temperature (^{o}C)	21.8	21.8	21.8	21.8	22	22
Flame height (mm)[c]	88	88±1	88	88±1	88	88±1
Fuel purity (%)	99.5		99.9		99.5	
Pressure (atm)	1		1		1	

a: Building shop air

b: Volumetric flow rate calculated based on temperature and vapor pressure at 20 ^{o}C

c: Maintained same flame heights for flames to keep same residence time

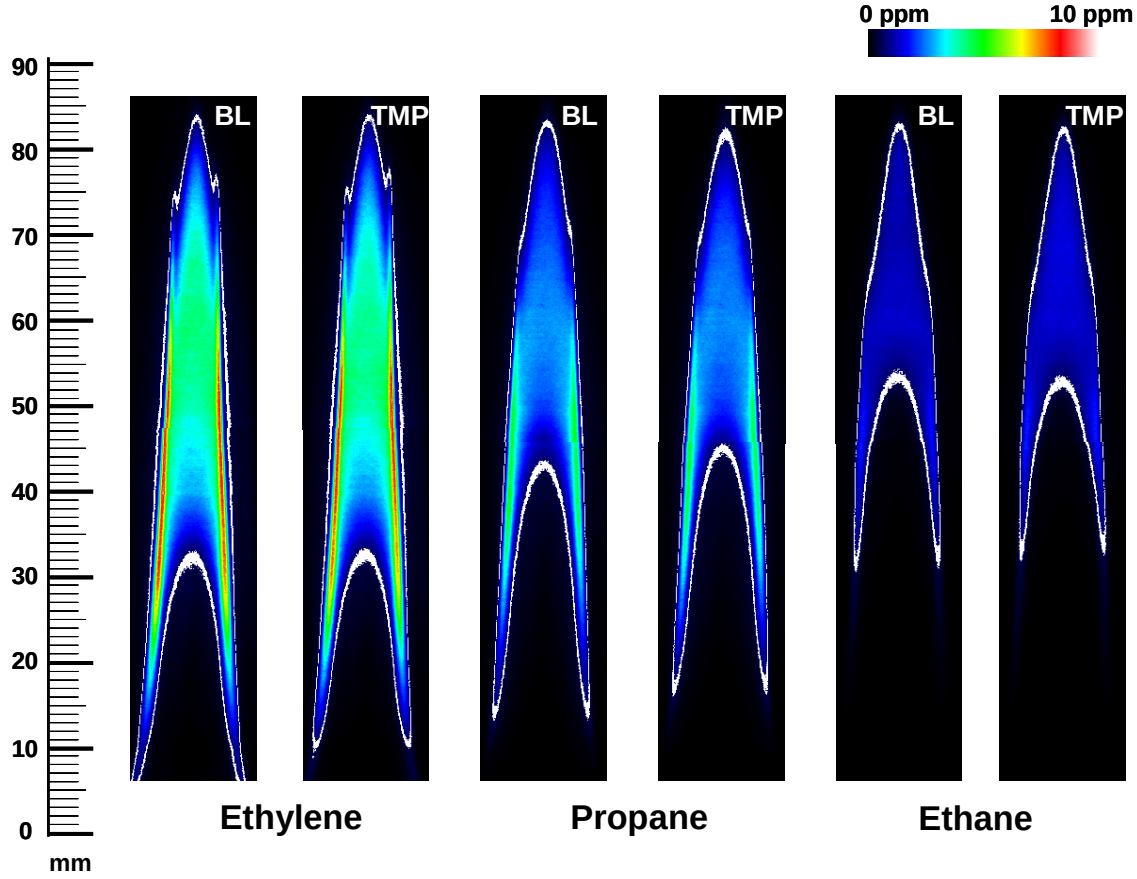

Figure 3.5.5-1. Soot Volume Fraction Fields for Baseline and TMP Addition Flames of Ethylene, Propane and Ethane. Contour of fv=0.5 ppm shown in white line is superimposed on soot volume fraction fields.

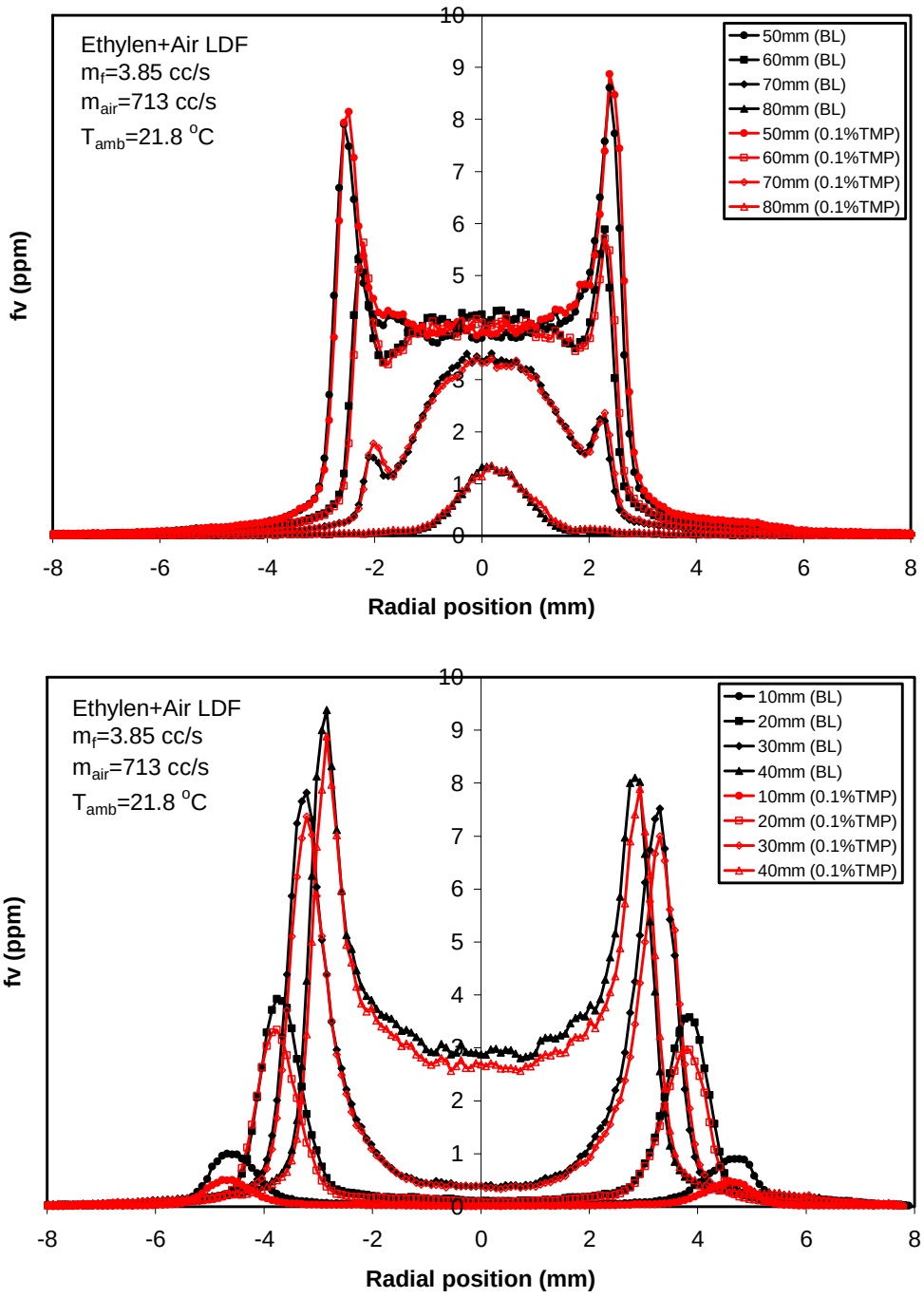

Figure 3.5.5-2. Soot Volume Fraction Profiles for Ethylene Flame with Baseline and TMP Addition.

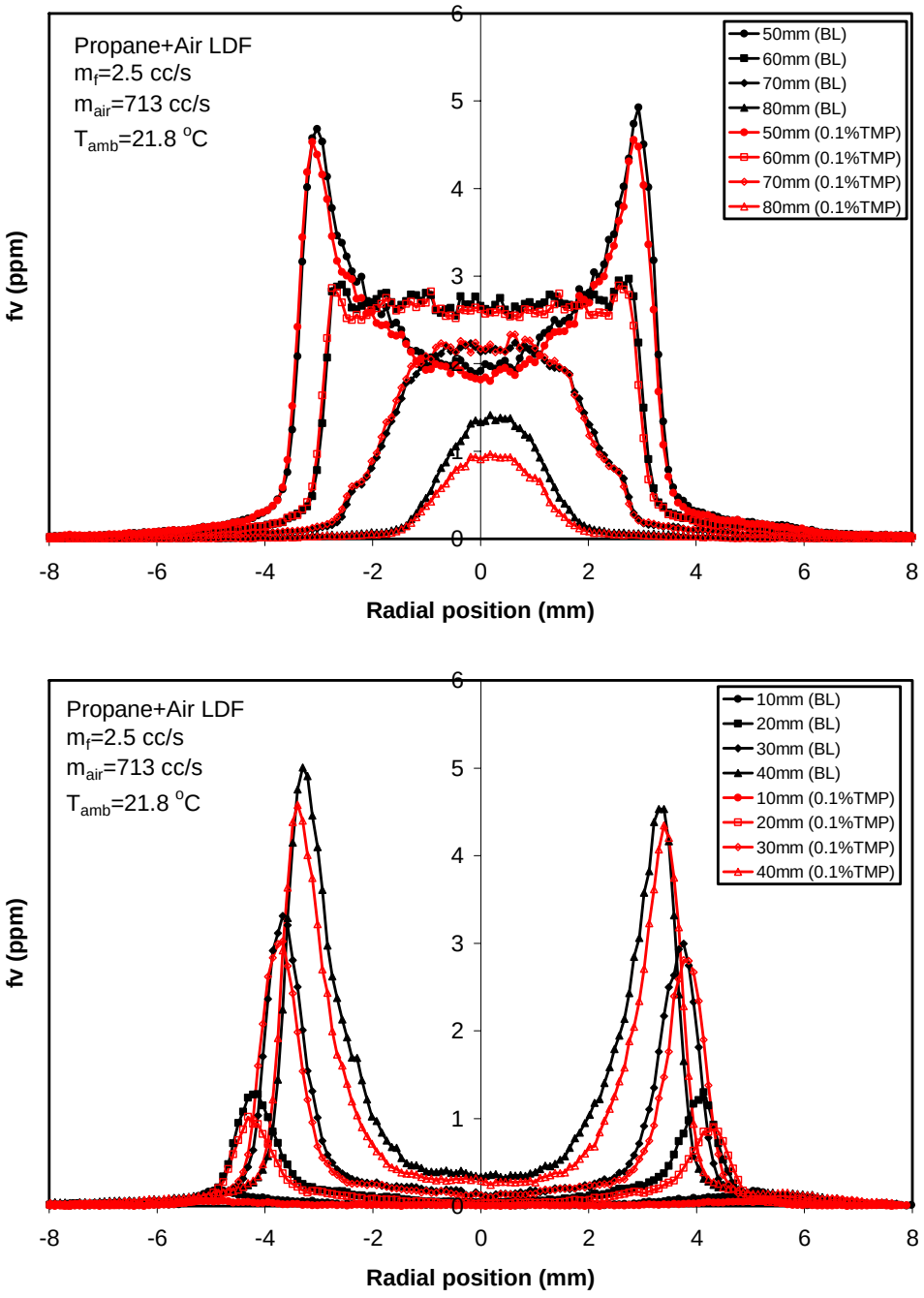

Figure 3.5.5-3. Soot Volume Fraction Profiles for Propane Flame with Baseline and TMP Addition.

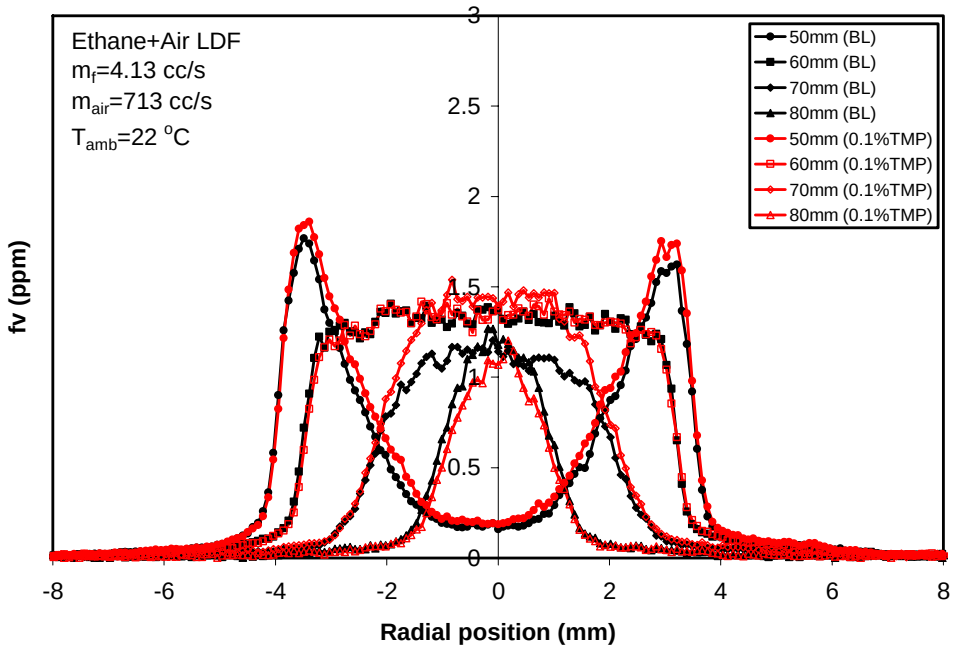

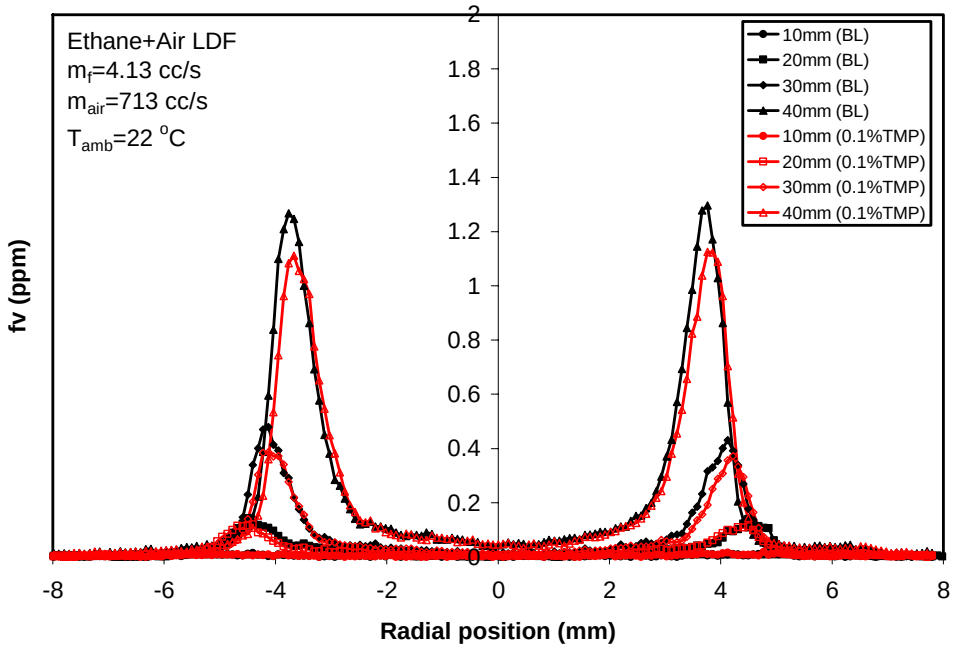

Figure 3.5.5-4. Soot Volume Fraction Profiles for Ethane Flame with Baseline and TMP Addition.

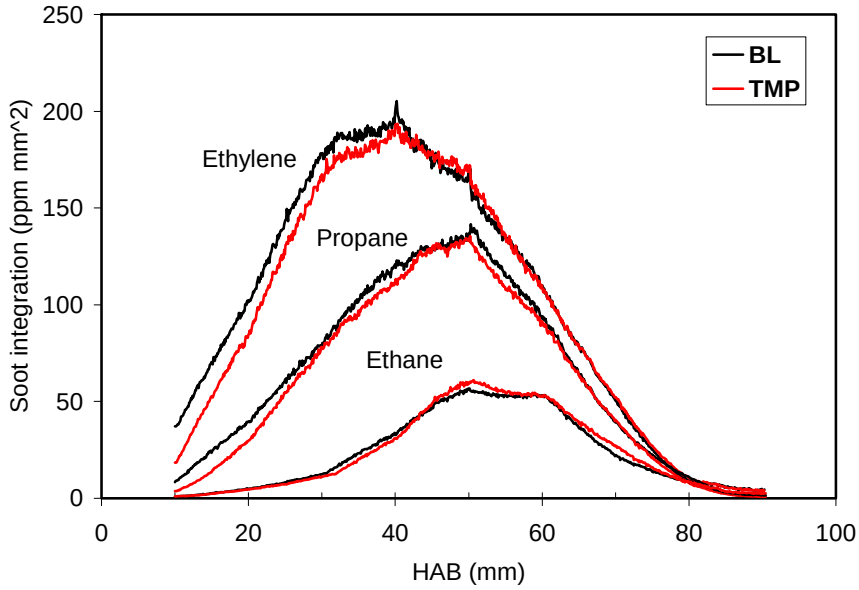

Figure 3.5.5-5. Integrated Soot Volume Fraction as a Height of the Flame

3.5.6 OPPOSED-FLOW DIFFUSION FLAME

Because of the availability of a chemical mechanism (with transport files) in CHEMKIN format, dimethylmethylphosphonate (DMMP) was chosen for investigation as a soot suppressant at ARL. Figure 3.5.6-1 shows the chemical structure of DMMP and provides some information on physical properties of DMMP and experimental conditions of the experiments in the opposed-flow burner. Figure 3.5.6-2 shows some photographs of ethylene/air opposed-flow flames to which DMMP has been added on the air side, at two different oxidizer global strain rates. Qualitatively, the addition of DMMP to the oxidizer (air) stream causes the flame to appear more whitish than the neat flame, increasing the apparent separation between combustion and sooting regions. Figures 3.5.6-3 and 3.5.6-4 show PLIF images of OH fluorescence and light scatter by particles for air and fuel side addition of DMMP to opposed flow ethylene/air flames. At the time of these experiments, we were capable of supplying additives to only the upper gas stream in the opposed-flow burner. For this reason, it was necessary to move the fuel stream to the upper burner duct so we could add DMMP to the ethylene fuel.

Figure 3.5.6-5 shows a summary of experimental measurements of DMMP to fuel and oxidizer streams for the opposed-flow ethylene/air flames. As with ethanol addition to ethylene/air flames, addition of DMMP to the oxidizer stream was more effective at particle

reduction than fuel side addition. However, it is worth mentioning that DMMP is a known flame suppressant.

A chemical kinetic mechanism for DMMP combustion in ethylene/air flames was compiled, in CHEMKIN format, with thermo and transport files. Figures 3.5.6-6 through 3.5.6-13 show calculations that predict species concentration versus flame position for fuel and oxidizer side addition of DMMP to the opposed-flow ethylene/air flames. The low vapor pressure of DMMP limits the amount that can be introduced as vapor at room temperature, and the initial parameters of the calculations reflect this limitation.

Figures 3.5.6-6 through 3.5.6-13 show that the calculations of DMMP addition to fuel and oxidizer sides of opposed-flow ethylene/air flames agree, qualitatively, with experiment. That is, addition of DMMP to the air side of the flame is predicted to be more effective at reducing soot precursors C2H2 and A1 than for fuel side addition. However, as mentioned previously, DMMP is a known fire suppressant. The mechanism for suppression is believed to be radical scavenging of H and OH in a catalytic-like cycle. This process is shown in Figure 3.5.6-14.

A detailed analysis of flame chemistry such as was performed for ethanol addition to flames was not performed for the DMMP addition. However, we do not believe DMMP would be a suitable soot suppressant because of its flame inhibition characteristics. Additionally, we have a qualitative observation that for addition to ethylene/air and heptane/air opposed-flow flames, addition of DMMP produces a particulate (off white in color) in addition to soot.

Global strain rate: 60 sec^{-1} – 200 sec^{-1}

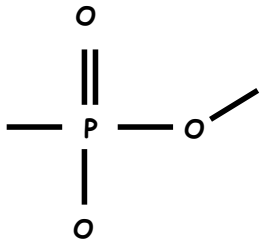

DMMP ($C_3H_9O_3P$)

Di-methyl methyl phosphonate

FW = 124.08
Density (20 C) = 1.17 g/cc
BP = 92-97 C
Clear liquid
Light, slightly unpleasant odor
Toxic
Nerve agent simulant
Fire suppressing agent

Figure 3.5.6-1. The Chemical Structure of DMMP and Information on Physical Properties of DMMP and Experimental Conditions of the Experiments in the Opposed Flow Burner.

C2H4/air flame

No additives

180 sec^{-1}

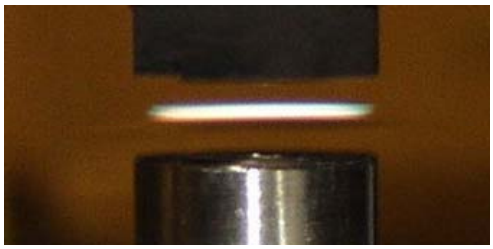

Air side addition of DMMP to C2H4/air flame

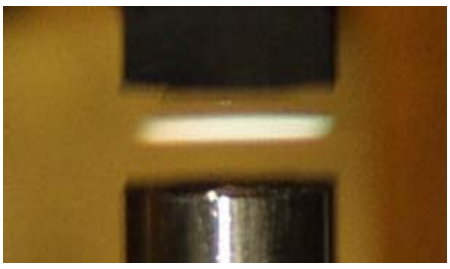

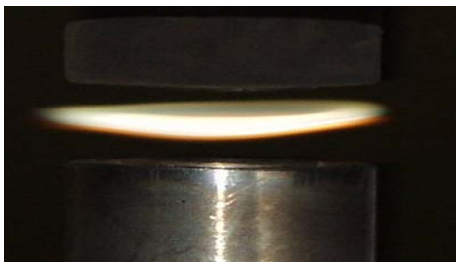

180 sec^{-1}

62 sec^{-1}

Figure 3.5.6-2. Photographs of Ethylene/Air Opposed Flow Flames to which DMMP has been Added on the Air Side.

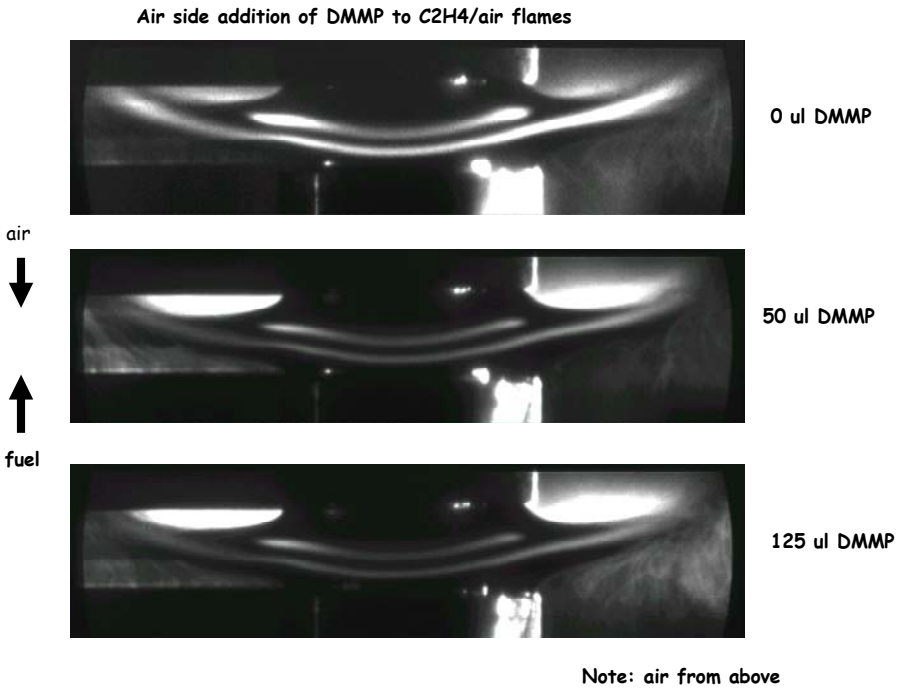

Figure 3.5.6-3**.** PLIF Images of Opposed Flow Ethylene/Air Flames to which DMMP has been Added to the Oxidizer (air) Stream. Note the air stream enters the flame from above.

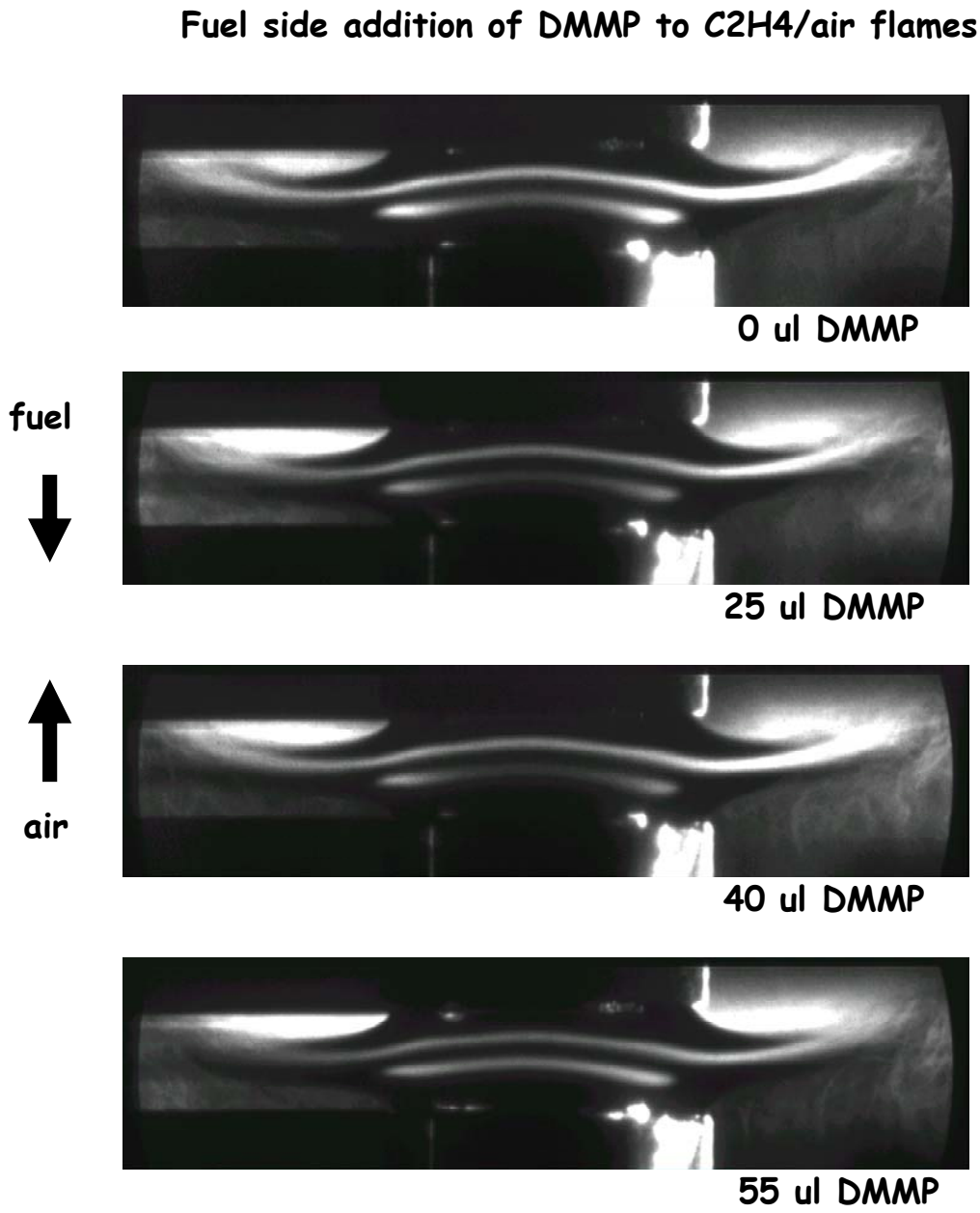

Figure 3.5.6-4. PLIF Images of Opposed Flow Ethylene/Air Flames to which DMMP has been Added to the Fuel (ethylene) Stream. Note the fuel stream enters the flame from above.

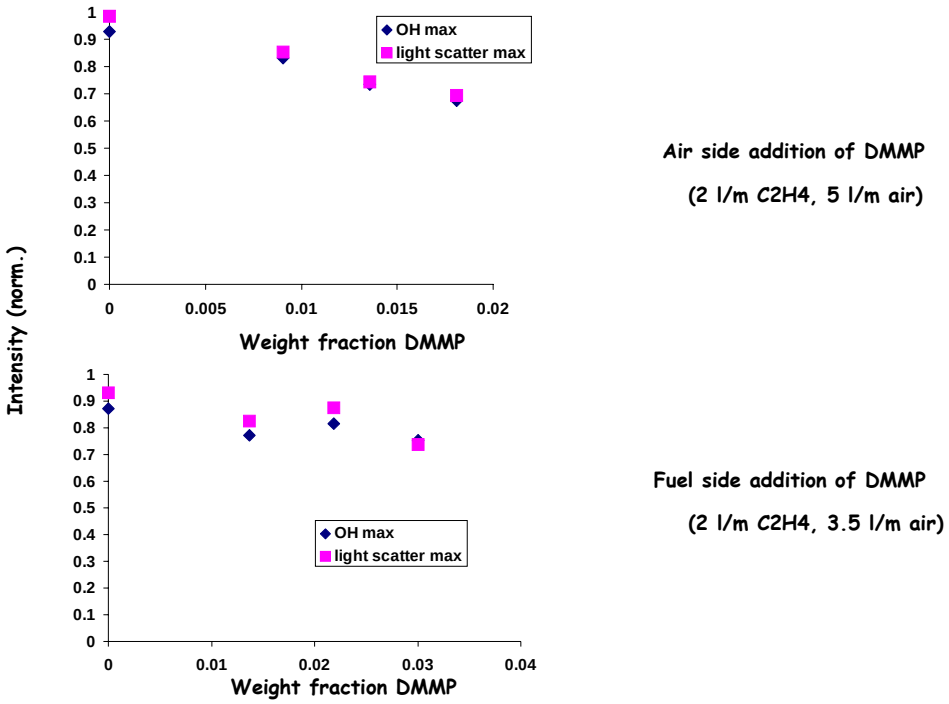

Figure 3.5.6-5. A Summary of Experimental Measurements of DMMP to Fuel and Oxidizer Streams for the Opposed Flow Ethylene/Air Flames.

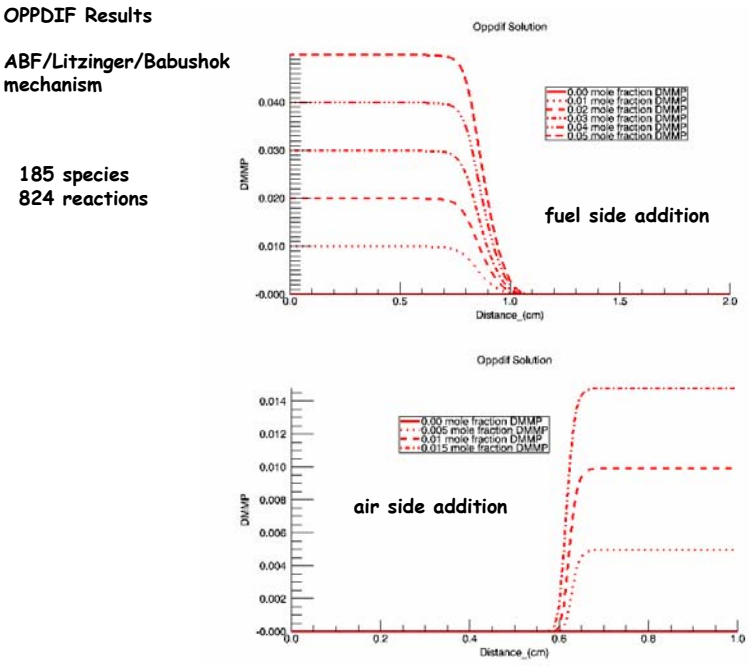

Figure3.5.6-6. DMMP Calculated Concentration vs Flame Position (centerline) for Fuel and Oxidizer Side Addition to Ethylene/Air Opposed Flow Flames.

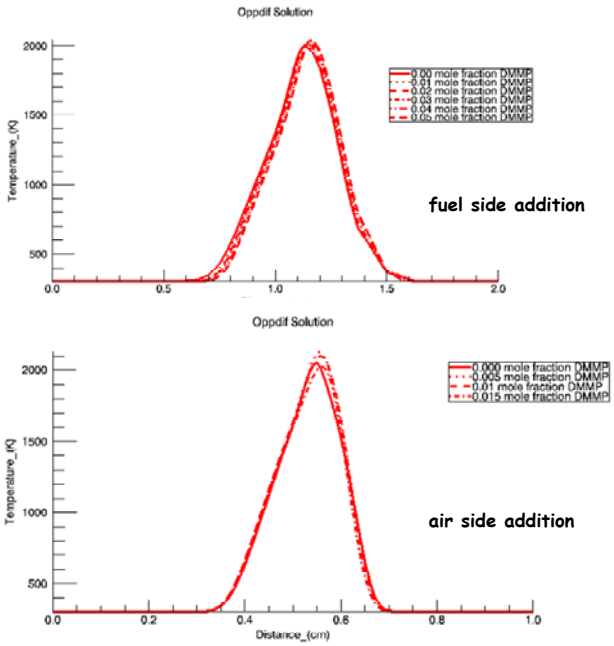

Figure 3.5.6-7. Calculated Temperature vs Flame Position (centerline) for Fuel and Oxidizer Side Addition to Ethylene/Air Opposed Flow Flames.

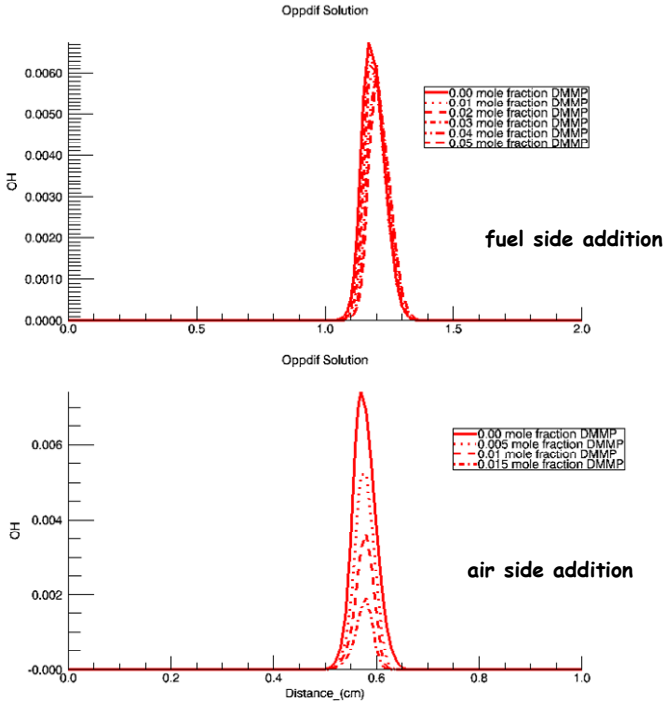

Figure 3.5.6-8. Calculated OH Concentration vs Flame Position (centerline) for Fuel and Oxidizer Side Addition to Ethylene/Air Opposed Flow Flames.

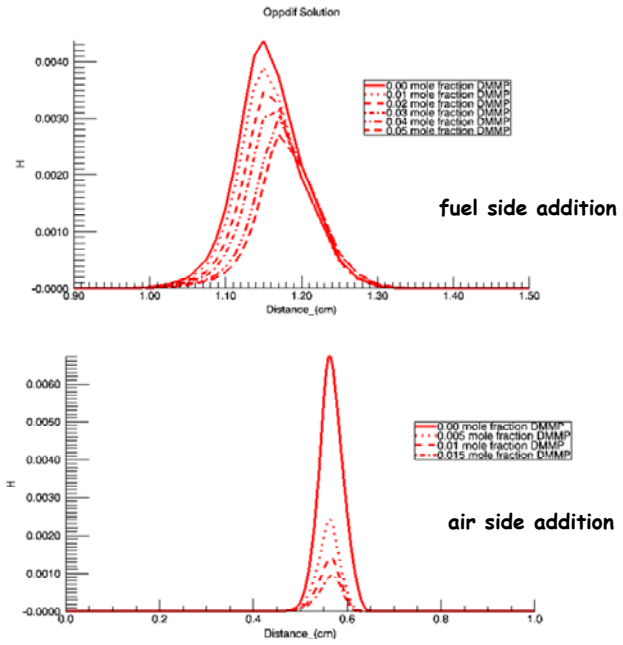

Figure 3.5.6-9. Calculated H Atom Concentration vs Flame Position (centerline) for Fuel and Oxidizer Side Addition to Ethylene/Air Opposed Flow Flames.

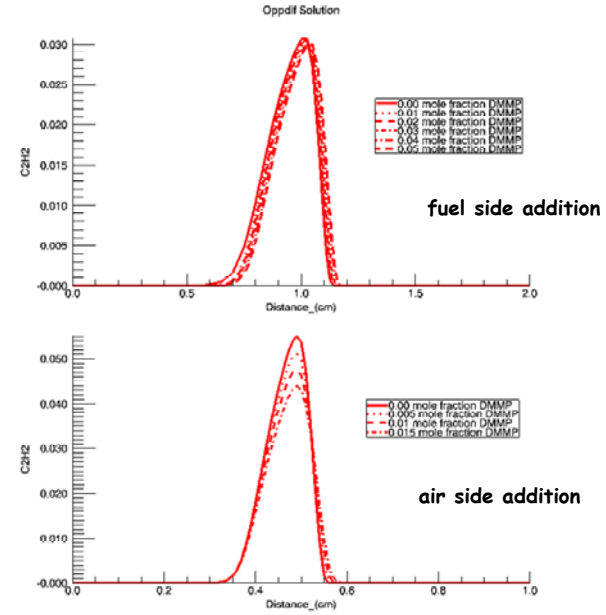

Figure 3.5.6-10. Calculated C2H2 Concentration vs Flame Position (centerline) for Fuel and Oxidizer Side Addition to Ethylene/Air Opposed Flow Flames.

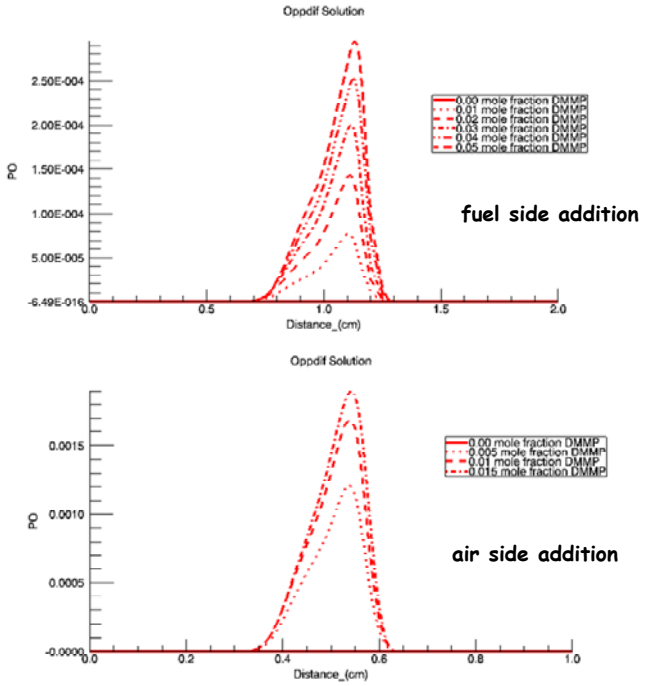

Figure 3.5.6-11. Calculated PO Concentration vs Flame Position (centerline) for Fuel and Oxidizer Side Addition to Ethylene/Air Opposed Flow Flames.

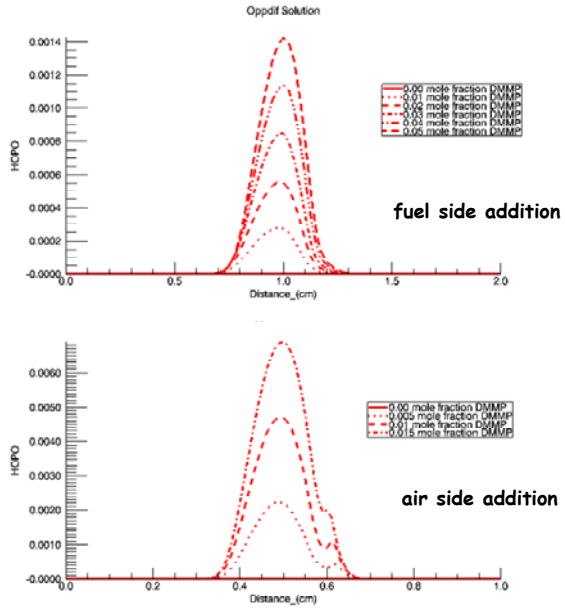

Figure 3.5.6-12. Calculated HOPO Concentration vs Flame Position (centerline) for Fuel and Oxidizer Side Addition to Ethylene/Air Opposed Flow Flames.

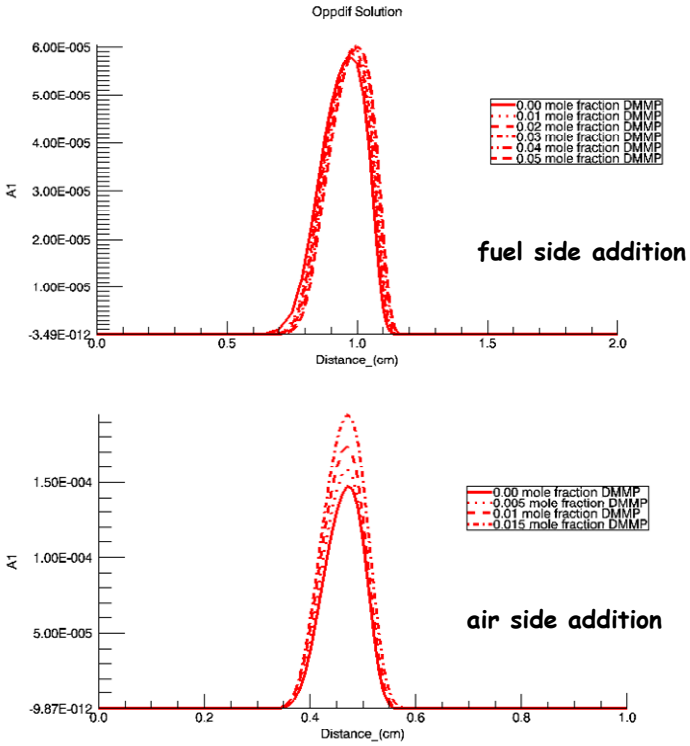

Figure 3.5.6-13. Calculated A1 (benzene) Concentration vs Flame Position (centerline) for Fuel and Oxidizer Side Addition to Ethylene/Air Opposed Flow Flames.

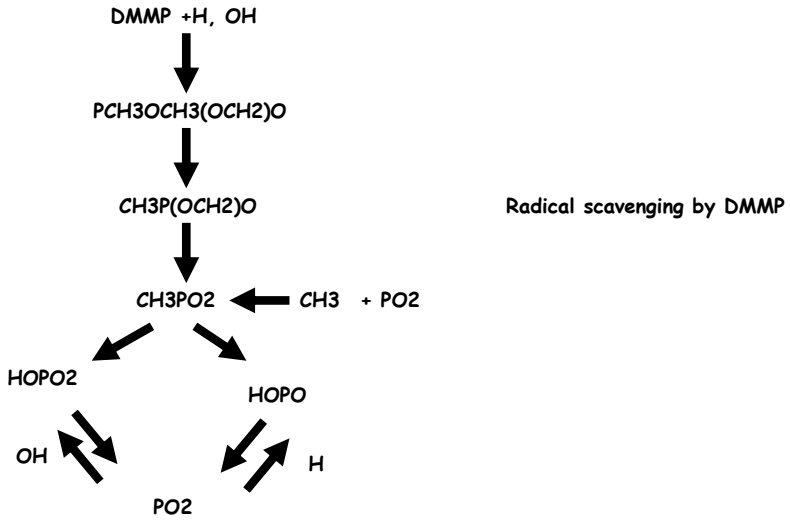

Figure 3.5.6-14. The Radical Scavenging Mechanism Believed to be Responsible for the Flame Suppression Effectiveness of DMMP.

3.5.7 CFM COMBUSTOR

For the current tests, a fuel mixture of 80% heptane and 20% toluene was used. This was done so that previous modeling work could be more readily compared to the data. The combustor overall equivalence ratio was varied from Φ=0.70 to 1.10, which resulted in a fuel flow rate of 112-175 ml/min. The airflow rate was constant at 28 gm/sec. Additive concentrations of 1000 ppm, 2500 ppm and 5000 ppm were tested.

Discussion of Results

A semi-log graph of particle number density (PND) as a function of the combustor equivalence ratio (Φ) for JP-8 3773 and the heptane/toluene blend is shown in Figure 3.5.7-1. Baseline data using JP-8 is always taken for comparison to any fuel being tested. This graph shows that heptane/toluene generally produces much fewer particles than JP-8. The general trend of the curve shows that there is a reduction of PND from a Φ of 0.7 to around 0.9, lean mixtures. This is believed to be for two reasons. The first is that there is more burnout of particles as the fuel flow rate is increased because the exhaust gas temperature is higher. It is also possible that any unburned fuel particles that may exist at Φ=0.7 are more likely to be vaporized at the higher temperatures. Secondly, to increase fuel flow rate, the pressure drop across the nozzle must increase. The higher nozzle pressure causes the fuel to atomize into smaller droplets and these smaller droplets burn more readily without producing soot. At equivalence ratios of Φ>0.9, there is a strong increase in PND with Φ. The exhaust gas temperature does not increase, but in fact decreases slightly in this range so no increase in particle burnout can occur. At the same time, the shorter residence time of the particles in the flame tube, combined with a lack of available oxygen, prevents any particles from oxidizing fully.

Additive tests are generally run at a lean (Φ=0.7) and a rich (Φ=1.1) equivalence ratio. The procedure is to operate the TSI particle instrumentation in a continuous measurement mode while the additive is cycled on and off several times using syringe pumps. During the additive cycling, adequate time is given for the fuel system and combustor to come to equilibrium. This demonstrates repeatability and readily shows if there are any hysteresis affects. This additive

required approximately 45-60 minutes for the particulate count to reach a steady state value, which is much longer than for most additives.

Figure 3.5.7-2 shows the results of adding 1000 ppm of diethyl allyl phosphate to the 80/20 heptane/toluene mixture. The additive substantially increases the particle count at 1000 ppm for both lean and rich conditions. The increase is several orders of magnitude for lean conditions and roughly an order of magnitude for rich conditions. At high PND, i.e., greater than 10000 counts, the particle counters operate in the photometric mode, which is less sensitive than the individual particle counting mode. This may explain why the increase in PND at rich conditions is not as dramatic as for lean conditions.

Additive concentration levels of 2500 ppm and 5000 ppm were also tested and were found to increase PND to a level such that our sampling system was not able to dilute the sample to a point at which we could get a measurement. Figures 3.5.7-3 and 3.5.7-4, (a) and (b), show pictures taken at Φ=0.7 and 1.1 both with and without the phosphorus additive. Figure 3.5.7-3(a) shows the typical blue, conical flame characteristic of this combustor. Since very little soot is produced at this condition, the downstream section is quite clear. When the additive was being injected at 1000 ppm, there was a visible color change to the exhaust gases, which filled the whole combustion chamber. These particles had an orange-yellow appearance, different from the mostly yellow color normally seen as soot. The photographs at Φ=1.1 are similar to the lean condition. Figure 3.5.7-4(a) shows a less well-defined conical flame, with the combustion chamber downstream of the flame being not nearly as clear as in Figure 3.5.7-3(a). There are also streaks of soot that can be seen downstream of the flame. Figure 3.5.7-4(b), similarly to Figure 3.5.7-3(b), shows a combustion chamber filled with soot particles, but without the streaks of soot seen in Figure 3.5.7-4(a). It appears that the phosphorus additive may be producing soot more evenly than the fuel alone does. It should be noted that the naked eye is not necessarily a good indicator of this behavior, and that further study would be needed to verify this point. Studying the fuel physical properties and spray characteristics both with and without the additive would be needed to test this.

Particle size data was also taken in this study and the results are summarized in Table 3.5.7-1. It can be seen from the table that JP-8 produces the largest mean particle size at an equivalence ratio of 1.1. The heptane/toluene mixture produces slightly smaller particles, while also producing less, as seen previously. The heptane/toluene mixture with 1000 ppm additive

produced the smallest average particle size, but also produced many more particles. This is what one would expect when burning a metal-containing additive. The data for Φ=0.7 is incomplete because not enough particles were produced at this condition to get an accurate sample from the SMPS.

Even though no particulate data could be taken for additive levels above 1000 ppm, emissions data was still taken at higher additive levels. This data is shown in Figure 3.5.7-5. For the two equivalence ratios tested, NOx emissions were reduced as the additive concentration increased, except for Φ= 1.1 at 5000 ppm. It is possible that this is an errant point, but further testing would be needed to verify this. This result is consistent with calculations presented elsewhere in this report that have shown NOx emissions reduction using a phosphorus-containing additive.

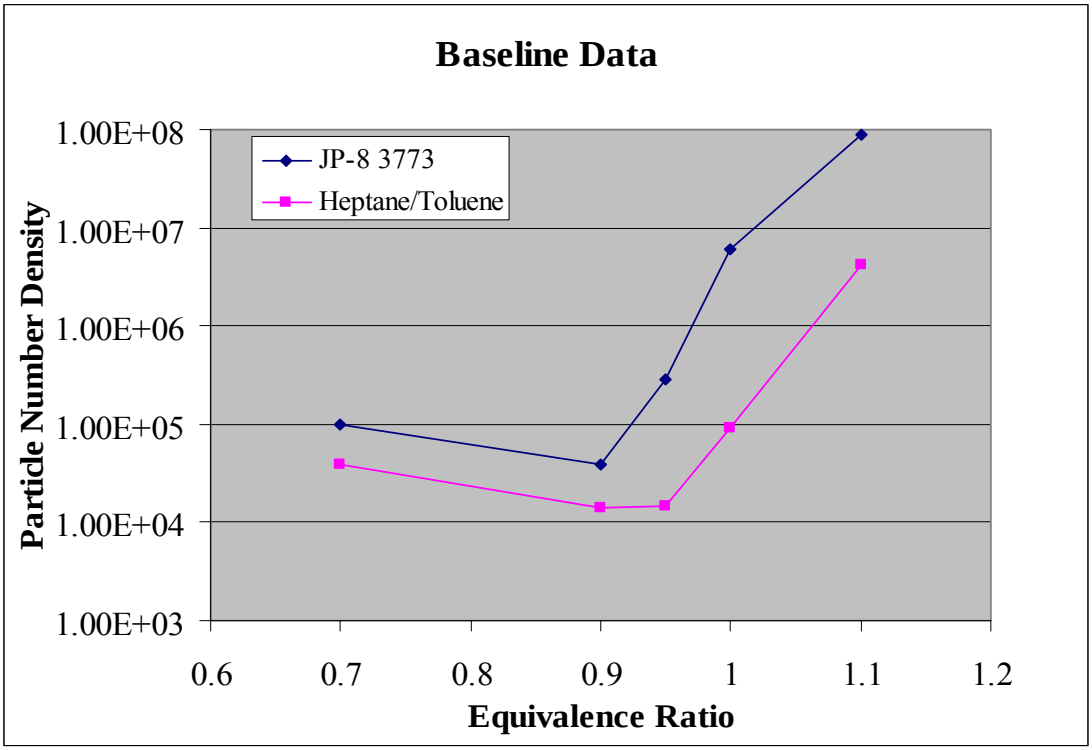

Figure 3.5.7-1. Particle Number Density as a Function of Equivalence Ratio for JP-8 3773 and Heptane/Toluene (80/20).

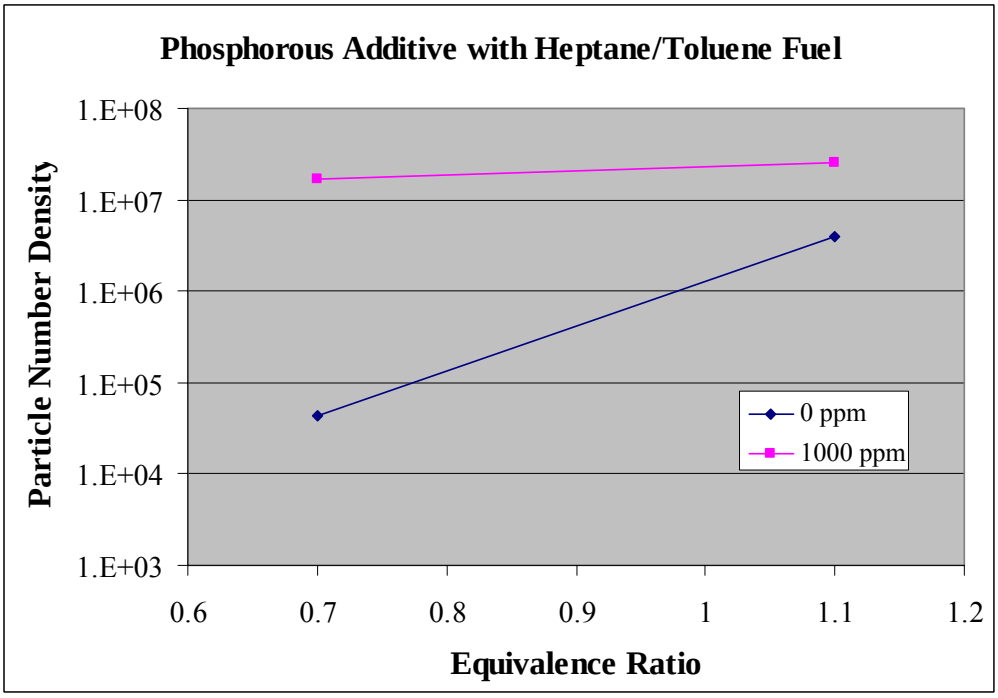

Figure 3.5.7-2. Particle Number Density Changes for Diethyl Allyl Phosphate Added to 80/20 Heptane/Toluene at 1000 ppm.

(a)

(b)

Figure 3.5.7-3. Photographs of Combustor Burning Heptane/Toluene at Φ=0.7: (top) no additive, (bottom) 1000 ppm.

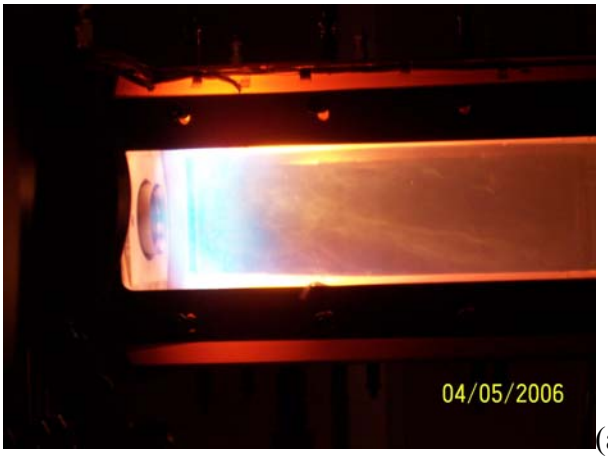

(a)

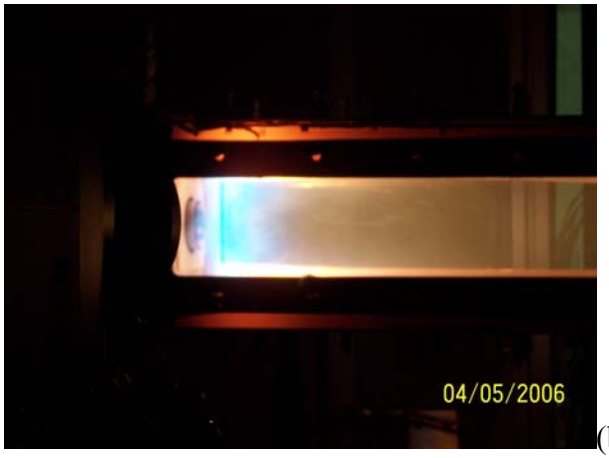

(b)

Figure 3.5.7-4. Photographs of Combustor Burning Heptane/Toluene at Φ=1.1: (top) no additive, (bottom) 1000 ppm.

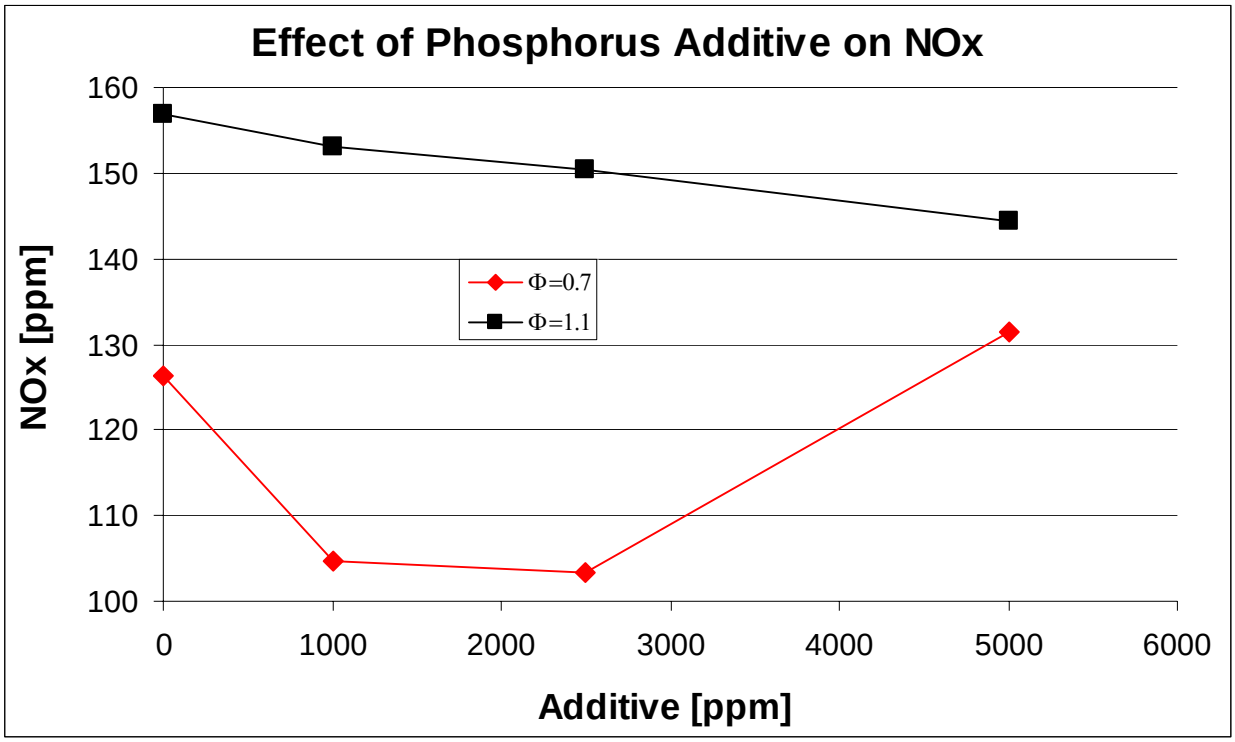

Figure 3.5.7-5. The Effect of the Phosphorus Additive on NOx Emissions.

Table 3.5.7-1. Mean Particle Size for Neat JP-8 and Heptane/Toluene and for 1000 ppm Additive in Heptane/Toluene,

Φ	JP-8	HEP/TOL	HEP/TOL 1000 PPM
0.7	NA	NA	15 nm
1.1	26 nm	22 nm	16 nm

3.5.8 JET FLAMES, UNICORN MODELING

Research on fire suppression during the early 1970s was focused on finding alternative additives as the use of super effective halogenated compounds was found to be impractical due to the corrosive effect on halogen acids on engines. Halogenated hydrocarbons were, later on, banned from their use as fire suppressants owing to their role in atmospheric ozone depletion [Anon 1995]. The search for effective replacements has led to a family of organophosphorus compounds, which showed considerable promise as flame inhibitors. Fortuitously, some researchers have found that the sooting characteristics of the flames they have been studying

seem to be altered when small quantities of phosphorus compounds were added [Hastie and Bonnell 1980]. From the fire suppression works it is known that small phosphor-bearing species such as $HOPO_2$ and HOPO produced from the organophosphorus compounds alter the flame chemistry by catalytically recombining the key flame radicals, especially H, O, and OH. As the concentrations of these radical species are also crucial in the formation of polycyclic aromatic hydrocarbons (PAHs) and in the soot oxidation process, it is natural to expect alteration to the sooting behavior of the flames when organophosphorus compounds are added.

A numerical and experimental study was initiated under this SERDP program for evaluating the effectiveness of trimethyl phosphate (TMP) and dimethyl methyl phosphate (DMMP) in reducing soot in various flames. Both the premixed and diffusion flames are considered for this study. Effectiveness of TMP in methane, propane and heptane flames is investigated. The time dependent, axisymmetric mathematical model (UNICORN) is used for the simulation of coflowing premixed and diffusion flames. The body force term due to the gravitational field is included in the axial momentum equation for simulating vertically mounted flames. A clustered mesh system is employed to trace the large gradients in flow variables near the flame surface. A detailed chemical kinetics model developed by NIST is incorporated into UNICORN for the investigation of PAH formation in heptane flames. The combustion inhibition chemistry of TMP developed by LLNL [Korobeinichev et al 2004] is also incorporated. The combined mechanism consists of 238 species and 3178 elementary reaction steps. A simple radiation model based on the optically thin media assumption is incorporated into the energy equation. Only radiation from CH_4, CO, CO_2, H_2O, and soot is considered. A two-equation model for soot with transport equations for particle number density and soot mass fraction is considered.

The code developed for the simulation of TMP effects on heptane flames could also be used for the simulation of methane, propane, or ethylene flames doped with TMP. Calculations are made for a propane flame with an equivalence ratio (phi) of 1.5. Fuel/air/TMP mixture is issued from a 6 mm-diameter tube at an average exit velocity of 0.5 m/s. Parabolic velocity profile which gives a peak value of 1.0 m/s is imposed at the exit of the tube. A low speed (0.01 m/s), coannular airflow is used in the region outside the flame. Distributions of temperature and soot volume fraction for the base flame (with no added TMP) are shown in Figures 3.5.8-1(a) and 3.5.8-1(b), respectively. Similarly, distributions for 0.1% added TMP are shown in Figures

3.5.8-1(c) and 3.5.8-1(d), and those for 1.0% TMP are shown in Figures 3.5.8-1(e) and 3.5.8-1(f). A common color scheme is used for each variable based on the peak value obtained from all the flames. As the peak soot concentration produced in the flame with 1% TMP (Figure 3.5.8-1(f)) is nearly two orders more than that of the base flame (Figure 3.5.8-1(b)), the linear color scale did not show the soot distribution in the latter flame.

As seen from Figure 3.5.8-1, addition of TMP to the propane premixed flame is decreasing the burning velocity and increasing the soot formation. The burning velocity computed based on the inner cone area (Figure 3.5.8-1(a)) for the phi =1.5 flame is about 0.20 m/s. In comparison the measured burning velocity at stoichiometry is 0.41 m/s. Based on the inner cone areas in Figures 3.5.8-1(c) and 3.5.8-1(e), the burning velocity has decreased by 45% and 56% when TMP was added by 0.1% and 1.0%, respectively. Decrease in burning velocity also resulted in an increase in flame standoff distance. This decrease compares favorably with that measured for stoichiometric flame. Addition of TMP has significantly increased soot formation (Figures 3.5.8-1(b), 3.5.8-1(d), and 3.5.8-1(f).

Calculations are made for the propane jet diffusion flame with various amounts of TMP added to the fuel jet. Results obtained for a 0.01-m/s jet velocity case are shown in Figure 3.5.8-2. Interestingly, TMP has very little effect on the stability of the diffusion flame for concentrations up to 1%. However, soot has decreased by about 20%. This is in contrast with the premixed flame in which soot increased with the addition of TMP. Similar calculations were made for a higher fuel jet velocity (0.1 m/s) and found that TMP has negligible impact either on the stability or on the soot production even for concentrations up to 1%.

The predicted effects of TMP in propane premixed and diffusion flames matched qualitatively with those obtained in the experiments. Both calculations and experiment yielded increase in soot and flame inhibition for premixed flames and decrease in soot for diffusion flames. Calculations made with methane fuel also resulted in similar trends. Results obtained for a diffusion flame are shown in Figure 3.5.8-3. Even though the flame stability is not affected much with the addition of TMP, soot has decreased more significantly than that noted in propane flames (Figure 3.5.8-2). However, quick experiments conducted for methane diffusion flame suggested an increase in soot production with TMP.

Calculations for heptane premixed and diffusion flames are performed with various amounts of TMP added to the fuel. The diameter of the fuel tube was 12 mm and the fuel jet

velocity was 0.005 m/s. Even with this low fuel velocity the diffusion flame formed is longer than those obtained for methane and propane fuels. This is inconsistent with the other diffusion flame calculations. Due to the length, the simulated heptane flame is insensitive to the added TMP. Results obtained for the base flame (0% TMP) are shown in Figure 3.5.8-4 in the form of temperature, soot, and nitricoxide concentration distributions. Variations along the centerline for different amounts of added TMP are shown in Figure 3.5.8-5. Flame structures are identical for 0% and 0.1% TMP cases. However, a trace amount of deviation is observed for the 1% case. Interestingly, NO has decreased significantly when 1% TMP is added.

Structures of the heptane premixed flame for 0%, 0.1% and 1.0% TMP concentrations are shown in Figures 3.5.8-6, 3.5.8-7, and 3.5.8-8, respectively. The fuel equivalence ratio is 2.0 and the fuel jet velocity is 1 m/s. As expected from the other premixed calculations, burning velocity for heptane fuel has also decreased with the addition of TMP. Based on the inner cone surface areas, burning velocity has decreased by 5% when 0.1% TMP was added and decreased by 19% with 1% TMP. As expected, concentration of OH decreased and that of soot increased with the amount of TMP. The radical recombination promoted by the P-based species caused OH concentration to decrease. The increase in soot concentration correlates to that in benzene concentration. Significant reduction in NO is also noted. It seems TMP reduces NO production in both premixed and diffusion flames.

The results of all the simulations made with methane, propane and heptane fuels are summarized in Table 3.5.8-1. In general, soot is enhanced in premixed flames and suppressed in diffusion flames when TMP is added. Premixed flames are more sensitive to the presence of TMP compared to diffusion flames. Also, large flames are less sensitive to TMP compared to small ones. Among the fuels studied, methane is more sensitive than propane, which is more sensitive than heptane to the presence of TMP.

Table 3.5.8-1. Effect of TMP on Soot Formation in Various Flames.

Fuel	Soot in	
	Premixed Flame	Diffusion Flame
Methane	Enhanced significantly	No change in large flames Decreased in small flames
Propane	Enhanced significantly	No change in large flames Decreased significantly in small flames
Heptane	Enhanced	No change for small amounts of TMP Decreased for large amounts of TMP

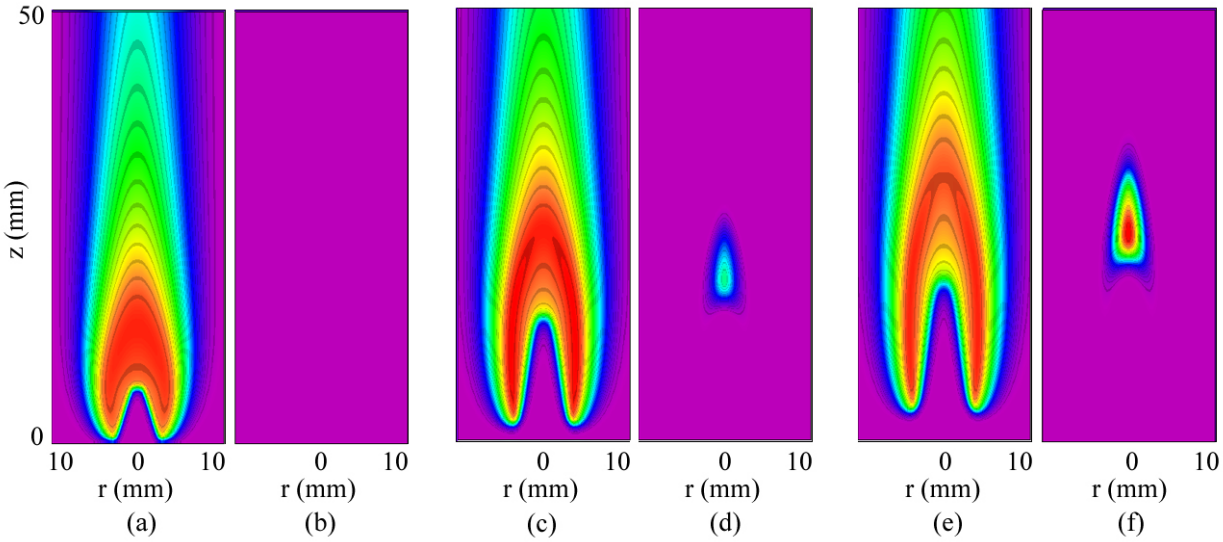

Figure 3.5.8-1. Effect of TMP on Premixed Propane Flame. Mixture of propane, air and TMP with phi = 1.5 is issued from a 6 mm tube at 0.5 m/s. Distributions of (a) temperature and (b) soot volume fraction for base flame with 0% TMP, (c) and (d) for the flame with 0.1% TMP and (e) and (f) are for the flame with 1% TMP.

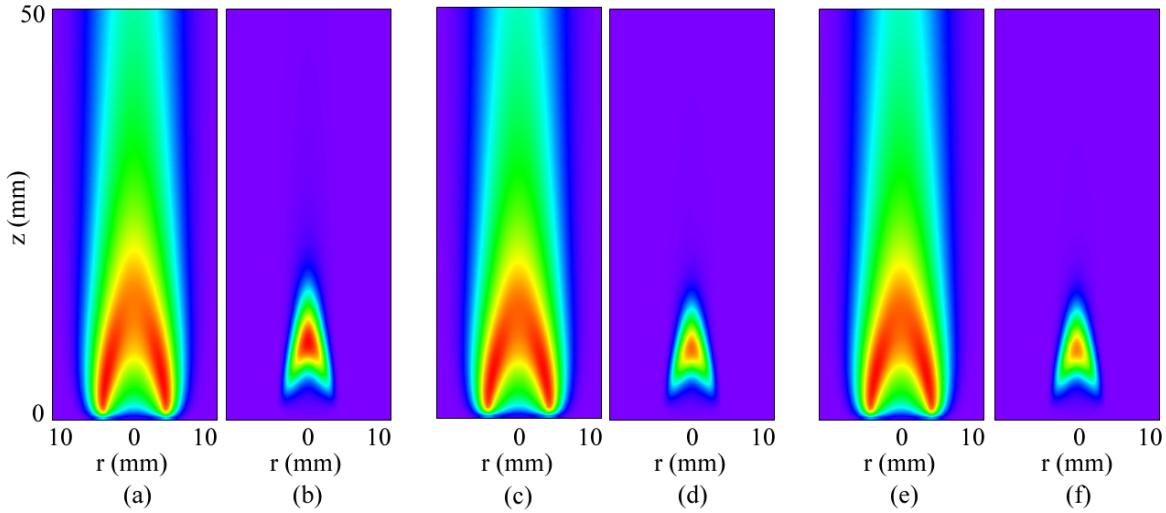

Figure 3.5.8-2. Effect of TMP on Propane Jet Diffusion Flame. Distributions of (a) temperature and (b) soot volume fraction for base flame with 0% TMP, (c) and (d) for the flame with 0.1% TMP, and (e) and (f) are for the flame with 1% TMP.

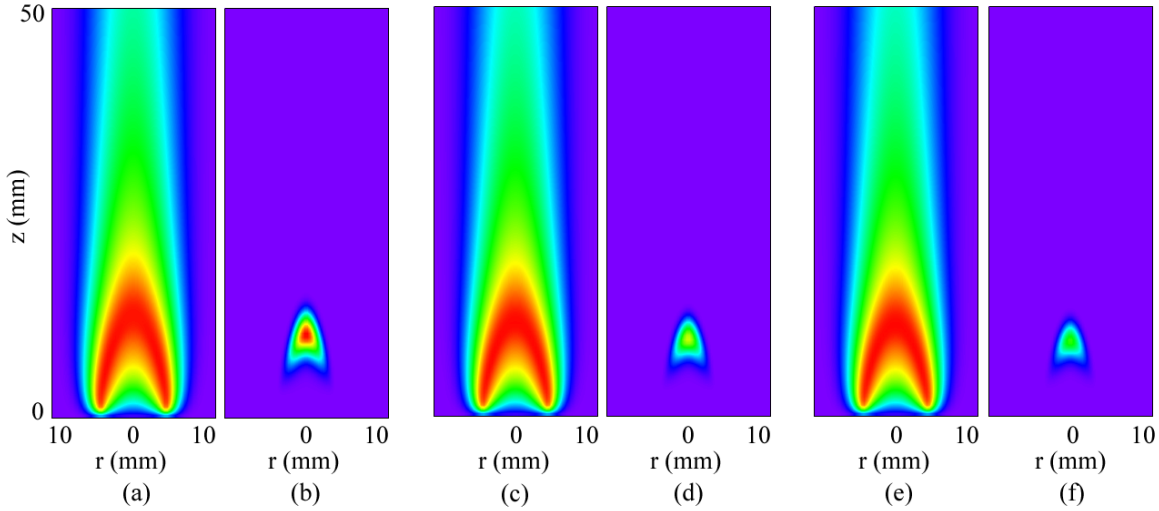

Figure 3.5.8-3. Effect of TMP on Methane Jet Diffusion Flame. Distributions of (a) temperature and (b) soot volume fraction for base flame with 0% TMP, (c) and (d) for the flame with 0.1% TMP, and (e) and (f) are for the flame with 1% TMP.

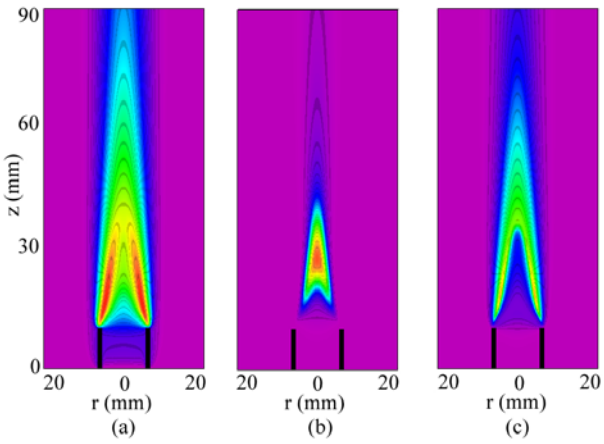

Figure 3.5.8-4. Heptane Jet Diffusion Flame. Distributions of (a) temperature, (b) soot volume fraction and (c) NO concentration.

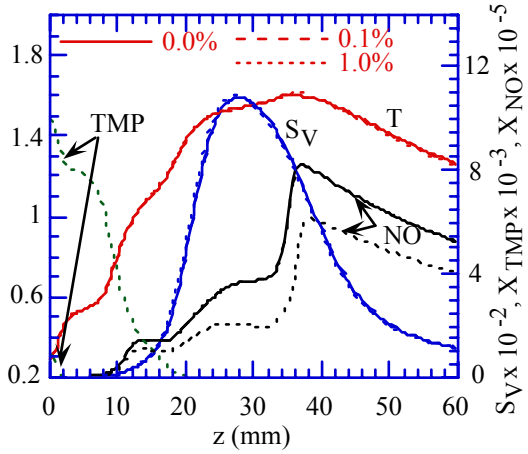

Figure 3.5.8-5. Effect of TMP on Heptane Jet Diffusion Flame. Distributions of T and species along the centerline.

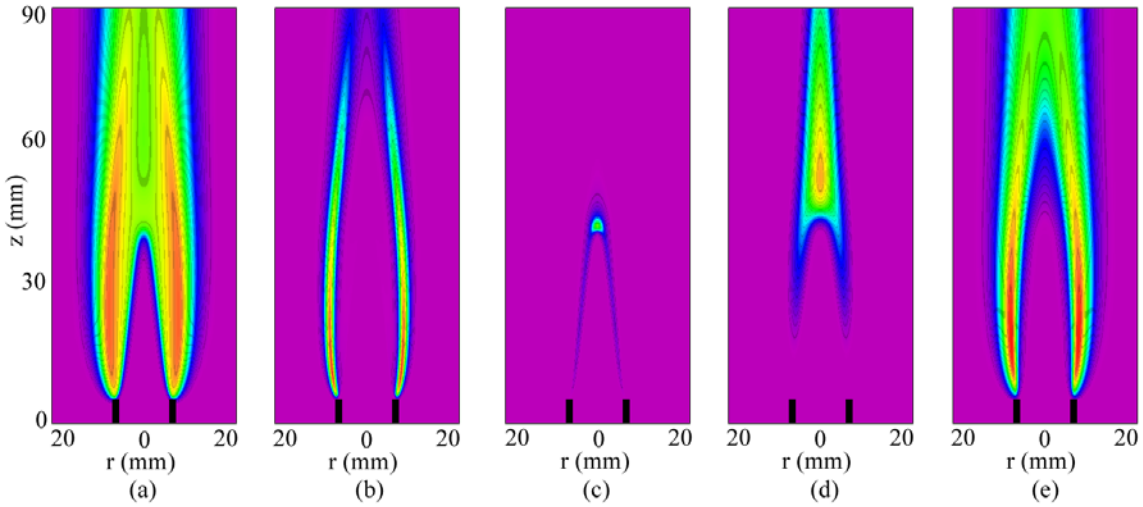

Figure 3.5.8-6. Heptane Premixed Flame with 0% TMP. Mixture of heptane and air with phi = 2.0 is issued from a 13 mm tube at 1.0 m/s. Distributions of (a) temperature, (b) OH, (c) benzene, (d) soot volume fraction, and (e) NO.

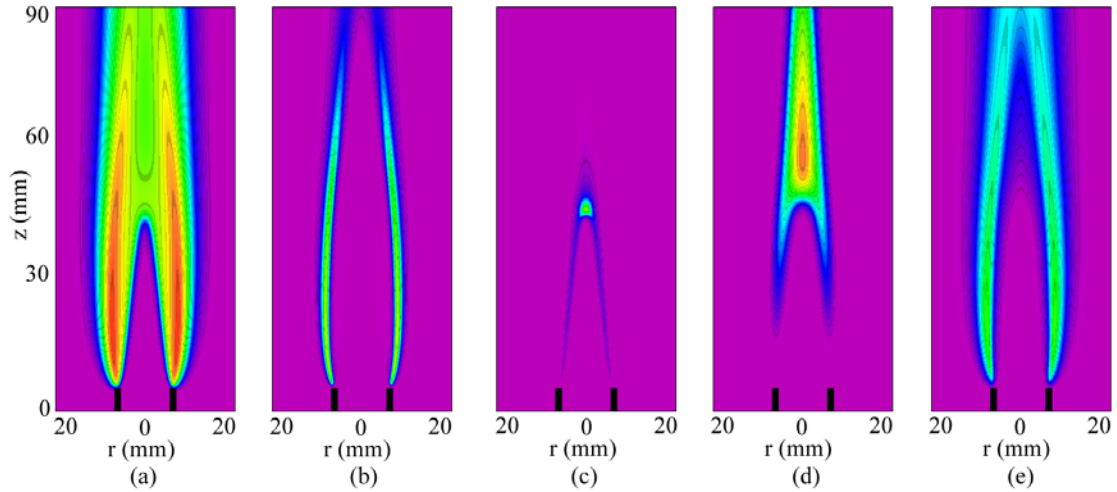

Figure 3.5.8-7. Heptane Premixed Flame with 0.1% TMP. Mixture of heptane and air with phi = 2.0 is issued from a 13 mm tube at 1.0 m/s. Distributions of (a) temperature, (b) OH, (c) benzene, (d) soot volume fraction, and (e) NO.

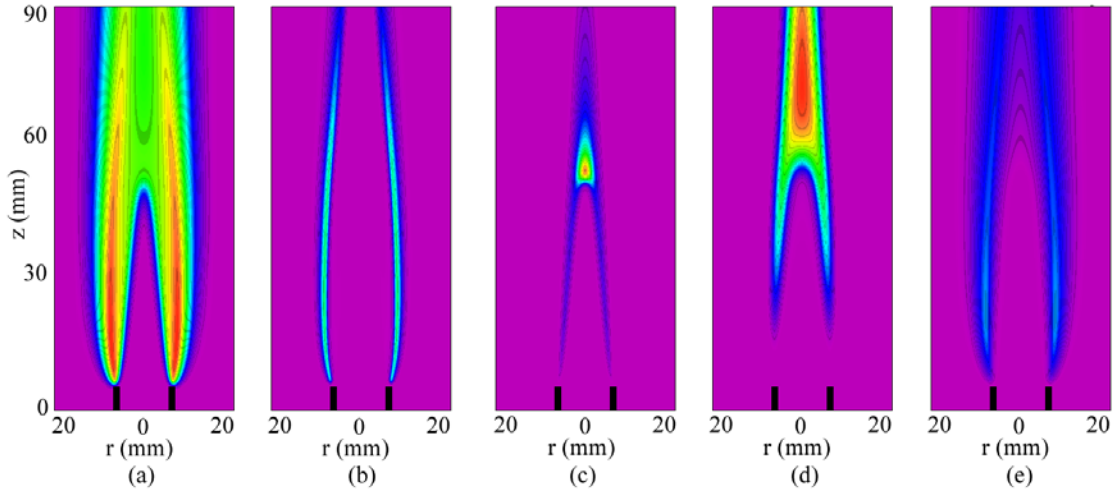

Figure 3.5.8-8. Heptane Premixed Flame with 1.0% TMP. Mixture of heptane and air with phi = 2.0 is issued from a 13 mm tube at 1.0 m/s. Distributions of (a) temperature, (b) OH, (c) benzene, (d) soot volume fraction, and (e) NO.

REFERENCES

Abramowitz, M. and Stegun, I. A. (Eds.). Handbook of Mathematical Functions with Formulas, Graphs, and Mathematical Tables, 9th printing. New York: Dover, p. 886, 1972.

Ai-Rubaie, M.A.R., Griffiths, J.F., Sheppard, C.G.W., SAE Paper No. 912333 (1991).

Alexiou, A., and Williams, A., "Soot Formation in Shock Tube Pyrolysis of Toluene, Toluene-Methanol, Toluene-Ethanol, and Toluene-Oxygen Mixtures", Combustion and Flame, Vol. 104, pp. 51-65 (1996).

Allen, Mark, personal communication, 1 April 1999, Physical Sciences, Inc., 20 New England Business Center, Andover MA 01810.

Appel, J., Bockhorn, H. and Frenklach, M.Y., Kinetic Modeling of Soot Formation with Detailed Chemistry and Physics: Laminar Premixed Flames of C_2 Hydrocarbons, Combustion and Flame, 121:122-136, (2000).

Babushok, V.I., and Tsang, W., *J. Propulsion and Power*, 20 (3) (2004) 403-414.

Baron, P., "Aerosol Calculator", available from pbaron@cdc.gov, Oct, 2001.

Beretta, F., D'Alessio A., D'Orsi, A., and Minutolo, P., Comb. Sci. & Tech., 85(1-6), 1992, 455-470.

Berry, M.V., and Percival, I.C. *Opt. Acta*, **33**, 577, (1986).

Bjorseth, A., Ed., Handbook of Polycyclic Aromatic Hydrocarbons, Marcel Dekker, NY (1985).

Bomse, D.S., Stanton, A.C., and Silver, J.A.,"Frequency modulation and wavelength modulation spectroscopies: comparison of experimental methods using a lead-salt diode laser", Appl. Optics, Vol. 31, 718-731 (1992).

Bowman, C.T., R.K. Hanson, D.F. Davidson, W.C. Gardiner, V. Lissianski, G.P. Smith, D.M. Golden, M. Frenklach, M. Goldenberg, University of California, Berkeley, GRIMech: http://www.me.berkeley.edu/gri_mech.

Brocklehurst, H. T., Pridden, C. H., and Moss, J. B. (1997). "Soot Predictions within an Aero Gas Turbine Combustor Chamber", ASME Paper 97-GT-148.

Calcote, H.F., *Combust. Flame* **42** (1981), pp. 215–242.

Charalampopoulos, T.T., and H. Chang, "Agglomerate Parameters and Fractal Dimension of Soot Using Light Scattering – Effects on Surface Growth", *Combust. Flame* **87** (1991), pp. 89-99.

REFERENCES (CONT)

Cheli, Stephen J., Development of a Particulate Matter On-line Real Time Physical and Chemical Characterization and Monitoring System (PMCMS). Phase I Report. AFRL-ML-TY-TR-1999-4549, Feb 1999, Distribution authorized to US Government Only.

Cheli, Stephen J., Development of a Particulate Matter On-Line Real Time Physical and Chemical Characterization and Monitoring System (PMCMS), AFRL-ML-TY-TR-2002-4526, June 2001, Distribution limited to US Government agencies only.

(a) Clothier, P.Q.E., Aguda, B.D., Moise, A., Pritchard, H.O., Chem. Soc. Rev., 1993, 22, 101-108.

(b) Clothier, P.Q.E., Pritchard, H.O., Poirier, M.A., Combust. Flame, 1993, 95, 427-429.

Colket, M. B. and Hall, R. J.(1994). In Soot Formation in Combustion, H. Bockhorn, ed., Springer Verlag, Berlin, p 417.

Colket, M. B., Hall, R. J., Stouffer, S. D., "Modeling Soot Formation in a Stirred Reactor", Proceedings of ASME Turbo Expo 2004, Paper No. GT2004-54001, Vienna, Austria, June 14-17, 2004.

Cundy, V.A., J.S. Morse, D.W. Senser, Rev. Sci. Instrum. 57(6) (1986) 1209-1210.

Curran, H.J., Pitz, W.J., Westbrook, C.K., Dagaut, P., Boettner, J.C., Cathonnet, M. (1998) "A wide range modeling study of dimethyl ether oxidation", *Intl. J. of Chem. Kin.,* 30, 229.

Curran, H.J., E.M. Fisher, P.A. Glaude, N.M. Marinov, W.J., Pitz, C.K. Westbrook, D.W., Layton, P.F. Flynn, R.P. Durrett, A.O. zur Loye, O.C. Akinyemi, and F.L. Dryer, Society of Automotive Engineer, No. 2001-01-0653 (2001).

Dalzell, W.H. and Sarofim, A.F., *A.S.M.E., J. Heat Transfer*, **91**,100 (1969).

Dennisenko, M.F., Pao, A., Tang, M-S., Pfeifer, G.P., "Preferential formation of benzo[a]pyrene adducts at lung cancer mutational hotspots in P53". Science, Vol. 273, pp. 430-432, (1996).

Dobbins, R.A. and Megaridis, C.M., *Langmuir*, **3**, 254-259, (1987)

Dockery, D.W., Pope, C.A., Xu, X., Spengler, J.D., Ware, J.H., Fay, M.E., Ferris, B.G. Speizer, F.E., New England Journal of Medicine, Vol. 329, pp. 1753-1759, (1993).

Du, D.X., Wang, H., and Law, C.K.; "Soot formation in counterflow ethylene diffusion flames from 1 to 25 atmospheres", Combustion and Flame, vol. 113, pp. 264-270 (1988).

Frenklach, M., available: http://www.me.berkeley.edu/soot/ December 2002.

REFERENCES (CONT)

Frenklach, M. and Wang, H. (1990) Detailed mechanism and modeling of soot particle formation. *Springer Series in Chemical Physics*, 59, 165.

Frenklach, M. and H. Wang, *Twentythird Symposium (International) on Combustion*, The Combustion Institute, Pittsburgh, p. 1559, 1991.

Frenklach, M., and J. Yuan, *Sixteenth Symposium (International) on Shock Tubes and Waves*, p. 487, 1987.

Frenklach, M., J. Yuan, and M. K. Ramachandra, *Energ. Fuels* 2:462, 1988.

Gehrke, Mark , Shubhen Kapila, Paul Nam, and Virgil Flanigan, *Chemosphere*, 43 (2001) pp. 479-483.

Gelbard, F. and Seinfield, J. H., (1980). *J. Coll. Int. Sci.* 78, 485.

Glarborg, P., Kee, R. J., Grcar, J.F., and Miller, J.A.. "PSR: A Fortran Program for Modeling Well-Stirred Reactors", Sandia Report, SAND86-8209, 1986.

Glassman, I., "Combustion", 2nd Edition, Academic Press, pp. 360-375, 1987.

Glassman, I., Twenty-Second Symposium (International) on Combustion, The Combustion Institute, Pittsburgh, PA, p. 295, 1989.

Glaude, P.A., Curran, H. J., Pitz, W. J., and Westbrook, C.K., Proceedings of the Combustion Institute, 28: 1749-1756, 2000.

Hall, R.J. and Colket, M. B. (1999). "Calculations of Soot Aggregate Growth and Oxidation Using a Sectional Size Representation," Chemical and Physical Processes of Combustion, Presentation to the Eastern States Section of The Combustion Institute, paper no. 79, North Carolina State University.

Hall, R.J., Smooke, M.D., and Colket, M.B., "Predictions of Soot Dynamics in Opposed Jet Diffusion Flames", in "Physical and Chemical Aspects of Combustion – A Tribute to Irvin Glassman", F.L. Dryer and R.F. Sawyer, Eds., pp. 189-230, Gordon and Breach Science Publishers, 1997.

Harris, S. J. and Weiner, A. M, *Combust. Sci. Tech.*, **32**, 267 (1983).

Hastie, J.W. and Bonnell, D. W., "Molecular Chemistry for Inhibited Combustion Systems," NBSIR 80-2169 (1980).

Haynes, B.S. and H.Gg. Wagner, *Prog. Energy Combust. Sci.* **7** (1981), pp. 229–273.

REFERENCES (CONT)

Hertzberg, G., *Infrared and Raman Spectra*, Van Nostrand Rheinhold Co., New York, 1945.

Higgins, B., Siebers, D., Mueller, C., Aradi, A., Proc. Combust. Inst., 1998, 2, 1873-1880.

Hobbs, P.C.D., "Ultrasensitive laser measurements without tears", Appl. Optics, Vol. 36, pp. 903-21, (1997).

Hore, N.R., K.D. Russell, *J. Chem. Soc.*, Perkin, Trans. 2 (1998) 269-275.

Howard, J.B., and Kausch, W.J., "Soot Control by Fuel Additives", Prog. Energy Combust. Sci., Vol. 6, pp.263-276, (1980).

Howard, R.P., "Experimental Characterization of Gas Turbine Emissions at Simulated Altitude Conditions", AEDC-TR-96-3, September 1996.

Hwang, J.Y. and Chung, S.H., "Growth of Soot Particles in Counterflow Diffusion Flames of Ethylene", Combustion and Flame, Vol. 125, pp. 752-762 (2001).

Ikeda, E., P. Nicholls, J.C. Mackie, *Proc. Combust. Inst.* 28 (2000) 1709.

Inal, F., S. Senkan, Combustion Science and Technology, 174 (2002) 1-19.

Inomata, T., Griffiths, J. F., Pappin, A.J., Proc. Combust. Inst., 1990, 23, 1759-1766.

Jayaweera, T. M., Melius, C. F., Pitz, W. J., Westbrook, C. K., Korobeinichev, O. P., Shvartsberg, V. M., Shmakov, A. G., Bolshova, T. A. and Curran, H., Combustion and Flame, in press, 2004; Lawrence Livermore National Laboratory, Livermore, CA, UCRL-CONF-202992.

(a) Kahandawala, M.S., Ph.D. Dissertation on "Fuel Composition Effects on Particle and PAH Emissions", University of Dayton, Dayton, OH 2004.

(b) Kahandawala, M. S., J. L. Graham and S. S. Sidhu, "Particulate Emission from Combustion of Diesel and Fischer-Tropsch Fuels: A Shock Tube Study", **Energy & Fuel** 18 (2), 289-295, 2004.

Kahandawala, M.S.P., S.A.P. Corera, S.S. Sidhu, *Proceedings of the 25th Symposium (International) on Shock Tubes and Waves*, Bangalore, India (2005).

Kahandawala, M. S., S. A. Corera, S. Williams, C. D. Campbell and S. S. Sidhu, "Investigation of kinetics of iso-octane ignition under scramjet conditions", **Int. J. Chem. Kinet.** 38, 194-201, 2006.

REFERENCES (CONT)

Kang, K.T., Hwang, J.Y., and Chung, S.H., "Soot Zone Structure and Sooting Limit in Diffusion Flames: Comparison of Counterflow and Coflow Flames", Combustion and Flame, Vol. 109, pp. 266-281, (1997).

Kee, R.J., Rupley, F.M., and Miller, J.A., "CHEMKIN-II: A Fortran Chemical Kinetics Package for the Analysis of Gas-Phase Chemical Kinetics", Sandia National Laboratories, Albuquerque NM, SAND89-8009, reprinted March 1991.

Kee, R.J., Rupley, F.M., Miller, J.A., Coltrin, M.E., Grcar, J.F., Meeks, E., Moffat, H.K., Lutz, A.E., Dixon-Lewis, G., Smooke, M.D., Warnatz, J., Evans, G.H., Larson, R.S., Mitchell, R.E, Petzold, L.R., Reynolds, W.C., Caracotsios, M., Stewart, W.E., Glarborg, P., Wang, C., Adigun, O., Houf, W.G., Chou, C.P., Miller, S.F., CHEMKIN Collection, Release 3.7, Reaction Design, Inc., San Diego, CA, 2002.

Kennedy, I.M., Combustion Science and Technology, Vol. 59, No. 107 (1988).

Klosterman, J. R. [2001] Klosterman, J. R., Striebich, R. C. and Rubey, W. A., "Direct Thermal Desorption of Combustion Residues by GC-MS," Pittcon Paper No. 1034, New Orleans, LA, 5-8 March 2001.

Kohse-Höinghaus, K., and J. Jeffries (Eds.) *Applied Combustion Diagnostics.* Taylor & Francis, New York, 2002 p. 359-383.

Korobeinichev, O. P., Shvartsberg, V. M., Shmakov, A. G., Bolshova, T. A., Jayaweera, T. M., Melius, C. F., Pitz, W. J. and Westbrook, C. K., Proceedings of the Combustion Institute, Vol. 30, Issue 2, pp. 2350-2357, 2004; Lawrence Livermore National Laboratory, Livermore, CA, UCRL-CONF-201585.

Koylu, U. O., McEnally, C. S., Rosner, D. E., and Pfefferle, L. D., *Combustion and Flame*, **110**, 494 (1997).

Krishnan, S.S., Lin, K.C., and Faeth, G.M., Journal of Heat Transfer, 123, 332-339, 2001.

Lee, K. and B. Chehroudi, "Structure of a swirl-stabilized spray flame relevant to gas turbine and furnaces," J. of Prop. and Power **11**, 1110-1117 (1995).

Lentati, A.M., and Chelliah, H.K., "Dynamics of Water Droplets in a Counterflow Field and Their Effect on Flame Extinction, Combustion and Flame, Vol. 115, pp. 158-179, (1998).

Linnerud, I., P. Kaspersen, and T. Jaeger, "Gas monitoring in the process industry using diode laser spectroscopy", Applied Physics B, Vol. 67, pp. 297-305, (1998).

REFERENCES (CONT)

Liscinsky, D. S., Colket, M. B., Hall, R. J., Bhargava, A., True, B., and Morford, S., "Comparison of Particle Sizing Techniques in Sooting Premixed Flames", AIAA – 2000 – 0954, *AIAA Aerospace Sciences Meeting*, Reno, NV, January 2000.

Liscinsky, D.S., Colket, M.B., Hautman, D.J., and True, B. (2001). "Effect of Fuel Additives on Particulate Formation in Gas Turbine Combustors," presented at the 37th AIAA/ASME/SAE/ASEE Joint Propulsion Conference, AIAA 2001-3745, Salt Lake City, Utah, July 8-11.

Litzinger, T.A., Penn State University, Internal Communication, 2004.

Lockett, R.D., Boulanger, B., Harding, S.C. and Greenhalgh, D.A., "The Structure and Stability of the Laminar Counter-flow Partially Premixed Methane/Air Triple Flame", Combustion and Flame, Vol. 119, pp. 109-120, (1999).

Mackie, J.C., M.B. Colket, P.F. Nelson, *J. Phys. Chem.* 94 (1990) 4099-4106.

Manzello, S.L., Mulholland, G.W., Donavan, M., Tsang, W., Park, K., Zachariah, M.R., and Stouffer, S.D, "On the Use of a Well Stirred Reactor to Study Soot Inception", presented at Fourth (4th) Joint Meeting of the U.S. Sections of The Combustion Institute, March 20-23, 2005, Philadelphia, PA, pp.1-6, 2005.

Manzello, S. L., Lenhert, D. B., Yozfatligil, A., Donovan, M. T., Mulholland, G. W., Zachariah, M. R., and Tsang, W., "Soot Particle Size Distributions in a Well-Stirred Reactor/Plug Flow Reactor", accepted for presentation at the 31st International Symposium on Combustion, Heidelberg, August, 2006.

Marinov, Nick M., "Detailed chemical kinetic model for high temperature ethanol oxidation" (Lawrence Livermore Natl Lab) Source: International Journal of Chemical Kinetics, v 31, n 3, Mar, 1999, p 183-220

McBride, B., and S. Gordon, S., *Computer Program for Calculation of Complex Chemical Equilibrium Compositions and Applications*. NASA Reference Publication 1311, 1996.

McEnally, C. S., Koylu, U. O., Pfefferle, L. D., and Rosner, D. E., *Combustion and Flame*, **109**, 701(1997).

McEnally, C. S., Schaffer, A. M., Long, M. B., Pfefferle, L. D., Smooke, M. D., Colket, M. B., and Hall, R. J., Proceedings of the Combustion Institute, 27, The Combustion Institute, p. 1497, (1998) and references contained therein.

McKinnon, J. T. and Howard, J. B. (1992). Twenty-Fourth Symposium (International) on Combustion, The Combustion Institute, Pittsburgh, PA, p. 965.

REFERENCES (CONT)

McNesby, K.L., R.T. Wainner, R.G. Daniel, R.R. Skaggs, J.B. Morris, A.W. Miziolek, W.M. Jackson, and I.A. McLaren, "Detection and measurement of middle distillate fuel vapors using tunable diode lasers", Applied Optics, Vol. 40, pp. 840-845 (2001).

Megaridis, C.M. and Dobbins, R.A, *Combust. Sci. and Tech.,* **7**, 95-109, (1990).

Morawska, L., N. D., Bofinger, L. Kocis, and A. Nwankwoala, *Env. Sci. Technol.*, 32:2033, 1998.

Mueller, M. , R Yetter, F. Dryer, *ChemKinet* 31 (1999) 705-724.

Naegeli, D.W. and K.H. Childress, "Lower Explosion Limits and Compositions of Middle Distillate Fuel Vapors", Proceedings of the Fall Meeting of the Society of Automotive Engineers, SAE paper # 982485, (1998), pp. 1-7.

Nagle, J. and Strickland-Constable, R.F., Proceedings of the Fifth Carbon Conference, pp. 154-164, Oxford Pergamon Press, 1962.

Nenniger, J. E., Kridiotis, A., Chomiak, J., Longwell, J. P., and Sarofim, A. F., "Characterization of a Toroidal Well Stirred Reactor," *Twentieth Symposium (International) on Combustion,* The Combustion Institute, pp. 473-479, 1984.

Neoh, K.G., Howard, J.B., and Sarofim, A.F., "Soot Oxidation in Flames," in *Particulate Carbon Formation During Combustion*, Edited by D.C. Siegla and G.W. Smith, pp 261-277 (1981).

Ni, T., J.A. Pinson, S. Gupta, R.J. Santoro, Applied Optics, 34 (30) (1995) 7083-7091.

Niedzwiecki, R., "Aircraft Technology and its Relation to Emissions", Chapter 7 of Report of The Intergovernmental Panel on Climate Change", IPCC, to be published.

Quay, B., The development of laser-induced incandescence for quantitative measurement of soot volume fraction in flames, Ph.D. Thesis, The Pennsylvania State University. (1998)

Ray, S.K. and Long, R., Combust. Flame, 1964, 8, 139-151.

Reich, R., Frayne, C., Zelina, J., Mayfield, H., Stouffer S, and Katta V., "Particulate Matter and Polycyclic Aromatic Hydrocarbon Determination Using a Well-Stirred Reactor," AIAA Paper No. 2003-0664, 41st AIAA Aerospace Sciences Meeting, Reno, Nevada, January 2003.

Reist, P.C., "Aerosol Science and Technology", 2nd Edition, McGraw Hill, New York, 1993, pp. 263-275.

REFERENCES (CONT)

Richter, H., and Howard, J.B., "Formation of polycyclic aromatic hydrocarbons and their growth to soot – a review of chemical reaction pathways", Progress in Energy and Combustion Science, Vol. 26, pp. 565-608, (2000)

"Reduced PM2.5 Emissions for Military Gas Turbine Engines Using Fuel Additives", administered by the Strategic Environmental Research and Development Program (DoD, EPA, DOE).

Roesler, J.F., Martinot, S., McEnally, C.S., Pfefferle, L.D., Delfau, J.L-, and Vovelle, C.; "Investigating the role of methane on the growth of aromatic hydrocarbons and soot in fundamental combustion processes" Combustion and Flame, Vol. 134, pp. 249-260 (2003)

Roesler, J.F., Auphan de Tessan, M., Montagne, X., Chemosphere, 2001, 42, 823-826.

Rosner, D.E., Mackowski, D.W., and Garcia-Ybarra, P., *Comb. Sci. and Tech.*, **80**, 87-101, (1991).

Rumminger, M.D., and Linteris, G.T., "The Role of Particles in the Inhibition of Counterflow Diffusion Flames by Iron Pentacarbonyl", Combustion and Flame, Vol. 128, pp. 145-164 (2002).

Santoro, R. J., Semerjian, H. J., and Dobbins, R. A., Soot Particle Measurements in Diffusion Flames, Combustion and Flame 51: 203-218 (1983)

Seizinger, D., U.S. Dept. of Energy, Bartlesville, OK., private communication by Ed. A. Bjorseth, Marcel Dekker, NY., 1980.

Senkan, S.M., Castaldi, M., Combust. Flame, 1996, 107, 141.

Sgro, L.A., P. Minutolo, G. Basile, A. D'Alessio, Chemosphere 42(5-7) (2001) 671-680.

Shaddix, C.R., Pro. National Heat Transfer Conference, 33 (1999).

Shaddix, C.R., Harrington, J.E., and Smyth, K.C., "Quantitative Measurements of Enhanced Soot Production in a Flickering Methane/Air Diffusion Flame", Combustion and Flame, Vol. 99, pp. 723-732 (1994).

Shaddix, C.R. and Smyth, K.C., "Laser-Induced Incandescence Measurements of Soot Production in Steady and Flickering Methane, Propane, and Ethylene Diffusion Flames", Combustion and Flame, Vol. 107, pp. 418-452, (1996).

Sidhu, S. S., J. L. Graham, D. R. Ballal, and H. C. Mongia, "Investigation of Heptane Combustion at 50 ATM Using a Shock Tube", AIAA 2005-1447, 2005.

REFERENCES (CONT)

Smooke, M. D., Hall, R. J., Colket, M. B., "Modeling The Transition From Non-Sooting To Sooting, Coflow Ethylene Diffusion Flames", presented to the Third Joint Meeting of the U.S. Sections of The Combustion Institute, Chicago, Ill, March 15-18, 2003.

Smooke, M. D., Hall, R. J., Colket M. B., Fielding, J., Long M. B., McEnally, C. S., and Pfefferle, L. D., Combustion Theory and Modeling, 8, pp. 593-606, 2004.

Smooke, M. D., Long M. B., Connelly, B. C., Colket M. B., and Hall, R. J., "Soot Formation in Laminar Diffusion Flames" Combustion and Flame, 143, pp. 613-628, 2005.

Smooke , M. D., Long, M. B., Hall R. J., and Colket, M. B., " Computational and Experimental Study of Soot Formation in Ethylene Coflow Diffusion Flames, presented at 2005 Joint Meeting of the US Sections of the Combustion Institute Drexel University, Philadelphia, PA, March 20-23, 2005.

Smyth, K.C., Shaddix, C.R., Everest, D.A., "Aspects of soot dynamics as revealed by measurements of broadband fluorescence and flame luminosity in flickering diffusion flames", Combustion and Flame, Vol. 111, pp. 185-207 (1997).

Song, K.H., Nag, P., Litzinger, T.A., and Haworth, D.C., "Effects of oxygenated additives on aromatic species in fuel-rich, premixed ethane combustion: a modeling study", Combustion and Flame, Vol. 135, pp. 341-349, (2003).

Stouffer, S. D., Striebich, R. C., Frayne, C. W., and Zelina, J., "Combustion Particulates Mitigation Investigation Using a Well-Stirred Reactor," AIAA Paper No. 2002-3723, 38th Joint Propulsion Conference, 2002.

(a) Stouffer, S.D., Mortimer B.M., Ostdiek, D.M., DeWitt, M.J., Pawlik, R., Reich, R.F., Frayne, C.W., and Mayfield, H.T., " Soot Reduction Research Using a Well-Stirred Reactor," AIAA 2005-1317, 43rd Aerospace Sciences Meeting, Reno, NV, January 13, 2005.

(b) Stouffer, S. D., Ballal, D. R., Zelina, J., Shouse, D. T., Hancock, R. D., and Mongia, H. C. "Development and Combustion Performance of a High Pressure WSR and TAPS Combustor," AIAA Paper 2005-1416, 2005.

Strehlow, R. A., Fundamentals of Combustion, International Textbook Company, Scranton, PA, pp. 221-227, 1968.

Sung, C. J., J. S. Kistler, M. Nishioka and C. K. Law, "Further studies on effects of thermophoresis on seeding particles in LDV measurements of strained flames", Combustion and Flame, Vol. 105, April 1996, Pages 189-201.

Suppes, G.J., Chen, Z., Chan, P.Y., SAE Paper No. 962064 (1996).

REFERENCES (CONT)

Syred, N., and J.M. Beer, *Combustion and Flame*, Vol. 23, p. 143-201. (1974)

Tein, C.L. and Lee, S.C. *Prog. Energy Combust. Sci*., **8**, 41-59, (1982)

Toland, A., Simmie, J.M., Combust. Flame, 2003, 132, 556-564.

Tolpadi, A. K., Danis, A. M., Mongia, H. C., and Lindstedt, R. P. (1997). "Soot Modeling in Gas Turbine Combustors", ASME Paper 97-GT-149.

Waldman, L. and Schmitt, K.H. Thermophoresis and Diffusiophoresis of Aerosols. In: Aerosol Science, Chap. VI. C.N. Davies (ed.) Academic Press, London (1966).

Wang, R., Cadman, P., Combust. Flame, 1998, 112, 359-370.

Wang, H., and Frenklach, M., "A detailed kinetic and modeling study of aromatics formation in laminar premixed acetylene and ethylene flames", Combustion and Flame, Vol. 110, pp. 173-221, (1997).

Welle, E.J., Roberts, W.L., Careter, C.D., and Donbar, J.M.; "The response of a propane-air counter-flow diffusion flame subjected to a transient flow field", Combustion and Flame, Vol. 135, pp. 285-297 (2003).

Werle, P., "A review of recent advances in semiconductor laser based gas monitors", Spectrochimica Acta Part A, Vol. 54, pp.197-236 (1998);

Willeke and Baron, eds, Aerosol Measurement, Van Nostrand Reinhold, NY, (1993).

Williams, T.C., Shaddix, C.R., Jensen, K.A., and Suo-Anttila, J.M., "Measurement of the Dimensionless Extinction Coefficient of Soot within Laminar Diffusion Flames," Proceedings of the Joint Meeting of the U.S. Sections of the Combustion Institute, Philadelphia, PA, 2005.

Wu, J., Song, K.H., Litzinger, T., Lee, S-Y., Santoro, R., Linevsky, M., "Reduction of PAH and soot in premixed ethylene-air flames by addition of dimethyl ether", Combustion Science and Technology, v. 178, n. 5, May 2006, p. 837-863.

Xu, F., Sunderland, P. B. and Faeth, G. M. "Soot Formation in Laminar Premixed Ethylene/Air Flames at Atmospheric Pressure", *Combust. Flame*, **108**, 471 – 493, 1997.

Yook, S.-J. and Pui, D.Y.H., "Penetration Efficiencies Through Sampling Line", available from Department of Mechanical Engineering, University of Minnesota, May 15, 2005.

Yu, L.E., Hildemann, L.M., Niksa, S., Fuel, 1999, 78, 377-385.

REFERENCES (CONT)

Zelina, J., "Combustion Studies in a Well-Stirred Reactor," Ph.D. Thesis, University of Dayton, Dayton, OH 1995.

Zhang, S-H., Akutsu, Y., Russell, L.M., Flagan, R.C., and Seinfield, J.H., Aerosol Science and Technology, vol 23, pp.357-372, 1995

Zhang, Y., Bauer, S.H., J. Phys. Chem., 1997, B101, 8717-8726.

Zhang, Y., Bauer, S.H., Int. J. Chem. Kinetics, 1999, 31 (9), 656-673.

Zhao, B., Yang, Z., Wang, J., Johnson, M., Wang, H., "Analysis of Soot Nanoparticles in a Laminar Premixed Ethylene Flame by Scanning Mobility Particle Sizer". Aerosol Science and Technology, Vol 37, pp611-620, 2003.

Zhao, B., Yang, Z., Johnston, M. V., Wang, H., Wexler, A. S., Balthasar, M., and Kraft, M., *Combust. Flame* **133**, pp. 173-188, 2003.

Zhao, B., Yang, Z., Li, Z., Johnston, M. V., and Wang, H., Proceedings of the Combustion Institute, 30, The Combustion Institute, pp. 1441-1448, 2005.

APPENDIX

Publications from SERDP Program PP-1179:

Menon, Arvind V., Seong-Young Lee, Milton J. Linevsky, Thomas A. Litzinger and Robert J. Santoro, Addition of NO2 to a Laminar Premixed Ethylene-air Flame: Effect on Soot Formation, accepted for the *2006 International Symposium on Combustion*

Wu, J., Song, K. H., Lee, S.-Y., Litzinger, T. A., and Santoro, R. J., "Reduction of Soot in Premixed Ethylene-Air Flames by Oxygenated Additives: Experiments and Modeling," *Combustion Science and Technology* (in press)

Wu, J., Song, K. H., Lee, S.-Y., Litzinger, T. A., Santoro, R. J., Colket, M., and Liscinsky, D., "Reduction of Soot in Premixed Ethylene-Air Flames by Oxygenated Additives: Experiments and Modeling," *Combustion and Flame* Vol. 144, pp. 675-687 (2006)

V. R. Katta and W. M. Roquemore, "Trimethylphosphate as Soot Reducing Agent—A Numerical Study on Jet Flames," *2006 Technical Meeting of the central States Section of The Combustion Institute*, May 21-23, Cleveland, OH, 2006.

Smooke, M.D., Long, M.B., Connelly, B.C., Colket, M.B. and Hall, R.J., "Soot Formation in Laminar Diffusion Flames," *Combustion and Flame,* v 143, n 4, December, 2005, p 613-628

McNesby, K.L., Andrzej W. Miziolek, Thuvan Nguyen, R. Reynolds Skagg, Valeri Babushok, and Thomas A. Litzinger, Experimental and Computational Studies of Oxidizer and Fuel-side Addition of Ethanol to Opposed-flow Air/Ethylene Diffusion Flames, *Combustion and Flame*, Vol. 142, No. 4, pp. 413-427. (2005)

V. R. Katta, L. G. Blevins, and W. M. Roquemore, "Dynamics of an Inverse Diffusion Flame and its Role on Polycyclic Aromatic Hydrocarbons and Soot Formation" *Combustion and Flame*, Vol. 142, 2005, pp 33-51.

Viswanath R. Katta and William M. Roquemore, "Effect of Nitromethane on Soot Formation in Heptane Jet Diffusion Flame", Proceedings of the *4th Joint Meeting of the US Sections of the Combustion Institute*, March 21-23, Philadelphia, PA, 2005.

Kahandawala, M. S. , S. A. Corera and S. S. Sidhu, "Impact of additives on Soot Yields at 20 bar – A Shock Tube Study", Shock Wave, Proc. *25th International Shock tube and Shock Wave Symposium*, Paper No. 1085-2a, 636-644, (2005).

Stouffer, et al, "Soot Reduction Research Using a Well-Stirred Reactor," paper no. AIAA-2005-1317, *43rd AIAA Aerospace Sciences Meeting*, Reno, NV, January 10-13, 2005

APPENDIX (CONT)

Menon, A., Milton Linevsky, Matthew McKeand, Suresh Iyer, Seong-Young Lee, Thomas Litzinger, and R.J. Santoro, Soot Reduction by NO2 in a Laminar Premixed Flame, Proceedings of the *2005 Technical Meeting of the Eastern States Section of the Combustion Institute*, Orlando, FL, December 2005, 4 pp.

Iyer, S., Thomas Litzinger, and Robert Santoro , Are the Fractal Dimensions of Soot Constant?, Proceedings of the *2005 Technical Meeting of the Eastern States Section of the Combustion Institute*, Orlando, FL, December 2005, 4 pp.

Iyer, S., T. A. Litzinger, and R.J. Santoro, In-situ Measurements of Primary Particle Diameter and Structure of Soot in a Laminar Diffusion Flame, Proceedings of the *2005 Technical Meeting of the Eastern States Section of the Combustion Institute*, Orlando, FL, December 2005, 4 pp.

Smooke, M. D., Hall, R. J., Colket, M. B., Fielding, J., Long, M. B., McEnally, C. S., Pfefferle, L. D., Investigation of the Transition Between Lightly Sooting and Heavily Sooting Coflow Ethylene Diffusion Flames, *Combust. Theory Modelling* 8:593–606 (2004).

Viswanath R. Katta and William M. Roquemore, "Simulation of PAHs in Trapped-Vortex Combustor", GT2004-54165, Proceedings of *ASME Turbo Expo 2004*, June 14-17, Vienna, Austria.

Viswanath R. Katta and William M. Roquemore, "Modeling Soot in a Swirl Combustor", AIAA-2004-0645, *42nd AIAA Aerospace Sciences Meeting and Exhibit*, Jan. 5-8, 2004, Reno, NV.

Colket, M.B., Hall, R.J., Stouffer, S., "Modeling Soot Formation in a Stirred Reactor", paper no. GT2004-54001 Proceedings of *ASME Turbo Expo 2004, Power for Land, Sea, and Air*, Vienna, Austria, June 14–17, 2004,

Song, K. H., Nag, P., Litzinger, T. A., and Haworth, D.C., "Reduction of Aromatic Species by Oxygenated Additives in Fuel-rich, Premixed Ethane Combustion: a Modeling Study," *Combustion and Flame*, Vol. 135, No. 3, pp. 341-349. (2003).

Litzinger, T.A. et al. "Reduction of Particulate Matter Emissions from Burners Part1: Effects of Ethanol." *Joint Meeting of U.S. Sections of Combustion Institute*, Chicago, Il, March 2003.

L. G. Blevins, K.A. Jensen, R.A. Ristau, N.Y.C. Yang, Sandia National Laboratories; C.W. Frayne, R.C. Striebich, M.J. DeWitt, S.D. Stouffer, E.J. Lee, R. A. Fletcher, J.M. Oran, J.M. Conny and G.W. Mulholland; "Soot Inception in a Well-Stirred Reactor" Presented at the *3rd Joint Meeting of the Combustion Institute*, Chicago, IL, 16-19 March, 2003

Viswanath R. Katta and William M. Roquemore, "Investigation of PAH Formation in Different Flames using UNICORN", Proceedings of the *3rd Joint Meeting of the US Sections of the Combustion Institute*, March 16-19, Chicago, IL, 2003.

APPENDIX (CONT)

V. R. Katta, L. G. Blevins, and W. M. Roquemore, "PAH Formation in an Inverse Diffusion Flame", AIAA-2003-0666, *41st AIAA Aerospace Sciences Meeting and Exhibit*, Jan. 5-8, 2003, Reno, NV.

R. F. Reich, S. D. Stouffer, V. R. Katta, H. T. Mayfield, C. W. Frayne, and J. Zelina, "Particulate Matter and Polycyclic Aromatic Hydrocarbon Determination Using a Well-Stirred Reactor" AIAA-2003-0664, *41st AIAA Aerospace Sciences Meeting and Exhibit*, Jan. 6-9, 2003, Reno, NV.

Smooke, M. D., Hall, R. J., and Colket, M. B., "Modeling The Transition From Non-Sooting To Sooting, Coflow Ethylene Diffusion Flames", *3rd Joint Meeting of the U.S. Sections of The Combustion Institute*, Chicago, IL, March 2003.

Moshan Kahandawala, John Graham, and Sukh Sidhu, "Investigation of the Impact of Fuel Composition on Soot Emissions", The Proceedings of the *3rd Joint Meeting of the Sections of the Combustion Institute*, March 16-19, 2003, Chicago, Illinois.

K.L. McNesby and A.W. Miziolek,"Fourier Transform Laser Spectroscopy", *Applied Optics*, Vol. 42, 2127-2131, (2003).

Corporan, E.; Roquemore, W.M; Harrison, W.E.; Jacobson, A. and Phelps, D.K. "Air Force Programs to Reduce Particulate Matter Emissions from Aircraft", *AIAA Joint Propulsion Conference 2002*.

Brown, M.S.; Meyer, T.R.; Gord, J.R.; Belovich, V. and Roquemore, W.M., "Laser-Induced Incandescence Measurements in the Reaction Zone of a Model Gas Turbine Combustor," AIAA Paper 2002-0393, *40th AIAA Aerospace Sciences Meeting and Exhibit*, 14-17 January 2002, Reno, NV.

Stouffer, S.D., Streibich, R.C., UDRI, and Frayne, C.W., and Zelina, J., "Combustion Particulates Mitigation Investigation Using a Well Stirred Reactor" Paper No. AIAA 2002-3723, *38th Joint Propulsion Conference*, 7-10th July 2002

Babushok, V.I.; Tsang, W.; McNesby, K.L. "Additive Influence on PAH Formation", *29th International Symposium On Combustion*, July 2002.

Nag, P., Litzinger, T. A., and Haworth, D.C., "Effect of Oxygenated Additive Molecular Structure on PAH Reduction: A Modeling Study," Proceedings of the *Eastern States Section of the Combustion Institute*, pp. 231-234, 2001.

ACKNOWLEDGEMENTS

The authors would like to express their appreciation to Lt Robert Pawlik, for taking inputs from six different sources and cutting and pasting them into a unified final report. Also, the authors would like to thank Ms. Gayle Byrd for the many hours she devoted to arranging the Figures, Tables, and References into an integrated document. We are also most greatful to Ms Byrd for the considerable time she spent editing the text and finding all of our mistakes. These activities were major undertakings and the hard work put in by Lt Pawlik and Ms. Byrd are most appreciated.

.